SEMMELWEIS EGYETEM

DOKTORI ISKOLA

Ph.D. értekezések

3131.

FELEGYI KRISTÓF

A gyógyszerészeti tudományok korszerű kutatási irányai

című program

Programvezető: Dr. Antal István, egyetemi tanár

Témavezető: Dr. Ványolós Attila, egyetemi docens

Isolation, characterization, and biological evaluation of secondary metabolites from two *Basidiomycetes* species: *Buglossoporus quercinus* and *Xylobolus subpileatus*

PhD thesis

Kristóf Felegyi

Pharmaceutical Sciences Doctoral School

Semmelweis University

Supervisor:	Dr. Attila Ványolós, PharmD, Ph.D.
Official reviewers:	Dr. Sándor Gonda, PhD.
	Dr. Petra Dunkel, PhD.

Head of the Complex Examination Committee:	Dr. Romána Zelkó, PhD.
Members of the Complex Examination Committee:	Dr. László Őrfi, PhD.
	Dr. András Darcsi, PhD.

Budapest

2024

Table of Contents

List of abbreviations

1D	One dimensional
2D	Two dimensional
AACT	Acetyl-CoA acetyltransferase
Abc	Blank control absorbance
Abs	Blank sample absorbance
Ac	Control absorbance
AChE	Acetylcholinesterase
As	Sample absorbance
BChE	Butyrylcholinesterase
BGS	Methods of *Buglossoporus quercinus*
$CHCl_3$	Chloroform
CI	Combination index
CO_2	Carbon dioxide
COSY	Correlation spectroscopy
CYP	Cytochrome P450
DMAPP	Dimethylallyl diphosphate
DMSO	Dimethyl-sulfoxid
DNA	Deoxyribonucleic acid
EC50	Half maximal effective concentration
ED_{50}	Growth inhibition dose
ESI-MS	Electrospray ionization mass spectrometry
EtOAc	Ethyl acetate
ETR	Ergostane-type triterpenoid
FAR	Fluorescence activity ratio
FBS	Fetal bovine serum
FC	Flash-chromatography
FL-1	Mean fluorescence
FPP	Farnesyl-pyrophosphate
FSC	Forward scatter count

GT	Ganoderma triterpenoid
HMBC	Heteronuclear multiple bond correlation
HMGR	3-hydroxy-3-methylglutaryl-CoA reductase
HMGS	3-hydroxy-3-methylglutaryl-CoA synthase
HPLC	High-performance liquid chromatography
HRMS	High-resolution mass spectrometry
HSQC	Heteronuclear single quantum coherence
IC_{50}	Inhibitory concentration 50
IDI	Isopentenyl diphosphate isomerase
IGF-1	Insulin-like growth factor-1
IPP	Isopentenyl pyrophosphate
J	Coupling constants
KR	Ketoreductase
L-DOPA	Levodopa
LTR	Lanostane-type triterpenoid
MCF7	Breast adenocarcinoma cells
MDR	Multidrug resistance
MeOH	Methanol
MIC	Minimum inhibitory concentration
MK	Mevalonate kinase
MPK	Phosphomevalonate kinase
MRC-5	Lung fibroblast cell line
MTT	Thiazolyl blue tetrazolium bromide solution
MVA	Mevalonate pathway
MVD	MVA-5-diphosphate decarboxylase
MVD	Phosphomevalonate decarboxylase
NMR	Nuclear magnetic resonance
NOE	Nuclear Overhauser Effect
NOESY	NOE spectroscopy
NP	Normal phase
NRP	Non-ribosomal peptide

NRPS	Non-ribosomal peptide synthase
OD	Optical density
OSC	2,3-oxidosqualene-lanosterol cyclase
PK	Polyketide
PKS	Polyketide synthetase
PLA2	Phospholipase A2
PSPP	Pre-squalene diphosphate
ROESY	Rotating frame Overhauser effect spectroscopy
ROS	Reactive oxygen species
RP	Reversed phase
RS	RediSep
SA	Salicylic acid
SAR	Structure-activity relationship
SD	Standard deviation
SDS	Sodium dodecyl sulfate
SQE	Squalene monooxygenase
SS	Squalene synthase
SSC	Side scatter count
TLC	Thin-layer chromatography
TOCSY	Total correlation spectroscopy
UHPLC	Ultrahigh-performance liquid chromatography
XB	Methods of *Xylobolus subpileatus*

I. Introduction

In the human history, nature has consistently served as a reservoir of a wide-range medicinal compounds, offering bioactive substances from living organisms that function as direct pharmaceuticals or as prototypes for drug development [1]. While plants have played a prominent role in global medical traditions, contributing significantly to both traditional and evidence-based medicine, the historical medicinal use of mushrooms, especially in Western contexts, has been predominantly confined to Asian regions [2, 3]. However, an increasing global interest in medicinal mushrooms is evident through increasing product sales, and a surge in scientific research.

Medicinal mushrooms, primarily higher *Basidiomycetes*, are macroscopic fungi utilized in extract or powder form for the prevention, alleviation, and healing of diseases, or for nutritional purposes [4]. Despite their current designation as dietary supplements or functional food, these mushrooms can become the latent potential to evolve into pharmaceutical agents within traditional and/or evidence-based medicine. Realizing this latent potential necessitates the development of high-quality products, adherence to regulatory standards, and legal authorization through comprehensive preclinical and clinical trials[5].

Important medicinal mushrooms include *Ganoderma lucidum*, *Trametes versicolor*, *Lentinula edodes*, *Agaricus brasiliensis*, *Cordyceps sinensis*, *Grifola frondosa*, *Hericium erinaceus*, among others. These species, steeped in traditional use, offer invaluable insights into *in vitro* activities, mode of action, and effects in animal assays. Despite the wealth of traditional knowledge, a comprehensive exploration of the pharmacology and chemistry of these mushrooms, as well as lesser-explored species, emerges as a pressing imperative [6].

The current situation underlines critical research gaps, including the exploration of structure-activity relationships, potential toxicological risks associated with mushroom products, clinical trials, and the establishment of more rigorous quality criteria for mushroom-derived products. Additionally, standardized methodologies are important to ensure careful control and uphold the quality of these products [6].

As the worldwide interest of medicinal mushrooms continues to grow, addressing the identified research gaps assumes importance for advancing our understanding of their

pharmacological potential. This effort is essential for ensuring the safe and effective integration of medicinal mushrooms into traditional and evidence-based medicine, promising the discovery of novel therapeutic agents derived from fungal sources.

1. General description of *Basidiomycota*

1.1. *Basidiomycota*: reproductive strategies and evolutionary significance

Fungi originally grouped with plants, are now recognized as a distinct terrestrial, achlorophyllous, and eukaryotic kingdom (Figure 1.), closely related to animals [7]. Shared characteristics with animals include the presence of chitin, glycogen as a stored food source, and the mitochondrial ribonucleic acid bases coding for tryptophan [8].

Figure 1. *Basidiomycota* colonization on oak trees [9] (left) and phylogenetic tree of life [10] (right)

The multicellular fungal body comprises filaments known as hyphae, forming the mycelium [9]. Fungi exhibit a simple organization but can develop various complex reproductive structures, adapting to diverse habitats worldwide. While around 100,000 fungal species have been described, estimates suggest over 1.5 million undiscovered species [10]. Fungi play crucial roles as principal decomposers, releasing carbon dioxide (CO_2) and nitrogenous compounds into the biosphere. They also contribute to bioweathering processes and mineral transformation [11]. Involved in various associations, fungi interact with other organisms, causing diseases or forming beneficial symbiotic relationships like mycorrhizae [12]. Despite their long geologic history, fungi

have only recently been extensively studied. The fossil record of fungi faced challenges due to perceived fragility, difficulties in recognition, and biases in fossil collection. Modern techniques, including quantitative field approaches, have addressed some biases, environmental conditions during deposition and fossilization also influence preservation. The literature on fossil fungi and their interactions is rapidly growing, though some details, especially regarding ecosystem-level fungal interactions, remain challenging to determine from fossils [13].

Phylogeny of the fungi was once based on morphology and, in some cases, characteristics in laboratory cultures. Today, the fungal tree of life is constantly refined using various molecular sequences [14]. Most analyses include five Phyla within the fungi, three of which, the *Glomeromycota*, *Ascomycota*, and *Basidiomycota*, are considered monophyletic (Figure 2.). The other fungi, which are considered to be the earliest-

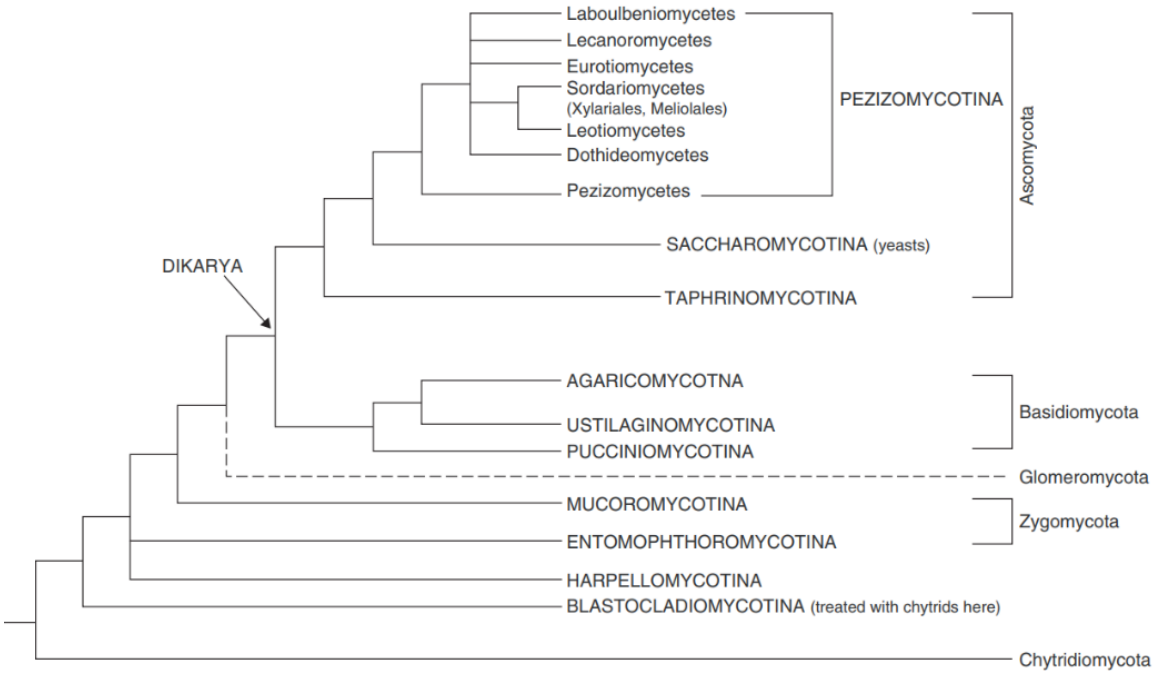

Figure 2. Relationships of major fungal groups [15]

diverging based on molecular phylogenies, include the paraphyletic groups, *Chytridiomycota* and *Zygomycota* [16, 17].

1.2. Characterizing *Basidiomycota*: diversity and functional insight

Basidiomycota, characterized by cellular hyphae, reproduce sexually with basidia producing basidiospores on large fruiting bodies called basidiocarps, commonly known as mushrooms [18]. True mushrooms have a cap with scales, gills for spore production, a stem with a skirt or ring, and a volva at the base. The mycelial threads underground serve as conduits for nutrients. The reproductive process involves basidiospores dispersing for new mycelial colonies [19]. Other *Basidiomycota* species include jelly fungi, rusts, and smuts, which differ significantly from typical mushrooms. Jelly fungi, exemplified by *Tremellales* and *Dacrymycetales*, form a paraphyletic group derived from a common ancestor [20]. Rusts, widespread plant pathogens, infect specific plant genera or species, appearing as orange or brown spore coatings on living plants. Smuts, belonging to *Ustilaginomycetes*, produce thick-walled teliospores and commonly affect the grass family *Poaceae*, impacting economically important crops like corn, barley, wheat, and sugarcane. Notably, *Ustilago maydis*, or corn smut, is considered a delicacy in Mexico. These non-mushroom *Basidiomycota* species showcase diverse ecological roles and interactions with plants [15].

1.3. *Basidiomycota* reproduction: Unraveling spore formation

Basidiomycota, distinct from organisms exhibiting clear male-female dichotomies, particularly in the context of the rusts, typically feature mutually indistinguishable, compatible haploids [21]. These haploids, often manifesting as mycelia composed of filamentous hyphae, undergo plasmogamy, culminating in the formation of dikarya wherein nuclear fusion is notably deferred. Subsequently, karyogamy transpires, leading to the establishment of a dikaryon characterized by the sustained pairing of compatible nuclei [22]. The resultant dikaryotic mycelium, demonstrably endowed with heightened vigor compared to individual monokaryotic mycelia, frequently dominates its substrate, exhibiting prolonged viability spanning years, decades, or even centuries (Figure 3.).

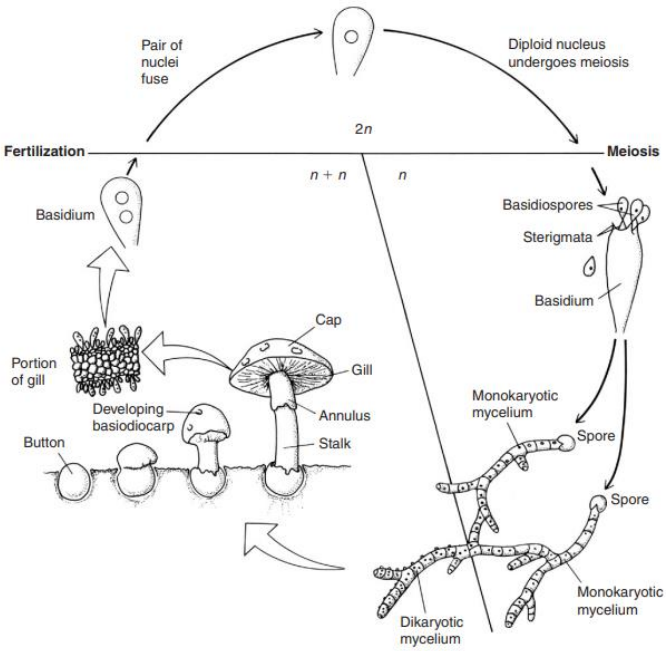

Figure 3. *Basidiomycota* life cycle [15]

The sustenance of dikaryotic states in *Basidiomycota* is facilitated by the formation of clamp connections. These structures, physically observable, seemingly contribute to the coordination and reinstatement of pairs of compatible nuclei following synchronized mitotic nuclear divisions [22]. Divergent patterns and variations characterize this phenomenon. In the conventional *Basidiomycota* lifecycle, persistent dikaryons periodically give rise to basidia, specialized club-shaped terminal cells, wherein a karyogamy event between a pair of compatible nuclei transpires, yielding a diploid cell [23]. Subsequent meiosis produces four haploid nuclei, which migrate into external basidiospores. The ballistic nature of basidiospores, often propelled by sterigmata, a kind of tapered spine on basidia, is a notable feature [24]. In certain *Basidiomycota*, spores may not be ballistic, and sterigmata might be straight, reduced to stubs, or altogether absent. Non-ballistosporic basidia may release spores via budding, dissolution, or disintegration [24].

In summary, the *Basidiomycota* life cycle is complexly orchestrated, with meiosis occurring within diploid basidia, resulting in haploid basidiospores that initiate new monokaryotic mycelia. The absence of traditional male and female designations is compensated by compatible thalli with diverse compatibility factors. Plasmogamy

triggers the establishment of a dikaryon, a notably enduring state that ultimately gives rise to either fruitbodies with basidia or basidia directly. The diploid basidium, following karyogamy, initiates the cycle anew.

2. Primary and secondary metabolites in fungi

2.1. Overview

A primary metabolite (Figure 4.) is a fundamental type of metabolite involved in essential processes like growth, development, and reproduction within an organism. It serves basic physiological functions and is commonly found across various organisms or cells. Often referred to as central metabolites, these compounds are crucial for the autonomous growth of cells or organisms. Examples of primary metabolites encompass ethanol, lactic acid, and specific amino acids. Certain primary metabolites act as precursors for the synthesis of secondary metabolites [25].

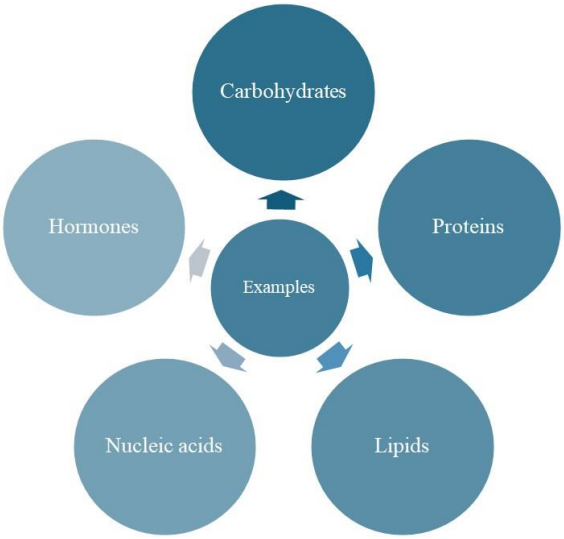

Figure 4. Primary metabolites in living organism [25]

Secondary metabolites represent chemical compounds synthesized through specific biosynthetic pathways, whose production is not indispensable for the typical growth and development of fungi. Nevertheless, their widespread presence across numerous species suggests they confer competitive advantages in natural environments. This entry aims to explore the principal families of secondary metabolites, elucidate the genetic foundations

and regulatory mechanisms governing their synthesis, and offer a brief overview of their chemical diversity [26] (Figure 5.).

- Polyketides (PKs)
- Non-ribosomal peptides (NRPs)
- Hybrid non-ribosomal peptide/Polyketides
- Terpenoids

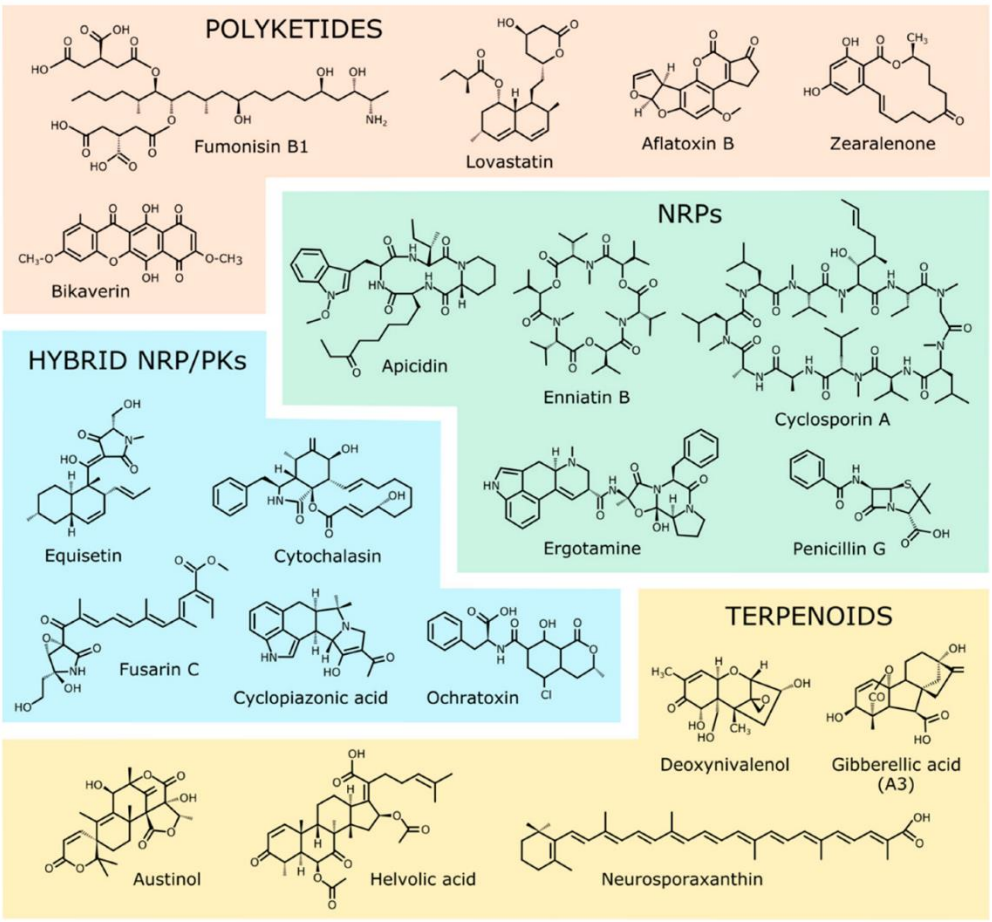

Figure 5. Structural depictions of representative secondary metabolites from the four major families discussed [27]

Polyketides

Polyketides represent a particularly abundant and diverse family of secondary metabolites. Their biochemical pathways commence with the addition of acetyl-coenzyme A units, yielding various structures through a diverse array of chemical reactions [28]. These pathways are initiated by a characteristic enzyme called polyketide

synthetase (PKS), first identified in bacteria. PKSs are classified into three types based on their structures and mechanisms: types I, II, and III [29]. Type I PKSs are large multifunctional enzymes structurally akin to fatty acid synthetases, featuring conserved domains such as acyltransferase, ketosynthase, and acyl carrier protein. Additional optional domains, like ketoreductase and dehydratase, further modify the elongating polyketide chain. PKSs can be iterative or non-iterative, with iterative PKSs extending the product in successive cycles and non-iterative PKSs functioning as modular units. Type II PKSs [30], prevalent in prokaryotes, produce aromatic compounds via multienzymatic complexes. Type III PKSs [31], found in both fungi and plants, are homodimeric enzymes involved in chalcone biosynthesis, differing from type I PKSs in their interaction with acyl CoA substrates. While PKs typically exhibit well-defined chemical structures, exceptions like melanins pose challenges due to their polymeric nature. Overall, PKs showcase vast chemical diversity, with examples synthesized by type I PKSs including zearalenone.

Non-ribosomal peptides

Non-ribosomal peptides are small peptides characterized by their diverse chemical compositions. Unlike typical proteins synthesized on ribosomes, NRPs are produced through a mechanism independent of ribosomal protein synthesis. Notably smaller in size compared to proteins, NRPs exhibit distinct structural features, often adopting cyclic forms and incorporating atypical amino acids like hydroxylated or methylated variants, as well as D forms [32]. Unlike proteins, which undergo modifications post-synthesis, NRPs undergo chemical alterations in their amino acids during their assembly process or by other enzymes after their release. Similar to PKs, NRPs are synthesized by large multi-enzyme complexes called NRP synthetases (NRPSs). These complexes are typically structured into modules, each comprising multiple catalytic domains that work in concert. A typical module consists of an adenylation domain and a thiolation domain, which sequentially add to the growing peptide chain [33].

Hybrid Non-Ribosomal Peptide/Polyketides

Certain secondary metabolites are produced through the collaborative action of both PKS and NRPS [34]. These enzymatic complexes may be encoded by separate genes yet work together within the same biosynthetic pathway. For instance, this setup is observed in the biosynthesis of ochratoxin A in *Aspergillus* and *Penicillium* species [35].

The structural similarities between type I PKS and NRPS modules have facilitated the emergence of chimeric genes, which incorporate both PKS and NRPS modules [36].

Terpenoids

Terpenoids, also referred to as isoprenoids, constitute one of the largest and most structurally diverse groups of natural compounds. The term "terpene" originally denoted hydrocarbons discovered in turpentine, with the suffix "ene" indicating the presence of olefinic bonds. Terpenoids are categorized according to the number and structural arrangement of carbons, which are formed by the sequential arrangement of isoprene units followed by cyclization and rearrangements of the carbon skeleton, guided by the isoprene rule. Isoprene, serving as the fundamental "building block" of terpenoids, is chemically represented as 2-methylbuta-1,3-diene (C_5H_8). The simplest class of terpenoids, hemiterpenoids, consists of a single isoprene unit. The classification of terpenoids is based on the number of isoprenoid units they contain. Notably, the primary groups of terpenoids include [37]:

Monoterpenes are composed of two isoprene units.

Sesquiterpenes consist of three isoprene units.

Diterpenes: are formed from four isoprene units.

Triterpenes: are composed of six isoprene units.

2.2. Structural diversity of secondary metabolites from *Basidiomycota*

Recent investigations into mushrooms have revealed structurally diverse bioactive fungal metabolites. Laccanthrilic acids A-C, previously undescribed anthranilic acid derivatives, were isolated from *Laccaria laccata* [38]. Pulvinic acid derivative pigments with significant antimicrobial and/or cytotoxic effects were isolated from the Thai edible basidiomycetes *Phlebopus portentosu*s and *P. spongiosus* [39]. *Mycena rosea*'s fruiting

bodies yielded mycenarubin C, an eight-membered ring molecule with a unique C1 unit [40]. Two highly *N*-methylated cyclic peptides were isolated from *Gymnopus fusipes* by Ványolós et al., gymnopeptide A and B [41] (Figure 6.).

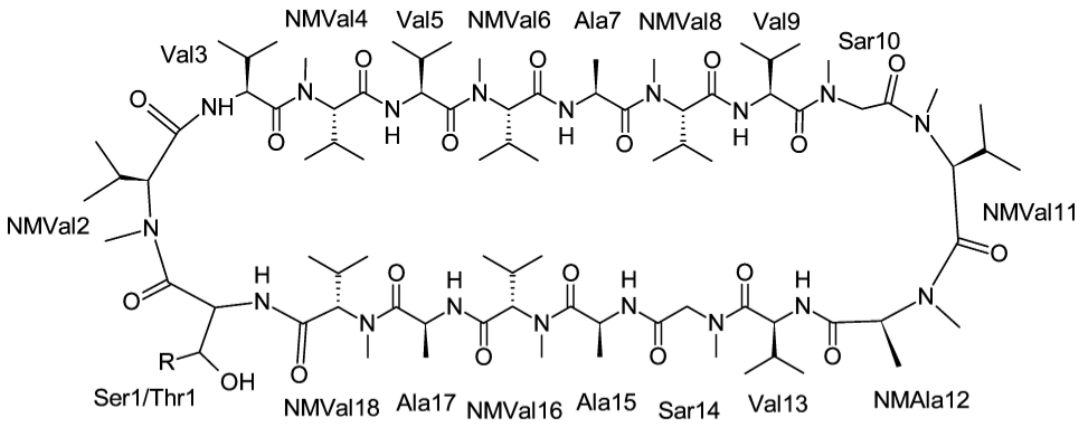

Figure 6. Sequences of gymnopeptides A (R = H) and B (R = CH3) [46]

Monoterpenoids (Figure 7.) and polyynes found in several basidiomycetes exhibited diverse bioactivities such as antibacterial, antifungal or antitumor activities. Hormone-like monoterpentriols were early isolates from the edible mushroom *Flammulina velutipes* [42]. Recently, a new menthane monoterpenoid, 4-hydroxy-4-isopropenylcyclohexanemethanol, was identified in *Craterellus cornucopioides* [43], while (*4S,5S*)-4-hydroxy-3,5-dimethoxycyclohex-2-enone was isolated from *Inonotus hispidus* [44]. Additionally, the polyyne derivative feldin was isolated from *Fistulina hepatica*, exhibiting high toxicity to *Saccharomyces* cerevisiae [45].

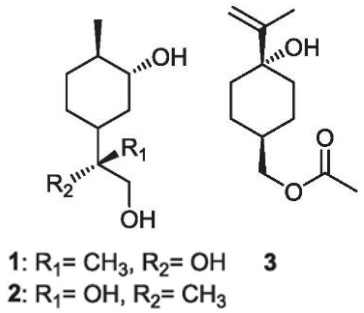

Figure 7. Monoterpenoids isolated from *Flammulina velutipes* (1-2) and *Craterellus cornucopioides* (3) [46];
1: (*1R, 2R, 4R, 8S*)-(-)-*p*-menthane-2,8,9-triol; **2**: (*1R, 2R, 4R, 8R*)-(-)-*p*-menthane-2,8,9-triol (2); **3**: 4-hydroxy-4-isopropenylcyclohexanemethanol

Sesquiterpenoids (Figure 8.) represent another vast class of secondary metabolites in fungi. These compounds display diverse biological activities, as an example tricyclic trichothecenes drawing attention due to their potential toxicity as contaminants in agriculture [47]. Newly discovered sesquiterpenoids from different mushroom species have garnered attention in recent studies. For example, compounds such as phelinanes sourced from *Tropicoporus linteus* are now utilized in mouthwash and toothpaste formulations [48]. Erinachromanes and erinaphenol from *Hericium erinaceus* demonstrate plant-growth regulatory effects [49], while drimane-type sesquiterpenoids, such as those from *Cyathus africanus*, show neuroprotective effects [50] (Figure 8.).

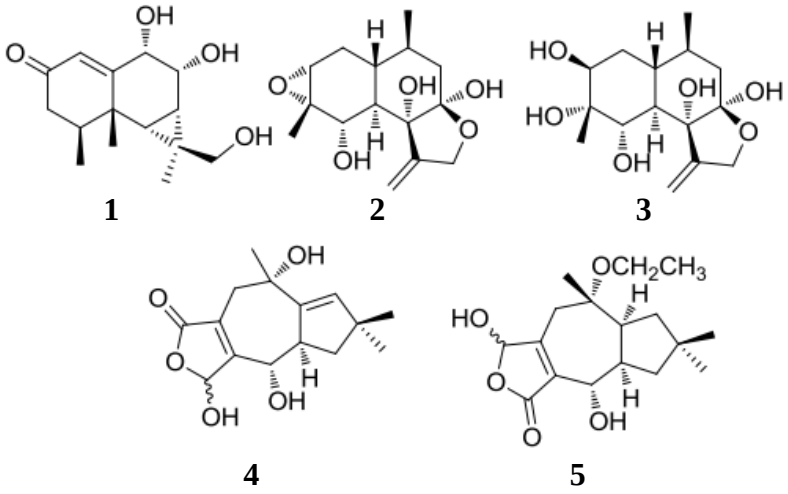

Figure 8. Chemical structure of sesquiterpenoids, cadenine and lactarane type fungal metabolites [51];

1: Rulepidatriol B from *Russula lepida*; **2-3**: Strobilol A and D from *Strobilurus ohshimae*; **4-5**: 1,2-Dehydrolactarolide A and 3- *O*- ethyllactarolide B from *Lactifluus vellereus*

Diterpenes (Figure 9.), a diverse group in the fungal terpenome, exhibit extensive modifications on the diterpene scaffold, catalyzed by various tailoring enzymes. Cyathane diterpenoids, notably cyathane-xylosides, found exclusively in mushroom-forming basidiomycetes, feature a unique 5–6–7 tricyclic carbon skeleton [52]. Fungi of the genus *Cyathus*, known as 'bird's nest fungi,' are prolific producers of cyathane diterpenes. Recent isolations from *Cyathus africanus* include new cyathane and drimane sesquiterpenoids [50] (Figure 9.).

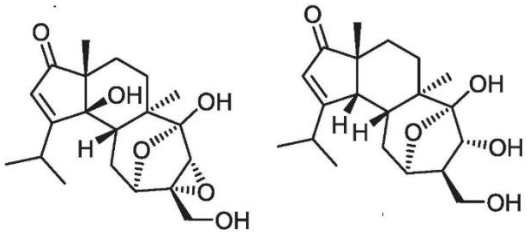

1 **2**

Figure 9. Chemical structure of diterpenes [46];

1-2: Cyafricanin G and H from *Cyathus africanus*

In conclusion, the division of *Basidiomycota* fungi stand out as a rich source of secondary metabolites. Despite ongoing discoveries, the full potential of these metabolites from the fungal phylum remains untapped.

2.3. Lanostane and ergostane-type triterpenoids

2.3.1 Structural features of lanostane and ergostane-type triterpenoids

Since our isolated compounds are primarily lanostane- and ergostane-type triterpenoids (LTR and ETR), therefore I would like to provide a more detailed introduction to these specific classes of secondary metabolites. Fungi have developed the capacity to synthesize a diverse array of specialized metabolites, which serve specific functional roles in their adaptation to natural changes. Triterpenoids, constituting one of the most extensive subclasses of these metabolites with over 50000 identified structures, contribute significantly to defense and development [53]. Additionally, these compounds exhibit promising applications in the fields of food and pharmaceuticals [54]. Triterpenoids can be accumulated in many medicinal plants and fungi and generally contain 29-35 carbon atoms with a wide variety of functional groups. There are several types of skeleton systems with different type and position of functionalization such as aldehydes, ketones or even carboxylic acids [37]. They can be classified in two groups according to the ring number: tetra and pentacyclic compounds. In contemporary research, tetracyclic triterpenoids, spanning diverse groups such as dammarane, cucurbitane, cycloartane, lanostane, and protostane, ergostane have garnered significant attention [55]. In contrast to plants and marine organisms, triterpenoids derived from medicinal fungi predominantly assume tetracyclic forms, particularly the lanostane-type and ergostane-

type, although examples of pentacyclic triterpenoids like lupane-type and ursane-type have also been observed [56]. Emphasizing the unique structural characteristics of triterpenoids across different medicinal fungi is crucial. For instance, the lanostane and ergostane skeleton comprises four fused rings identified as A, B, C, and D (Figure 10.).

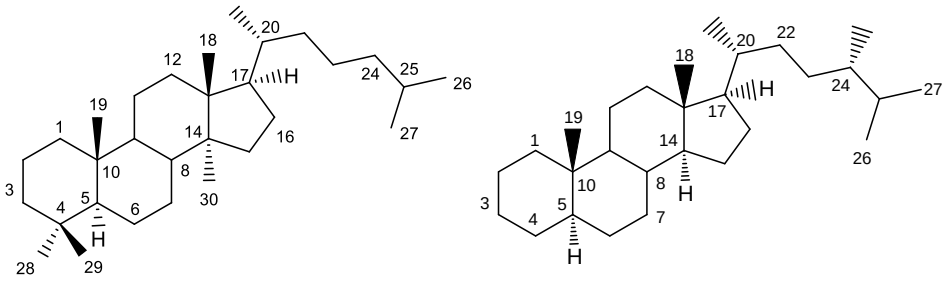

Figure 10. General structure of lanostane-type (left) and ergostane-type (right) triterpenoids

Ring A: Typically comprising a six-membered ring, feature one or more oxygen atoms, manifesting as hydroxyl (-OH), ester (-COOR), or ether (-OR) groups. The three-dimensional conformation of the molecule can exhibit considerable variability. Within triterpenes, functional groups may adopt axial or equatorial orientations. If positioned above the plane of the ring system, they are labeled as β, while those below the plane are denoted as α. In instances where the orientation of substituents is uncertain, it is represented by the symbol ξ. The sites of unsaturation in triterpenoids are indicated using the Greek letter Δ.

Ring B: Typically, a six-membered ring, fused to ring A and containing several different types of carbon atoms ie. sp^2, alkene-type or sp^3 alkane-type.

Ring C: Usually a six-membered ring, fused to ring B and functionalized with oxygen containing group ie. hydroxyl (-OH) or ketone (=O) groups.

Ring D: Typically, a five-membered ring, fused to ring C and may contain oxygen atoms.

Functional groups: Lanostane and ergostane triterpenoids often contain various functional groups such as hydroxyl (-OH) groups, ketones (=O) and sometimes esters (-COOR) [57, 58].

Stereochemistry: The specific arrangement of atoms in space can vary among different lanostane-type triterpenoids, influencing their biological activity and properties. The cyclization of 2,3-oxidosqualene leads to a chair-boat-chair A-B-C ring conformation in the case of lanostane and ergostane-type triterpenoids [59].

Substituents: Methyl (-CH_3) or other side chains may be present on the rings, influencing the compound's overall chemical and physical properties. In the case of lanosta type derivatives a 4,4-dimethyl group is observable meanwhile in the case of ETRs it is absent. Another observable feature is the presence of the C30 methyl group in the LTRs group.

Due to their structural complexity, these compounds serve as important lead compounds for the development of pharmaceuticals and other bioactive agents. The structural variations among triterpenoids (Figure 11.) contribute to their wide range of biological activities and potential therapeutic applications [60].

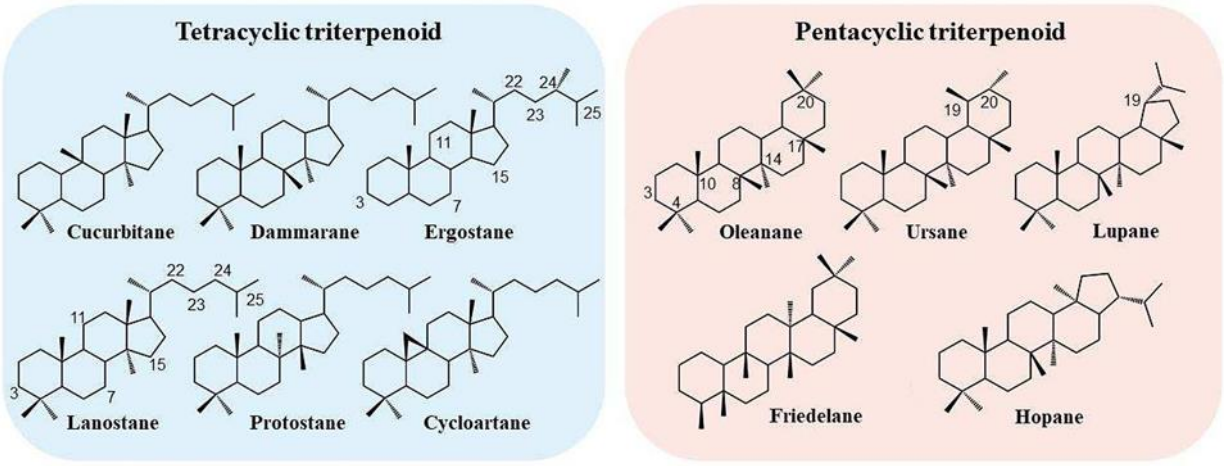

Figure 11. Structures of the main tetracyclic and pentacyclic triterpene skeletons [61, 62].

2.3.2 Biosynthesis of LTR and ETRs

Among *Basidiomycetes, Ganoderma* species synthetize triterpenes of a spectacular diversity, also known as ganoderma triterpenoid (GTs) compounds. The biosynthesis of these secondary metabolites occurs through the mevalonate pathway (MVA) [63], starting from acetyl-coenzyme A. The MVA pathway enzymes are distributed in different subcellular compartments. This pathway involves several processes, including

condensation, construction, conversion and post-modification, leading to the formation of isopentenyl pyrophosphate (IPP) and possibly dimethylallyl phosphate. First from acetyl-coenzyme A to isopentenyl diphosphate and dimethylallyl diphosphate (DMAPP) via ATP-dependent phosphorylation with isopentenyl diphosphate isomerase (IDI). IDI is used to produce the DMAPP and MVA-5-diphosphate decarboxylase (MVD) is used to produce IPP. The IPP precursor is involved in the production of all terpenoid and higher order terpenoid building blocks trough the fusion of IPP and DMAPP to farnesyl-pyrophosphate (FPP) and geranyl-geranyl-pyrophosphate [59]. These building blocks undergo self-condensation and other processes to produce triterpenoid skeletons, which are further modified through oxidation, reduction, conjugation, and isomerization reactions [64]. The conversion of FPP to squalene involves two sequential reactions. Initially, squalene synthase (SS) catalyzes the fusion of two FPP molecules, leading to the formation of pre-squalene diphosphate (PSPP). Subsequently, in the second reaction, PSPP is transformed into squalene under the influence of SS. Squalene monooxygenase (SQE), also known as squalene epoxidase, is a flavin adenine dinucleotide-dependent epoxidase enzyme. SQE utilizes NADPH and molecular oxygen to oxidize squalene, converting it into 2,3-oxidosqualene, which is also referred to as squalene epoxide. This initial oxygenation step in terpenoid biosynthesis is catalyzed by SQE and is a crucial and potentially rate-limiting enzyme in the pathway. Despite its significance, the lack of comprehensive understanding regarding the structure and function of SQE has impeded the development of inhibitors targeting this enzyme. Numerous scientists are actively engaged in elucidating the structural basis and the specificity of the SQE-catalyzed epoxidation reaction. This knowledge is decisive for the rational design and development of the next generation of inhibitors [65]. It is noteworthy that 2,3-oxidosqualene serves as a common precursor for the biosynthesis of various compounds, including steroidal saponins, triterpenoid saponins, and phytosterols. For the summary and without further detail just to see how complicated the biosynthetic pathway is the MVA pathway involves enzymes such as acetyl-CoA acetyltransferase (AACT), 3-hydroxy-3-methylglutaryl-CoA synthase (HMGS), 3-hydroxy-3-methylglutaryl-CoA reductase (HMGR), the rate-determining enzyme is anchored to the endoplasmic reticulum, mevalonate kinase (MK), phosphomevalonate kinase (MPK), phosphomevalonate decarboxylase (MVD), IDI,

farnesyl diphosphate synthase, SS, SQE, and 2,3-oxidosqualene-lanosterol cyclase (OSC) (Figure 12.) [55]. Several studies on GTs, particularly in *G. lucidum*, have focused on understanding the relationship between triterpenoid content and the expression levels of key genes. Genes involved in the MVA pathway, including HMGR, farnesyl diphosphate synthase, SS, and OSC, have been identified and cloned [66-68]. Researchers have explored the impact of various factors, such as salicylic acid (SA) and calcium ions on triterpenoid biosynthesis [69]. In summary, understanding the key enzyme genes and their regulation in the biosynthetic pathways of GTs provides valuable insights for optimizing triterpenoid production and exploring their potential applications.

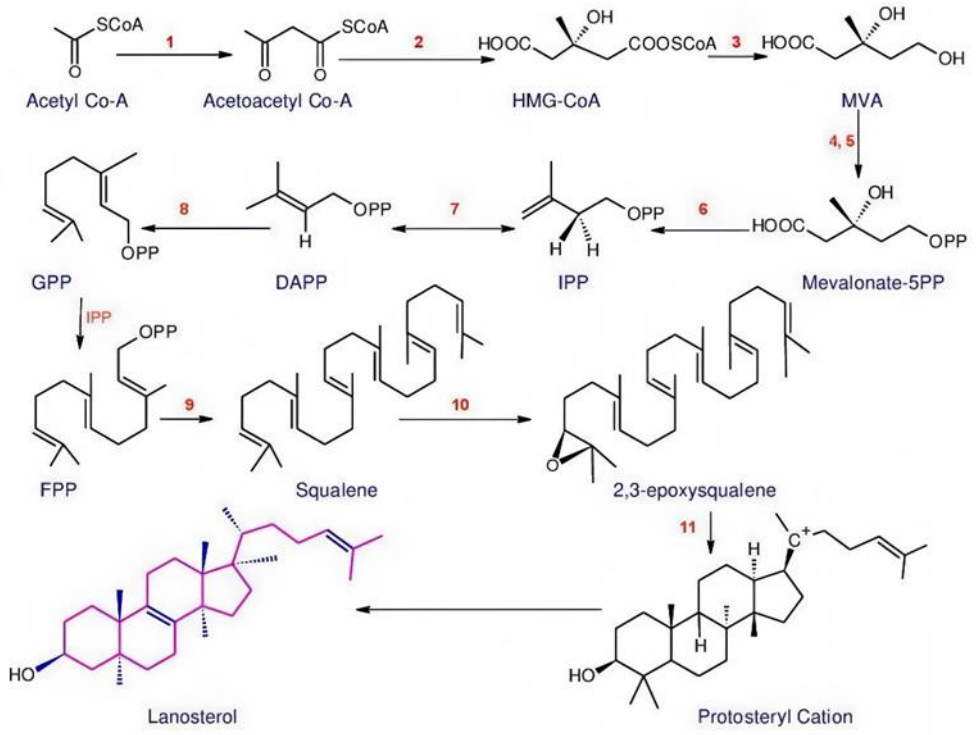

Figure 12. Elucidating the biosynthesis pathway of MVA and lanostane-type triterpenoids: A comprehensive overview of enzymatic processes: 1. AACT; 2. HMGS; 3. HMGR; 4. MK; 5. MPK; 6. MVD; 7. IDI; 8. FPP; 9. SS; 10. SQE; 11. OSC [55, 70]

The prevailing consensus is that the cyclization of 2,3-oxidosqualene into sterols involves the protosteryl cation and proceeds through a conformational arrangement termed "chair-boat-chair". In contrast, triterpenoid biosynthesis, facilitated by the dammarenyl cation,

follows a conformational pattern known as "chair-chair-chair" in the conversion of 2,3-oxidosqualene [71] (Figure 13.).

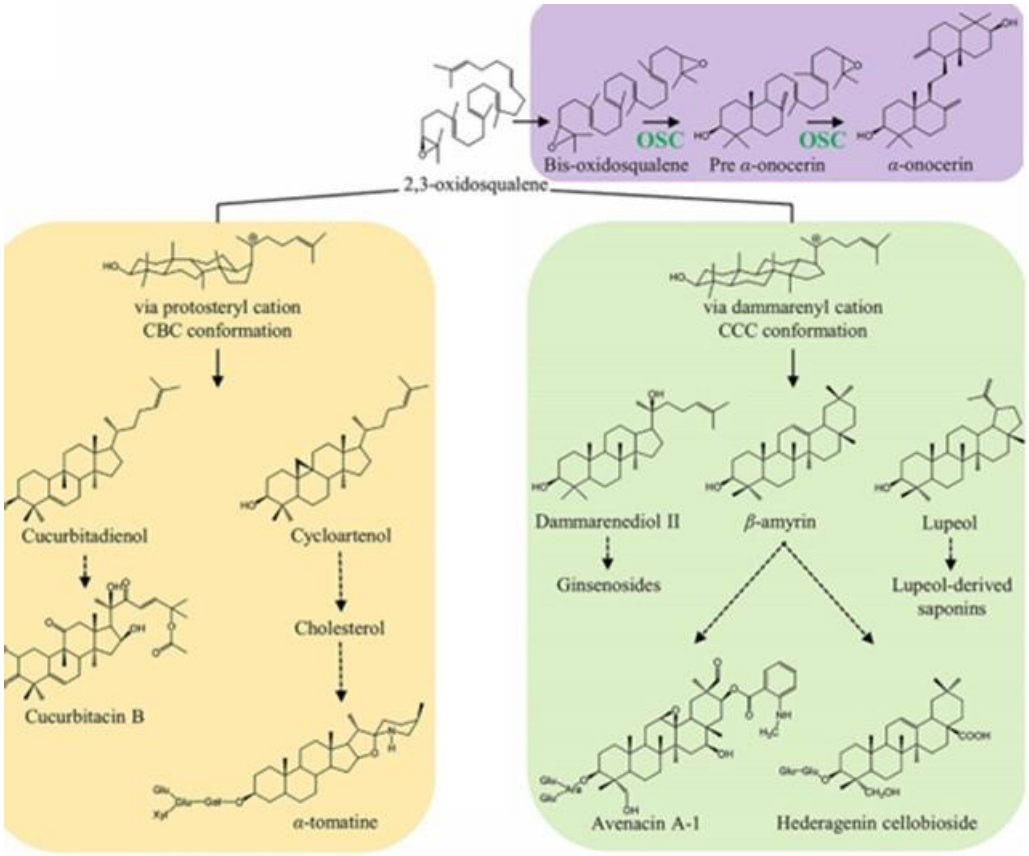

Figure 13. Simplified representation of the biosynthesis of sterols and other triterpenoids [71]

Studies have identified candidate genes responsible for encoding biologically active compounds derived from *Antrodia cinnamomea*. One such gene, AcCyp51, encodes cytochrome P450 (CYP) sterol 14-α-demethylase. It has been demonstrated that AcCyp51 is involved the cyclization of squalene into a lanostane triterpene skeleton, subsequent demethylation to ergostane, and further modification into various triterpenoids. Notably, the expression level of AcCyp51 in fruiting bodies surpassed that in other tissues. Moreover, five genes encoding the CYP512 P450 enzyme and three genes encoding the CYP5140 enzyme exhibited peak expression levels in the fruiting body.

This suggests their potential involvement in the modification of ergostane-type triterpenoids [72].

2.3.3 Bioactivity of lanostane-type triterpenoids

Lanostane-type triterpenes, a class of natural compounds primarily found in various fungi, have shown promising bioactivity across a range of physiological and pathological conditions. They have a wide range of bioactive potential in addressing metabolic disorders such as Type 2 diabetes mellitus, inflammatory diseases, and as anticancer agents.

Bioactivity in Type 2 Diabetes Mellitus

Type 2 diabetes mellitus is characterized by chronic hyperglycemia due to insulin resistance and insufficient insulin secretion [73]. Lanostane triterpenes have been studied for their effect in these conditions by targeting key enzymes involved in carbohydrate metabolism:

- **Inhibition of Aldose Reductase**: Ganoderic acid Df, isolated from *G. lucidum*, has shown potential as an inhibitor of human aldose reductase with an inhibitory concentration 50 (IC_{50}) of 22.8 μM [74] in comparison to quercetin, which had an IC_{50} of 4.8 ± 0.4 μM.
- **α-Glucosidase Inhibition**: Studies involving *Inonotus obliquus* have highlighted lanostanoids such as inotolactone A and B, which exhibited superior inhibitory activity on α-glucosidase compared to acarbose, a standard inhibitor [75].

Anti-inflammatory Properties

Lanostane-type triterpenes also exhibit significant anti-inflammatory effects by targeting enzymes like phospholipase A2 (PLA2), which are involved in the pathogenesis of chronic autoimmune diseases:

- **PLA2 Inhibition**: Compounds such as those isolated from *G. lucidum* have demonstrated efficacy *in vivo* against various models of inflammation in mice. The inactivation of PLA2 by these compounds suggests a mechanism involving the blocking of the enzyme's catalytic site, crucial in controlling the inflammatory cascade [76].

Anticancer Potential

Lanostane triterpenes have shown cytotoxic activities against various cancer cell lines, offering a promising avenue for cancer treatment:

- **Cytotoxic and Anti-metastatic Effects**: Ganoderic acid T [77] and specific ganoderic acids like A and H have been reported to exert dose-dependent cytotoxic effects on carcinoma cell lines and suppress metastatic behaviors in breast cancer models [78]. These effects are attributed to the inhibition of key transcription factors and signaling molecules involved in cancer cell proliferation and metastasis.

Antimicrobial Activity

The antimicrobial activity of these compounds can vary significantly. This variable activity highlights the need for further investigation into the antimicrobial potential of these compounds. For instance, cattienoids A-C, isolated from the fruiting bodies of *Tomophagus cattienensis* [79] did not exhibit antimicrobial activity according to studies by Hien et al. In contrast, lanostane-type triterpenes isolated from *Fomitopsis pinicola* and *G. lucidum* displayed modest antimicrobial effects [80, 81]. A notable example of this activity involves the assay of five lanostanes against *Bacillus cereus*, where they demonstrated minimum inhibitory concentration (MIC) values ranging from 16 to 64 μg/mL[81]

2.3.4 Bioactivity of ergostane-type triterpenoids

Ergosterol derivatives: Ergosterol has demonstrated significant therapeutic potential in treating and managing various diseases, particularly through its anti-inflammatory, anti-diabetic, and anticancer properties:

- **Anti-inflammatory:** Ergosterol derivatives such as 9-dehydroergosterol have been shown to reduce neurotoxicity and prevent neuronal death induced by over-activated microglia, suggesting a role in preventing dementia [82].
- **Diabetic nephropathy:** Ergosterol has shown efficacy in attenuating kidney damage in diabetic mice by restoring blood glucose and serum insulin levels and improving renal functions. Its action in promoting glucose uptake positions it as a potential hypoglycemic agent [83] .
- **Cancer:** Ergosterol has been explored for its anticancer properties across multiple cancer cell lines (lung, liver, breast, gastric, prostate), and has been particularly

noted for enhancing the cytotoxicity of chemotherapy drugs like adriamycin in resistant cancer cell models [84].

Endoperoxides: Endoperoxides such as ergosterol peroxide and 9,11-dehydroergosterol peroxide have been investigated for their robust cytotoxic activities and potential antibacterial properties:

- **Cytotoxicity:** These compounds have demonstrated significant cytotoxic effects across a range of cancer cell lines, though the variability in cytotoxic measurements underscores the complexity of their biological interactions. Ergosterol peroxide and 9,11-dehydroergosterol peroxide are frequently derived from identical fungal sources, displaying broadly comparable biological characteristics. However, dehydroergosterol showed slightly higher cytotoxicity compared to ergosterol peroxide in tests on Hep 3B cell viability, with IC_{50} values of 16.7 μg/mL and 19.4 μg/mL, respectively. Both compounds demonstrated pronounced cytotoxic effects compared to cells treated with the DMSO control. These compounds have shown a high level of cytotoxicity against various cancer cell lines compared to DMSO treated cells. However, variability in cytotoxic measurements highlights the complexity of their biological effects [85].
- **Antibacterial and Antitubercular Activity:** Endoperoxides have demonstrated effectiveness against bacterial pathogens, including *Mycobacteria tuberculosis*, with differences in activity linked to specific molecular structures like the 9,11-double bond. As an example a Δ9,11-derivative exhibited great effectiveness against tuberculosis H37Rv, with MIC values of 16 μg/mL, in comparison to ciprofloxacin, which exhibited a MIC of 0.5 μg/mL [86].

Epoxides: The diverse group of epoxides derived from ergosterol has been studied for their broad spectrum of biological activities:

- **Cytotoxic and Anti-inflammatory Properties:** 5α,6α-epoxides with specific structural modifications have shown considerable cytotoxic effects against cancer cells. Their biological activity varies with structural features such as the presence of hydroxy or keto groups and specific double bonds. As an example, compounds extracted from the culture of the basidiomycete *Polyporus ellisii*, were assessed for cytotoxic effects against five human cancer cell lines. While the initial two

compounds showed minimal activity, an epoxide derivative demonstrated significant cytotoxicity against all evaluated cell lines, with IC_{50} values ranging between 1.5 and 3.9 μM in comparison to DDT (IC_{50}: 1.8–16.7 μM) and taxol (IC_{50}: < 0.008 μM). [87].

- **Enzyme Inhibition:** These compounds have been tested for their ability to inhibit enzymes like acetylcholinesterase (AChE) and α-glucosidase, indicating their potential in treating diseases related to enzyme dysfunction [88].

3. Morphological characterization of investigated fungal species

Buglossoporus quercinus

B. quercinus belongs to the genus *Buglossoporus (Fomitopsidaceae)* which was established by Kotlába and Pouzar in 1966 to accommodate *B. quercinus*, this rare brown-rot polypore species described from Europe [89].

Description [90]:

Cap: The cap measures 10–20 cm across, often partially fused with neighboring caps. It is semicircular to tongue-shaped, broadly convex, and lacks a distinct cuticle. The texture is soft and sub-velvety, ranging in color from dull yellow to brownish yellow, with a paler margin. Bruising results in a noticeable pink to purplish discoloration.

Pore surface: Cream-colored with very small pores (3–5 per mm), bruising pink to purplish, then slowly turning brown. Tubes extend up to 5 mm in length.

Stem: Absent.

Flesh: Whitish, staining pink to purplish when bruised or sliced. The texture is corky.

Odor: Typically, subfragrant, reminiscent of toast or chicory.

Ecology: *B. quercinus* exhibits both saprobic and parasitic behaviors, affecting living and dead oaks, causing a brown rot. It appears annually, growing alone or gregariously during the summer. Originally described in Germany, it is widely distributed in Europe.

Microscopic features: Spores are allantoid, measuring 6–8 x 2.5–3.5 μm, smooth, and hyaline in KOH, with no amyloid properties. Cystidia and setae are not present. The hyphal system is dimitic, with skeletal hyphae in the context and thin-walled hyphae (2.5–3 μm wide) in the tube trama, appearing smooth, hyaline to orange-brown in KOH, and featuring clamp connections.

Distribution and rarity:

B. quercinus, while rare, exhibits a widespread distribution across Europe and has been documented in certain regions of Asia such as Azerbaijan, Georgia, Siberia, Turkey, and Japan [91].

Xylobolus subpileatus

Xylobolus P. Karst. is a small fungal genus that primarily inhabits wood and is globally distributed [92]. It belongs to the order *Russulales* and the family *Stereaceae*.
The majority of species within this genus are found in subtropical or tropical regions, with only four species known from Europe: *X. apricans*, *X. frustulatus*, *X. illudens*, and *X. subpileatus* [93].

Description [93]:
Cap: Typically forming small, shelf-like structures with caps measuring 2–5 cm in diameter. The caps are kidney-shaped, fan-shaped, or semicircular, featuring concentric zones. The upper surface is hairy or velvety, with a texture ranging from dry to slightly sticky. Colors vary from buff to brown.
Pore surface: The underside presents a cream to pale yellow pore surface, often bruising brown. Pores are angular and elongated, sometimes labyrinthine.
Stem: Absent or rudimentary.
Flesh: Thin and leathery.
Ecology: *X. subpileatus* is a saprobe, primarily found on decaying hardwood logs and branches. It contributes to the decay of wood, playing a role in the recycling of organic matter.
Microscopic features: The spores are cylindrical to slightly curved, measuring 4–5 x 1–1.5 μm. Basidia are club-shaped, and cystidia are absent.
Distribution: Commonly encountered in North America, *X. subpileatus* is part of the fungal community associated with wood decomposition in temperate forests.
X. subpileatus often appears as part of a complex of fungi contributing to the breakdown of wood in forest ecosystems. Its small, shelf-like structures make it an interesting component of the fungal kingdom, playing a crucial role in nutrient cycling [93].

4. Methods focusing on identification of secondary metabolites

Solvent extraction remains a widely accepted method for isolating secondary metabolites from fungi, but our exploration extends beyond traditional liquid approaches. Biological samples can undergo diverse processes like liquid-liquid extraction or solid-phase

extraction. Soxhlet extraction, established since 1879, is applied in specific contexts for metabolite isolation [94, 95].

In the realms of physics, chemistry, and materials science, percolation—derived from the Latin term percolare, signifying 'to filter' or 'trickle through'—captures the complex dynamics of fluid movement and filtration through porous materials [96].

Ultrasound-assisted methods, including high-intensity ultrasound-assisted extraction (sonication), offer accelerated extraction times. Microwave-assisted extraction is a fast and reliable method for extracting secondary metabolites from fungi. Non-selective solid-phase extraction, using alkyl-bonded silica or copolymer sorbents, is widely adopted for analyte extraction and enrichment from samples containing fungal secondary metabolites.

In terms of separation techniques, classical liquid chromatography methods, often on normal-phase or reversed-phase like C_{18}, remain the go-to for fungal secondary metabolite analysis. Advances, such as smaller diameter columns and smaller stationary phase particle sizes, have reduced retention times and increased resolution. Ultrahigh-performance liquid chromatography (UHPLC) and columns with a monolithic stationary phase are effective in separating secondary metabolites from fungi.

According to the literature, the described methods or processes typically begin with the percolation of fungal material, often using polar solvents like alcohols. Solvent-solvent partition with increasing polarity allows for prefractionation, separating compounds based on polarity. Commonly used solvents include *n*-hexane, dichloromethane, chloroform, ethyl acetate, and diethyl ether. Various chromatographic steps, utilizing normal-phase silica with eluent systems such as *n*-hexane:acetone or chloroform:acetone or ethyl acetate, precede reverse-phase flash chromatography or high-performance liquid chromatography for compound isolation

In conclusion, the landscape of secondary metabolite extraction and separation techniques from fungi is diverse. Continuous refinement and exploration of new technologies promise to enhance the efficiency and accuracy of fungal secondary metabolite analysis across different sample matrices. These metabolites are subsequently characterized using advanced analytical instruments (Figure 14.).

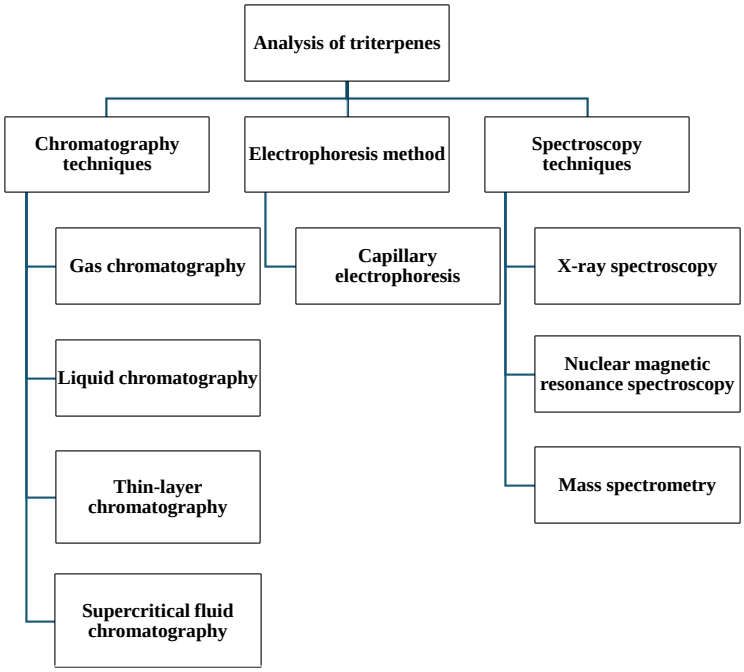

Figure 14. Analyzing techniques of triterpenoids [97].

4.1. Characterization by Mass Spectrometry

In a study by Lingxiao et al., an extensive array of triterpenoid derivatives in *Ganoderma resinaceum* is detailed, encompassing 55 triterpenoids, with 34 definitively identified through reference standards [98]. The remaining unidentified compounds were tentatively characterized using an established identification strategy. Employing UHPLC combined with mass spectrometry (MS), the fragmentation behaviors of these triterpenoids were explored, yielding a comprehensive summary of their pathways. This valuable information formed the basis for a systematic strategy to identify triterpenoids.

The primary triterpenoids in *Ganoderma resinaceum* were systematically classified into six types (designated as type 1-1, 1-2, 2-1, 2-2, 3-1, and 3-2) within a three-step classification system. Identification relied on ion extraction and UHPLC combined with high resolution MS (HRMS) analysis, covering three main types of compounds: type 1, type 1-2, and type 2.

For type 1 compounds, fifteen were identified, with three further confirmed using reference compounds. In the case of type 1-2 compounds, the unknown compound called C_{18}, exhibited characteristic fragments pointing to a hydroxy group at the R4 position, with the R5 side chain identified as type 7, akin to their reference. Nineteen compounds of type 2 were successfully identified using reference compounds.

Examining type 2-2 compounds, unknown compound C3 showcased characteristic fragments indicative of a type 2-2 compound with a type 16 basic chain for the R5 side chain. Similar identification patterns were observed for other type 2-2 compounds (C4, C5, C8, C9–C11, C14, and C15). Overall, the study provides comprehensive insights into the structural characteristics of the identified compounds within these three main types [98] (Figure 15.). In our study we combined the MS/MS fragmentation method with other techniques like nuclear magnetic resonance spectroscopy (NMR) to characterize our isolated products.

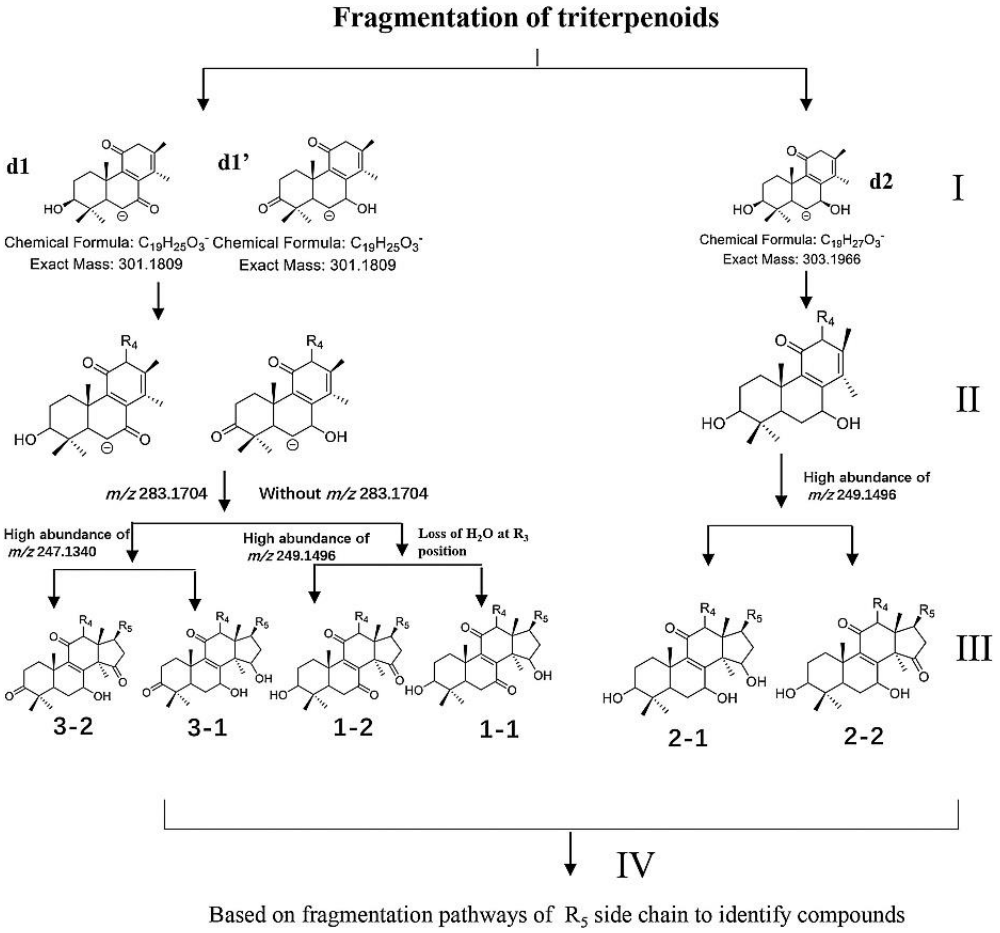

Figure 15. Strategy for triterpenoids resolution by Lingxiao [98].

In the article by Gui-Fang Genf the pursuit of comprehensive compound identification within complex mixtures, an analytical strategy was devised, necessitating the establishment of a HRMS database and an in-house compound library. Leveraging

UHPLC in conjunction with high-resolution tandem data-independent mass spectrometry and ion mobility mass spectrometry, untargeted multidimensional mass spectral data were acquired. Subsequently, a novel and dependable multidimensional MS analytical workflow was formulated, involving the targeted filtration of acquired data through the UNIFI™ software using their in-house compound library.

This robust methodology led to the identification of 121 lanostane-type triterpene acids, determined by their high-resolution molecular mass, fragment ions, and collision cross-section values. Eight triterpene acids were unequivocally identified through a meticulous comparison of retention time and MS/MS data with reference compounds. Additionally, the discovery of three compounds, reported here for the first time, relied on their distinctive neutral losses, characteristic ions, and fragmentation pathways when compared with known compounds. This analytical approach holds the potential for swift screening and characterization of various compounds, particularly within herbal medicines, where multiple isomers may be prevalent. This introduction sets the stage for a comprehensive exploration of the developed analytical workflow and its applicability to the complex landscape of compound identification (Figure 16.) [99].

In the preceding chapter, I illustrated the significance of MS and fragmentation analysis in the identification and characterization of isolated compounds. While fragmentation patterns may not always be straightforward, their analysis remains crucial. Therefore, it is essential for detailed characterization of biological compounds where it can assist NMR spectroscopy for the comprehensive structure elucidation.

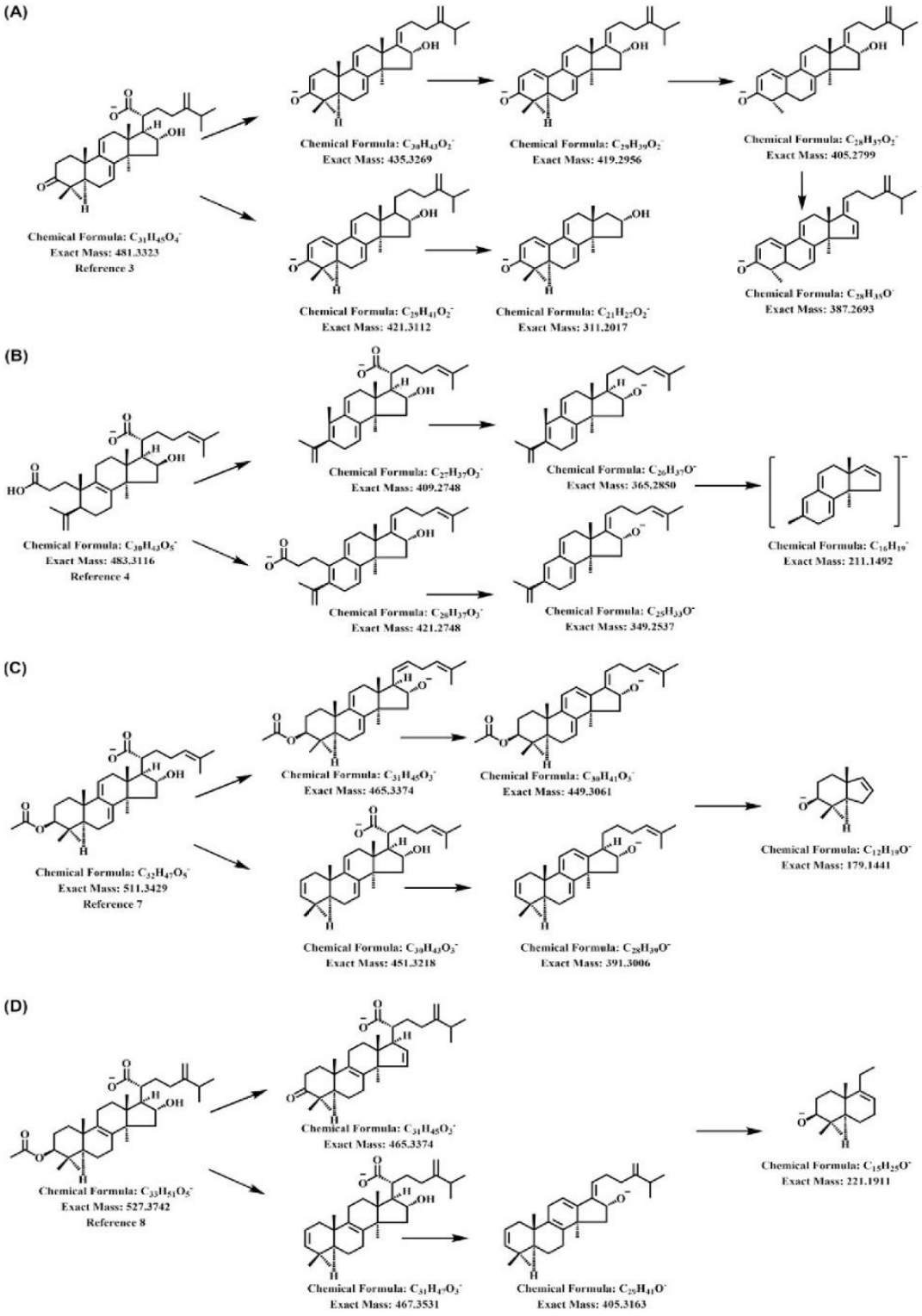

Figure 16. Proposed fragmentation pathways of triterpenoid from *P. cocos*: (A) polyporenic acid C, (B) poricoic B, (C) pachymic acid and (D) 3–*O*–acetyl–16α–hydroxydehydro-trametenolic acid [99].

4.2. Characteritazion with Nuclear Magnetic Resonance Spectroscopy

In the wide spectrum of secondary metabolites, the application of NMR spectroscopy stands as one of the most important tools for identifying their molecular structure. Despite the challenge of requiring relatively substantial sample quantities, one- and two-dimensional (1D and 2D) NMR experiments offer insights into the types and numbers of atoms and their connectivity within these complex molecules.

In concert with ^{1}H NMR, the synergy of ^{13}C NMR data adds a layer of depth to the structural elucidation process, often employing a diverse array of 2D experiments to augment resolution.

^{13}C NMR spectroscopy, particularly through DEPT experiments, is essential for the detailed analysis and identification of quaternary carbon atoms in complex organic molecules, such as triterpenes.

Fundamental homonuclear 2D techniques such as Correlation Spectroscopy (COSY) and Total Correlation Spectroscopy (TOCSY) are strategically employed to isolate ^{1}H resonances, providing a detailed map of the molecular architecture. Additionally, Heteronuclear Single Quantum Coherence (HSQC) and Heteronuclear Multiple Bond Correlation (HMBC) play crucial roles in establishing correlations between protons and the attached carbons, contributing to a comprehensive understanding of the molecular connectivity.

Utilizing the Nuclear Overhauser Effect (NOE), especially through the lens of 2D NOESY (NOE spectroscopy), facilitates the exploration of connectivities through space. This proven to be invaluable in solving complex structures. The application of Rotating Frame Overhauser Effect Spectroscopy (ROESY) finds resonance in the study of secondary metabolites, serving as a powerful tool to establish stereochemistry and elucidate subtle structural nuances.

In summary, the arsenal of advanced spectroscopic techniques, prominently led by NMR, plays an instrumental role in navigating the structural details of secondary metabolites. Beyond their role in structural elucidation, these methodologies offer profound insights into the complex interactions between secondary metabolites and biomolecules,

contributing significantly to the expanding landscape of chemical and biological understanding.

II. Objectives

The aim of this study is to explore the chromatographic separation of secondary metabolites from two fungal species from the *Basidiomycota* phylum, *B. quercinus* and *X. subpileatus*. The primary objectives include revealing the chemical profile of the selected fungi, characterizing the isolated metabolites and conducting *in vitro* enzyme activity tests to evaluate their potential bioactive properties (Figure 17.).

Extraction, chromatographic separation, and characterization:

- Perform an exhaustive percolation extraction process of fungal samples
- Utilize chromatographic techniques, such flash-chromatography (FC), high-performance liquid chromatography (HPLC) to separate and isolate individual metabolites.
- Characterization of metabolites:
- Identify and characterize the chemical constituents of the extracted secondary metabolites using spectroscopic techniques, such as HRMS and NMR.
- Determine the structural properties, molecular weights, and functional groups of the isolated compounds.

Enzyme activity and biological activity tests:

- Evaluate the bioactive potential of the isolated metabolites by conducting *in vitro* bioactivity tests.
- Target specific enzymes relevant to biological processes or diseases, such as tyrosinase and cholinesterase enzymes.

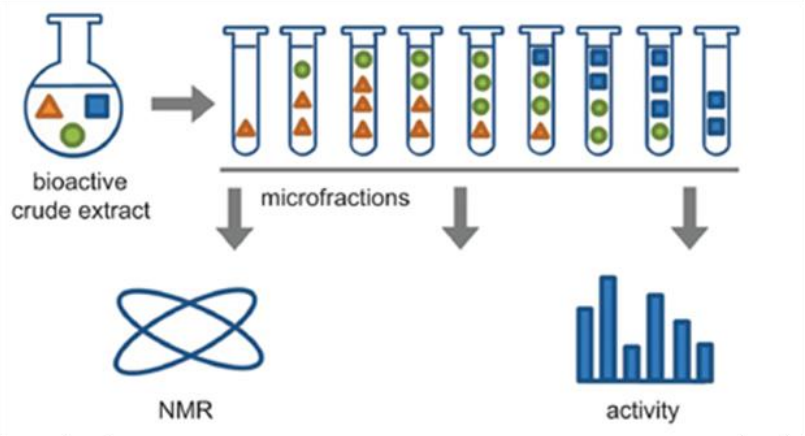

Figure 17. Schematic overview of the proposed workflow [100].

- Discuss the potential pharmacological or biotechnological applications of the characterized secondary metabolites.
- Explore the significance of the findings in the context of drug discovery, natural product-based therapeutics, or industrial applications.

By achieving these objectives, the study aims to contribute valuable insights into the chemical diversity of *B. quercinus* and *X. subpileatus*, providing a foundation for further research on the bioactive potential and applications of their secondary metabolites.

III. Materials and methods

1. Mushroom materials

1.1. *B. quercinus*

The sporocarps of *B. quercinus* were gathered in the Vértes Mountains, Hungary, precisely located at coordinates: N47.379678, E18.327107, on 6th of August 2020. The authentication of the collected fungal specimens was performed by Viktor Papp, ensuring the accuracy and reliability of the identified species. To maintain the integrity of the fungal samples, a thorough cleaning process was undertaken to eliminate any potential contaminants, including soil particles or remnants of plant material. Following this meticulous cleansing, the specimens were carefully preserved by storing them at a temperature of -20°C, ensuring the preservation of their biological properties. In adherence to standard scientific practices, a voucher specimen, identified as No. VPapp-2008061, has been officially deposited at the Department of Botany, Hungarian University of Agriculture and Life Sciences, situated in Budapest, Hungary. This voucher specimen serves as a verifiable record of the collected sporocarps, facilitating future reference and research in the field of mycology and biodiversity studies.

1.2. *X. subpileatus*

Biological sample of the basidiomes of *X. subpileatus*, were collected in Vértes Mountains, Hungary on August 6, 2020. Authentication of the collected specimens was conducted by Viktor Papp.

Thorough decontamination measures were executed to eliminate any pollutants, including soil contaminants and residual plant matter.

Following the purification process, the collected specimens were stored at -20 °C, a temperature conducive to maintaining their structural and biochemical properties over an extended period.

In adherence to established protocols in scientific documentation, a voucher specimen, identified as No. VPapp-200806xs, was meticulously prepared. This voucher specimen was deposited in the repository at the Department of Botany, Hungarian University of Agriculture and Life Sciences, Hungary.

2. Extraction of fungal samples

2.1. *B. quercinus*

The initial step in sample preparation involved the lyophilization of 2.1 kg of fresh mushroom material, resulting in a yield of 205 g of dried sample. Subsequently, the dried sample underwent percolation with methanol (MeOH) using a 10 L volume at room temperature. The resultant dry methanol extract, totaling 45 g, was then resolubilized in a 50% aqueous MeOH solution (600 mL). To further refine the extraction, a solvent−solvent partition technique was employed. This partitioning procedure involved sequential treatments with different organic solvents, each time using a volume of 300 mL. The series of solvents utilized for partitioning included *n*-hexane (3 × 300 mL), followed by chloroform ($CHCl_3$) (3 × 300 mL), and finally, ethyl acetate (EtOAc) (3 × 300 mL) in order of increasing polarity. Through this comprehensive extraction and partitioning process, the goal was to selectively isolate and concentrate specific components from the mushroom material. Each solvent partition is designed to extract compounds with varying polarities, thereby allowing for a more nuanced separation of the chemical constituents present in the original mushroom material. The resulting fractions from each solvent partition can subsequently be subjected to further analysis or bioassays to elucidate the nature and potential bioactivity of the extracted compounds.

2.2. *X. subpileatus*

The freeze-drying of basidioms of *X. subpileatus* (2.1 kg) yielded 275 g of fungal sample. The dried sporocarps were subsequently ground, and the resulting material was subjected to extraction with MeOH (14 L) at ambient temperature. The methanol extract (21.17 g) obtained was concentrated under vacuum and reconstituted in 50% aqueous MeOH (600 mL). This mixture underwent liquid−liquid extraction, employing the following organic solvents sequentially: *n*-hexane (3 × 300 mL), $CHCl_3$ (3 × 300 mL), and then EtOAc (3 × 300 mL).

For the separation of the *n*-hexane and $CHCl_3$ fraction (5.28 g and 7.30 g), the solvent was evaporated under reduced pressure to yield a concentrated extract. These fractions could be further analyzed or subjected to additional purification steps to isolate and characterize specific compounds of interest.

3. Purification and isolation of compounds

3.1. Thin-layer chromatography

Thin-layer chromatographic (TLC) analyses were conducted using aluminum sheets coated with normal phase (NP) silica gel (Merck, TLC Silica gel 60 F254, Darmstadt, Germany) and reversed phase (RP) silica gel (Merck, TLC Silica Gel 60 RP-18 F254S, Darmstadt, Germany).

3.2. Flash column chromatography

FC was conducted utilizing the advanced CombiFlash Rf+ Lumen instrument, equipped with integrated UV and UV–Vis detections. Both normal-phase (silica 20, 40, and 80 g, 0.045–0.063 mm, Molar Chemicals, and RediSep (RS) Rf Gold silica, Teledyne Isco, Lincoln, NE, USA) and reversed-phase flash columns (30, 50, and 150 g RediSep Rf Gold C18, Teledyne Isco, Lincoln, NE, USA) were employed to achieve the separation objectives. Results can be found in Sections IV.1.1 and IV.1.2.

Normal-phase flash chromatography methods of *B. quercinus* (BGS) and *X. subpileatus* (XB):

BGS-CHCl$_3$-FC-NP-1: Increasing polarity of *n*-hexane:acetone (acetone 0 V/V% to 30 V/V%, t: 60 min, RS NP 80 g column)
BGS-CHCl$_3$-FC-NP-2: Increasing polarity of *n*-hexane:acetone (acetone 0 V/V% to 35 V/V%, t: 50 min, RS NP 80 g column)
BGS-CHCl$_3$-FC-NP-3: Increasing polarity of *n*-hexane:acetone (acetone 0 V/V% to 35 V/V%, t: 50 min, RS NP 80 g column)
BGS-CHCl$_3$-FC-NP-4: Increasing polarity of *n*-hexane:acetone (acetone 15 V/V% to 25 V/V%, t: 60 min, RS NP 80 g column)
BGS-CHCl$_3$-FC-NP-5: Increasing polarity of *n*-hexane:acetone (acetone 0 V/V% to 35 V/V%, t: 45 min, RS NP 80 g column)
BGS-CHCl$_3$-FC-NP-8: Increasing polarity of *n*-hexane:acetone (acetone 0 V/V% to 25 V/V%, t: 40 min, RS NP 40 g column)

BGS-$CHCl_3$-FC-NP-12: Increasing polarity of chloroform:methanol (acetone 0 V/V% to 5 V/V%, t: 30 min, RS NP 4 g column)

XB-Hexane-FC-NP-1: Increasing polarity of *n*-hexane:acetone (acetone 0 V/V% to 100 V/V%, t: 60 min, RS NP 80 g column)

XB-$CHCl_3$-FC-NP-1: Increasing polarity of *n*-hexane:acetone (acetone 0 V/V% to 45 V/V%, t: 80 min, RS NP 80 g column)

XB-$CHCl_3$-FC-NP-8: Increasing polarity of chloroform:methanol (acetone 0 V/V% to 40 V/V%, t: 50 min, RS NP 12 g column)

XB-$CHCl_3$-FC-NP-9: Increasing polarity of dichloromethane:methanol (acetone 0 V/V% to 50 V/V%, t: 50 min, RS NP 40 g column)

Reversed-phase flash chromatography of BGS and XB:

BGS-$CHCl_3$-FC-RP-6: Increasing polarity of H_2O:methanol (methanol 50 V/V% to 80 V/V%, t: 50 min, RS RP 30 g column)

BGS-$CHCl_3$-FC-RP-7: Increasing polarity of H_2O:methanol (methanol 30 V/V% to 95 V/V%, t: 50 min, RS RP 30 g column)

BGS-$CHCl_3$-FC-RP-9: Increasing polarity of H_2O:methanol (methanol 60 V/V% to 100 V/V%, t: 50 min, RS RP 30 g column)

BGS-$CHCl_3$-FC-RP-10: Increasing polarity of H_2O:methanol (methanol 80 V/V% to 100 V/V%, t: 50 min, RS RP 15.5 g column)

BGS-$CHCl_3$-FC-RP-11: Increasing polarity of H_2O:methanol (methanol 30 V/V% to 100 V/V%, t: 50 min, RS RP 150 g column)

BGS-$CHCl_3$-FC-RP-13: Increasing polarity of H_2O:methanol (methanol 80 V/V% to 100 V/V%, t: 70 min, RS RP 30 g column)

BGS-$CHCl_3$-FC-RP-14: Increasing polarity of H_2O:methanol (methanol 70 V/V% to 100 V/V%, t: 60 min, RS RP 15.5 g column)

BGS-$CHCl_3$-FC-RP-15: Increasing polarity of H_2O:methanol (methanol 70 V/V% to 100 V/V%, t: 70 min, RS RP 150 g column)

BGS-$CHCl_3$-FC-RP-16: Increasing polarity of H_2O:methanol (methanol 60 V/V% to 100 V/V%, t: 70 min, RS RP 150 g column)

XB-Hexane-FC-RP-2: Increasing polarity of H_2O:methanol
(methanol 70 V/V% to 100 V/V%, t: 60 min, RS RP 15.5 g column)
XB-Hexane-FC-RP-3: Increasing polarity of H_2O:methanol
(methanol 90 V/V% to 100 V/V%, t: 60 min, RS RP 30 g column)
XB-Hexane-FC-RP-4: Increasing polarity of H_2O:methanol
(methanol 90 V/V% to 100 V/V%, t: 60 min, RS RP 30 g column)
XB-Hexane-FC-RP-5: Increasing polarity of H_2O:methanol
(methanol 80 V/V% to 100 V/V%, t: 60 min, RS RP 30 g column)
XB-Hexane-FC-RP-6: Increasing polarity of H_2O:methanol
(methanol 75 V/V% to 100 V/V%, t: 90 min, RS RP 15.5 g column)
XB-Hexane-FC-RP-7: Increasing polarity of H_2O:methanol
(methanol 75 V/V% to 100 V/V%, t: 60 min, RS RP 15.5 g column)
XB-Hexane-FC-RP-8: Increasing polarity of H_2O:methanol
(methanol 90 V/V% to 100 V/V%, t: 60 min, RS RP 150 g column)
XB-Hexane-FC-RP-9: Increasing polarity of H_2O:methanol
(methanol 85 V/V% to 100 V/V%, t: 50 min, RS RP 150 g column)
XB-$CHCl_3$-FC-RP-2: Increasing polarity of H_2O:methanol
(methanol 60 V/V% to 100 V/V%, t: 45 min, RS RP 15.5 g column)
XB-$CHCl_3$-FC-RP-3: Increasing polarity of H_2O:methanol
(methanol 60 V/V% to 100 V/V%, t: 55 min, RS RP 30 g column)
XB-$CHCl_3$-FC-RP-4: Increasing polarity of H_2O:methanol
(methanol 60 V/V% to 100 V/V%, t: 40 min, RS RP 15.5 g column)
XB-$CHCl_3$-FC-RP-5: Increasing polarity of H_2O:methanol
(methanol 10 V/V% to 100 V/V%, t: 50 min, RS RP 15.5 g column)
XB-$CHCl_3$-FC-RP-6: Increasing polarity of H_2O:methanol
(methanol 60 V/V% to 100 V/V%, t: 50 min, RS RP 15.5 g column)

3.3. High-performance liquid chromatography methods of *B. quercinus* and *X. subpileatus*:

For reversed phase HPLC separation of BGS and XB, a Waters 2690 HPLC system equipped with a Waters 996 diode array detector (Waters Corporation, Milford, MA,

USA) was employed. A Kinetex C18 100 Å column (150 × 10 mm i.d., 5 μm; Phenomenex Inc., Torrance, CA, Canada) served as the stationary phase in this process. The chemicals utilized were sourced from Sigma-Aldrich Kft. (Budapest, Hungary) and Molar Chemicals (Halásztelek, Hungary). Results can be found in Sections IV.1.1 and IV.1.2.

BGS-CHCl$_3$-HPLC-1: Isocratic eluent of H_2O : methanol
(methanol 85 V/V% to 95 V/V%, t: 35 min, Kinetex C18 column)
BGS-CHCl$_3$-HPLC-2: Decreasing polarity of H_2O : methanol
(methanol 80 V/V% to 100 V/V%, t: 35 min, Kinetex C18 column)
BGS-CHCl$_3$-HPLC-3: Decreasing polarity of H_2O : methanol
(methanol 80 V/V% to 95 V/V%, t: 35 min, Kinetex C18 column)
BGS-CHCl$_3$-HPLC-4: Decreasing polarity of H_2O : methanol
(methanol 75 V/V% to 100 V/V%, t: 35 min, Kinetex C18 column)
BGS-CHCl$_3$-HPLC-5: Decreasing polarity of H_2O : methanol
(methanol 80 V/V% to 100 V/V%, t: 60 min, Kinetex C18 column)
BGS-CHCl$_3$-HPLC-6: Decreasing polarity of H_2O : methanol
(methanol 75 V/V% to 85 V/V%, t: 35 min, Kinetex C18 column)
BGS-CHCl$_3$-HPLC-7: Decreasing polarity of H_2O : methanol
(methanol 75 V/V% to 85 V/V%, t: 35 min, Kinetex C18 column)
XB-Hexane-HPLC-1: Decreasing polarity of H_2O : methanol
(methanol 75 V/V% to 100 V/V%, t: 35 min, Kinetex C18 column)
XB-Hexane-HPLC-2: Decreasing polarity of H_2O : methanol
(methanol 75 V/V% to 85 V/V%, t: 35 min, Kinetex C18 column)
XB-Hexane-HPLC-3: Decreasing polarity of H_2O : methanol
(methanol 80 V/V% to 95 V/V%, t: 35 min, Kinetex C18 column)
XB-CHCl$_3$-HPLC-1: Decreasing polarity of H_2O : methanol
(methanol 87 V/V% to 100 V/V%, t: 60 min, Kinetex C18 column)
XB-CHCl$_3$-HPLC-2: Decreasing polarity of H_2O : methanol
(methanol 85 V/V% to 95 V/V%, t: 40 min, Kinetex C18 column)
XB-CHCl$_3$-HPLC-3: Decreasing polarity of H_2O : methanol

(methanol 80 V/V% to 100 V/V%, t: 35 min, Kinetex C18 column)

4. Structure determination

4.1. Optical rotation

The measurement of optical rotations was conducted through the utilization of a Jasco P-2000 digital polarimeter (JASCO International, Co., Ltd., Hachioji, Tokyo, Japan). The analysis was carried out specifically at the Na_D line, showcasing the precision and accuracy of the instrument in providing valuable data on optical rotation properties.

4.2. Nuclear magnetic resonance spectroscopy

NMR spectra were recorded in deuterated chloroform (chloroform-*d*, 99.8 atom% D, with 0.03% (*v*/*v*) TMS, Sigma-Aldrich Kft., Budapest, Hungary), methanol (methanol-d_4, 99.8 atom% D, with 0.03% (*v*/*v*) TMS, Sigma-Aldrich), pyridine (pyridine-d_5, 99.8 atom% D, Sigma-Aldrich), or tetrahydrofuran (tetrahydrofuran-d_8, 99.5 atom% D, Sigma-Aldrich) on a Bruker Avance III HD 600 (600/150 MHz) instrument equipped with a Prodigy cryo-probehead (Bruker Biospin GmbH, Rheinstetten, Germany) at 295 K. The pulse programs were taken from the Bruker software library (TopSpin 3.5, pl 7). ^{1}H and ^{13}C chemical shifts (δ) are given in ppm relative to the NMR solvent or relative to the internal standard (TMS), while the coupling constants (*J*) are given in Hz. The complete ^{1}H and ^{13}C assignments (shown in Tables 1,2,3 and Table A1, A2, A3) were achieved by widely accepted strategies based on ^{1}H NMR, ^{13}C NMR, ^{1}H-^{1}H COSY, ^{1}H-^{1}H TOCSY, ^{1}H-^{1}H NOESY, ^{1}H-^{13}C HSQC, and ^{1}H-^{13}C HMBC correlations.

4.3. High resolution mass spectrometry

The samples were analyzed by HRMS methods. The Dionex Ultimate 3000 UHPLC system (3000RS diode array detector, TCC-3000RS column thermostat, HPG-3400RS pump, SRD-3400 solvent rack degasser, and WPS-3000TRS autosampler) (Thermo Fischer Scientific, Waltham, MA, USA) was used connected to an Orbitrap Q Exactive Focus Mass Spectrometer with an electrospray ionization source (Thermo Fischer Scientific, Waltham, MA, USA). The ionization source was operated both in positive and negative ionization modes, and operation parameter optimization was automatic using the

built-in software. The following working parameters were applied: spray voltage (+), 3500 V, spray voltage (−), 2500 V; capillary temperature, 320 °C; sheath gas (N_2), 47.5 °C; auxiliary gas (N_2), 11.25; purge gas (N_2), 2.25 arbitrary units. The full scan resolution was 70,000, and the scanning range was between 120 and 2000 *m*/*z* units. Parent ions were fragmented with a normalized collision energy of 15%, 30%, and 45%. The VDIA isolation range selection was selected by previous measurements. The samples were prepared in methanol and filtered through MF-Millipore membrane filters (0.45 μm, mixed cellulose esters) (Billerica, MA, USA).

5. Biological assay

5.1. Cell cultures

The human colon adenocarcinoma cell lines, Colo 205 (ATCC-CCL-222) doxorubicin-sensitive and Colo 320/Multidrug (MDR)-LRP (ATCC-CCL-220.1) resistant to doxorubicin expressing P-glycoprotein (ABCB1), were purchased from LGC Promochem (Teddington, UK). The cells were cultured in RPMI-1640 medium supplemented with 10% heat-inactivated fetal bovine serum (FBS), 2 mM L-glutamine, 1 mM Na-pyruvate, 10 mM Hepes, nystatin, and a penicillin−streptomycin mixture in concentrations of 100 U/L and 10 mg/L, respectively. The human embryonic lung fibroblasts (MRC-5, ATCC-CCL-171) human embryonic lung fibroblast cell line (LGC Promochem) was cultured in EMEM medium, supplemented with 1% nonessential amino acid mixture, 10% heat-inactivated FBS, 2 mM L-glutamine, 1 mM Na-pyruvate, nystatin, and a penicillin−streptomycin mixture in concentrations of 100 U/L and 10 mg/L, respectively. The cell lines were incubated in a humidified atmosphere (5% CO_2, 95% air) at 37 °C.

5.2. Antiproliferative activity study

The effects of increasing concentrations of the compounds on cell growth were evaluated in 96-well flat-bottomed microtiter plates. The 2-fold serial dilutions of the isolated constituents were made starting with 100 μM. Then, 6×10^3 human colonic adenocarcinoma cells in 100 μL of the medium (RPMI-1640) were added to each well, except for the medium control wells. Culture plates were incubated at 37 °C for 72 h; at

the end of the incubation period, 20 µL of thiazolyl blue tetrazolium bromide solution (MTT) (from a 5 mg/mL stock solution) was added to each well. After incubation at 37 °C for 4 h, 100 µL of sodium dodecyl sulfate (SDS) solution (10% SDS in 0.01 M HCl) was added to each well, and the plates were further incubated at 37 °C overnight. Cell growth was determined by measuring the optical density (OD) at 540 nm (ref 630 nm) with a Multiscan EX ELISA reader (Thermo Labsystems, Cheshire, WA, USA). Inhibition of cell growth was expressed as IC_{50} values defined as the inhibitory dose that reduces the growth of the cells exposed to the tested compounds by 50%. IC_{50} values and the standard deviation (SD) of triplicate experiments were calculated by using GraphPad Prism software version 5.00 for Windows with nonlinear regression curve fit (GraphPad Software, San Diego, CA, USA; www.graphpad.com (accessed on 28 March 2023).

5.3. Multidrug resistane efflux pump inhibitory activity study

The cell numbers of the human colon adenocarcinoma cell lines were adjusted to 2×10^6 cells/mL, resuspended in serum-free RPMI-1640 medium, and distributed in 0.5 mL aliquots into Eppendorf centrifuge tubes. The analyzed fungal metabolites were added at 20 µM concentrations, and the samples were incubated for 10 min at room temperature. Tariquidar was used as the positive control at 0.2 µM. dimethyl-sulfoxid (DMSO) at 2% *v/v* was applied as solvent control. Then, 10 µL (5.2 µM final concentration) of the fluorochrome and ABCB1 substrate rhodamine 123 (Sigma-Aldrich) were added to the samples, and the cells were incubated for a further 20 min at 37 °C, washed twice, and resuspended in 1 mL of phosphate-buffered saline for analysis. The fluorescence of the cell population was determined with a PartecCyFlow flow cytometer (Partec, Münster, Germany). The fluorescence activity ratio (FAR) was calculated as the quotient between FL-1 of the treated/untreated resistant Colo 320 cell line over the treated/untreated sensitive Colo 205 cell line according to the following equation (Eq. 1.):

$$\mathrm{FAR} = \frac{\mathrm{Colo320_{treated}}/\mathrm{Colo320_{control}}}{\mathrm{Colo205_{treated}}/\mathrm{Colo205_{control}}} \qquad \text{Eq. 1}$$

5.4. Chemosensitizing activity study

In the present study, a checkerboard microplate method was used to investigate the effect of drug interactions between the compounds and the chemotherapeutic drug doxorubicin. The assay was performed on the Colo 320 colon adenocarcinoma cell line. The final concentration of the compounds and doxorubicin used in the combination experiment was chosen in accordance with their antiproliferative activity towards this cell line. The dilutions of doxorubicin were made in a horizontal direction in 100 μL, and the dilutions of the compounds vertically in the microtiter plate in 50 μL volume. Then, 6×10^3 of Colo 320 cells in 50 μL of the medium were added to each well, except for the medium control wells. The plates were incubated for 72 h at 37 °C in a 5% CO_2 atmosphere. The cell growth rate was determined after MTT staining. At the end of the incubation period, 20 μL of MTT solution (from a stock solution of 5 mg/mL) was added to each well. After incubation at 37 °C for 4 h, 100 μL of SDS solution (10% in 0.01 M HCl) was added to each well and the plates were further incubated at 37 °C overnight. OD was measured at 540 nm (ref. 630 nm) with a Multiscan EX ELISA reader. Combination index (CI) values at 50% of the growth inhibition dose (ED_{50}) were established using CompuSyn software (ComboSyn, Inc., Paramus, NJ, USA) to plot four to five data points at each ratio. CI values were calculated by means of the median-effect equation, according to the Chou–Talalay, which quantitatively characterizes the relationship between two compounds. According to this method, CI values are interpreted as follows: $CI < 0.1$ indicates very strong synergism, $0.1 \leq CI < 0.3$ represents strong synergism, $0.3 \leq CI < 0.7$ denotes synergism, $0.7 \leq CI < 0.85$ reflects moderate synergism, and $0.85 \leq CI < 0.9$ suggests slight synergism. A nearly additive effect is observed when $0.9 \leq CI \leq 1.1$. Conversely, CI values of $1.1 < CI \leq 1.2$ indicate moderate antagonism, $1.2 < CI \leq 1.45$ represent antagonism, $1.45 < CI \leq 3.3$ signify strong antagonism, and $CI > 3.3$ corresponds to very strong antagonism. [101, 102].

5.5. Anti-tyrosinase activity study

The methanol, *n*-hexane, and chloroform extracts and the isolated compounds (**XB-2–7**) from *X. subpileatus* were dissolved in DMSO to achieve a concentration of 8 mg/mL. The spectrophotometric method developed by Lim et al. [103], with some modifications

outlined by Studzińska-Sroka et al., was employed. In brief, 25 µL of the sample, 75 µL of 0.02 M phosphate buffer (pH 6.8), and 50 µL of tyrosinase solution (192 U/mL in phosphate buffer) were mixed. The samples were then incubated at room temperature (25 °C) for 10 min with shaking (500 rpm). Subsequently, 50 µL of levodopa (L-DOPA) (2 mM in phosphate buffer) was added and incubated for 20 min with shaking (500 rpm) under the same temperature conditions (25 °C). Blank samples were prepared using 50 µL of the buffer instead of L-DOPA solutions. The control sample contained DMSO instead of the tested substances. The control blank contained 25 µL of DMSO instead of samples and 50 µL of the buffer instead of L-DOPA solution. Azelaic acid solution served as the reference. Absorbance was measured at 475 nm using Multiskan GO 1510 (Thermo Fisher Scientific, Vantaa, Finland). Two independent experiments were conducted for each investigated substance, and the average from n = 2 measurements was calculated. The percentage of tyrosinase inhibition was determined using the formula (Eq. 2.):

$$Tyrosinase\ inhibition\ [\%] = 100 - \frac{As - Abs}{Ac - Abc} * 100 \qquad \text{Eq. 2}$$

where (As) is the absorbance of the sample, (Abs) is the absorbance of the sample blank, (Ac) is the absorbance of the control, and (Abc) is the blank of the control. All chemicals used in the tyrosinase activity experiment were obtained from Sigma–Aldrich (St. Louis, MO, USA).

5.6 Acetylcholinesterase and butyrylcholinesterase inhibitory activity

The methanol, *n*-hexane, and $CHCl_3$ extracts (preparation see Section IV.1.2) and compounds (**XB-2–7**) (for isolation, see Section IV.1.2) were dissolved in DMSO to obtain a 20 mg/mL concentration. Ellman's spectrophotometric method [104] was used with some modifications described previously by Studzińska-Sroka et al. [105]. Briefly, 5.0 µL of the sample, 60.0 µL of TRIS-HCl buffer (50 mM, pH = 8), and 30 µL of AChE or butyrylcholinesterase (BChE) (0.2 U/mL) were mixed. Subsequently, the plate was incubated for 5 min at 25 °C with shaking (500 rpm). Next, 30.0 µL of acetylthiocholine iodide (1.5 mM) and 125.0 µL of 5,5′-dithiobis(2-nitrobenzoic acid) (0.3 mM with 10

mM NaCl and 2 mM $MgCl_2 \cdot 6H2O$) were added and incubated with shaking (500 rpm) at the same temperature condition (25 °C, 30 min). The blanks of samples were prepared with 30 µL of the buffer instead of AChE. The control sample contained DMSO instead of the test substance. The blank of control contained 5 µL of DMSO instead of samples and 30 µL of the buffer instead of AChE or BChE solution. Absorbance was measured at 405 nm (Multiskan GO 1510, Thermo Fisher Scientific, Vantaa, Finland). Two independent experiments were carried out for the investigated substances, and the average from n = 3 measurements was calculated. The percentage of AChE/BChE inhibition was calculated as follows (Eq. 3.):

$$\text{AChE/BChE inhibiton } [\%] = 100 - \frac{\text{As} - \text{Abs}}{\text{Ac} - \text{Abc}} * 100 \qquad \text{Eq. 3}$$

The chemicals used in the cholinesterase activity assays were purchased from Sigma–Aldrich (St. Louis, MO, USA).

5.7. Statistical analysis

The data collected were presented as means ± SD. A one-way analysis of variance (ANOVA) was utilized for statistical analysis, and Duncan's post hoc tests were used to identify significant differences, with a significance level set at $p < 0.05$. All statistical evaluations were conducted using Statistica 13.1 software (StatSoft, Krakow, Poland).

IV. Results

1. Isolation of compounds from the investigated species

1.1. Isolation of compounds from *B. quercinus*

Following the initial separation protocol BGS-$CHCl_3$-FC-NP-1/2/3, fractions with similar compositional characteristics were combined according to TLC resulting in 15 major fractions designated as BQ1–BQ15 (Figure 18.).

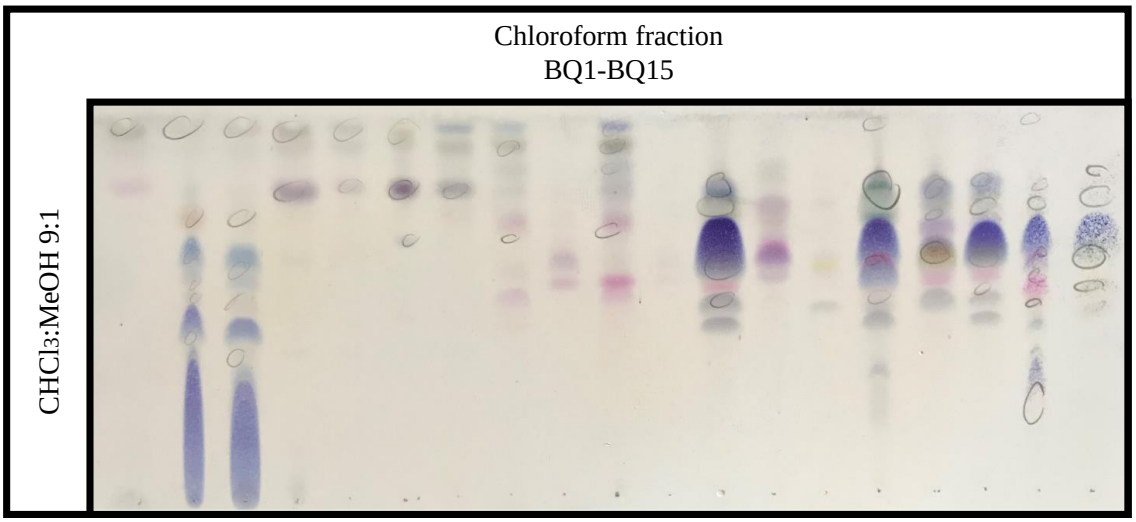

Figure 18. TLC chromatogram of fractions BQ1-BQ15 obtained by flash chromatography of the chloroform fraction of *B. quercinus*. Detected by vanilin-sulphuric acid solution used as spraying reagent (Eluent: $CHCl_3$:MeOÍH – 9:1).

The specific fraction of interest, BQ6 (44 mg) was further purified by NP-FP, employing a mobile phase of *n*-hexane-acetone, with a gradient elution from 0 V/V% to 35 V/V% acetone in 45 minutes (BGS-$CHCl_3$-FC-NP-5), then RP-FP (BGS-$CHCl_3$-FC-RP-10), later RP-HPLC (BGS-$CHCl_3$-HPLC-1**)**, utilizing gradient elution with H_2O-MeOH (ranging from 85% to 95% MeOH over 35 minutes), ultimately resulting in the isolation of **BGS-3** (1.5 mg).

Concurrently, the combined fraction BQ-7 (200 mg) underwent a sequential separation process, starting with RP-FC using the BGS-$CHCl_3$-FC-RP-11 method. This involved a gradient elution of H_2O:MeOH, increasing the methanol concentration from 30 V/V% to 100 V/V% over 50 minutes on an RS RP 150 g column. The separation was continued

with another RP-HPLC step using the BGS-$CHCl_3$-HPLC-6 method, where the organic content of the H_2O:MeOH mixture was increasing from 75 V/V% to 85 V/V% over 35 minutes on a Kinetex C18 column, ultimately leading to the isolation of **BGS-10** (2.4 mg).

The isolation procedures for **BGS-2** (2 mg), **BGS-4** (3.8 mg), **BGS-5** (1.9 mg) and **BGS- 9** (1.2 mg) from fraction BQ8 (616 mg) involved a combination of RP-FC and RP-HPLC. All compounds were initially isolated using the BGS-$CHCl_3$-FC-RP-9 method, which involved increasing the organic content of H_2O:MeOH from 60 V/V% to 100 V/V% over 50 minutes. Following this initial isolation, **BGS-2**, **BGS-4**, and **BGS-5** were further purified using the BGS-$CHCl_3$-HPLC-4 method, utilizing H_2O:MeOH from 75 V/V% to 100 V/V% over 35 minutes.

BGS-9, similarly isolated first using BGS-$CHCl_3$-FC-RP-9, was further purified using the BGS-$CHCl_3$-HPLC-5 method, with a gradient increase of H_2O:methanol from 80 V/V% to 100 V/V% over 60 minutes.

Fraction BQ10 (5.12 g) underwent further chromatography steps, starting with the BGS-$CHCl_3$-FC-NP-8 method, where the polarity of the *n*-hexane:acetone mixture was increased from 0 V/V% to 25 V/V% acetone over 40 minutes on an RS NP 40 g column. This was followed by additional purification using the BGS-$CHCl_3$-FC-NP-12 method, where the polarity of the chloroform:methanol mixture was increased from 0 V/V% to 5 V/V% methanol over 30 minutes on an RS NP 4 g column. The isolation of **BGS-8** (900 mg) and **BGS-11** (2.7 mg) was achieved during the final NP-FC step (Figure 19.).

Figure 19. Crystals of the isolated compound **BGS-8**

BGS-1 (0.9 mg), **BGS-7** (0.8 mg) and **BGS-12** (400 mg) were obtained from fraction BQ11 (6.53 g) through a careful sequence of chromatographic steps. The process began with NP-FC using the BGS-$CHCl_3$-FC-NP-4 method, which involved increasing the polarity of *n*-hexane:acetone from 15 V/V% to 25 V/V% over 60 minutes. This was followed by RP-FC using the BGS-$CHCl_3$-FC-RP-6 method, where the organic content of H_2O:MeOH increased from 50 V/V% to 80 V/V% over 50 minutes. Finally, the compounds were purified using RP-HPLC. For **BGS-1**, this final purification was performed using the BGS-$CHCl_3$-HPLC-3 method, involving an increase in the polarity of H_2O:methanol from 80 V/V% to 95 V/V% over 35 minutes. For **BGS- 7** and **BGS-12**, the final purification was conducted using the BGS-$CHCl_3$-HPLC-2 method, where the organic content of H_2O:MeOH increased from 80 V/V% to 100 V/V% over 35 minutes.
Finally, **BGS-6** (400 mg) was isolated from BQ12 (310 mg) using two chromatography methods. Initially, BGS-$CHCl_3$-FC-RP-7 was applied to purify the compound through RP-FC. This separation was carried out with a mobile phase of H_2O:MeOH. The elution gradient increased the polarity of the solvent mixture from 30 V/V% to 95 V/V% methanol over 50 minutes. Following this, BGS-$CHCl_3$-HPLC-7 was utilized for further purification via RP-HPLC. This step was performed on a Kinetex C18 column, with the mobile phase consisting of H_2O:MeOH. The gradient increased the methanol concentration from 75 V/V% to 85 V/V% over 35 minutes.
This systematic isolation and purification strategy facilitated the successful isolation of 12 compounds, highlighting the meticulous and effective application of chromatographic techniques in the effort of elucidating the chemical constituents within the studied fractions (Figure 20.) [106].

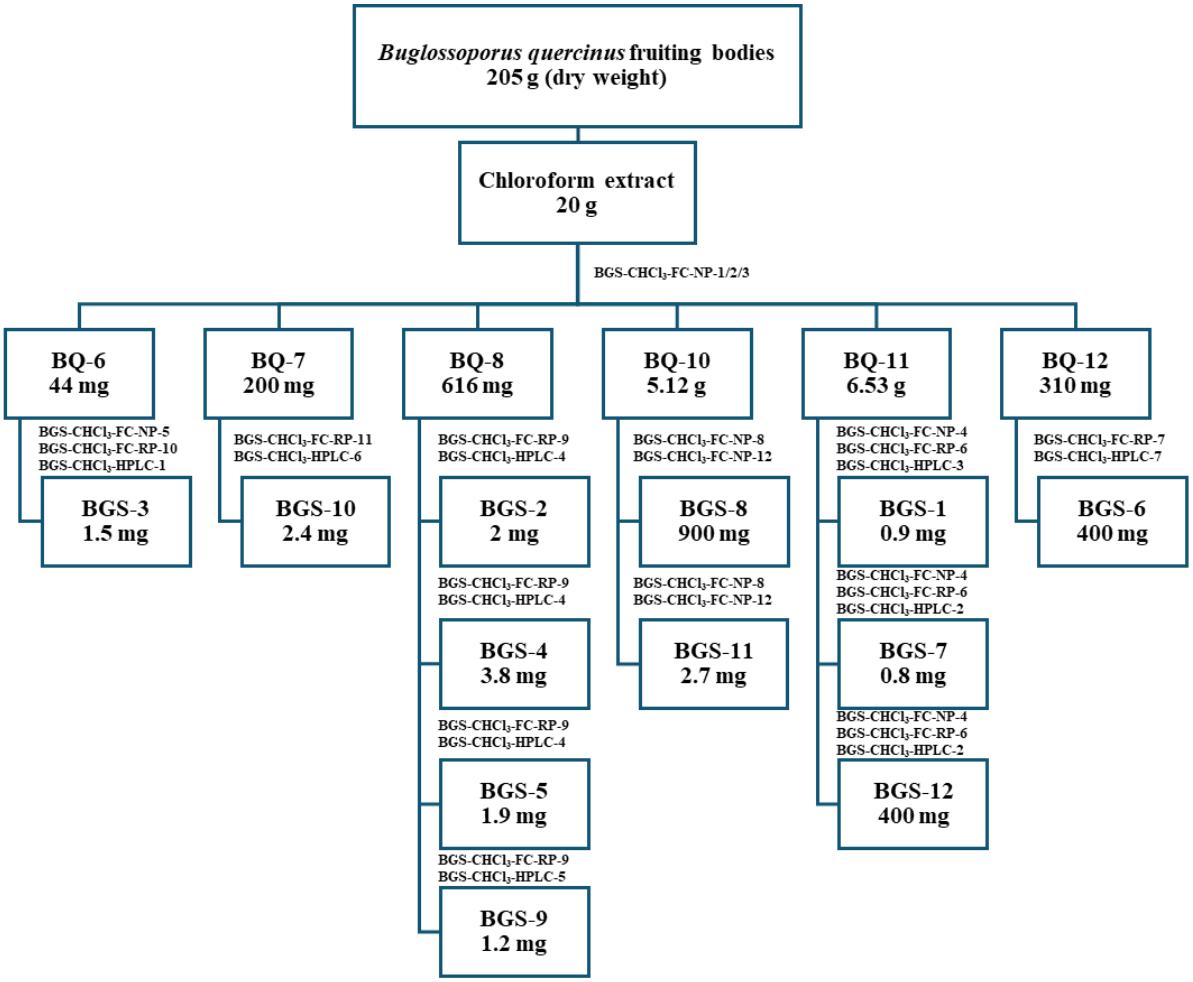

Figure 20. Isolation scheme for *B. quercinus*.

1.2. Isolation of compounds of *X. subpileatus*

In the process of isolating the *n*-hexane fraction (5.28 g), an accurately designed approach was employed. Initially, normal-phase flash chromatography (NP-FC) was conducted, utilizing a gradient system of *n*-hexane and acetone (0–100% *n*-hexane gradient elution in 60 minutes). Subsequently, fractions displaying similar characteristics were combined based on thin-layer chromatography monitoring, yielding fractions denoted as XH1–XH6.

The targeted fraction XH4 (530 mg) was initially purified using the XB-Hexane-FC-RP- 5 method, where the organic content of the H_2O:MeOH mixture was increased from 80 V/V% to 100 V/V% MeOH over 60 minutes on an RS RP 30 g column. Following

this, the fraction was further purified using the XB-Hexane-FC-RP-8 method on an RS RP 150 g column, where the organic content of the H_2O:MeOH mixture was increased from 90 V/V% to 100 V/V% MeOH over 60 minutes. Finally, the fraction underwent RP-HPLC using the XB-Hexane-HPLC-1 method, where the organic content of the H_2O:MeOH mixture was increased from 75 V/V% to 100 V/V% over 35 minutes on a Kinetex C18 column. This combined approach led to the successful isolation of compounds **XB-1** (5.4 mg) and **XB-2** (2.5 mg). Simultaneously, the fraction XH3 (352 mg) was purified using the XB-Hexane-FC-RP-4 method, which involved increasing the organic content of the H_2O:MeOH mixture from 90 V/V% to 100 V/V% over 60 minutes, utilizing an RS RP 30 g column. Following this, the fraction was further purified using the XB-Hexane-HPLC-2 method, where the organic content of the H_2O:MeOH mixture was increased from 75 V/V% to 85 V/V% MeOH over 35 minutes on a Kinetex C18 column. This process resulted in the isolation of compounds **XB-3** (10 mg) and **XB-4** (21.8 mg). The fraction XH6 (150 mg) from the *n*-hexane fraction was purified using the XB-Hexane-FC-RP-7 method, which involved increasing the organic content of the H_2O:MeOH mixture from 75 V/V% to 100 V/V% over 60 minutes on an RS RP 15.5 g column. Following this, the fraction underwent further purification using the XB-Hexane-HPLC-3 method, where the organic content of the H_2O:MeOH mixture was increased from 80 V/V% to 95 V/V% MeOH over 35 minutes on a Kinetex C18 column. This process led to the isolation of compounds **XB-6** (6.9 mg) and **XB-7** (33.3 mg).

The chloroform fraction (7.3 g) underwent further purification through NP-FC, employing a gradient system of *n*-hexane and acetone (0–45% *n*-hexane gradient elution in 80 minutes, XB-$CHCl_3$-FC-NP-1). Fractions with analogous compositions were combined based on TLC monitoring, resulting in fractions labeled as XC1–XC7 (Figure 21.).

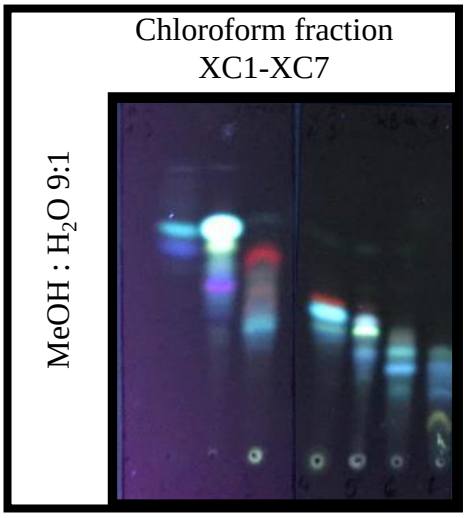

Figure 21. TLC chromatogram of fractions obtained by flash chromatography of $CHCl_3$ extract from *X. subpileatus* under UV at 366 nm.

For the fraction XC2 (267 mg), an initial separation was carried out using RP-FC with the XB-$CHCl_3$-FC-RP-3 method, which involved increasing the organic content of the H_2O:MeOH mixture from 60 V/V% to 100 V/V% MeOHover 55 minutes, utilizing an RS RP 30 g column. The final purification step was performed using the XB-$CHCl_3$-HPLC-2 method, which employed RP-HPLC with a gradient elution of H_2O:MeOH from 85 V/V% to 95 V/V% MeOH over 40 minutes on a Kinetex C18 column, ultimately yielding **XB-5** (4.8 mg) (Figure 22. and 23.) [107].

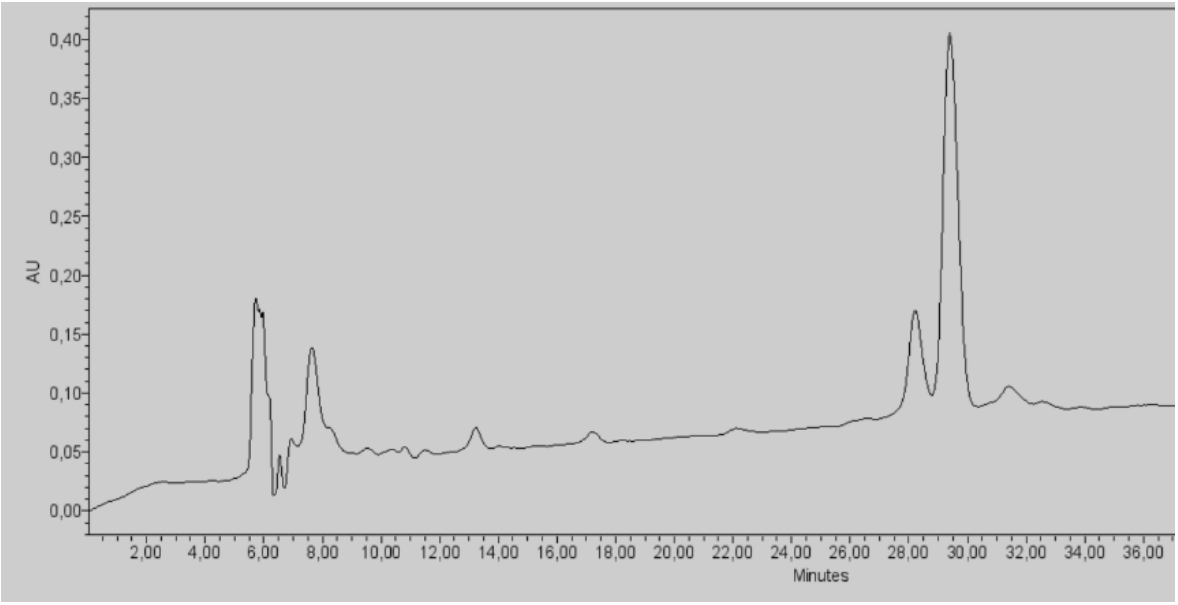

Figure 22. RP-HPLC chromatogram of the purification of **XB-5**

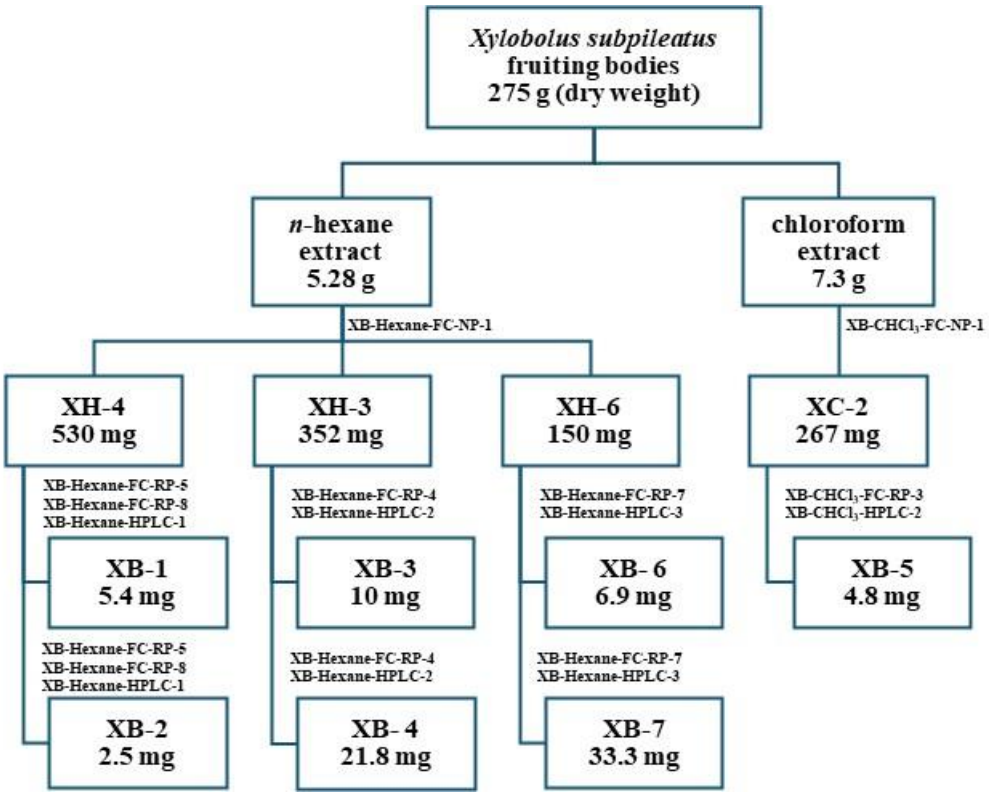

Figure 23. Isolation scheme for *Xylobolus subpileatus*

2. Structure determination of the novel isolated compounds

2.1. Compounds of *B. quercinus*

The structural elucidation of twelve polyporenicacid -type secondary metabolites from *B. quercinus* commenced with an initial examination utilizing electrospray ionization mass spectrometry/mass spectrometry (ESI-MS/MS). This high-resolution mass spectrometric analysis provided foundational insights into molecular weights and fragmentation patterns, establishing a basis for subsequent structural characterization (Figure 24.).

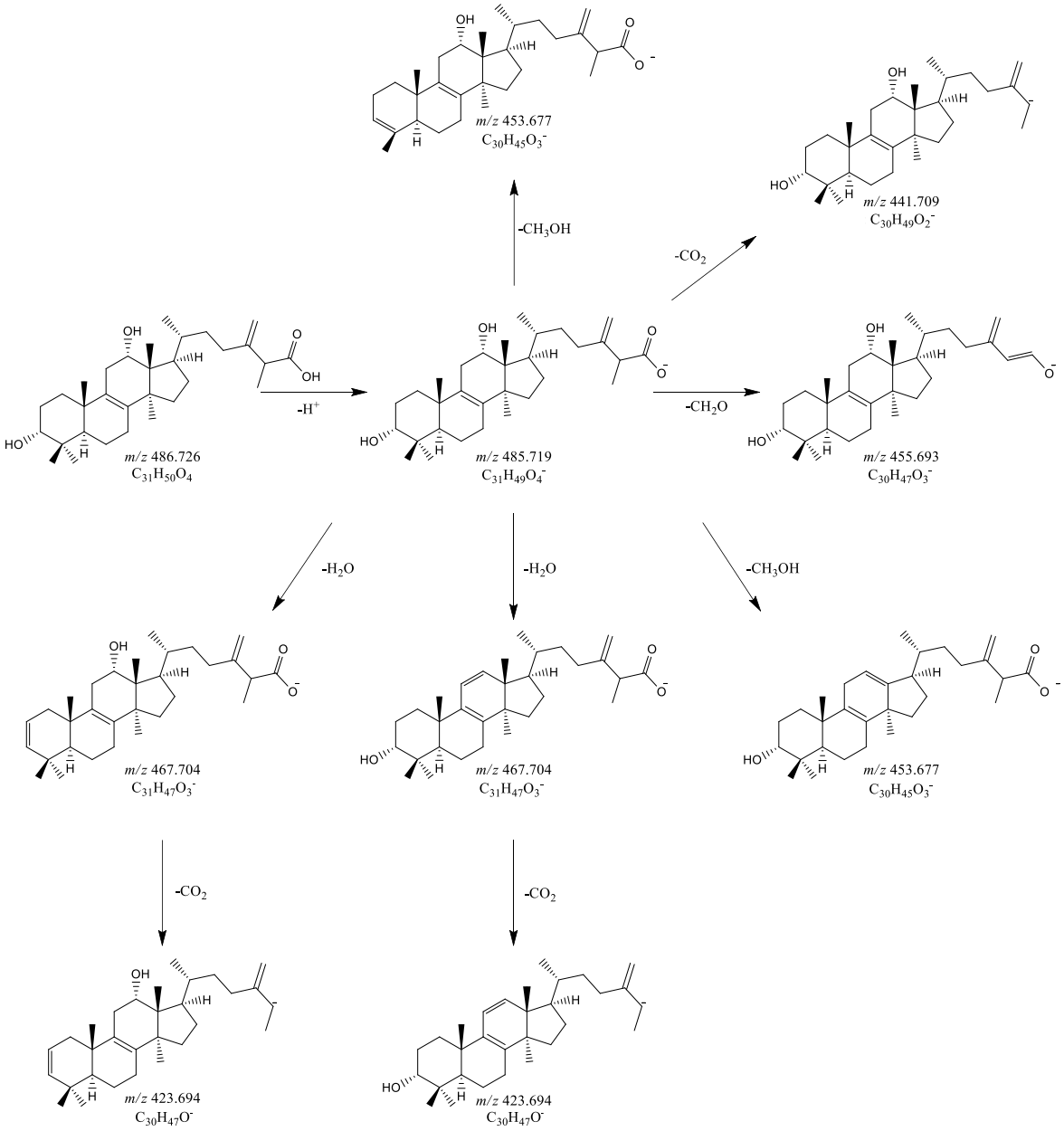

Figure 24. Fragmentation pattern of polyporenic acid A (**BGS-10**) from *B. quercinus*

A comprehensive exploration of molecular structures ensued through advanced NMR techniques, encompassing both 1D (^{1}H and ^{13}C) and 2D (HSQC, HMBC, and NOESY) NMR spectroscopy.

The subsequent application of 2D NMR techniques, including HSQC, HMBC and NOESY, facilitated the elucidation of complex molecular connectivity, long-range couplings, and spatial relationships between protons. These advanced techniques played a pivotal role in resolving stereochemical questions and confirming the precise structural features of the newly identified natural products.

The synergistic integration of ESI-MS/MS and NMR methodologies not only confirmed the existence of five new natural products but also unveiled one compound as a novel stereoisomer of a known compound, enriching our knowledge of the secondary metabolites within *B. quercinus* (Figure 25.).

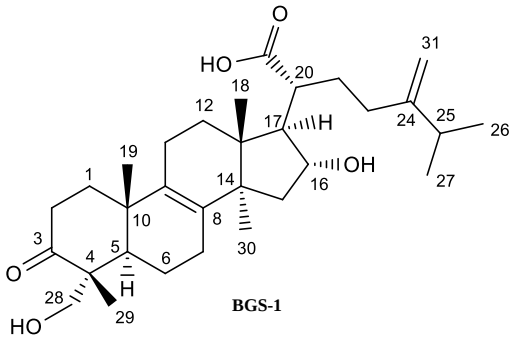

BGS-1

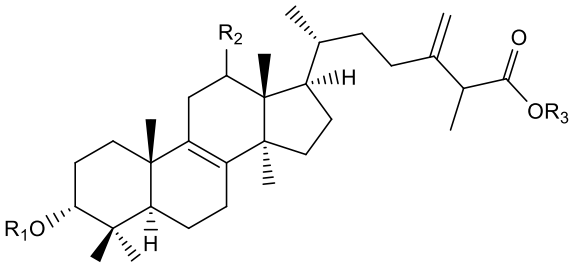

	R_1	R_2	R_3
BGS-2	H (β)	=O	H
BGS-3	Ac (α)	=O	H
BGS-4	Mln (α)	H	H
BGS-5	HMG (α)	OH (α)	CH_3

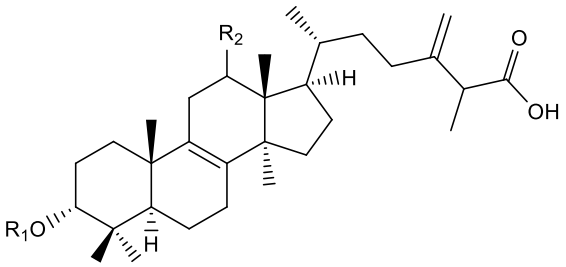

	R_1	R_2
BGS-6	Mln	OH (α)
BGS-7	HMG	OH (α)
BGS-8	MeMln	OH (α)
BGS-9	H	=O
BGS-10	H	OH (α)
BGS-11	Ac	OH (α)

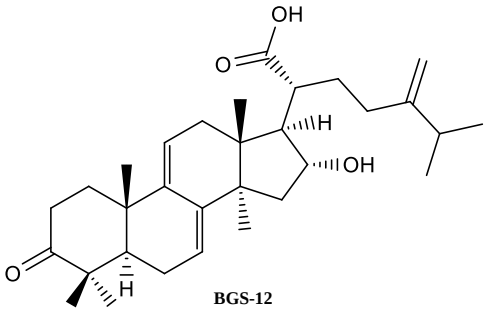

BGS-12

Figure 25. Isolated compounds from *B. quercinus*

Polyporenic acid N (**BGS-1**): amorphous solid; α_D^{25} + 10.4 (*c* 0.3, CH_3OH); HRMS (+) *m/z* 501.3568 $[M + H]^+$ (501.3575 calcd for $C_{31}H_{49}O_5$ Δ −1.3 ppm); HRMSMS (CID = 15%, 30%, 45%) 483.346, 465.336, 453.335.

Polyporenic acid O (**BGS-2**): amorphous solid; α_D^{25} + 26.7 (*c* 0.2, CH_3OH); HRMS (+) *m/z* 485.3620 $[M + H]^+$ (485.3625 calcd. for $C_{31}H_{49}O_4$ Δ −1.0 ppm); HRMSMS (CID = 15%, 30%, 45%) 468.943, 454.837.

Polyporenic acid P (**BGS-3**): amorphous solid; α_D^{25}+1.1 (*c* 4.4, CH_3OH); HRMS (+) *m/z* 527.3721 $[M + H]^+$ (527.3731 calcd. for $C_{33}H_{51}O_5$ Δ −2.0 ppm); HRMSMS (CID = 15%, 30%, 45%) 509.361, 481.367, 467.350, 449.340, 421.345.

Polyporenic acid Q (**BGS-4**): amorphous solid; α_D^{25}+5.5 (*c* 0.4, CH_3OH); HRMS (−) *m/z* 555.3694 $[M - H]^-$ (555.3680 calcd. for $C_{34}H_{51}O_6$ Δ 2.6 ppm); HRMSMS (CID = 15%, 30%, 45%) m/z 511.378.

Polyporenic acid R (**BGS-5**): amorphous solid; α_D^{25} − 2.6 (*c* 4.3, CH_3OH); HRMS (+) *m/z* 645.4342 $[M + H]^+$ (645.4361 calcd. for $C_{38}H_{61}O_8$ Δ 2.8 ppm); HRMSMS (CID = 15%, 30%, 45%) 627.424, 465.371 (Table 1.) [106].

Table 1. NMR spectroscopic data (600 MHz, $CDCl_3$ [a], pyridine-d_5 [b], tetrahydrofuran-d_8 [c], or methanol-d:pyridine-d_5 19:1 [d]) for compounds **BGS-1**–**5**.

	1 [c]			**2** [c]			**3** [a]			**4** [a]			**5** [b]		
Position	**δ_C**	**Type**	**δ_H (*J* in Hz)**	**δ_C**	**Type**	**δ_H (*J* in Hz)**	**δ_C**	**Type**	**δ_H (*J* in Hz)**	**δ_C**	**Type**		**δc**	**Type**	**δ_H (*J* in Hz)**
1	35.7	CH_2	1.82, m 1.54, m	36.4	CH_2	1.51, m 1.09, m	30.7	CH_2	1.43, m 1.37, m	30.6	CH_2	1.49, m 1.41, m	31.6	CH_2	1.75, m 1.55, m
2	36.8	CH_2	2.31, dd, (10.0, 8.0) 2.28, dd, (8.0, 3.4)	28.8	CH_2	1.48, m	23.1	CH_2	1.87, m 1.67, m	23.2	CH_2	1.90, m 1.72, m	24.1	CH_2	1.90, m 1.78, m
3	216.0	C		78.3	CH	2.97, m	77.6	CH	4.68, br s	80.6	CH	4.76, br s	78.4	CH	4.97, br s
4	52.8	C		39.7	C		36.7	C		36.8	C		37.4	C	
5	44.3	CH	2.17, m	51.5	CH	0.96, m	45.2	CH	1.50, m	45.3	CH	1.47, m	46.4	CH	1.83, m
6	20.2	CH_2	1.49, m 1.44, m	19.1	CH_2	1.65, m 1.49, m	17.8	CH_2	1.67, m 1.56, m	18.0	CH_2	1.59, m 1.49, m	18.8	CH_2	1.62, m 1.52, m
7	27.2	CH_2	2.03, m 1.93, m	27.2	CH_2	2.06, m 1.95, m	25.8	CH_2	2.12, m 2.07, m	25.9	CH_2	2.04, m	26.8	CH_2	2.17, m 2.12, m
8	136.6	C		135.8	C		135.0	C		134.2	C		135.5	C	
9	134.0	C		136.6	C		135.1	C		134.3	C		134.2	C	
10	37.6	C		37.8	C		36.7	C		36.8	C		37.5	C	
11	21.4	CH_2	1.94, m	40.5	CH_2	2.82, m 2.49, m	39.9	CH_2	2.90, m 2.71, m	20.9	CH_2	2.01, m	34.9	CH_2	2.76, m 2.50, m
12	30.0	CH_2	1.71, m 1.39, m	210.5	C		212.7	C		30.9	CH_2	1.74, m 1.69, m	72.5	CH	4.27, d (7.6)
13	46.5	C		55.0	C		54.5	C		44.5	C		50.5	C	
14	49.4	C		60.0	C		59.4	C		49.9	C		50.4	C	
15	44.0	CH_2	2.03, m 1.15, m	30.9	CH_2	1.75, m 1.20, m	30.1	CH_2	1.82, m 1.35, m	30.8	CH_2	1.60, m 1.18, m	33.1	CH_2	1.76, m 1.25, m
16	77.1	CH	3.89, m	28.6	CH_2	1.91, m 1.29, m	27.8	CH_2	2.01, m 1.37, m	28.2	CH_2	1.94, m 1.31, m	28.7	CH_2	2.11, m 1.40, m
17	57.3	CH	1.96, m	43.5	CH	2.06, m	42.4	CH	2.19, m	50.3	CH	1.50, m	43.5	CH	2.65, m
18	17.8	CH_3	0.69, s	12.9	CH_3	0.94, s	12.6	CH_3	1.05, s	15.7	CH_3	0.69, s	17.2	CH_3	0.77, s
19	19.2	CH_3	0.95, s	19.5	CH_3	0.98, s	19.0	CH_3	1.08, s	18.9	CH_3	1.00, s	19.4	CH_3	1.03, s
20	48.3	CH	2.24, m	37.7	CH	1.18, m	36.6	CH	1.27, m	36.3	CH	1.41, m	37.3	CH	1.53, m
21	177.4	C		19.6	CH_3	0.78, d (6.4)	19.0	CH_3	0.89, d (5.8)	18.6	CH_3	0.93, m	18.3	CH_3	1.28, m
22	31.6	CH_2	1.92, m 1.64, m	35.3	CH_2	1.53, m 1.14, m	34.0	CH_2	1.62, m 1.27, m	34.2	CH_2	1.58, m 1.19, m	35.4	CH_2	1.77, m 1.38, m
23	33.4	CH_2	1.96, m 1.87, m	32.9	CH_2	2.14, m 1.09, m	32.1	CH_2	2.21 2.02	31.7	CH_2	2.19, m 2.00, m	32.7	CH_2	2.37, m 2.17, m
24	156.7	C		150.9	C		148.5	C		148.3	C		150.2	C	
25	34.8	CH	2.14, m	46.2	CH	2.96, m	45.1	CH	3.17, m	45.0	CH	3.18, q (7.0)	46.2	CH	3.32, q (7.1)
26	22.4	CH_3	0.91, d (6.9)	175.6	C		177.7	C		179.6	C		175.3	C	
27	22.2	CH_3	0.92, d (6.9)	17.0	CH_3	1.10, d (7.4)	16.3	CH_3	1.31, d (6.7)	16.1	CH_3	1.31, d (7.0)	17.1	CH_3	1.38, d (7.1)
28	68.3	CH_2	3.39, dd (10.2, 2.4) 3.16, dd (10.2, 2.4)	28.5	CH_3	0.88, s	27.5	CH_3	0.88, s	27.6	CH_3	0.88, s	28.5	CH_3	1.04, s
29	17.5	CH_3	0.78, s	16.1	CH_3	0.69, s	21.7	CH_3	0.94, s	21.7	CH_3	0.93, m	22.4	CH_3	0.91, s
30	25.3	CH_3	1.05, s	24.3	CH_3	0.65, s	24.1	CH_3	0.82, s	24.2	CH_3	0.91, s	25.7	CH_3	1.43, s
31	106.9	CH_2	4.61, br s	110.3	CH_2	4.77, br s 4.71, br s	111.1	CH_2	4.97, br s 4.94, br s	111.4	CH_2	4.97, br s 4.94, br s	111.3	CH_2	5.10, br s 5.06, br s
1′							170.8	C		167.2	C		172.4 [d]	C	
2′										40.2	CH_2	3.64, m	47.0 [d]	CH_2	2.64 [d], m
3′										170.6	C		71.0 [d]	C	
4′													47.0 [d]	CH_2	2.64 [d], m
5′													172.4 [d]	C	
1′-CH_3							21.3	CH_3	2.07, s						
3′-CH_3														27.9 [d]	CH_3
26-CH_3														52.3 [d]	CH_3

2.2. Compounds of *X. subpileatus*

The exploration of secondary metabolites from *X. subpileatus* resulted in the isolation of seven compounds, which included a novel stereoisomer (**XB-1**) and one benzofuran-type molecule (**XB-3**). The analysis commenced with electrospray ionization mass spectrometry/mass spectrometry (ESI-MS/MS), providing insights into molecular weights and fragmentation patterns. Subsequent structural elucidation employed advanced NMR techniques, encompassing 1D (^{1}H and ^{13}C) and 2D (HSQC, HMBC, NOESY) NMR spectroscopy. The application of 2D NMR techniques, including HSQC, HMBC, and NOESY, unraveled molecular connectivity and stereochemical intricacies (Table 2.). The MS and NMR methodologies not only confirmed the existence of a novel stereoisomer **(XB-1**) and a benzofuran-type molecule (**XB-3**), but also deepened our comprehension of *X. subpileatus* secondary metabolites (Figure 26.).

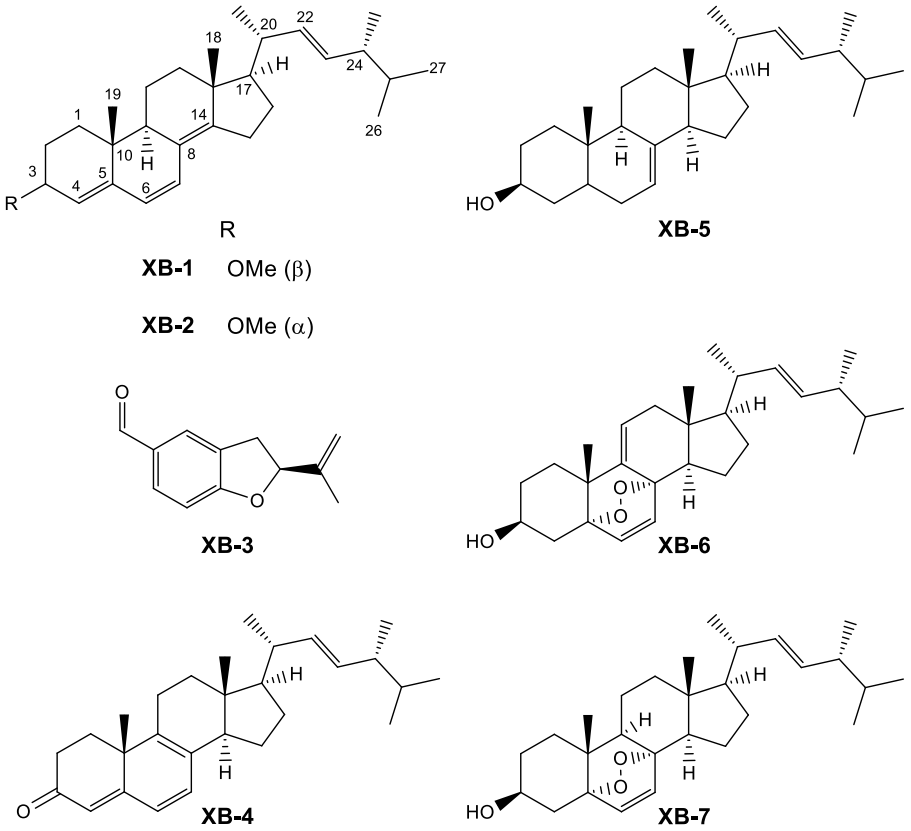

Figure 26. Isolated compounds from *X. subpileatus*

Table 2. Complete ^{1}H and ^{13}C NMR resonance assignments for **XB-1** and **XB-2**

No.	**1**			**2**		
	δ ^{13}C	δ ^{1}H	m, *J*	δ ^{13}C	δ ^{1}H	m, *J*
1	33.4	1.73	m	29.7	1.53	m
		1.38	m		1.26	m
2	25.0	2.09	m	23.6	1.96	m
		1.62	m		1.76	m
3	76.6	3.93	ddd, 10.1, 6.5, 2.0 Hz	72.5	3.73	b t, 4.6 Hz
4	123.1	5.49	b s	120.9	5.59	d, 4.6 Hz
5	145.5	-	-	147.4	-	-
6	125.8	5.88	d, 9.6 Hz	125.9	5.88	d, 9.7 Hz
7	126.0	6.17	d, 9.6 Hz	126.8	6.21	d, 9.7 Hz
8	124.8	-	-	124.9	-	-
9	45.5	1.97	m	44.9	2.05	m
10	35.9	-	-	36.0	-	-
11	19.1	1.60	m	19.4	1.64	m
		1.52	m		1.52	m
12	36.3	2.02	m	36.4	2.00	m
		1.26	m		1.25	m
13	43.5	-	-	43.6	-	-
14	149.7	-	-	149.7	-	-
15	25.0	2.40	m	25.0	2.40	m
		2.29	m		2.28	m
16	27.9	1.77	m	27.9	1.77	m
		1.44	m		1.44	m
17	55.9	1.21	m	55.8	1.22	m
18	19.2	0.92	s	19.1	0.92	s
19	18.2	0.89	s	17.1	0.82	s
20	39.4	2.11	m	39.4	2.11	m
21	21.2	1.04	d, 6.7 Hz	21.2	1.04	d, 6.8 Hz
22	135.3	5.21	m	135.4	5.22	m
23	132.2	5.22	m	132.1	5.22	m
24	42.8	1.86	m	42.8	1.87	m
25	33.1	1.48	m	33.1	1.47	m
26	19.7	0.83	d, 6.8 Hz	19.7	0.83	d, 6.8 Hz
27	20.0	0.84	d, 6.8 Hz	20.0	0.84	d, 6.8 Hz
28	17.6	0.92	d, 6.8 Hz	17.6	0.93	d, 6.8 Hz
3-OCH_3	55.4	3.40	s	56.1	3.36	s

3β-methoxy-ergosta-6,8 14 ,22-trien (**XB-1**): amorphous solid; + 87.8 (c 0.42, $CHCl_3$, 25.4 °C); HRMS *m/z* 377.,3194 $[M+H-CH_3OH]^+$ (Δ2.2 ppm; $C_{28}H_{41}$); HRMSMS (CID = 15%, 30%, 45%; rel int %) *m/z* 293.226, 251.179.

3α-methoxy-ergosta-6,8 14 ,22-trien (**XB-2**): amorphous solid; − 10.0 (c 0.09, $CHCl_3$, 25.5 °C) HRMS *m/z* 377.,3192 $[M+H-CH_3OH]^+$ (Δ2.2 ppm; $C_{28}H_{41}$); HRMSMS (CID = 15%, 30%, 45%; rel int %) *m/z* 293.226, 251.179 [107].

One of the most interesting secondary metabolites is fommanoxin labeled as **XB-3**. The main UV peaks are 228 and 296 nm (Figure 27.). According to the HRMS-ESI measurements the compound has a relatively small molecular mass 189.0906 Da with Δ 2.1 ppm (Figure 28.). The NMR measurements are collected in Table 3.

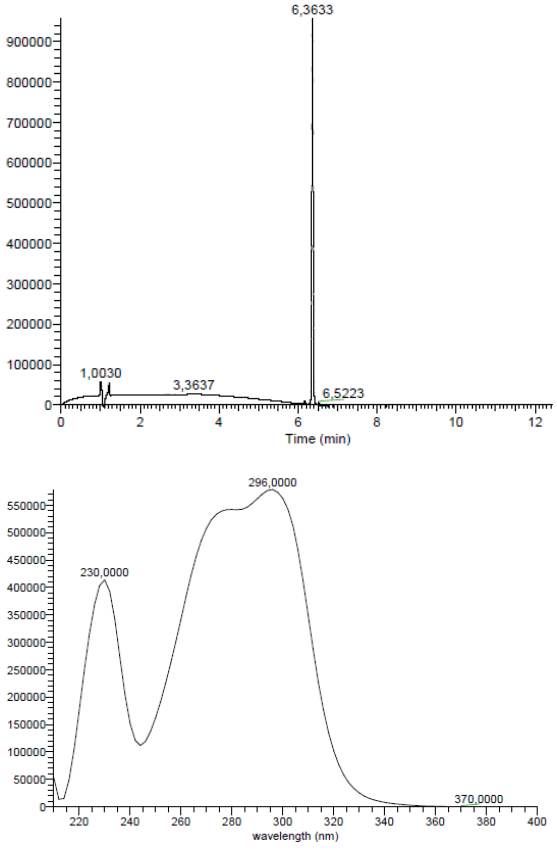

Figure 27 Chromatogram (top) and UV absorbance (bottom) of **XB-3** (fommanoxin)

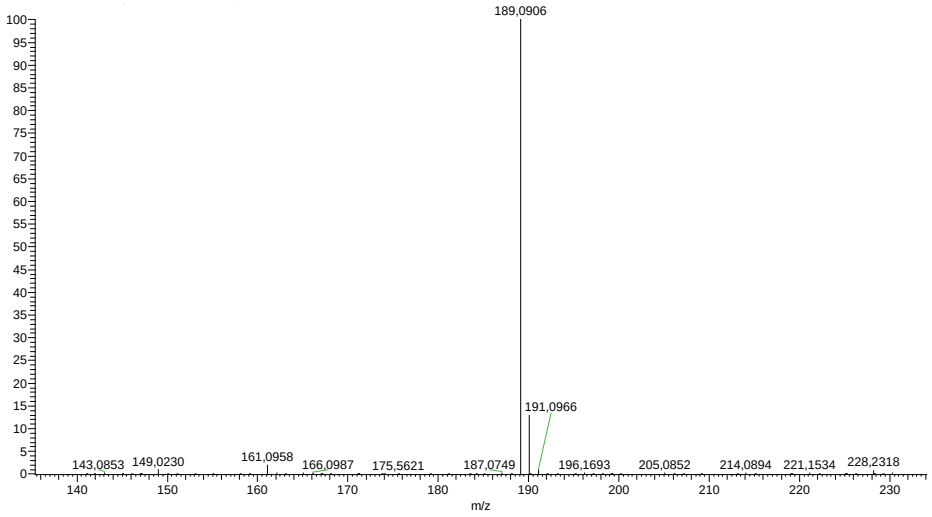

Figure 28. HRMS spectrum of **XB-3** (fommanoxin)

Table 3. Complete ^{1}H and ^{13}C NMR resonance assignments for **XB-3**

No.	**XB-3**		
	δ **^{13}C**	***δ*** **^{1}H**	**m, *J***
2	87.2	5.30	dd, 9.7; 7.9 Hz, 1H
3	33.7	3.41	dd, 15.9; 9.7 Hz, 1H
		3.09	dd, 15.9; 7.9 Hz, 1H
3a	128.2	-	-
4	125.8	7.73	M
5	130.4	-	-
6	133.2	7.68	dd, 8.2; 1.7 Hz
7	109.5	6.90	d, 8.2 Hz
7a	165.2	-	-
1'	143.1	-	-
2'	112.8	5.10	M
		4.95	M
3'	17.0	1.77	S
1"	190.7	9.83	S

3. Pharmacological activities of the isolated compounds

3.1. Cytotoxic activity of the isolated compounds from *B. quercinus*

The isolated compounds (**BGS-1**−**12**) were tested for their antiproliferative activity on resistant Colo 320 cell line using the MTT assay with doxorubicin used as a positive control. The results are collected in Table 4 [106].

Table 4. Antiproliferative activity of compounds **BGS-1–12**

	Colo 320 (IC_{50} µmol)	
Compound	**Mean**	**SD**
BGS- 1	85.65	1.45
BGS- 2	106.20	7.14
BGS- 3	29.78	2.77
BGS- 4	69.16	7.47
BGS- 5	36.55	0.91
BGS- 6	87.37	3.29
BGS- 7	61.71	3.86
BGS- 8	36.18	2.73
BGS- 9	39.46	1.71
BGS- 10	48.97	1.24
BGS- 11	29.74	0.36
BGS- 12	20.71	2.13
doxorubicin *	0.39	0.09

* positive control

3.2. Multidrug efflux pump inhibitory activity of the compounds from *B. quercinus*

The isolated fungal metabolites **BGS-1** to **12** were further investigated for their potential efflux pump inhibitory activity by measuring the intracellular accumulation of rhodamine

123, a widely used P-glycoprotein (ABCB1, P-gp) substrate fluorescent dye, within the MDR Colo 320 cells expressing P-gp (Table 5) [106].

Table 5. MDR efflux pump inhibitory activity results for compounds isolated from *B. quercinus* (most active highlighted)

Samples	**conc. µM**	**FSC**	**SSC**	**FL-1**	**FAR**
Tariquidar	0.2	1557	1038	45.800	15.091
BGS-1	20	1696	898	2.350	0.774
BGS-2	20	1603	947	3.190	1.051
BGS-3	20	1239	889	13.500	**4.448**
BGS-4	20	1349	930	4.060	1.338
BGS-5	20	1332	1012	23.100	**7.611**
BGS-6	20	1681	845	1.170	0.386
BGS-7	20	1593	865	1.800	0.593
BGS-8	20	1356	916	6.310	**2.079**
BGS-9	20	1427	928	2.860	0.942
BGS-10	20	1383	902	11.600	**3.822**
BGS-11	20	1463	940	7.560	**2.491**
BGS-12	20	1420	1007	6.880	**2.267**
DMSO	2%	1654	675	1.220	0.402

FSC: forward scatter count; SSC: side scatter count; FL-1: mean fluorescence; FAR: fluorescence activity ratios

3.3. Chemosensitizing activity of the compounds from *B. quercinus*

Compounds **BGS-3**-**4** and **BGS-7**–**12** were selected for the study of their capacity to decrease the resistance of the MDR Colo 320 cell line to doxorubicin (Table 6) [106].

Table 6. Chemosensitizing activity of the isolated compounds (best drug:doxo ratio ratio highlighted)

Doxo: doxorubicin, CI: combination index, SD: standard deviation

Range	Description
<0.1	Very strong synergism
0.1-0.3	Strong synergism
0.3-0.7	Synergism
0.7-0.85	Moderate Synergism
0.85-0.9	Slight synergism
0.9-1.1	Nearly additive
1.1-1.2	Moderate antagonism
1.2-1.45	Antagonism
1.45-3.3	Strong antagonism
3.3-10	Very strong antagonism

Compound	c(IC_{50}*4) [uM]	Drug:Doxo ratio	CI at ED_{50}	SD	type
BGS-3	119.13	13.82:1	0.907	0.12	Nearly additive
		27.64:1	0.601	0.0495	Synergism
		55.28:1	0.972	0.081	Nearly additive
		110.56:1	1.027	0.1133	Nearly additive
		221.12:1	0.944	0.1212	Nearly additive
		442.24:1	1.471	0.3143	Strong antagonism
BGS-4	276.66	32.08:1	0.816	0.2102	Moderate synergism
		64.16:1	0.691	0.0705	Synergism
		128.32:1	0.734	0.0845	Moderate synergism
		256.64:1	0.739	0.092	Moderate synergism
		513.28:1	0.904	0.1805	Nearly additive
		1026.56:1	1.421	0.2691	Antagonism
BGS-7	246.84	28.63:1	1.002	0.0372	Nearly additive
		57.26:1	0.972	0.1029	Nearly additive
		114.52:1	0.419	0.0697	Synergism
		229.04:1	1.371	0.1618	Antagonism
		458.08:1	1.347	0.2608	Antagonism
		916.16:1	1.295	0.1921	Antagonism

BGS-8	144.74	16.8:1	0.905	0.0877	Nearly additive
		33.6:1	0.889	0.0332	Slight synergism
		67.2:1	0.574	0.0698	Synergism
		134.4:1	0.713	0.0972	Moderate synergism
		268.8:1	0.64	0.0956	Synergism
		537.6:1	1.042	0.0934	Nearly additive
BGS-9	157.84	18.23:1	1.316	0.21	Antagonism
		36.64:1	0.656	0.0528	Synergism
		73.28:1	0.653	0.0839	Synergism
		146.56:1	0.447	0.0534	Synergism
		293.12:1	0.559	0.0681	Synergism
		586.24:1	0.276	0.096	Strong synergism
BGS-10	195.9	22.72:1	1.258	0.3766	Antagonism
		45.44:1	1.09	0.1509	Nearly additive
		90.88:1	0.779	0.0819	Moderate synergism
		181.76:1	0.798	0.1561	Moderate synergism
		363.52:1	0.988	0.2678	Nearly additive
		727.04:1	1.438	0.3819	Antagonism
BGS-11	118.96	13.8:1	1.456	0.2324	Strong antagonism
		27.6:1	0.841	0.14	Moderate synergism
		55.2:1	0.911	0.2554	Nearly additive
		110.4:1	1.491	0.2423	Strong antagonism
		220.8:1	1.89	0.3337	Strong antagonism
		441.6:1	1.938	0.3863	Strong antagonism
BGS-12	82.85	9.62:1	1.992	0.3279	Strong antagonism
		19.24:1	1.42	0.2308	Antagonism
		38.48:1	0.608	0.0324	Synergism
		76.96:1	0.895	0.0678	Slight synergism
		153.92:1	0.736	0.0458	Moderate synergism
		307.84:1	0.824	0.2692	Moderate synergism

3.4. Anti-tyrosinase activity of *X. subpileatus*

The methanol, *n*-hexane, and chloroform extracts and compounds **XB-2** to **7** were selected for anti-tyrosinase activity test in 20 mg/mL concentration (Table 7.) [107].

Table 7. Anti-tyrosinase activity of extracts and compounds of *X. subpileatus.*

Compound/ Extract (8 mg/mL)	**Inhibition (%)**	**SD**
Methanol extract	25.41 $^{c/d}$	7.08
Hexane extract	15.51 ^{d}	2.88
Chloroform extract	38.33 ^{c}	1.16
XB-2	Na	-
XB-3	51.62 ^{b}	11.80
XB-4	Na	-
XB-5	Na	-
XB-6	Na	-
XB-7	Na	-
Azelaic acid (2 mg/mL) *	91.63 ^{a}	0.58

Mean values within a column with the same letter are not significantly different at *p* 0.05 using Duncan's test. The first letter of the alphabet for the highest values, the next for statistically significant decreasing values. * Reference compound, na: not active.

3.5. Anti-Acetylcholinesterase and butyrylcholinesterase activity of compounds from *X. subpileatus*

The methanol, *n*-hexane, and chloroform extracts and **XB-2** to **7** were selected for anti AChE and BChE activity test in 20 mg/mL concentration (Table 8.) [107].

Table 8. Anti-AChE and anti-BChE activities of extracts and compounds of *X. subpileatus*

Compound/ Extract (20 mg/mL)	**AChE Inhibition (%)**	**SD**	**BChE Inhibition (%)**	**SD**
Methanol extract	31.67 ^{d}	0.54	45.93 ^{b}	3.24
Hexane extract	Na	-	22.18 $^{c/d}$	3.57
Chloroform extract	94.05 ^{a}	6.44	86.75 ^{a}	9.07
XB-2	Na	-	Na	-
XB-3	67.66 ^{c}	5.92	83.86 ^{a}	9.79
XB-4	31.28 ^{d}	5.08	32.99 ^{c}	14.08
XB-5	Na	-	6.98 $^{e/f}$	1.24
XB-6	Na	-	18.28 $^{d/e}$	1.38
XB-7	Na	-	0.49 ^{f}	1.67
Galanthamine (0.2 mg/mL) *	76.21 ^{b}	1.57	58.38 ^{b}	7.21

Mean values within a column with the same letter are not significantly different at p 0.05 using Duncan's test. The first letter of the alphabet for the highest values, the next for statistically significant decreasing values. * Reference compound, na: not active.

V. Discussion

1. Structure elucidation

1.1. Structure elucidation of compounds isolated from *B. quercinus*

The structure determination was carried out by extensive spectroscopic analysis, including 1D and 2D NMR and HRMS experiments. Based on the HRMS measurement, the molecular formula of **BGS-1** is $C_{31}H_{48}O_5$. The NMR spectra of the sample suggested a 24-methylene lanostane skeleton with the characteristic resonances of the methylene moiety at C-31 (δ C 106.9) and H-31 (δ H 4.61) (Table 1). The resonances at δ C 136.6 and 134.0 indicated the presence of an unsaturation in the triterpenoid backbone. According to their HMBC correlations with methyl groups H 3 -30 and H 3 -19, they were assigned to C-8 and C-9, respectively. The resonance at δ H 3.89 with HSQC correlation to δ C 77.1 allowed us to conclude that the lanostane skeleton also carries a hydroxyl group. Its position at C-16 was confirmed by COSY cross-peaks with adjacent atoms and NOE correlations to H 3 -19 and H-20. δ C 177.4 and its HMBC correlations to H-20 and H-17 revealed a carboxylic group at the C-20 position. The compound also contained a keto group (δ C 216.0) in position 3, assigned by the HMBC correlations to H 2 -1, H 2 -2, and H 3 -29. Considering the lanostane backbone, a rather unusual hydroxymethyl resonance appeared at δ H 3.39 and 3.16 with HSQC cross-peaks to δ C 68.3. HMBC correlations of the diastereotopic protons with C-3 and C-5 suggested C-28 or C-29 as the site of the hydroxymethyl group. Their NOE correlation with H-5 confirmed the hydroxymethyl group in position 28 (Figure 29.). Thus, compound **BGS- 1** was assigned as 16,28-dihydroxy-24-methylene-3-oxo-lanost-8-en-21-oic acid and named polyporenic acid N.

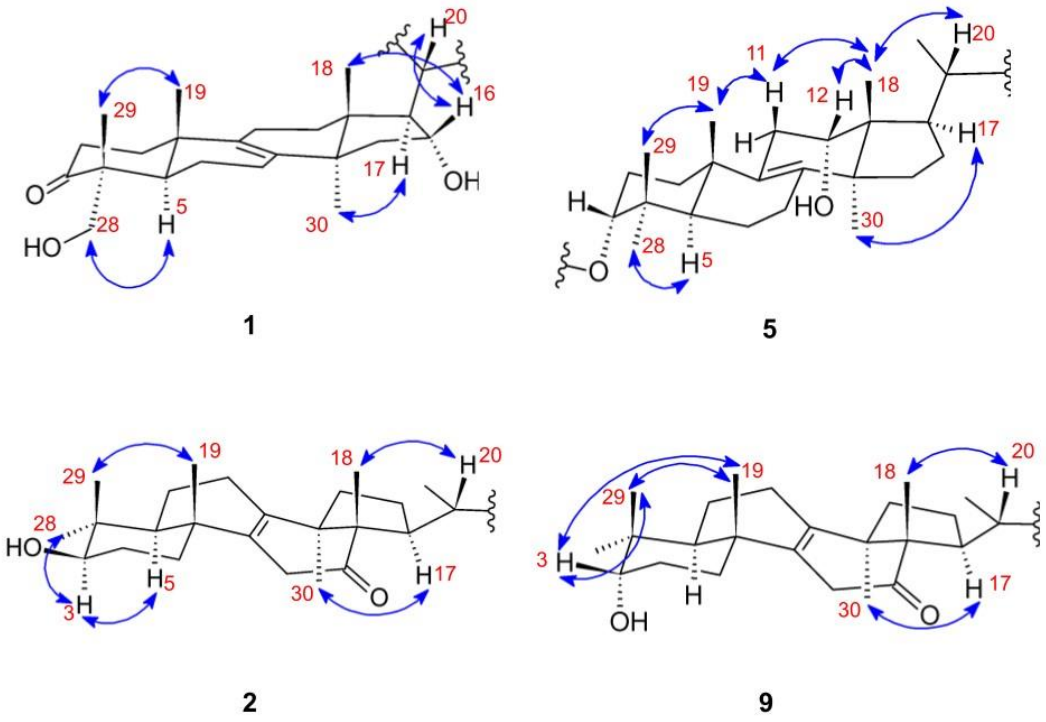

Figure 29. Key NOESY correlations of polyporenic acid N (**BGS-1**), polyporenic acid R (**BGS-5**), polyporenic acid O (**BGS-2**), and polyporenic acid H (**BGS-9**)

Related 29-hydroxy lanostane derivatives were identified in *P. cocos* [108], while the 4,4-dimethyl derivative of polyporenic acid N was reported from *Daedaleopsis confragosa* var. *tricolor* [109].

According to HRMS data, the molecular formula of **BGS-2** was found to be $C_{31}H_{48}O_4$. The compound exhibited the same molecular formula as polyporenic acid H [110] (**BGS-9**); however, significant ^{1}H and ^{13}C NMR resonance differences were observed in positions 3, 4, 5, 28, and 29. While in the case of **BGS-9**, NOE correlations were detected between H-3 and H_3-19, H_3-28, and H_3-29 (Figure 29), in the case of **BGS-2**, NOE correlations were shown between H-3 and H-5, H_3-28 (Figure 29).

These correlations highlighted that **BGS-9** and **BGS-2** differ in the configuration of the hydroxyl group at the C-3 position. To provide further evidence, the ^{1}H NMR resonances and the H-3 multiplicity also differed from that of the 3α-OH substitution pattern [111]. Contrary to 3α-OH, the 3β-OH substitution is characterized by an indicative H-3–H-5

NOE correlation and the ~dd multiplicity of the H-3 resonance (Figures 29 and A17). Thus, **BGS-2** was found to be the C-3 epimer of polyporenic acid H (**BGS-9**), determined as 3β-hydroxy-24-methylene-12-oxo-lanost-8-en-26-oic acid and named polyporenic acid O.

HRMS data indicated a molecular formula of $C_{33}H_{50}O_5$ for **BGS-3**. The NMR data of **BGS-3** were similar to that of polyporenic acid H [110] (**BGS-9**) except for resonances of an extra acetyl group. According to the HMBC correlations between the ester carbonyl (δ_C 170.8) and H-3, the polyporenic acid H skeleton bears the acetyl ester group at the C-3 position. The coupling pattern [110] and the observed NOE correlations with only the "adjacent" (H_2-2, H_3-28, and H_3-29) protons of the H-3 proton suggested the α-orientation of the substituent. Therefore, **BGS-3** was assigned as 3α-*O*-acetylpolyporenic acid H and named polyporenic acid P.

Based on the HRMS data, a molecular formula of $C_{34}H_{52}O_6$ for **BGS-4** can be presented. The 1D and 2D NMR spectra of the compound suggested a 24-methylene lanostane backbone by the typical methylene resonances at C-24 (δ_C 148.3), exhibiting a ^{13}C chemical shift at δ_C 111.4 and ^1H chemical shifts at δ_H 4.97, 4.94 at C-31. A carboxylic group (δ_C 179.6) was assigned to the C-25 position by their HMBC correlations with H-25 and H_3-27. The compound contained an unsaturation (δ_C 134.3 and 134.2), whose position at C-8–C-9 was established by their HMBC cross-peaks C-8/H_3-30 and C-9/H_3-19. This polyporenic acid structure (named polyporenic acid D, $C_{31}H_{50}O_3$) was described by Thappa et al. in 1981 [112], yet no detailed NMR characterization of this compound has been published since then. Moreover, the elemental composition difference and the HMBC correlations of H_2-2′/C-1′, C-3′ of **BGS-4** indicated the presence of an additional malonyl moiety to the previously described skeleton. The position of the substituent was confirmed by the HMBC correlation between H-3 and C-1′ (malonyl carbonyl group). Since the NOE correlations and multiplicity pattern of the H-3 proton were characteristic of a 3α-O substitution [111], compound **BGS-4** was described as 3α-malonyl-24-methylene-lanost-8-en-26-oic acid (3α-malonylpolyporenic acid D) and named polyporenic acid Q.

Data on HRMS of **BGS-5** showed a molecular formula of $C_{38}H_{60}O_8$. The NMR spectra of **BGS-5** also proposed a 24-methylene lanostane backbone. An unsaturation between

C-8–C-9 and a carbonyl group attached to C-25 was confirmed by their HMBC cross-peaks. The resonance at δ_H 4.27 (d, J = 8.0 Hz) with HSQC correlation to δ_C 72.5 suggested the presence of an oxymethine moiety. Based on their COSY cross-peaks with H_2-11 and the HMBC correlations to C-9, C-14, and C-18, a hydroxyl group was assigned to the C-12 position. The key correlations of H-12/H-18/H-20 confirmed the α-orientation of 12-OH. Furthermore, Zhao et al. previously reported that the doublet multiplicity of the H-12 resonance suggests an α-orientation, while the triplet-like multiplicity indicates a β-orientation of 12-OH in the ^{1}H NMR spectra of lanostane-type C_{31} triterpenoids [16]. Although this described polyporenic acid structure (named polyporenic acid A, $C_{31}H_{50}O_4$) was isolated and reported in several previous works, no reliable NMR assignment can be found for polyporenic acid A (hereby referred to as **BGS-10**) [113-116]. In addition, the NMR spectra showed a singlet resonance at δ_H 3.67 with an HSQC cross-peak at δ_C 52.2. This characteristic resonance with the HMBC correlation to C-26 indicated that **BGS-5** is a methyl-ester derivative of polyporenic acid A at C-26. MS/MS fragmentation also suggested the presence of a 3'-hydroxy-3′-methyl-glutaryl moiety, however, the NMR spectra recorded in pyridine-d_5 did not support this assumption. To avoid signal broadening, the NMR spectra of **BGS-5** were also recorded in a methanol-*d*:pyridine-d_5 19:1 solvent mixture. By using this solvent mixture, the ^{1}H and ^{13}C resonances of the proposed substituent and their 2D NMR correlations could be observed. Therefore, this novel polyporenic A derivative was assigned as methyl-3α-(3′-hydroxy-3′-methyl-glutaryl)-24-methylene-12α-hydroxy-lanost-8-en-26-oate, and named polyporenic acid R. Regarding the absolute configuration of polyporenic acids, in a previous study written by King et al [113], the absolute configuration of C_{25} was established based on single crystal X-ray crystallographic analysis of the methyl ester of polyporenic acid A, and it was found to be 25 (S). Another study by Kamo et al. [114] presented the results of a semisynthetic preparative work performed on derivatives of polyporenic acid A to determine the absolute configuration. The results confirmed that the examined fungal metabolites are (25*S*,3′*S*)-(+)-12*R*-hydroxy-3*R*-(3′-hydroxy-3′-methylglutaryloxy)-24-methyllanosta derivatives.

Assuming that the same metabolic pathways lead to the recently isolated polyporenic acid N-S and the previous members of the same series of polyporenic acids, an identical configuration of chiral centers is suggested for compounds described in the current study. The known compounds were identified as (25*S*)-(+)-12*R*-hydroxy-3*R*-malonyloxy-24-methyllanosta-8,24(31)-dien-26-oic acid [114] (**BGS-6**), (25*S*,3′*S*)-(+)-12α-hydroxy-3α-[3′-hydroxy-3′-methylglutaryloxy]-24-methyllanosta-8,24(31)-dien-26-oic acid [113, 116] (**BGS-7**), (25S)-(+)-12α-hydroxy-3α-methylcarboxyacetate-24-methyllanosta-8,24(31)-diene-26-oic acid [21,22] (**BGS-8**), polyporenic acid H [13] (**BGS-9**), polyporenic acid A [114] (**BGS-10**), 3α-*O*-acetylpolyporenic acid A[117], (**BGS-11**), and polyporenic acid C [110, 114, 118], (**BGS-12**) based on their NMR spectra, HRMS data and previously reported characteristics [106].

The NMR and MS spectra for all the isolated compounds from *B. quercinus* (Figures A1–A104). and the complete ^{1}H and ^{13}C NMR resonance assignments (Tables A1–A2) can be found in the Appendix.

1.2. Structure elucidation of compounds isolated from *X. subpileatus*

Based on the HRMS data, the molecular formula of **XB-2** was determined to be $C_{29}H_{44}O$. Analysis of the NMR spectra indicated the presence of an ergostane skeleton, with resonances of two adjacent protons at δ_H 6.21 (d, J = 9.7 Hz, 1H) and 5.88 (d, J = 9.7 Hz, 1H) suggesting unsaturation in the backbone. These protons, assigned to positions C-7 and C-6, respectively, were confirmed by HMBC correlations (Figure 30.). Additionally, a quaternary ^{13}C resonance at δ_C 149.7, with HMBC cross-peaks to H-7 and H_3-18, was assigned to C-14. The ergostane skeleton was further revealed to contain unsaturation between C-4 and C-5, as evidenced by the resonance at δ_H 5.59 (d, J = 4.6 Hz, 1H) with COSY correlation with H-3. Furthermore, an additional double bond between positions C-22 and C-23 was supported by the appearance of a characteristic resonance at δ_H 5.22 (m, 2H) with HSQC cross-peaks to δ_C 135.4 and 132.1. The presence of a methoxy group at C-3 was confirmed by the ^{1}H resonance at δ_H 3.36 (s, 3H) with HSQC cross-peak to δ_C 56.1. The proposed molecular structure of 3-methoxy-ergosta-4,6,8^{14},22-tetraene was deduced from these NMR correlations.

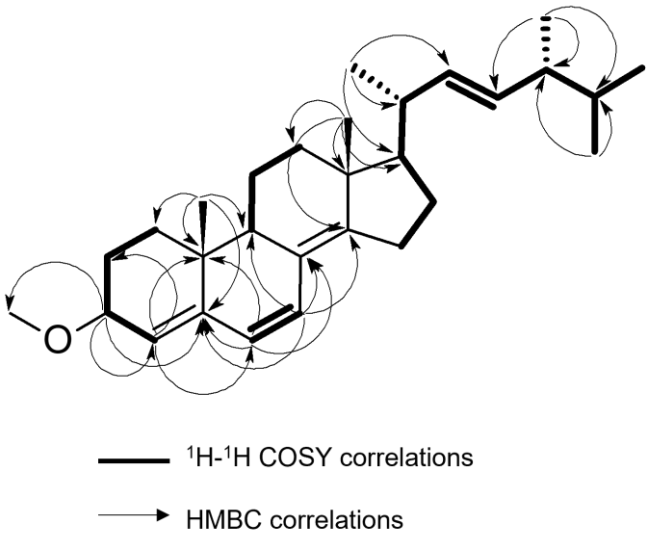

Figure 30. Key ^{1}H—^{1}H COSY and HMBC correlations in both **XB-1** and **XB-2**

.

XB-1 shared the same molecular formula as **XB-2**, and their NMR spectra exhibited similar characteristics, indicating an identical planar structure. However, notable differences in the ^{1}H and ^{13}C NMR resonances at positions 3 and 4 were detected. At position 3 in **XB-1** δ_H 3.93 and δ_C 76.6 were observed, whereas in **XB-2**, these values shifted to δ_H 3.73 and to δ_C 72.5. Similarly, at position 4, **XB-1** exhibited resonances at δ_H 5.49 and δ_C 123.1, while in **XB-2** resonances δ_H 5.59 and δ_C 120.9 were assigned to the same position. The coupling patterns of H-3 in **XB- 1** and **2** were also indicative of the different stereochemistry at C-3. While the H-3 proton in **XB-1** exhibit a large $^{3}J_{H3\text{-}H2}$ value of 10.1 Hz (characteristic for an "axial-axial" coupling), the same $^{3}J_{H3\text{-}H2}$ value in **XB-2** was found to be 4.2 Hz (Table 2.). These disparities in the NMR properties strongly suggest a distinct orientation of the methoxy substituent at position C-3.

Based on the NOE correlations, the recommendation is made that **XB-1** and **2** can be identified as C-3 epimers, with **XB- 1** showing correlations from H_3-19 to H-1β and H-2β along with H-3 to H-1α, while **XB-2** exhibited correlations from H_3-19 to H-1β and H-2β together with H-3 to H-1β (Figure 31). Although **XB-2** displayed identical NMR resonance assignments with that of the natural compound isolated by Lee et al., our detailed stereochemical examination led to the proposal of the α orientation of the Ome group, contrary to their representation [119]. To our knowledge, this research marks the inaugural instance in which both C-3 epimers of the compound were successfully isolated

from a natural source, followed by the determination of their stereochemical properties through a comprehensive NMR analysis. Thus, **XB-2** was assigned as (3α,22E)-3-methoxy-ergosta-4,6,8^{14},22-tetraene, and **XB-1** was characterized as (3β,22E)-3-methoxy-ergosta-4,6,8^{14},22-tetraene. Despite the characterization of the synthetic desmethoxy derivative of compound **XB-2** by Mahé et al. in 1981, the structure has not been reported in the literature [120]. Complete ^{1}H and ^{13}C NMR resonance assignments for **XB-1** and **2** are provided in Table 2.

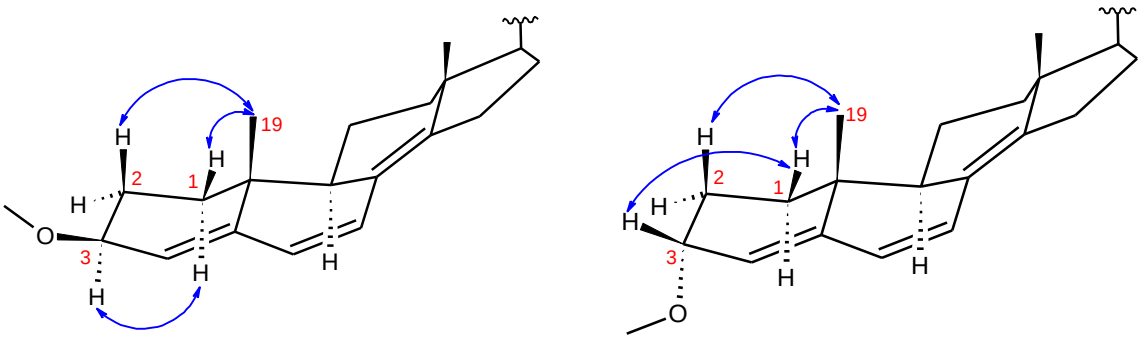

1 **2**

Figure 31. Key ^{1}H—^{1}H NOE correlations in **XB-1** and **XB-**2.

Known compounds **XB-4–7** were also found to be ergostane-type triterpenes identified previously from several fungal species. Their NMR and HRMS spectra suggested ergosta-4,6-8,22-tetraen-3-one (**XB-4**) [121, 122], ergosta-7,22-dien-3-ol (**XB-5**) [123], 9,11-dehydroergosterol peroxide (**XB-6**) [124, 125] and ergosterol peroxide (**XB-7**) [124, 125] structures.

XB-3 was identified as a benzohydrofuran; fomannoxin, based on its NMR spectra, HRMS data and previously published characteristics [126]. Fomannoxin was isolated for the first time from *Fomes annosum* (current name *Heterobasidion annosum*), one of the most important pathogens of coniferous forests widespread in the Northern Hemisphere [127]. It was also identified in other species e.g., the termite nest-derived medicinal fungus *Xylaria nigripes* [128], and *Lauriliella taxodii* [107, 129].

The NMR and MS spectra for all the isolated compounds (Figures A105–A157) and the complete ^{1}H and ^{13}C NMR resonance assignments (Tables A3) from *X. subpileatus* can be found in the Appendix.

2. Biological activities of the compounds of investigated species

2.1. Antiproliferative activity of the compounds from *B. quercinus*

The examined polyporenic acid type constituents demonstrated antiproliferative activity against the Colo 320 tumor cell line with IC_{50} values in the range of 20.7–106.2 μM. **BGS-3**, **11**, and **BGS-12** exerted a more pronounced activity, while **BGS-1-2** and **BGS-6** proved to possess a weaker inhibitory activity [106] (Table 4.).

In a previous study anti-inflammatory and antibacterial properties of several polyporenic acid type compounds derived from *Piptoporus betulinus* and *Wolfiporia cocos* were investigated through various assays. In the mouse ear inflammation test, polyporenic acid derivatives from *P. betulinus* exhibited significant suppression of edema induced by 12-*O*-tetradecanoylphorbol-13-acetate, outperforming glycyrrhetic acid and indomethacin in reducing inflammation. Similarly, 24-methyl-lanostane compounds isolated by Masahika et al. were evaluated for their antibacterial activities against *Bacillus cereus* and *Enterococcus faecium*, as well as their cytotoxic effects on cancer cell lines (NCI-H187, MCF-7, and KB) and noncancerous Vero cells. Among these compounds, the HMG derivative of polyporenic acid A demonstrated activity against Gram-positive bacteria with minimal cytotoxicity [114, 116].

Furthermore, polyporenic acid B exhibited significant cytotoxicity, while polyporenic acid C showed potential as an anti-inflammatory agent by inhibiting 3α-hydroxysteroid dehydrogenase. Additionally, lanostanoids isolated from *P. betulinus* were found to selectively inhibit bacterial hyaluronate lyase, suggesting a promising candidate for antibacterial therapy without affecting bovine hyaluronidase [118].

Moreover, lanostane triterpenoids from *Wolfiporia cocos* showed stimulatory effects on glucose uptake. Following positive outcomes in the anti-inflamatory protein tyrosine phosphatase 1 B inhibition assay, compounds such as formipinic acid D, 3α-(3′-hydroxy-4′-carboxyl-3′-methyl-1,5-dioxopentyloxy)-24-methylene-5α-lanost-8-en-21-oic acid, polyporenic acid D, and pinicolic acid C were tested for their effects on glucose uptake in insulin-resistant HepG2 cells. These compounds exhibited no cytotoxicity at doses up to 100 μM and enhanced insulin-stimulated uptake of 2-NBDG at 12.5 μM, with formipinic acid D showing the most significant enhancement, comparable to the positive

control rosiglitazone. Notably, polyporenic acid D had minimal impact on glucose uptake. These findings highlight the potential therapeutic significance of polyporenic acid-type triterpenoids in modulating glucose uptake and warrant further investigation [130].

Yazdani et al. identified compounds consisting of lanostane derivatives or featuring trinorlanostane backbones, each carrying either a 3-hydroxy-3-methylglutaroyl group or its 6-methyl ester derivative. Five of these compounds (pholiol L, pholiol M, pholiol O, pholiol Q and pholiol S) were evaluated for their antiproliferative and cytotoxic effects *in vitro* using the MTT assay across various cell lines including breast cancer (MCF-7), human colon adenocarcinoma (sensitive Colo 205 and resistant Colo 320), non-small cell lung cancer (A549), and human embryonic lung fibroblasts (MRC-5). Among them, compounds pholiols M and O demonstrated notable antiproliferative activity against the MCF-7 breast cancer cell line, achieving IC_{50} values of 2.48 μM and 9.95 μM, respectively [131].

2.2. Multidrug resistance efflux pump inhibitory activity of compounds from *B. quercinus*

In the investigation of MDR efflux pump inhibitory activity, tariquidar, a potent P-gp inhibitor, was employed as the positive control. The examined constituents were dissolved in DMSO, and the final concentration of the solvent (2.00%) was scrutinized for any impact on the retention of rhodamine 123 (Table 5). Fungal metabolites exhibiting a FAR greater than 2 were considered as active P-gp inhibitors, while those with FAR values exceeding 10 were deemed strong MDR modulators. According to our results, **BGS-3**, **5**, **8**, and **10–12** demonstrated significant inhibitory effects on P-gp MDR efflux pump activity. Among the tested fungal metabolites, polyporenic acid R (**BGS-5**), characterized by a 3′-hydroxy -3′-methyl-glutaryl moiety at C3, emerged as the most potent with a FAR value of 7.611. These findings underscore the potential of these fungal metabolites, particularly polyporenic acid R (**BGS-5**), as promising candidates for further exploration and development as MDR modulators in therapeutic applications. The identification of compounds with notable inhibitory activity against P-gp MDR efflux pumps contributes valuable insights to the ongoing efforts in overcoming multidrug resistance in medical treatments.

In a previous study similar, pholiol-type triterpenoids were tested for their inhibitory effects on P-glycoprotein-mediated efflux. The compounds isolated from *Pholiota populnea* were assessed within Colo 320 MDR cells by Yazdane et al. Tariquidar served as the positive control. The findings indicated that pholiols A and B along with an acyclic triterpene tetraol, effectively inhibited P-gp MDR efflux pump activity. For the purposes of this study, compounds with FAR values above 1 were categorized as active P-gp inhibitors, and those with FAR values exceeding 10 were classified as robust MDR modulators [131]. Notably, the sterol compound with methyl ester functionality on the C3 position and the polyhydroxy-squalene derivative displayed the most significant anti-MDR effects, with FAR values of 6.880 and 6.638, respectively. The compound isolated from *B. quercinus* labeled as **BGS-5** containing HMG on the C3 carbon exerted higher FAR value of 7.611, demonstrating a significant potential (Table 5.).

2.3. Chemosensitizing activity of compounds from *B. quercinus*

In the course of combination studies involving doxorubicin, a checkerboard microplate combination assay was conducted, representing one of the most suitable *in vitro* methods for assessing drug interactions. The acquired data underwent analysis using CompuSyn software 1.0, facilitating the identification of the most efficient ratios of combined agents and the calculation of CI. The CI values provided insights into the type of interaction for the examined combinations of fungal metabolites and doxorubicin.

BGS-3–4, **7–8**, and **12** exhibited synergistic behavior with CI values at ED_{50}: 0.601, 0.691, 0.419, 0.574, and 0.608, respectively. Particularly noteworthy was the potency of **BGS-9**, characterized as demonstrating strong synergism with a CI value of 0.276. Intriguingly, **BGS-9** exhibited moderate efflux pump inhibitory activity while showcasing robust synergism in combination with doxorubicin. This observation prompts further exploration into the potential mechanisms underlying the pharmacological activity of **BGS-9**, thereby contributing valuable insights to the understanding of its synergistic effects in combination therapies with doxorubicin. These findings enhance our understanding of the complex interactions between fungal metabolites and doxorubicin, offering potential avenues for the development of more effective combination therapies in cancer treatment.

Pholiols B and D from *Pholiota populnea*, fungal triterpenes containing a 3-hydroxy-3-methyl-glutarate methyl ester group, demonstrated synergistic interactions, with CI values at 50% of the ED_{50} recorded at 0.348 and 0.660, respectively[131].

Another study also covered a broader range of triterpene compounds from *Momordica balsamina* including balsaminol A-C, E, balsaminagenin C, cucurbalsaminol B-C, and karavilagenin E, all of which consistently showed synergistic interactions with doxorubicin. These findings highlight the capability of these compounds to enhance doxorubicin's effectiveness by modulating P-gp-mediated drug efflux, potentially addressing the clinical challenges linked to P-gp overexpression which often contributes to drug resistance in cancer therapy. Additionally, kuguaglycoside A emerged as a significant modulator, achieving a CI value of 0.956 which suggests its potent role as an effective MDR modulator with a FAR of 49.1 at 20 μM. This result indicates that kuguaglycoside A might operate through mechanisms beyond just P-gp modulation [132].

Our isolated compound **BGS-9** exerted strong synergism with doxorubicin, higher than those of pholiols B and D or kuguaglycoside A introduced previously.

2.4. Biological activity of the isolated compounds from *X. subpiletaus*

Analysis of the results obtained from the tyrosinase activity experiments, as presented in Table 7, highlights the notable inhibitory activity of fomannoxin (**XB-3**) at 51.62%. In contrast, the other isolated fungal constituents did not exhibit such inhibitory effects. It is well-established that tyrosinase is present in the substantia nigra brain region [133]. The enzymatic activity of tyrosinase can lead to the generation of reactive oxygen species (ROS) in this specific brain area, potentially contributing to an elevated risk of developing Parkinson's disease [134].

The implications of our research findings suggest that fomannoxin, with its significant ability to inhibit tyrosinase, may play a role in the prevention of Parkinson's disease. By modulating the enzymatic activity of tyrosinase, fomannoxin could potentially mitigate the increase in ROS levels associated with the brain regio, substantia nigra. The identification of fungal metabolites, such as fomannoxin, with promising inhibitory activity against tyrosinase opens avenues for further exploration into their neuroprotective

potential and their role in strategies for preventing or managing neurodegenerative disorders, particularly Parkinson's disease.

Upon comparing the results of the acetyl- and butyrylcholinesterase activity tests it is revealed that the chloroform extracts exhibited the highest efficacy in both cholinesterase experiments, followed by the methanol extract, while the *n*-hexane extract demonstrated the lowest activity (Table 8). Notably, the AChE enzyme appeared to be less susceptible to the fungal isolates in our assays compared to BChE. All investigated metabolites, except **XB-2**, demonstrated inhibitory activity against BChE, while only **XB-3–4** exhibited activity against AChE.

In the tyrosinase assay, once again, fomannoxin proved to be the most active metabolite, displaying substantial activity percentages of 67.66% and 83.86% in AChE and BChE assays, respectively. AChE and BChE are enzymes associated with the degradation of acetylcholine in the brain, and their increased activity is linked to Alzheimer's disease, leading to reduced acetylcholine levels. Cholinesterase inhibitors, including fomannoxin, are considered potential candidates for the development of novel drugs for Alzheimer's therapy. The cholinesterase inhibitory results for fomannoxin obtained in the present study can be considered valuable addition to a prior study by González-Ramírezet al. where fomannoxin demonstrated potent neuroprotective effects against amyloid-β peptide toxicity in a cellular model, suggesting its potential anti-Alzheimer disease activity. González-Ramírez and her colleagues investigated the neuroprotective properties of fomannoxin, isolated from *Aleurodiscus vitellinus*. They discovered that fomannoxin maintains cell viability across a broad concentration range (10^{-11} to 10^{-4} M) and reduces amyloid-β-induced toxicity in PC12 cells in a concentration-dependent manner. Viability assays confirmed that fomannoxin did not exhibit inherent toxicity, unlike the mitochondrial uncoupler carbonylcyanide-p-trifluoromethoxy-phenylhydrazone used as a control, validating the method's sensitivity [135].

Fomannoxin, characterized by its simple benzofuran structure, not only exhibits significant biological activity but also holds promise as a lead compound for further pharmacological experiments. These findings emphasize the versatile potential of fomannoxin in therapeutic applications, particularly in the context of neurodegenerative disorders such as Alzheimer's disease.

Subsequent studies on synthetic benzofurans have demonstrated that targeted chemical modifications at positions 2, 3, and 5 of the benzofuran structure significantly enhance neuroactivity. These findings emphasize the potential of benzofurans in mitigating key aspects of Alzheimer's disease progression. However, the lack of comprehensive structure-activity relationship (SAR) studies limits the development of effective treatments. Recent SAR analyses of dihydrobenzofuran derivatives have uncovered critical insights: the advantage of lipophilic substituents at the 2-position, the significant role of the molecular configuration of the linker, and the impact of substituents on the terminal aryl ring.

This research identified a series of benzofuran derivatives with notable neuroprotective effects, particularly enhanced by insulin-like growth factor-1 (IGF-1). Among these, the compound 1-(4-methoxyphenyl)-4-(2,2,4,6,7-pentamethyl-2,3-dihydro-1-benzofuran-5-yl)piperazine was distinguished for its strong activity and ability to penetrate brain tissue. Detailed SAR analysis revealed that both the addition and removal of substituents on the benzofuran ring, as well as modifications to the linker structure, significantly influence the compound's efficacy and metabolic stability. The neuroprotective effects of the compound, combined with IGF-1, were thoroughly examined. IGF-1 alone modestly increased neuronal survivability by up to 1.3-fold at concentrations ranging from 3 to 100 ng/mL, independent of concentration. The derivative alone at 1 μmol/L tripled neuronal survival rates. Furthermore, in combination with IGF-1, the derivative substantially enhanced neuroprotective effects by up to 6-fold, depending on IGF-1 concentration. Under physiological-like conditions (100 ng/mL of IGF-1), synthesized benzofurane derivative increased neuronal survival in a concentration-dependent manner, with an half maximal effective concentration (EC_{50}) of 0.15 μM, plateauing at 0.33 μM with a threefold increase in survival rates [136]. These findings demonstrate that both IGF-1 and benzofuran derivatives individually promote neuroprotection, but their combined use significantly amplifies this effect, providing potent neuroprotective activity.

Our enzyme-targeted bioactivity experiments revealed that fomannoxin exhibited significant inhibitory activity in both AChE and BChE assays, moreover it also showed notable inhibitory properties in tyrosinase experiments. Our current study emphasizes the

need for further pharmacological research, particularly towards developing treatments for neurodegenerative diseases.

VI. Conclusions

1. *Buglossoporus quercinus:*

1. **Chemical Analysis:**
    - Five novel polyporenic acids (**BGS-1–5**) and seven known derivatives (**BGS-6–12**) identified.
    - Significantly expands the understanding of *B. quercinus*'s chemical diversity.
2. **Pharmacological Experiments:**
    - Certain fungal triterpenoids (**BGS-3**, **5, 8,** and **10–12**) inhibit the activity of cancer cell efflux pumps.
    - Synergistic interactions with doxorubicin suggest potential for combination therapies in the case of **BGS-3-4**,**7-8** and **12**.
    - **BGS-9** shows potent synergism, emphasizing therapeutic potential.
3. **Implications:**
    - Highlights *B. quercinus* as a source of bioactive natural products.
    - Urges further investigation into medicinal applications.
    - Identifies novel compounds for future therapeutic development.

2. *Xylobolus subpileatus*:

1. **Chemical Profile:**
    - First chemical study of wild growing *X. subpileatus*.
    - Identifies seven secondary metabolites, including new triterpene (**XB-1**) and benzofuran compound fomannoxin (**XB-3**).
2. **Bioactivity Experiments:**
    - Compounds **XB-3** and **XB-4** show significant inhibitory activities in AchE and BchE assays, suggesting neuroprotective properties.
    - Fomannoxin (**XB-3**) exhibits considerable inhibitory effects in tyrosinase experiments, indicating multifaceted biological activities.
3. **Implications:**
    - Fomannoxin (**XB-3**) holds promise for drug development in neurodegenerative diseases.
    - Unique structure positions it for further pharmacological experiments.

Overall Contribution:

1. **Significance:**
    - Contributes significantly to understanding the chemical diversity and pharmacological potential of *B. quercinus* and *X. subpileatus*.
    - Identifies novel compounds with promising pharmacological activities.
2. **Future Research:**
    - Provides a foundation for future research endeavors.
    - Offers opportunities for the development of novel therapeutic agents derived from these fungal species.
3. **Broader Impact:**
    - Valuable contribution to the fields of mycology and pharmacology.
    - Presents potential applications in medicine and drug development.

VII. Összefoglaló

A jelen dolgozat két, hazai poroid gombafaj, a tölgyfa-kérgestapló (*Buglossoporus quercinus)* és a gyapjas mozaikgomba (*Xylobolus subpileatus)* jellegzetes vegyületeinek izolálását, szerkezetmeghatározását és hatástani vizsgálatát ismerteti.

A *B. quercinus* idős tölgyek törzsén élő parazita vagy szaprobionta életmódot folytató, egész Európában ritka faj. A gomba metanolos kivonatából öt új 24-metilén-lanosztán triterpént, a poliporén sav N-R komponenseket (**BGS-1–5**) azonosítottuk, további hét már ismert poliporénsav-származék (**BGS-6–12**) mellett. Az izolált másodlagos anyagcseretermékek szerkezetét spektroszkópiai módszerek (1D és 2D NMR és a HRMS) segítségével határoztuk meg. Az azonosított gombametabolitok antiproliferatív aktivitását *in vitro* vizsgáltuk a P-glikoprotein (ABCB1) expresszióját mutató multidrogrezisztens Colo 320 dganatos sejtvonalon MTT módszerrel (IC_{50}:20,7-től 106,2 μM-ig). A lanosztán triterpének mérsékelt antiproliferatív aktivitást mutattak, továbbá gátolták a Colo 320 daganatos sejtek efflux pumpa tevékenységét. Kísérleteink során vizsgáltuk a gomba triterpének doxorubicinnel való kölcsönhatását is, a **BGS-3–4** és **7–12** vegyületek szinergista aktivitást mutattak doxorubicinnel.

A gyapjas mozaikgomba (*X. subpileatus*) egy széles körben elterjedt fehérkorhasztó évelő faj. A gomba metanolos kivonatának mélyreható mikokémiai vizsgálata során hét vegyület sikerült izolálni (**XB-1–7**). Az azonosított komponensek között találjuk a (3β,22*E*)-3-metoxi-ergoszta-4,6,8^{14},22-tetraént (**XB-1**) amely új természetes vegyület, illetve ennek korábban már ismert epimerjét (**XB-2),** amelynek a szakirodalomban már meglévő NMR adatait az elvégzett méréseink eredményeivel kiegészítettük és újraértékeltük. Ezen két vegyület mellett további öt komponenst izoláltunk, mint a fomannoxint (**XB-3**), amely egy benzohidro-furán típusú vegyület, illetve négy ergosztán típusú triterpént (**XB-4–7**). Az izolált metabolitok szerkezetének meghatározását egy- és kétdimenziós NMR és MS mérések segítségével határoztuk meg. Az izolált vegyületek (**XB-2–7**) illetve az *X. subpileatus* kivonatai esetén tirozináz-, AChE- és a BChE-gátló *in vitro* kísérleteket végeztünk. A fomannoxin (**XB-3**) kiemelkedő antitirozináz aktivitást mutatott, míg az **XB-3–4** komponensek számottevő AChE gátló aktivitással bírtak. A etanolos és kloroformos kivonatok, valamint a **XB-3** és **XB-4** vegyületek esetén kiemelkedő BChE-gátlási aktivitást tapasztaltunk.

VIII. Summary

The dissertation presents two comprehensive studies elucidating the chemical constituents and biological activities of fungal species, *Buglossoporus quercinus* and *Xylobolus subpileatus*.

From *B. quercinus*, a series of novel 24-methylene lanostane triterpenes named polyporenic acids N-R (**BGS-1–5**) were identified alongside seven known polyporenic acids (**BGS-6–12**). Extensive spectroscopic analyses, including 1D and 2D NMR and HRMS experiments, were employed for structure determination. The antiproliferative activity of isolated fungal metabolites was evaluated in vitro using the MTT assay on Colo 320 human colon adenocarcinoma cells expressing P-glycoprotein (ABCB1). The lanostane triterpenes demonstrated moderate antiproliferative activity with IC_{50} values ranging from 20.7 to 106.2 μM. Notably, certain fungal metabolites (**BGS-3**, **5**, **8**, and **10–12**) exhibited the ability to inhibit the efflux pump activity of cancer cells, as highlighted by a P-glycoprotein efflux pump modulatory test on resistant Colo 320 cells. Furthermore, the study investigated drug interactions of triterpenes with doxorubicin using the checkerboard method, revealing synergistic interactions for compounds **BGS-3–4** and **7–12**.

In the study on *Xylobolus subpileatus*, a widely distributed crust fungus, mycochemical analysis of its methanol extract led to the isolation of seven compounds (**XB-1–7**). Among them, compound **XB-1**, identified as (3β,22*E*)-3-methoxy-ergosta-4,6,8^{14},22-tetraene, represents a new natural product, while the NMR assignment of its known epimer (**XB-2**) was revised. Additionally, a benzohydrofuran derivative, fomannoxin (**XB-3**), and four ergostane-type triterpenes (**XB-4–7**) were identified. Structure elucidation of these metabolites was conducted using one- and two-dimensional NMR and MS analysis. Evaluation of the isolated compounds (**XB-2–7**) as well as the chloroform, *n*-hexane, and methanol extracts of *X. subpileatus* revealed their inhibitory properties against tyrosinase, AChE and BChE. Fomannoxin (**XB-3**) exhibited notable antityrosinase activity, while compounds **XB-3–4** demonstrated noteworthy AChE inhibitory activity. Regarding BChE inhibition, methanol and chloroform extracts, along with compounds **XB-3** and **XB-4**, displayed significant activity.

References

1. Mushtaq S, Abbasi BH, Uzair B, Abbasi R. Natural products as reservoirs of novel therapeutic agents. Excli J, 2018;17:420-51.

2. Lysakowska P, Sobota A, Wirkijowska A. Medicinal mushrooms: Their bioactive components, nutritional value and application in functional food production-a review. Molecules, 2023;28.

3. Stamets P, Zwickey H. Medicinal mushrooms: Ancient remedies meet modern science. Integr Med (Encinitas), 2014;13:46-7.

4. Gargano ML, van Griensven LJLD, Isikhuemhen OS, Lindequist U, Venturella G, Wasser SP, Zervakis GI. Medicinal mushrooms: valuable biological resources of high exploitation potential. Plant Biosyst, 2017;151:548-65.

5. Sullivan R, Smith JE, Rowan NJ. Medicinal mushrooms and cancer therapy: translating a traditional practice into Western medicine. Perspect Biol Med, 2006;49:159-70.

6. Lindequist U, Kim HW, Tiralongo E, Van Griensven L. Medicinal mushrooms. Evid Based Complement Alternat Med, 2014;2014:806180.

7. Nagy LG, Toth R, Kiss E, Slot J, Gacser A, Kovacs GM. Six key traits of fungi: Their evolutionary origins and genetic bases. Microbiol Spectr, 2017;5.

8. Lang BF. Mitochondrial genomes in fungi. In: Wells RD, Bond JS, Klinman J, Masters BSS, editor. Molecular life sciences: An encyclopedic reference. New York, NY: Springer New York; 2018. p. 722-8.

9. Berlanga M. Brock Biology of Microorganisms (11th edn). San Francisco: Benjamin Cummings 2010.

10. L. Hawksworth D. The magnitude of fungal diversity: the 1.5 million species estimate revisited. Mycol Res, 2001;105:1422-32.

11. Burford EP, Kierans M, Gadd GM. Geomycology: Fungi in mineral substrata. Mycologist, 2003;17:98-107.

12. Tadych M, White JF. Endophytic microbes. In: Schaechter M, editor. Encyclopedia of microbiology Oxford: Academic Press; 2009. p. 431-42.

13. Lepage BA, Currah RS, Stockey RA. The fossil fungi of the Princeton chert. Int J Plant Sci, 1994;155:828-36.

14. Hibbett DS, Binder M, Bischoff JF, Blackwell M, Cannon PF, Eriksson OE, Huhndorf S, James T, Kirk PM, Lücking R, Thorsten Lumbsch H, Lutzoni F, Matheny PB, McLaughlin DJ, Powell MJ, Redhead S, Schoch CL, Spatafora JW, Stalpers JA, Vilgalys R, Aime MC, Aptroot A, Bauer R, Begerow D, Benny GL, Castlebury LA, Crous PW, Dai Y-C, Gams W, Geiser DM, Griffith GW, Gueidan C, Hawksworth DL, Hestmark G, Hosaka K, Humber RA, Hyde KD, Ironside JE, Kõljalg U, Kurtzman CP, Larsson K-H, Lichtwardt R, Longcore J, Miądlikowska J, Miller A, Moncalvo J-M, Mozley-Standridge S, Oberwinkler F, Parmasto E, Reeb V, Rogers JD, Roux C, Ryvarden L, Sampaio JP, Schüßler A, Sugiyama J, Thorn RG, Tibell L, Untereiner WA, Walker C, Wang Z, Weir A, Weiss M, White MM, Winka K, Yao Y-J, Zhang N. A higher-level phylogenetic classification of the Fungi. Mycol Res, 2007;111:509-47.

15. Taylor TN, Taylor EL, Krings M. Fungi, Bacteria, and Lichens. In: Taylor TN, Taylor EL, Krings M, editor. Paleobotany (Second Edition). London: Academic Press; 2009. p. 71-119.

16. Manoharachary C, Kunwar IK, Reddy SV. Biodiversity, phylogeny and evolution of fungi. In: Sharma VP, editor. Nature at Work: Ongoing Saga of Evolution. New Delhi: Springer India; 2010. p. 141-58.

17. Voigt K, James TY, Kirk PM, Santiago A, Waldman B, Griffith GW, Fu M, Radek R, Strassert JFH, Wurzbacher C, Jeronimo GH, Simmons DR, Seto K, Gentekaki E, Hurdeal VG, Hyde KD, Nguyen TTT, Lee HB. Early-diverging fungal phyla: taxonomy,

species concept, ecology, distribution, anthropogenic impact, and novel phylogenetic proposals. Fungal Divers, 2021;109:59-98.

18. Volk TJ. Encyclopedia of Biodiversity. San Diego: Academic Press 2001.

19. Volk TJ. Fungi. In: Scheiner SM, editor. Encyclopedia of Biodiversity Oxford: Academic Press; 2013. p. 771-92.

20. Millanes AM, Diederich P, Ekman S, Wedin M. Phylogeny and character evolution in the jelly fungi (*Tremellomycetes*, *Basidiomycota*, Fungi). Mol Phylogenet Evol, 2011;61:12-28.

21. Raper JR. Genetics of Sexuality in Higher Fungi. New York: Ronald Press Company 1966.

22. Meinhardt F, Esser K, Lemke Ph.D PA. Sex determination and sexual differentiation in filamentous fungi. Crit Rev Plant Sci, 1990;9:329-41.

23. Nieuwenhuis BPS, Billiard S, Vuilleumier S, Petit E, Hood ME, Giraud T. Evolution of uni- and bifactorial sexual compatibility systems in fungi. Heredity, 2013;111:445-55.

24. Boekhout T, Fonseca Á, Sampaio JP, Bandoni RJ, Fell JW, Kwon-Chung KJ. Discussion of teleomorphic and anamorphic basidiomycetous yeasts. In: Kurtzman CP, Fell JW, Boekhout T, editor. The Yeasts London: Elsevier; 2011. p. 1339-72.

25. Jawaharlal Nehru Krishi Vishwa Vidyalaya. http://jnkvv.org/. 2023 [updated 15 May 2024; cited 02 May 2024]. Available from: chrome-extension://efaidnbmnnnibpcajpcglclefindmkaj/http://www.jnkvv.org/PDF/11042020204520primary%20and%20secondary%20metabolites%20and%20their%20applications%20(3%20files%20merged).pdf

26. Keller NP. Fungal secondary metabolism: regulation, function and drug discovery. Nat Rev Microbiol, 2019;17:167-80.

27. Avalos J, Limón MC. Fungal secondary metabolism. Encyclopedia, 2022;2:1-13.

28. Staunton J, Weissman KJ. Polyketide biosynthesis: a millennium review. Nat Prod Rep, 2001;18:380-416.

29. Shen B. Polyketide biosynthesis beyond the type I, II and III polyketide synthase paradigms. Curr Opin Chem Biol, 2003;7:285-95.

30. Hertweck C, Luzhetskyy A, Rebets Y, Bechthold A. Type II polyketide synthases: gaining a deeper insight into enzymatic teamwork. Nat Prod Rep, 2007;24:162-90.

31. Dao T, Linthorst H, Verpoorte R. Chalcone synthase and its functions in plant resistance. Phytochem Rev, 2011;10:397-412.

32. Süssmuth RD, Mainz A. Nonribosomal peptide synthesis-principles and prospects. Angew Chem, Int Ed Engl, 2017;56:3770-821.

33. Finking R, Marahiel MA. Biosynthesis of nonribosomal peptides. Annu Rev Microbiol, 2004;58:453-88.

34. Boettger D, Hertweck C. Molecular diversity sculpted by fungal PKS–NRPS hybrids. Chembiochem, 2013;14:28-42.

35. Gil-Serna J, García-Díaz M, González-Jaén MT, Vázquez C, Patiño B. Description of an orthologous cluster of ochratoxin A biosynthetic genes in *Aspergillus* and *Penicillium* species. A comparative analysis. Int J Food Microbiol, 2018;268:35-43.

36. Du L, Sánchez C, Shen B. Hybrid peptide–polyketide natural products: biosynthesis and prospects toward engineering novel molecules. Metab Eng, 2001;3:78-95.

37. Ludwiczuk A, Skalicka-Woźniak K, Georgiev MI. Terpenoids. In: Badal S, Delgoda R, editor. Pharmacognosy. Boston: Academic Press; 2017. p. 233-66.

38. Schrey H, Müller FJ, Harz P, Rupcic Z, Stadler M, Spiteller P. Nematicidal anthranilic acid derivatives from *Laccaria species*. Phytochemistry, 2019;160:85-91.

39. Chuankid B, Schrey H, Thongbai B, Raspé O, Arnold N, Hyde KD, Stadler M. Secondary metabolites of P*hlebopus species* from Northern Thailand. Mycol Prog, 2020;19:1525-36.

40. Himstedt R, Wagner S, Jaeger RJR, Lieunang Watat ML, Backenkohler J, Rupcic Z, Stadler M, Spiteller P. Formaldehyde as a chemical defence agent of fruiting bodies of *Mycena rosea* and its role in the generation of the alkaloid mycenarubin C. Chembiochem, 2020;21:1613-20.

41. Vanyolos A, Dekany M, Kovacs B, Kramos B, Berdi P, Zupko I, Hohmann J, Beni Z. Gymnopeptides A and B, cyclic octadecapeptides from the mushroom *Gymnopus fusipes*. Org Lett, 2016;18:2688-91.

42. Hirai Y, Ikeda M, Murayama T, Ohata T. New monoterpentriols from the fruiting body of *Flammulina velutipes*. Biosci Biotechnol Biochem, 1998;62:1364-8.

43. Guo H, Diao QP, Zhang B, Feng T. Two new illudane sesquiterpenoids and one new menthane monoterpene from cultures of *Craterellus cornucopioides*. J Asian Nat Prod Res, 2019;21:123-8.

44. Yang S, Bao H, Wang H, Li Q. Anti-tumour effect and pharmacokinetics of an active ingredient isolated from *Inonotus hispidus*. Biol Pharm Bull, 2019;42:10-7.

45. Lee J, Shi YM, Grun P, Gube M, Feldbrugge M, Bode H, Hennicke F. Identification of feldin, an antifungal polyyne from the beefsteak fungus *Fistulina hepatica*. Biomolecules, 2020;10.

46. Sum WC, Ebada SS, Clement Matasyoh J, Stadler M. Recent progress in the evaluation of secondary metabolites from *Basidiomycota*. Curr Res Biotechnol, 2023;6:100155.

47. Wu Q, Dohnal V, Kuca K, Yuan Z. Trichothecenes: structure-toxic activity relationships. Curr Drug Metab, 2013;14:641-60.

48. Cheng T, Chepkirui C, Decock C, Matasyoh JC, Stadler M. Sesquiterpenes from an eastern african medicinal mushroom belonging to the genus *Sanghuangporus*. J Nat Prod, 2019;82:1283-91.

49. Wu J, Uchida K, Ridwan AY, Kondo M, Choi JH, Hirai H, Kawagishi H. Erinachromanes A and B and Erinaphenol A from the culture broth of *Hericium erinaceus*. J Agric Food Chem, 2019;67:3134-9.

50. Kou RW, Du ST, Li YX, Yan XT, Zhang Q, Cao CY, Yin X, Gao JM. Cyathane diterpenoids and drimane sesquiterpenoids with neurotrophic activity from cultures of the fungus *Cyathus africanus*. J Antibiot (Tokyo), 2019;72:15-21.

51. Duru M, Tel-Çayan G. Biologically active terpenoids from mushroom origin: A review. Rec Nat Prod, 2015;9:456-83.

52. Tang D, Xu YZ, Wang WW, Yang Z, Liu B, Stadler M, Liu LL, Gao JM. Cyathane diterpenes from cultures of the bird's nest fungus *Cyathus hookeri* and their neurotrophic and anti-neuroinflammatory activities. J Nat Prod, 2019;82:1599-608.

53. Kasangana PB, Stevanovic T. Studies of pentacyclic triterpenoids structures and antidiabetic properties of *Myrianthus* genus. In: Atta ur R, editor. Studies in natural products chemistry. Amsterdam: Elsevier; 2021. p. 1-27.

54. Sandeep, Ghosh S. Triterpenoids: Structural diversity, biosynthetic pathway, and bioactivity. In: Atta ur R, editor. Studies in natural products chemistry. Amsterdam: Elsevier; 2020. p. 411-61.

55. Hamid K, Alqahtani A, Kim MS, Cho JL, Cui PH, Li CG, Groundwater PW, Li GQ. Tetracyclic triterpenoids in herbal medicines and their activities in diabetes and its complications. Curr Top Med Chem, 2015;15:2406-30.

56. Hao DC, Gu X-J, Xiao PG. Phytochemistry and biology of Ilex pharmaceutical resources. In: Hao DC, Gu X-J, Xiao PG, editor. Medicinal Plants. Cambridge: Woodhead Publishing; 2015. p. 531-85.

57. Xiao WL, Li RT, Huang SX, Pu JX, Sun HD. Triterpenoids from the *Schisandraceae* family. Nat Prod Rep, 2008;25:871-91.

58. Shi YM, Xiao WL, Pu JX, Sun HD. Triterpenoids from the *Schisandraceae* family: an update. Nat Prod Rep, 2015;32:367-410.

59. Noushahi HA, Khan AH, Noushahi UF, Hussain M, Javed T, Zafar M, Batool M, Ahmed U, Liu K, Harrison MT, Saud S, Fahad S, Shu S. Biosynthetic pathways of triterpenoids and strategies to improve their biosynthetic efficiency. J Plant Growth Regul, 2022;97:439-54.

60. Nguyen VT, Tung NT, Cuong TD, Hung TM, Kim JA, Woo MH, Choi JS, Lee J-H, Min BS. Cytotoxic and anti-angiogenic effects of lanostane triterpenoids from *Ganoderma lucidum*. Phytochem Lett, 2015;12:69-74.

61. Faustino C, Pinheiro L, Duarte N. Triterpenes as potential drug candidates for rheumatoid arthritis treatment. Life, 2023;13.

62. Zhao P, Guan M, Tang W, Walayat N, Ding Y, Liu J. Structural diversity, fermentation production, bioactivities and applications of triterpenoids from several common medicinal fungi: Recent advances and future perspectives. Fitoterapia, 2023;166:105470.

63. Sawai S, Saito K. Triterpenoid biosynthesis and engineering in plants. Front Plant Sci, 2011;2:25.

64. Shi L, Ren A, Mu D, Zhao M. Current progress in the study on biosynthesis and regulation of ganoderic acids. Appl Microbiol Biotechnol, 2010;88:1243-51.

65. Abdjul DB, Yamazaki H, Maarisit W, Rotinsulu H, Wewengkang DS, Sumilat DA, Kapojos MM, Losung F, Ukai K, Namikoshi M. Oleanane triterpenes with protein tyrosine phosphatase 1B inhibitory activity from aerial parts of *Lantana camara* collected in Indonesia and Japan. Phytochemistry, 2017;144:106-12.

66. Shang CH, Zhu F, Li N, Ou-Yang X, Shi L, Zhao MW, Li YX. Cloning and characterization of a gene encoding HMG-CoA reductase from *Ganoderma lucidum* and its functional identification in yeast. Biosci Biotechnol Biochem, 2008;72:1333-9.

67. Ding YX, Ou-Yang X, Shang CH, Ren A, Shi L, Li YX, Zhao MW. Molecular cloning, characterization, and differential expression of a farnesyl-diphosphate synthase gene from the basidiomycetous fungus *Ganoderma lucidum*. Biosci Biotechnol Biochem, 2008;72:1571-9.

68. Liu D, Gong J, Dai W, Kang X, Huang Z, Zhang HM, Liu W, Liu L, Ma J, Xia Z, Chen Y, Chen Y, Wang D, Ni P, Guo AY, Xiong X. The genome of *Ganoderma lucidum* provides insights into triterpenes biosynthesis and wood degradation [corrected]. PLoS One, 2012;7:e36146.

69. Ye L, Liu S, Xie F, Zhao L, Wu X. Enhanced production of polysaccharides and triterpenoids in *Ganoderma lucidum* fruit bodies on induction with signal transduction during the fruiting stage. PLoS One, 2018;13:e0196287.

70. Galappaththi MCA, Patabendige NM, Premarathne BM, Hapuarachchi KK, Tibpromma S, Dai DQ, Suwannarach N, Rapior S, Karunarathna SC. A review of ganoderma triterpenoids and their bioactivities. Biomolecules, 2022;13:24.

71. Cardenas PD, Almeida A, Bak S. Evolution of structural diversity of triterpenoids. Front Plant Sci, 2019;10:1523.

72. Wang Q, Cao R, Zhang Y, Qi P, Wang L, Fang S. Biosynthesis and regulation of terpenoids from basidiomycetes: exploration of new research. AMB Express, 2021;11:150.

73. Ríos JL, Francini F, Schinella GR. Natural products for the treatment of type 2 diabetes mellitus. Planta Med, 2015;81:975-94.

74. Fatmawati S, Shimizu K, Kondo R. Ganoderic acid Df, a new triterpenoid with aldose reductase inhibitory activity from the fruiting body of *Ganoderma lucidum*. Fitoterapia, 2010;81:1033-6.

75. Ying YM, Zhang LY, Zhang X, Bai HB, Liang DE, Ma LF, Shan WG, Zhan ZJ. Terpenoids with alpha-glucosidase inhibitory activity from the submerged culture of *Inonotus obliquus*. Phytochemistry, 2014;108:171-6.

76. Tung NT, Cuong TD, Hung TM, Lee JH, Woo MH, Choi JS, Kim J, Ryu SH, Min BS. Inhibitory effect on NO production of triterpenes from the fruiting bodies of *Ganoderma lucidum*. Bioorg Med Chem Lett, 2013;23:1428-32.

77. Tang W, Liu JW, Zhao WM, Wei DZ, Zhong JJ. Ganoderic acid T from *Ganoderma lucidum* mycelia induces mitochondria mediated apoptosis in lung cancer cells. Life Sci, 2006;80:205-11.

78. Jiang J, Grieb B, Thyagarajan A, Sliva D. Ganoderic acids suppress growth and invasive behavior of breast cancer cells by modulating AP-1 and NF-κB signaling. Int J Mol Med, 2008;21:577-84.

79. Hien B, Hoa L, Tham L, Quang D. Cattienoids A-C, three novel steroids from the mushroom *Tomophagus cattienensis*. Fitoterapia, 2013;91:125-7.

80. Liu DZ, Zhu YQ, Li XF, Shan WG, Gao PF. New triterpenoids from the fruiting bodies of *Ganoderma lucidum* and their bioactivities. Chem Biodivers, 2014;11:982-6.

81. Liu XT, Winkler AL, Schwan WR, Volk TJ, Rott M, Monte A. Antibacterial compounds from mushrooms II: lanostane triterpenoids and an ergostane steroid with activity against *Bacillus cereus* isolated from *Fomitopsis pinicola*. Planta Med, 2010;76:464-6.

82. Ano Y, Kutsukake T, Hoshi A, Yoshida A, Nakayama H. Identification of a novel dehydroergosterol enhancing microglial anti-inflammatory activity in a dairy product fermented with *Penicillium candidum*. PLoS One, 2015;10:e0116598.

83. Xiong M, Huang Y, Liu Y, Huang M, Song G, Ming Q, Ma X, Yang J, Deng S, Wen Y. Antidiabetic activity of ergosterol from *Pleurotus ostreatus* in KK-Ay mice with spontaneous type 2 diabetes mellitus. Mol Nutr Food Res, 2018;62:1700444.

84. Hu X, Jiang D, Li F, Wu Z, Huang Y, Song S, Wang Z. Ergosterol reverses multidrug resistance in SGC7901/Adr cells. Pharmazie, 2014;69:396-400.

85. Chen YK, Kuo YH, Chiang BH, Lo JM, Sheen LY. Cytotoxic activities of 9,11-dehydroergosteroi peroxide and ergosterol peroxide from the fermentation mycelia of *Ganoderma lucidum* cultivated in the medium containing leguminous plants on Hep 3B cells. J Agric Food Chem, 2009;57:5713-9.

86. Cateni F, Doljak B, Zacchigna M, Anderluh M, Piltaver A, Scialino G, Banfi E. New biologically active epidioxysterols from *Stereum hirsutum*. Bioorg Med Chem Lett, 2007;17:6330-4.

87. Wang S, Zhang L, Liu L-Y, Dong Z-J, Li Z-H, Liu J-K. Six novel steroids from culture of basidiomycete *Polyporus ellisii*. Nat prod bioprospect, 2012;2:240-4.

88. Zhabinskii VN, Drasar P, Khripach VA. Structure and biological activity of ergostane-type steroids from fungi. Molecules, 2022;27:2103.

89. Kotlába F. *Buglossoporus* gen. nov.-A new genus of polypores. Ceska Mykol, 1966;20:81-9.

90. Leif R, Irenela M, Tuomo N. Poroid fungi of Europe. Oslo: Fungiflora 2014: 455.

91. Crockatt ME, Campbell A, Allum L, Ainsworth AM, Boddy L. The rare oak polypore *Piptoporus quercinus*: Population structure, spore germination and growth. Fungal Ecol, 2010;3:94-106.

92. Cao YF, He SH. *Xylobolus austrosinensis sp*. nov. (*Stereaceae*, *Russulales*) and notes on the genus. Phytotaxa, 2020;452:200-8.

93. Papp V. Adatok a *Xylobolus* nemzetség magyarországi előfordulásáról. Clusiana, 2011;50:173-82.

94. Clement RE, Hao C. Liquid–liquid extraction: Basic principles and automation. In: Pawliszyn J, editor. Comprehensive sampling and sample preparation. Oxford: Academic Press; 2012. p. 51-63.

95. Zygler A, Słomińska M, Namieśnik J. Soxhlet extraction and new developments such as soxtec. In: Pawliszyn J, editor. Comprehensive sampling and sample preparation. Oxford: Academic Press; 2012. p. 65-82.

96. Mukherjee PK. Extraction and other downstream procedures for evaluation of herbal drugs. In: Mukherjee PK, editor. Quality control and evaluation of herbal drugs. Amsterdam: Elsevier; 2019. p. 195-236.

97. Garg A, Sharma R, Dey P, Kundu A, Kim HS, Bhakta T, Kumar A. Analysis of triterpenes and triterpenoids. In: Sanches Silva A, Nabavi SF, Saeedi M, Nabavi SM, editor. Recent Advances in Natural Products Analysis. Amsterdam: Elsevier; 2020. p. 393-426.

98. Chen L, Chen X, Wang S, Bian Y, Zhao J, Li S. Analysis of triterpenoids in *Ganoderma resinaceum* using liquid chromatography coupled with electrospray ionization quadrupole-time-of-flight mass spectrometry. Int J Mass Spectrom, 2019;436:42-51.

99. Feng GF, Zheng Y, Sun Y, Liu S, Pi ZF, Song FR, Liu ZQ. A targeted strategy for analyzing untargeted mass spectral data to identify lanostane-type triterpene acids in *Poria cocos* by integrating a scientific information system and liquid chromatography-tandem mass spectrometry combined with ion mobility spectrometry. Anal Chim Acta, 2018;1033:87-99.

100. Grienke U, Foster PA, Zwirchmayr J, Tahir A, Rollinger JM, Mikros E. 1H NMR-MS-based heterocovariance as a drug discovery tool for fishing bioactive compounds out of a complex mixture of structural analogues. Sci Rep, 2019;9:11113.

101. Chou TC. Drug combination studies and their synergy quantification using the chou-talalay method. Cancer Res, 2010;70:440-6.

102. Chou TC. Theoretical basis, experimental design, and computerized simulation of synergism and antagonism in drug combination studies. Pharmacol Rev, 2006;58:621-81.

103. Lim TY, Lim YY, Yule CM. Evaluation of antioxidant, antibacterial and anti-tyrosinase activities of four *Macaranga* species. Food Chemistry, 2009;114:594-9.

104. Ellman GL, Courtney KD, Andres V, Featherstone RM. A new and rapid colorimetric determination of acetylcholinesterase activity. Biochem Pharmacol, 1961;7:88-95.

105. Studzinska-Sroka E, Majchrzak-Celinska A, Bandurska M, Rosiak N, Szwajgier D, Baranowska-Wojcik E, Szymanski M, Gruszka W, Cielecka-Piontek J. Is caperatic acid the only compound responsible for activity of lichen *Platismatia glauca* within the nervous system? Antioxidants (Basel), 2022;11.

106. Felegyi K, Garadi Z, Racz B, Toth G, Papp V, Boldizsar I, Dancso A, Spengler G, Beni S, Vanyolos A. Polyporenic acids from the mushroom *Buglossoporus quercinus* possess chemosensitizing and efflux pump inhibitory activities on Colo 320 adenocarcinoma cells. J Fungi (Basel), 2023;9:923.

107. Felegyi K, Garadi Z, Studzinska-Sroka E, Papp V, Boldizsar I, Dancso A, Beni S, Zalewski P, Vanyolos A. Anticholinesterase and antityrosinase secondary metabolites from the fungus *Xylobolus subpileatus*. Molecules, 2023;29:213.

108. Zhou L, Zhang Y, Gapter LA, Ling H, Agarwal R, Ng KY. Cytotoxic and anti-oxidant activities of lanostane-type triterpenes isolated from *Poria cocos*. Chem Pharm Bull (Tokyo), 2008;56:1459-62.

109. Rösecke J, König WA. Constituents of the fungi *Daedalea quercina* and *Daedaleopsis confragosa* var. tricolor. Phytochemistry, 2000;54:757-62.

110. Sofrenic I, Andelkovic B, Todorovic N, Stanojkovic T, Vujisic L, Novakovic M, Milosavljevic S, Tesevic V. Cytotoxic triterpenoids and triterpene sugar esters from the medicinal mushroom *Fomitopsis betulina*. Phytochemistry, 2021;181:112580.

111. Peng XR, Su HG, Liu JH, Huang YJ, Yang XZ, Li ZR, Zhou L, Qiu MH. C30 and C31 Triterpenoids and triterpene sugar esters with cytotoxic activities from edible mushroom *Fomitopsis pinicola (Sw*. Ex Fr.) Krast. J Agric Food Chem, 2019;67:10330-41.

112. Thappa RK, Agarwal SG, Dhar KL, Atal CK. A new triterpenic acid from the wood rotting fungi. Phytochemistry, 1981;20:1746-7.

113. King TJ, Smith RW, Begley MJ, Goad LJ. The stereochemistry of polyporenic acid a methyl ester. Tetrahedron Lett, 1984;25:3489-92.

114. Kamo T, Asanoma M, Shibata H, Hirota M. Anti-inflammatory lanostane-type triterpene acids from *Piptoporus betulinus*. J Nat Prod, 2003;66:1104-6.

115. Khalilov Q, Li L, Liu Y, Tohtahon Z, Chen X, Aisa HA, Yuan T. Piptolinic acids F–J, five new lanostane-type triterpenoids from *Piptoporus betulinus*. Nat Prod Rep, 2019;33:3044-51.

116. Isaka M, Chinthanom P, Suvannakad R, Thummarukcharoen T, Feng T, Liu JK. Fomitopsins I and J, 24-methyl-lanostane triterpenoids from fruiting bodies of the wood-rot basidiomycete *Fomitopsis sp*. Phytochem Lett, 2019;29:178-81.

117. Zhao J, Yang Y, Yu M, Yao K, Luo X, Qi H, Zhang G, Luo Y. Lanostane-type C31 triterpenoid derivatives from the fruiting bodies of cultivated *Fomitopsis palustris*. Phytochemistry, 2018;152:10-21.

118. Wangun HVK, Berg A, Hertel W, Nkengfack AE, Hertweck C. Anti-inflammatory and anti-hyaluronate lyase activities of lanostanoids from *Piptoporus betulinus*. J Antibiot, 2004;57:755-8.

119. Lee S, Kim CS, Yu JS, Kang H, Yoo MJ, Youn UJ, Ryoo R, Bae HY, Kim KH. Ergopyrone, a styrylpyrone-fused steroid with a hexacyclic 6/5/6/6/6/5 skeleton from a mushroom *Gymnopilus orientispectabilis*. Org Lett, 2021;23:3315-9.

120. Mahé C, Patin H, Van Hulle MT, Barton DHR. Structure and chemistry of π-allyl palladium complexes from steroids. J Chem Soc, Perkin Trans 1, 1981:2504-8.

121. Chobot V, Opletal L, Jahodář L, Patel AV, Dacke CG, Blunden G. Ergosta-4,6,8,22-tetraen-3-one from the edible fungus, *Pleurotus ostreatus* (oyster fungus). Phytochemistry, 1997;45:1669-71.

122. Tanemossu SAF, Franke K, Arnold N, Schmidt J, Wabo HK, Tane P, Wessjohann LA. Rare biscoumarin derivatives and flavonoids from *Hypericum riparium*. Phytochemistry, 2014;105:171-7.

123. Niedermeyer THJ, Lindequist U, Mentel R, Gördes D, Schmidt E, Thurow K, Lalk M. Antiviral terpenoid constituents of *Ganoderma pfeifferi*. J Nat Prod, 2005;68:1728-31.

124. Chen YK, Kuo YH, Chiang BH, Lo JM, Sheen LY. Cytotoxic activities of 9,11-dehydroergosteroi peroxide and ergosterol peroxide from the fermentation mycelia of Ganoderma lucidum cultivated in the medium containing leguminous plants on Hep 3B cells. Journal of Agricultural and Food Chemistry, 2009;57:5713-9.

125. Lee D, Ko Y, Pang C, Ko YJ, Choi YK, Kim KH, Kang KS. Estrogenic activity of mycoestrogen (3β,5α,22E)-ergost-22-en-3-ol via estrogen receptor α-dependent signaling pathways in MCF-7 Cells. Molecules 2021;27:36.

126. Hansson D, Menkis A, Olson K, Stenlid J, Broberg A, Karlsson M. Biosynthesis of fomannoxin in the root rotting pathogen *Heterobasidion occidentale*. Phytochemistry, 2012;84:31-9.

127. Hirotani M, O'Reilly J, Donnelly DMX, Polonsky J. Fomannoxin - a toxic metabolite of *Fomes annosus*. Tetrahedron Lett, 1977;18:651-2.

128. Chang JC, Hsiao G, Lin RK, Kuo YH, Ju YM, Lee TH. Bioactive constituents from the termite nest-derived medicinal fungus *Xylaria nigripes*. J Nat Prod, 2017;80:38-44.

129. Arnone A, Assante G, Nasini G, Pava O. ChemInform abstract: secondary mould metabolites. Part 38. Isolation and structure elucidation of dihydrobenzofurans isolated from *Laurilia taxodii*. Chem Inform, 2010;23:261-.

130. Zhang J, Chen B, Liang J, Han J, Zhou L, Zhao R, Liu H, Dai H. Lanostane triterpenoids with PTP1B inhibitory and glucose-uptake stimulatory activities from mushroom *Fomitopsis pinicola* collected in North America. J Agric Food Chem, 2020;68:10036-49.

131. Yazdani M, Beni Z, Dekany M, Szemeredi N, Spengler G, Hohmann J, Vanyolos A. Triterpenes from *Pholiota populnea* as cytotoxic agents and chemosensitizers to overcome multidrug resistance of cancer cells. J Nat Prod, 2022;85:910-6.

132. Ramalhete C, Mulhovo S, Molnar J, Ferreira MU. Triterpenoids from *Momordica balsamina*: reversal of ABCB1-mediated multidrug resistance. Bioorg Med Chem, 2016;24:5061-7.

133. Carballo-Carbajal I, Laguna A, Romero-Giménez J, Cuadros T, Bové J, Martinez-Vicente M, Parent A, Gonzalez-Sepulveda M, Peñuelas N, Torra A, Rodríguez-Galván B, Ballabio A, Hasegawa T, Bortolozzi A, Gelpi E, Vila M. Brain tyrosinase overexpression implicates age-dependent neuromelanin production in Parkinson's disease pathogenesis. Nat Commun, 2019;10:973.

134. Dias V, Junn E, Mouradian MM. The role of oxidative stress in parkinson's disease. J Parkinsons Dis, 2013;3:461-91.

135. González-Ramírez M, Gavilán J, Silva-Grecchi T, Cajas-Madriaga D, Triviño S, Becerra J, Saez-Orellana F, Pérez C, Fuentealba J. A natural benzofuran from the patagonic aleurodiscus vitellinus fungus has potent neuroprotective properties on a cellular model of amyloid-β peptide toxicity. J Alzheimer's Dis, 2018;61:1463-75.

136. Wakabayashi T, Tokunaga N, Tokumaru K, Ohra T, Koyama N, Hayashi S, Yamada R, Shirasaki M, Inui Y, Tsukamoto T. Discovery of benzofuran derivatives that collaborate with insulin-like growth factor 1 (IGF-1) to promote neuroprotection. J Med Chem, 2016;59:5109-14.

List of Publications

Regarding the topic of the thesis:

Felegyi, K, Garádi, Z, Rácz, B, Tóth, G, Papp, V, Boldizsár, I, Dancsó, A, Spengler, G, Béni, S, Ványolós, A. (2023). Polyporenic acids from the mushroom *Buglossoporus quercinus* possess chemosensitizing and efflux pump inhibitory activities on Colo 320 adenocarcinoma cells. J. fungi, 9(9), 923.

Felegyi, K, Garádi, Z, Studzińska-Sroka, E, Papp, V, Boldizsár, I, Dancsó, A, Béni, S, Zalewski, P, Ványolós, A. Anticholinesterase and antityrosinase secondary metabolites from the fungus *Xylobolus subpileatus*. Molecules 2024, *29*, 213.

Felegyi et al. (2022) - Conference Abstract

Title:" Triterpén vegyületek a tölgyfa-kérgestaplóból"; (Hungarian Herbal Conference, 2022)

Garádi et al. (2021) - Conference Abstract

Title: "NMR-based Structural identification of bioactive metabolites in Hungarian poroid fungi"; (PhD Scientific Days 2021)

Felegyi et al. (2021) - Conference Abstract

Title: "Isolation and structure determination of metabolites from *Buglossoporus quercinus*"; (Interdisciplinary Doctoral Conference, 2021)

Garádi et al. (2021) – Conference Abstract

Title: "Structural analysis of secondary metabolites from oak bracket fungus".

Other publication:

Felegyi-Tóth CA, Tóth Z, Garádi Z, Boldizsár I, Nedves AN, Simon A, **Felegyi K**, Alberti Á, Riethmüller E. (2022) Membrane Permeability and Aqueous Stability Study of Linear and Cyclic Diarylheptanoids from *Corylus maxima*. Pharmaceutics. 14(6):1250.

Acknowledgements

First of all, I wish to express my deep gratitude to my supervisor, **Dr. Attila Ványolós** for his guidance and encouragement, especially during the more challenging moments of my work.

I would like to thank **Dr. Szabolcs Béni**, former Director, and **Dr. Ágnes Alberti-Dér**, present Director of the Department of Pharmacognosy, for the possibility and their support of my work.

I am grateful to **Dr. Viktor Papp** for his help in collecting the mushroom material. I also wish to thank my co-authors, **Dr. Szabolcs Béni** and **Zsófia Garádi** for the NMR investigations, **Dr. Imre Boldizsár** for the MS measurements. I thank **Dr. Gabriella Spengler**, **Bálint Rácz**, **Dr. Elżbieta Studzińska-Sroka** and **Dr. Przemysław Zalewski** for the bioassays. Special thanks to **Tamás Czeglédi**, who provided daily support throughout the years I worked on this project. I wish to thank all those who devoted substantial time to hunt for spelling and typographical errors. My thanks are also due to all members of the team in the Department of Pharmacognosy for the unique workplace atmosphere offered.

I would like to extend my heartfelt gratitude to my colleagues at Carbohyde, especially **Dr. Milo Malanga**, **Mihály Bálint** and **Daniel Bisericaru**, for their invaluable assistance and support during the writing of my thesis.

I am also thankful to my **family**, above all I would like to thank my wife **dr. Csenge Anna Felegyi-Tóth** for her love and constant support, my sons **Boti** and **Kori** for their support at all times for the successful completion of this project.

Appendix

Spectra and spectral data on BGS-1

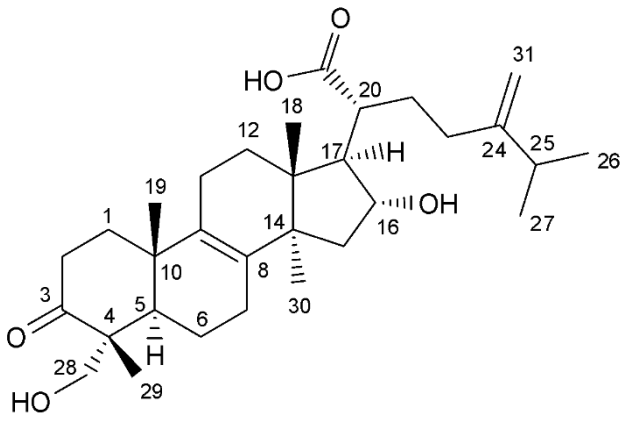

HRMS (+) *m/z* 501.3568 $[M+H]^+$ (501.3575 calcd. for $C_{31}H_{49}O_5$; *Δ* -1.3 ppm); HRMSMS (CID = 15%, 30%, 45%) 483.3460, 465.3365, 453.3355

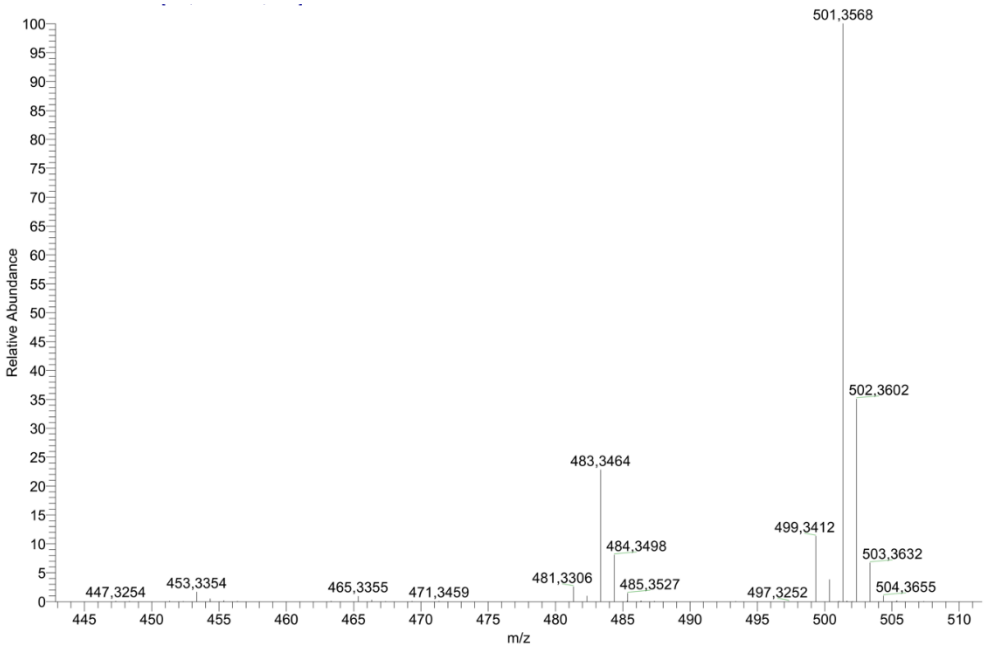

Figure A1. HRMS spectrum of **BGS-1**

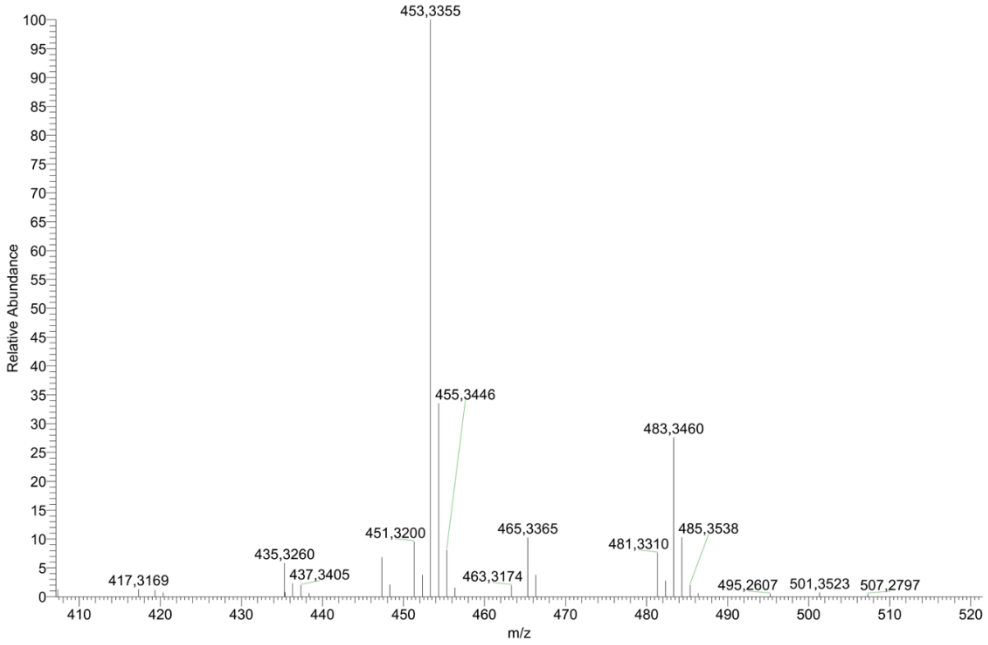

Figure A2. MS-MS spectrum of **BGS-1**

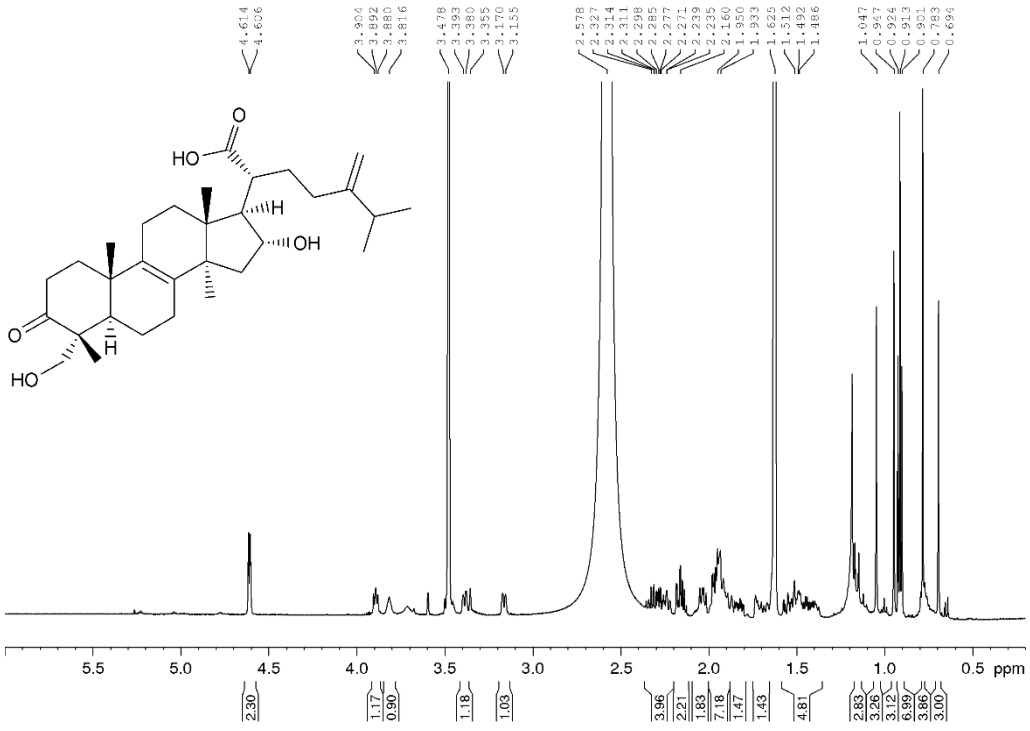

Figure A3. ^{1}H spectrum of **BGS-1** (600 MHz, THF-d_8, 295 K)

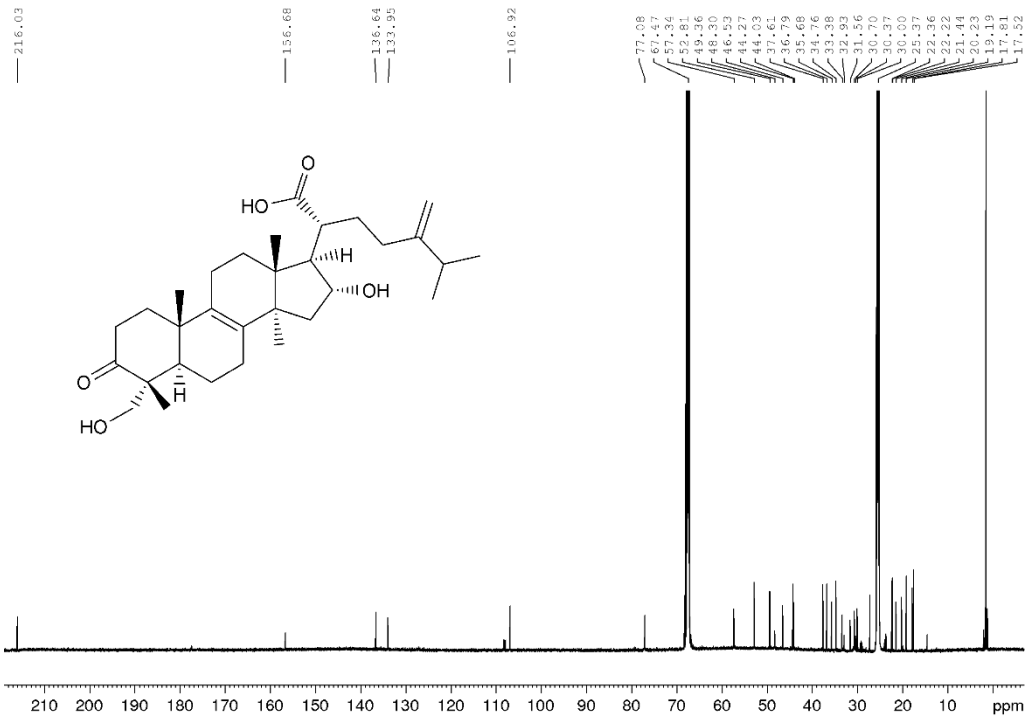

Figure A4. ^{13}C spectrum of **BGS-1** (150 MHz, THF-d_8, 295 K)

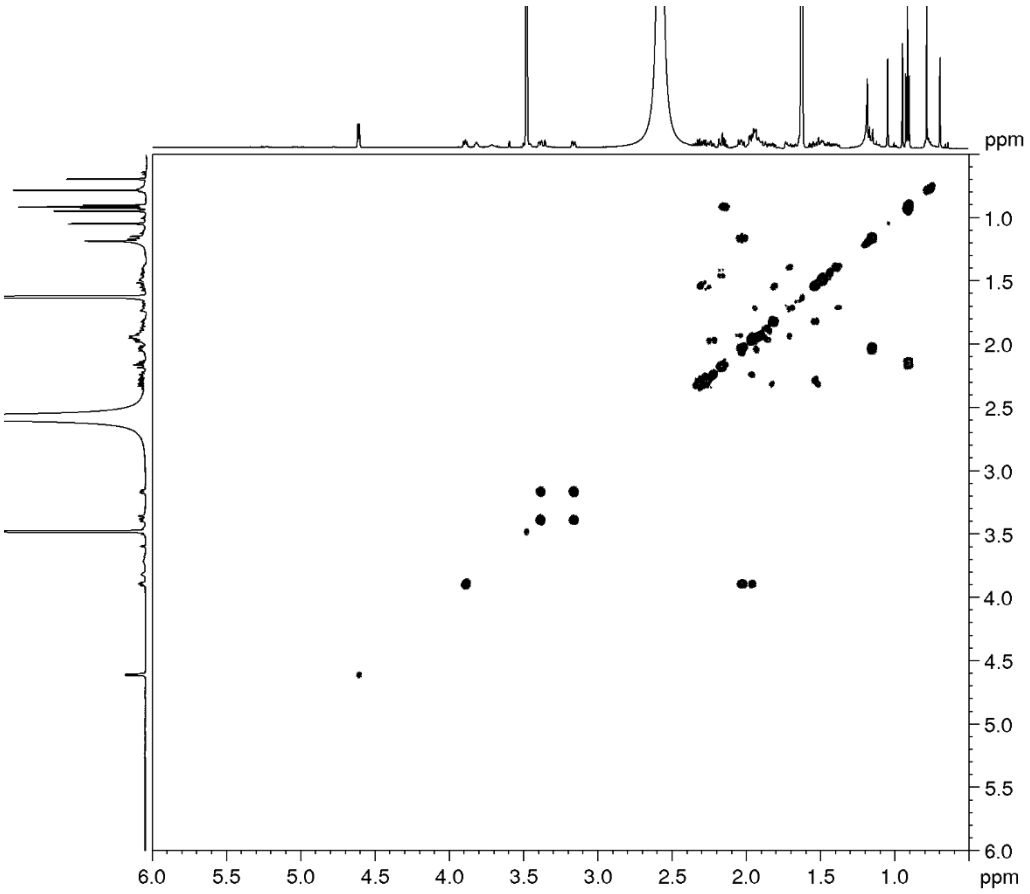

Figure A5. COSY spectrum of **BGS-1** (600 MHz, THF-d_8, 295 K)

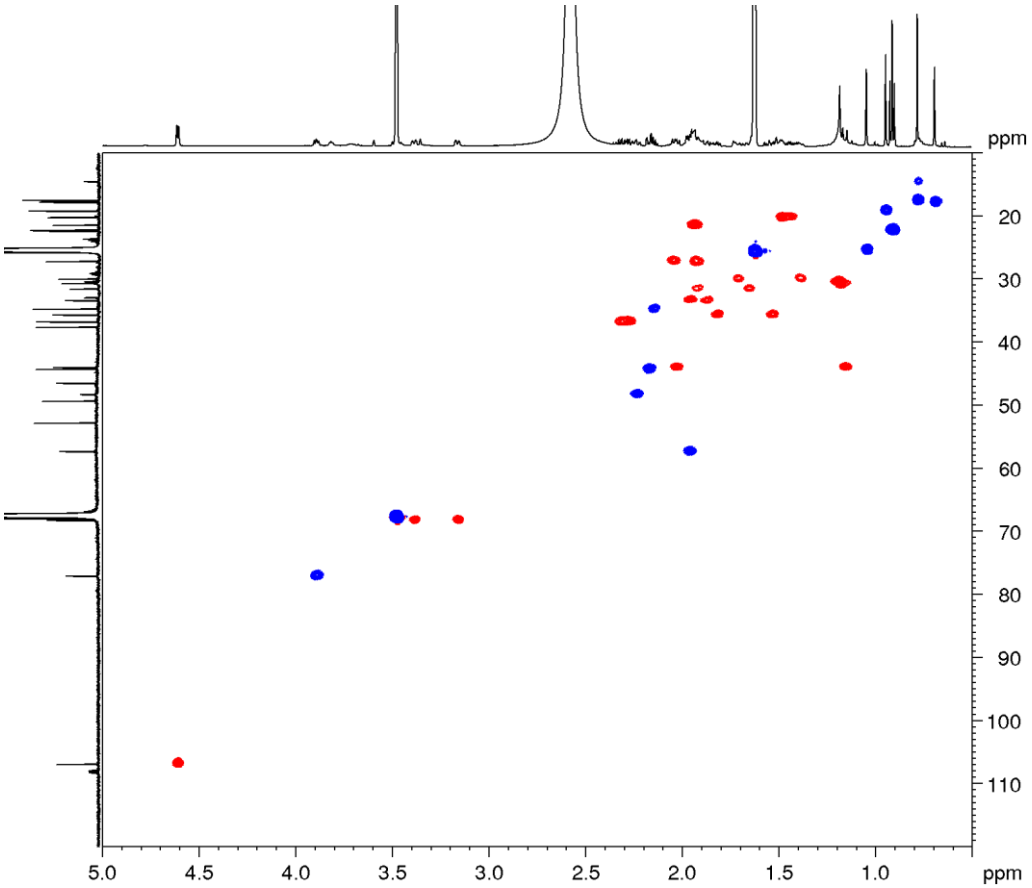

Figure A6. DEPT-edited HSQC spectrum of **BGS-1** (600 MHz, THF-d_8, 295 K)

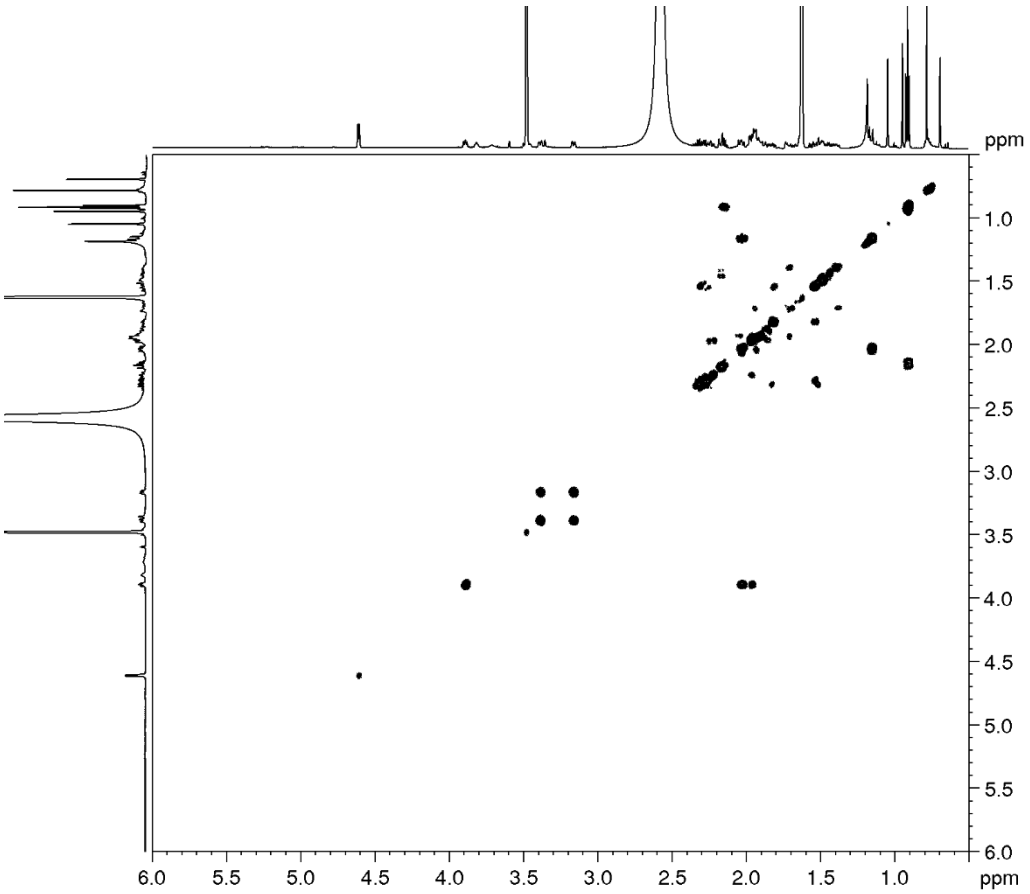

Figure A7. HMBC spectrum of **BGS-1** (600 MHz, THF-d_8, 295 K)

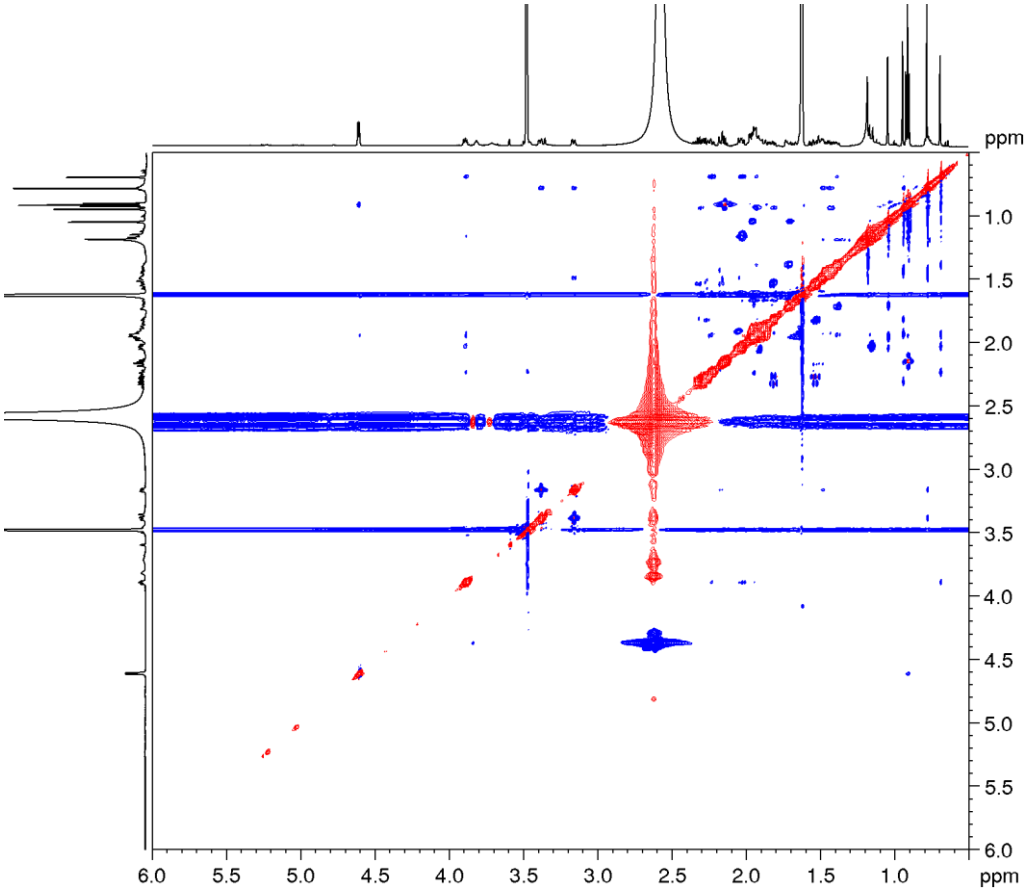

Figure A8. NOESY spectrum of **BGS-1** (600 MHz, THF-d_8, 295 K)

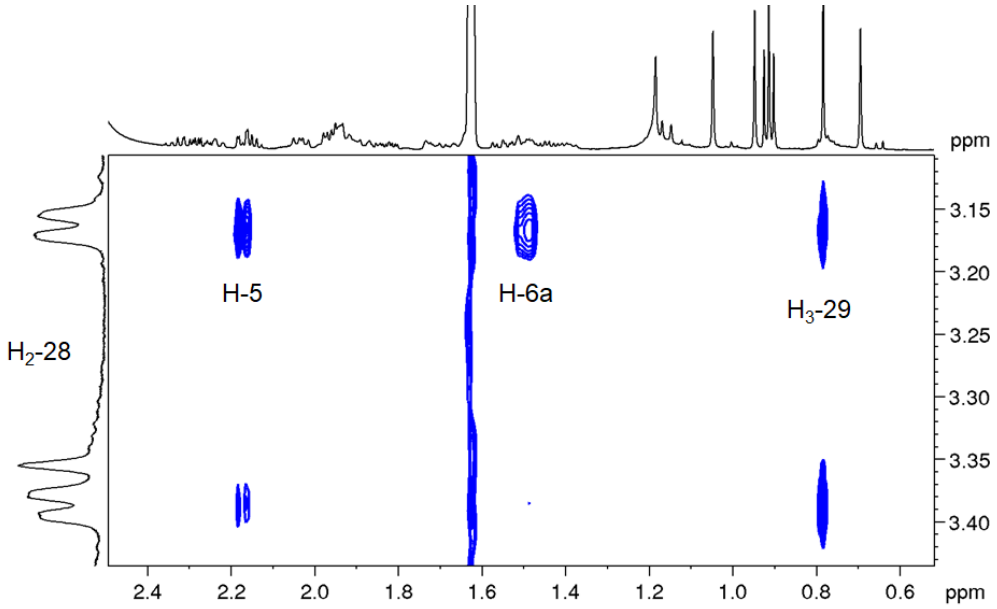

Figure A9. Selected region of the NOESY spectrum of **BGS-1** (600 MHz, THF-d_8, 295 K)

Spectra and spectral data on BGS-2

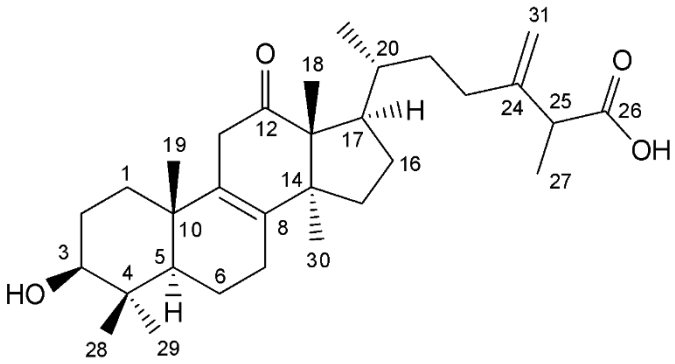

HRMS (+) *m/z* 485.3620 $[M+H]^+$ (485.3625 calcd. for $C_{31}H_{49}O_4$; Δ -1.0 ppm); HRMSMS (CID = 15%, 30%, 45%) 468.9432, 454.8377

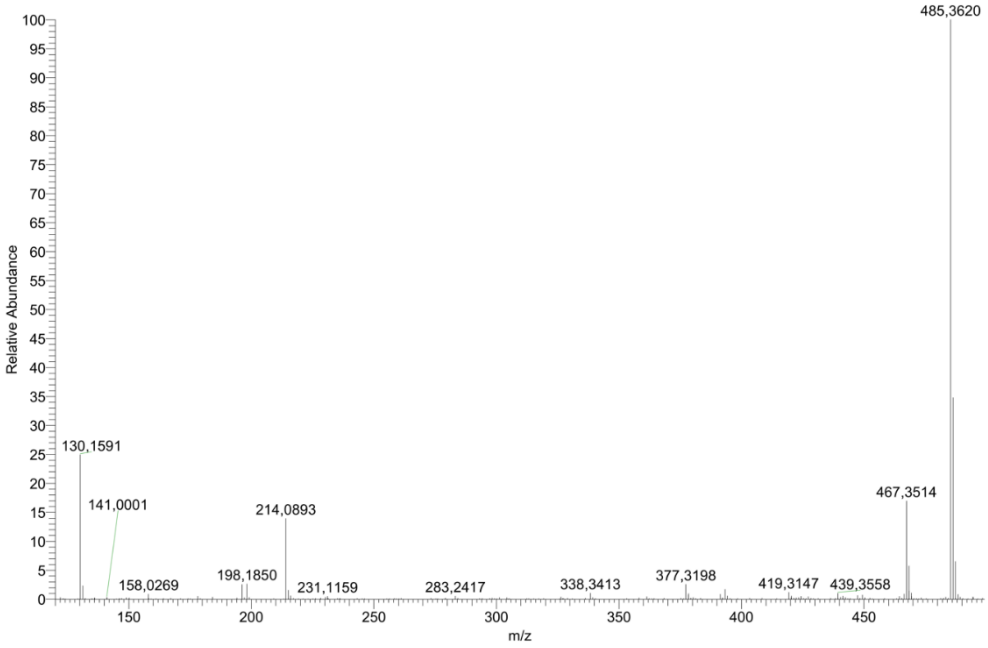

Figure A10. HRMS spectrum of **BGS-2**

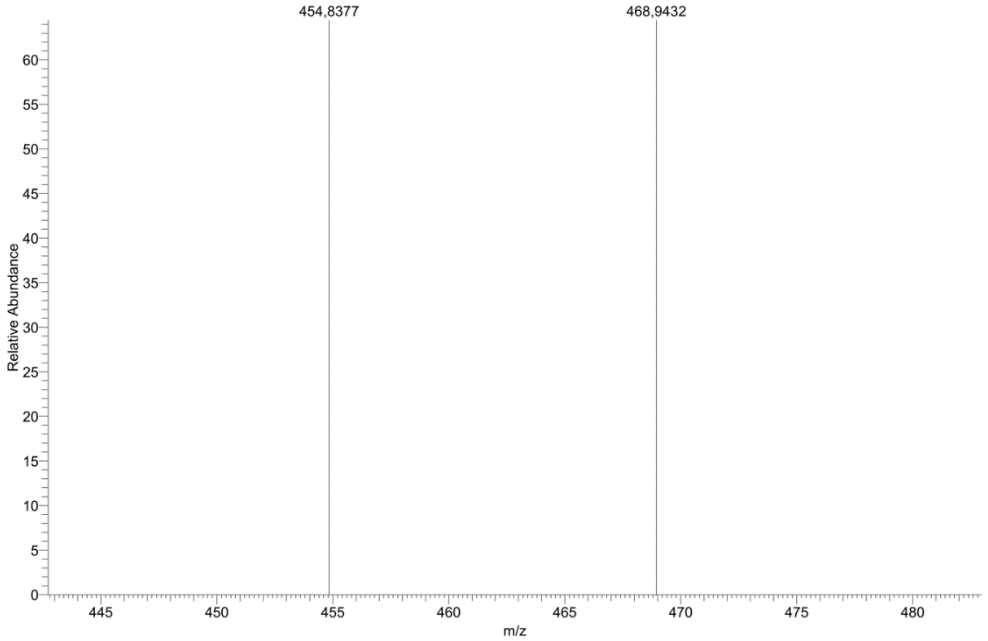

Figure A11. MS-MS spectrum of **BGS-2**

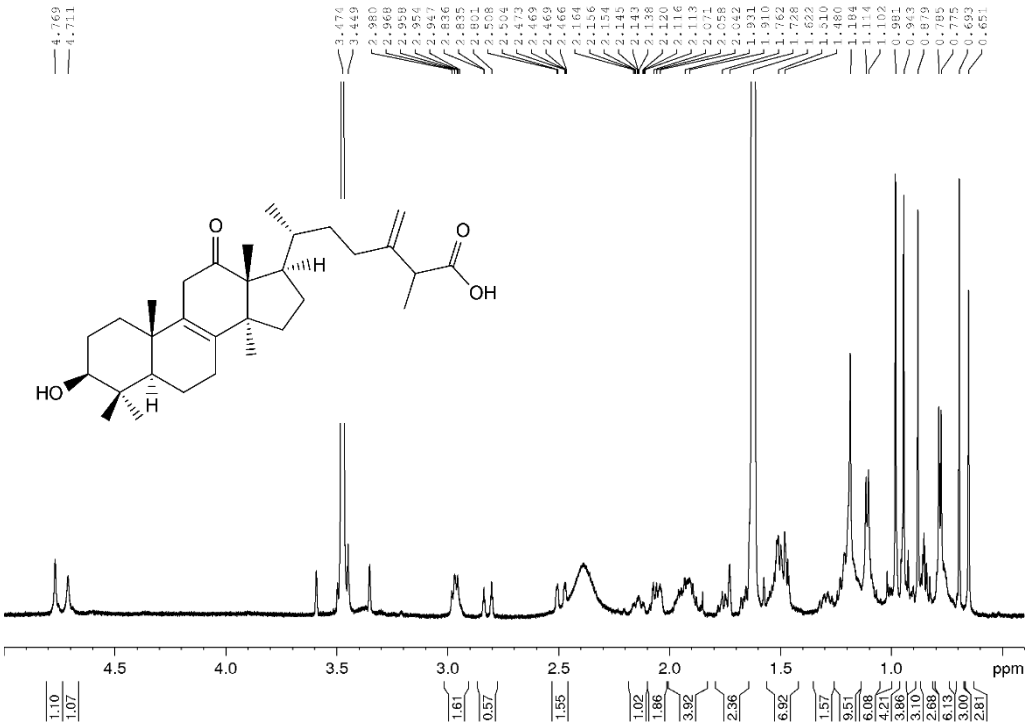

Figure A12. ^{1}H spectrum of **BGS-2** (600 MHz, THF-d_8, 295 K)

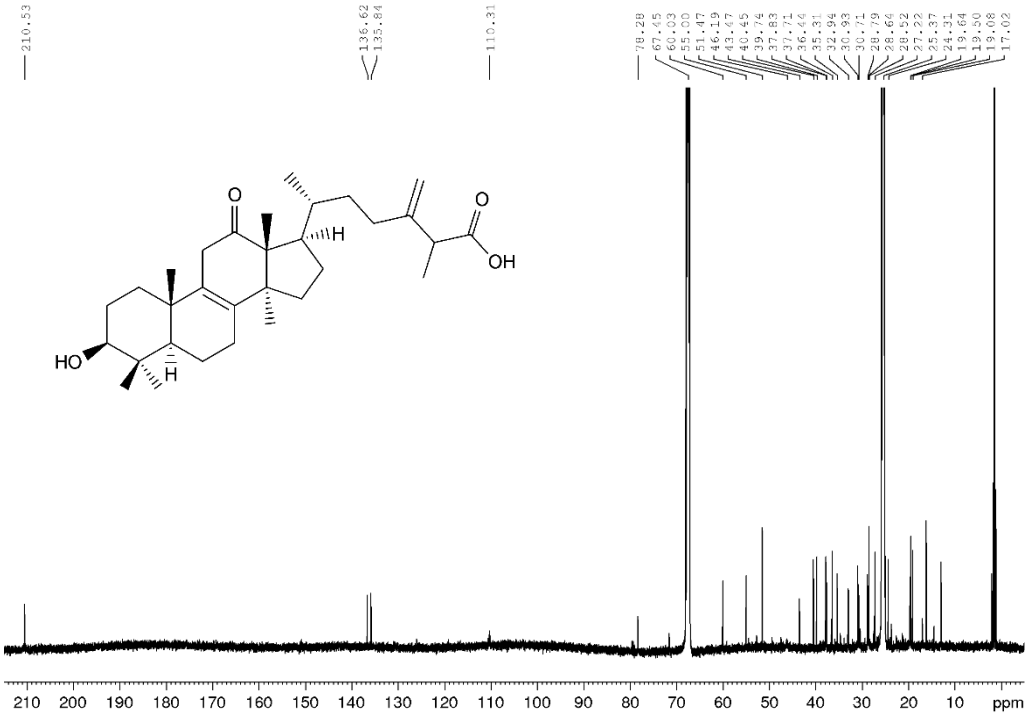

Figure A13. ^{13}C spectrum of **BGS-2** (150 MHz, THF-d_8, 295 K)

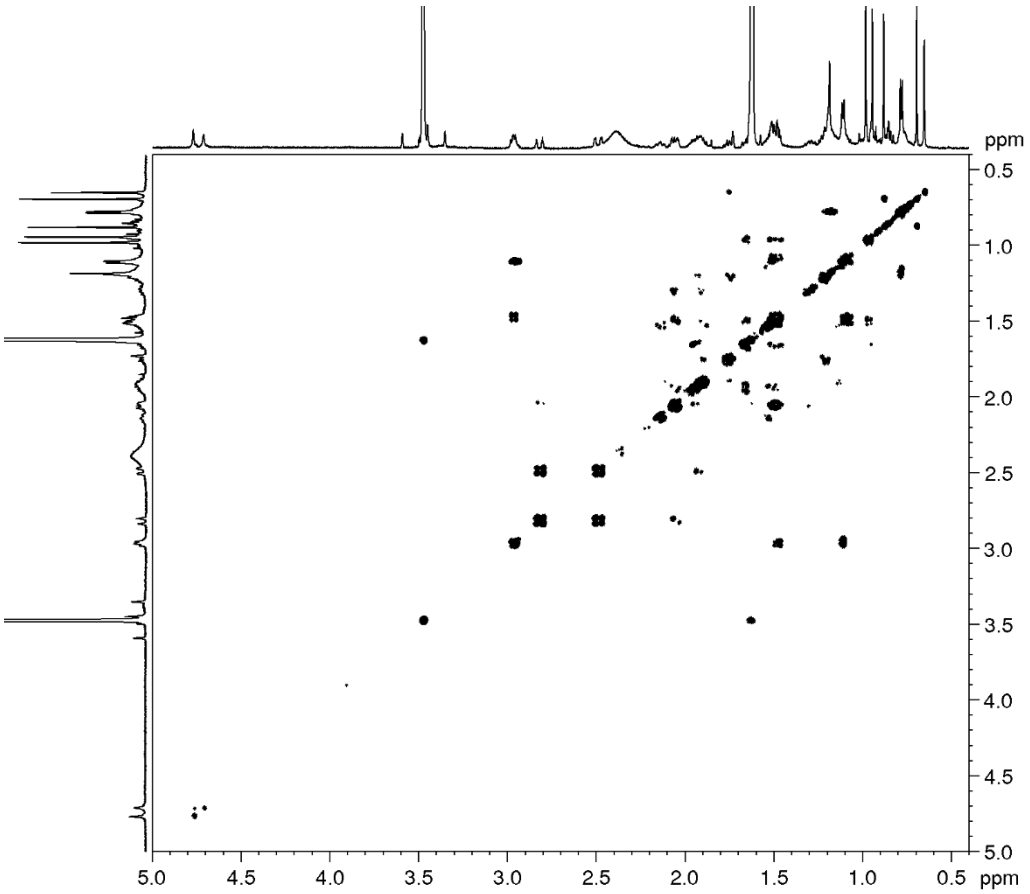

Figure A14. COSY spectrum of **BGS-2** (600 MHz, THF-d_8, 295 K)

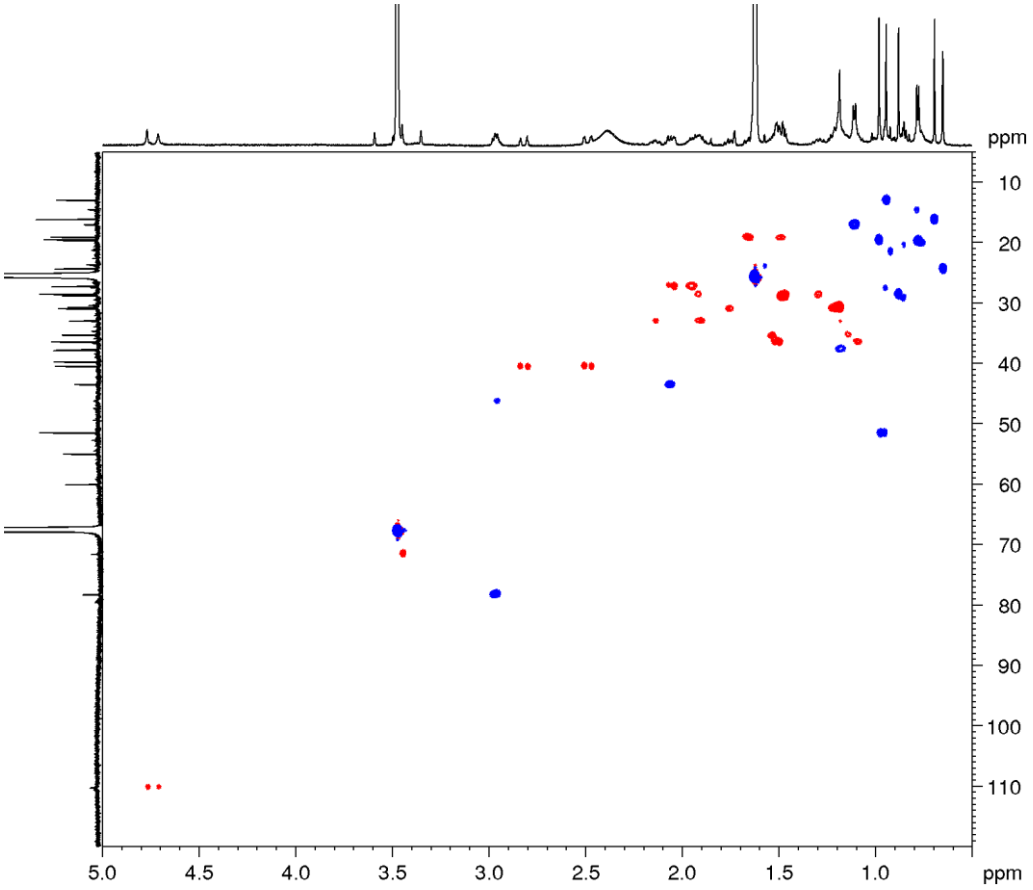

Figure A15. DEPT-edited HSQC spectrum of **BGS-2** (600 MHz, THF-d_8, 295 K)

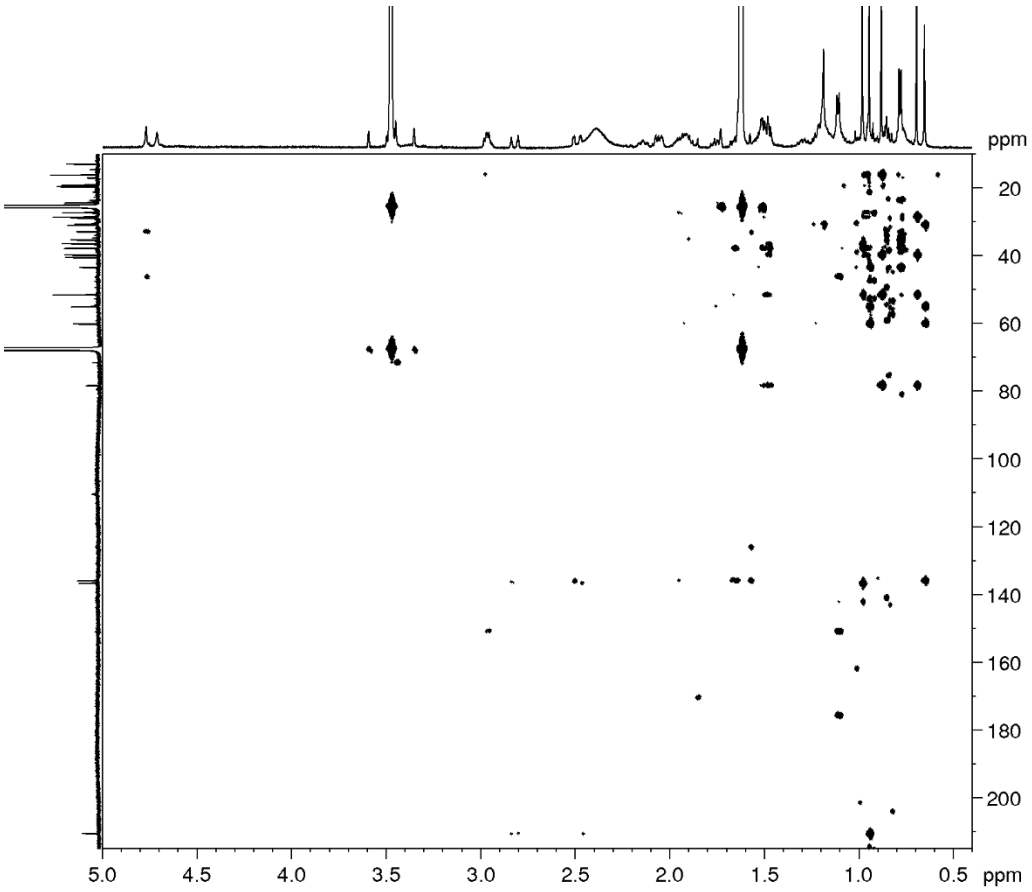

Figure A16. HMBC spectrum of **BGS-2** (600 MHz, THF-d_8, 295 K)

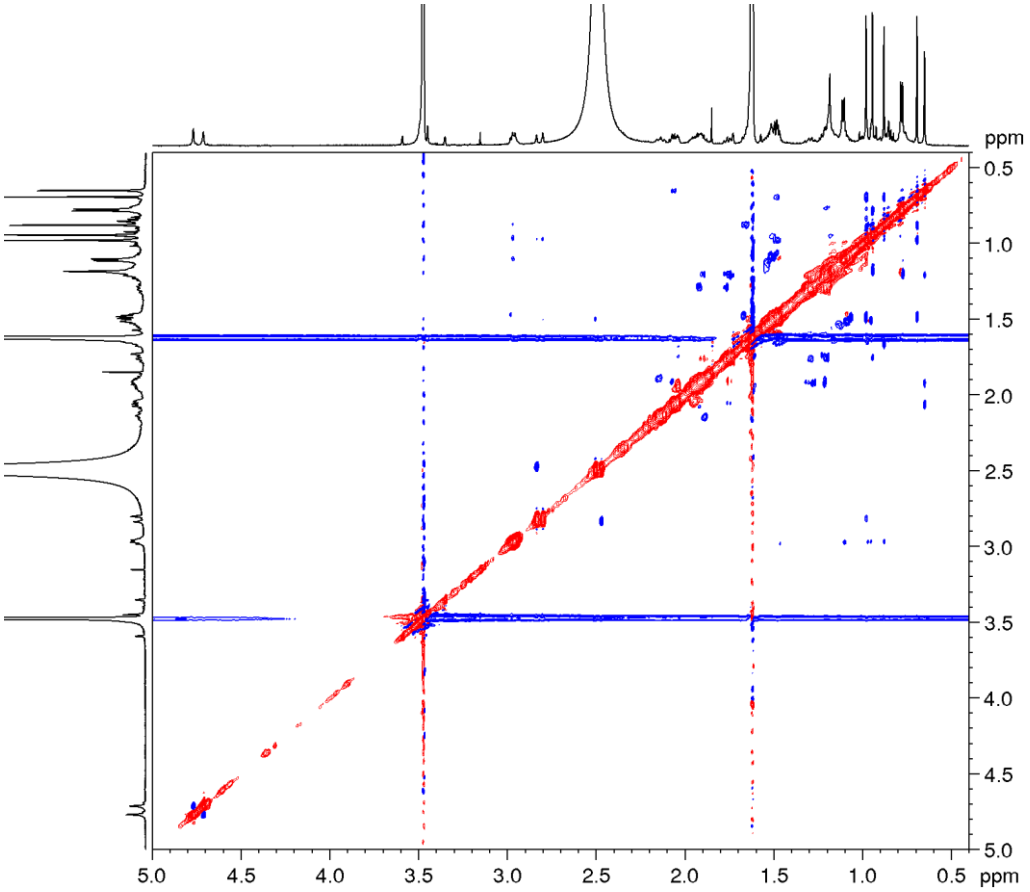

Figure A17. NOESY spectrum of **BGS-2** (600 MHz, THF-d_8, 295 K)

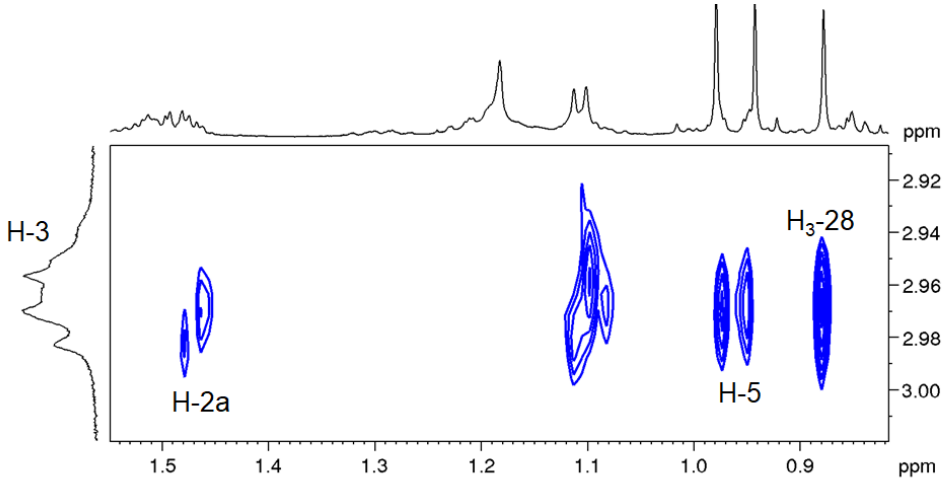

Figure A18. Selected region of the NOESY spectrum of **BGS-2** (600 MHz, THF-d_8, 295 K)

Spectra and spectral data on BGS-3

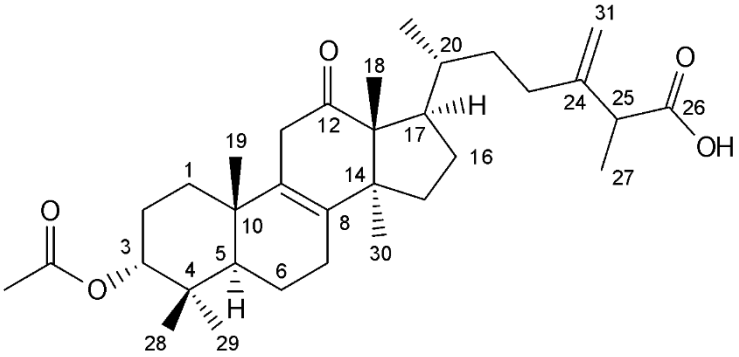

HRMS (+) *m/z* 527.3721 $[M+H]^+$ (527.3731 calcd. for $C_{33}H_{51}O_5$; Δ -2.0 ppm); HRMSMS (CID = 15%, 30%, 45%) 509.3611, 481.3671, 467.3504, 449.3400, 421.3456

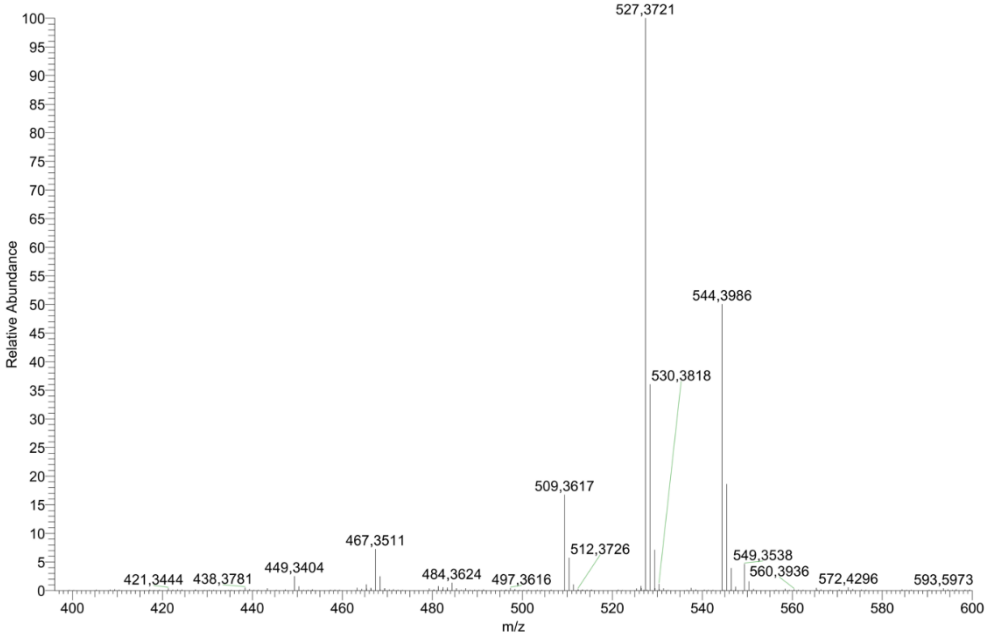

Figure A19. HRMS spectrum of **BGS-3**

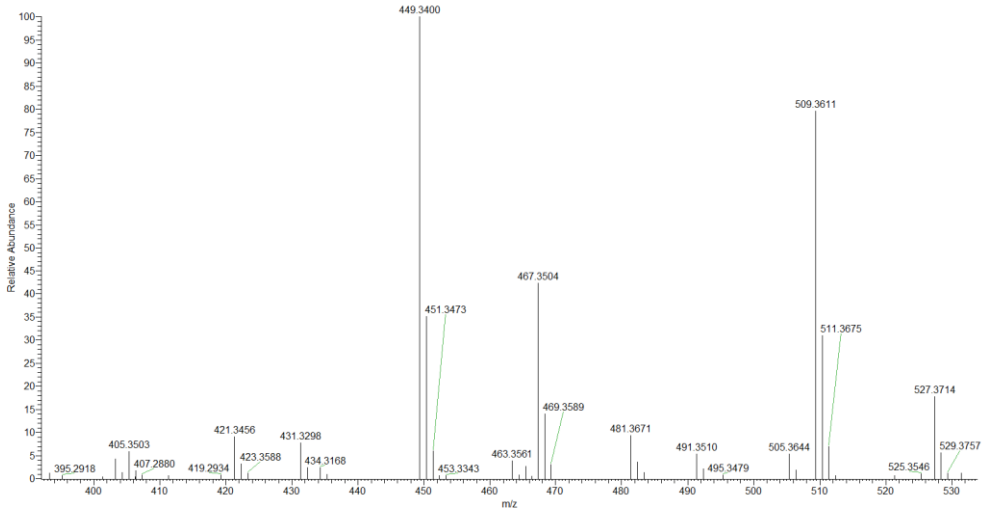

Figure A20. MS-MS spectrum of **BGS-3**

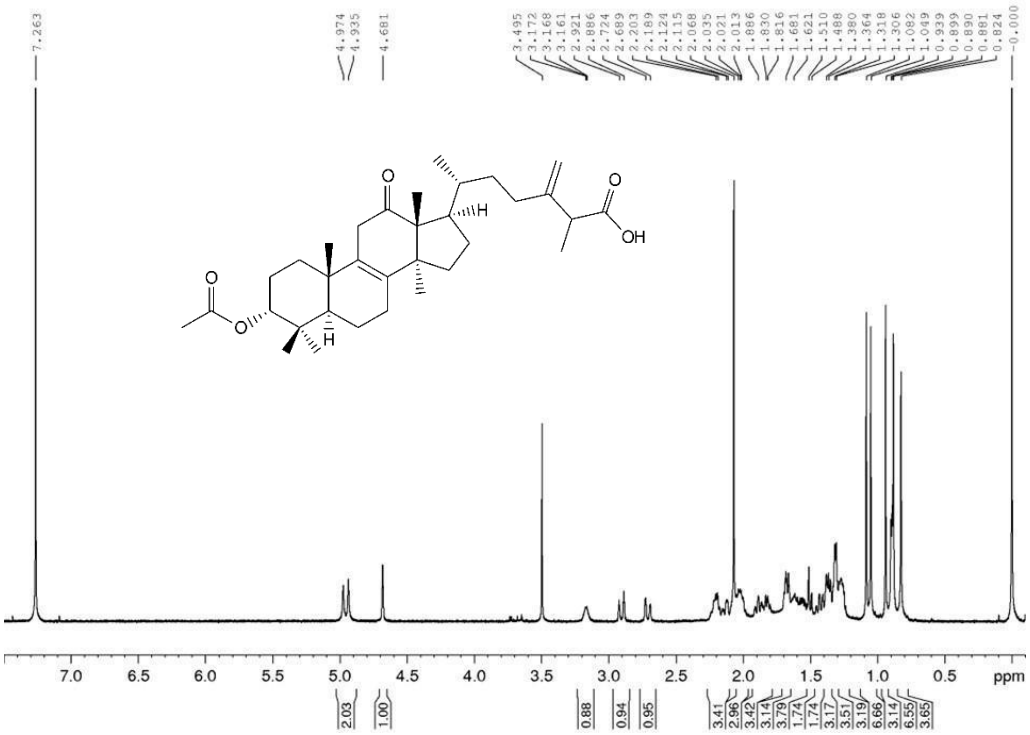

Figure A21. ^{1}H spectrum of **BGS-3** (600 MHz, $CDCl_3$, 295 K)

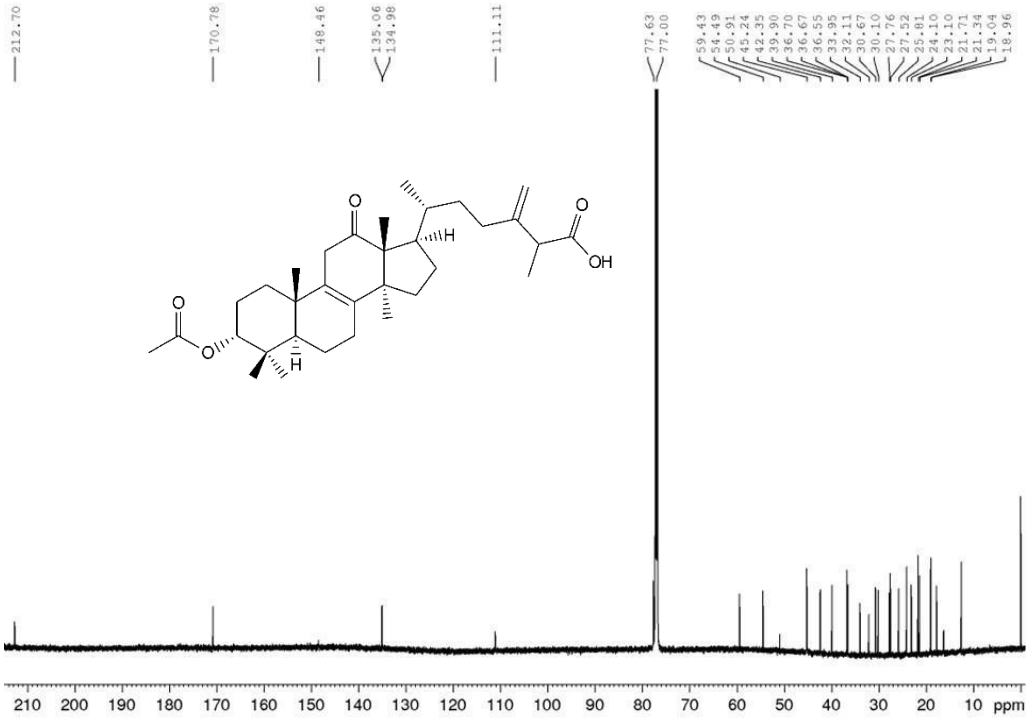

Figure A22. ^{13}C spectrum of **BGS-3** (150 MHz, $CDCl_3$, 295 K)

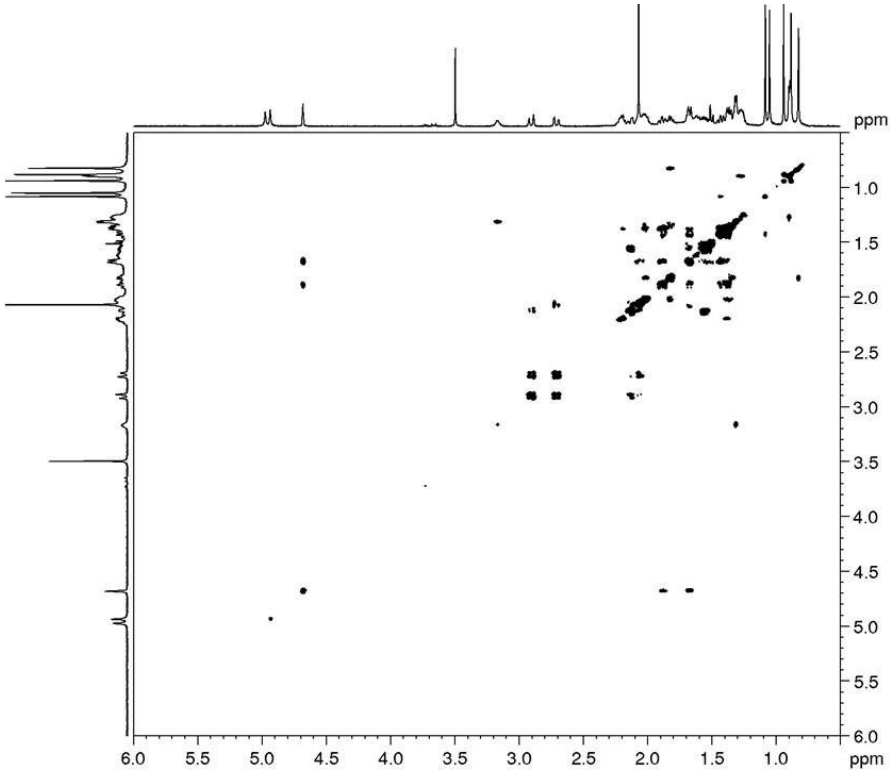

Figure A23. COSY spectrum of **BGS-3** (600 MHz, $CDCl_3$, 295 K)

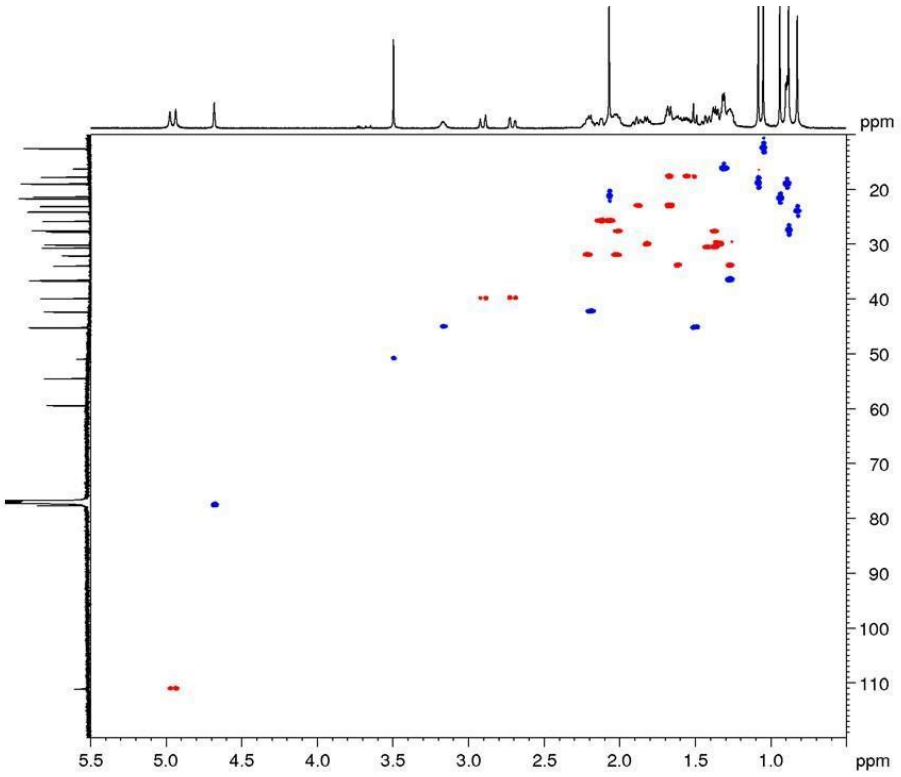

Figure A24. DEPT-edited HSQC spectrum of **BGS-3** (600 MHz, $CDCl_3$, 295 K)

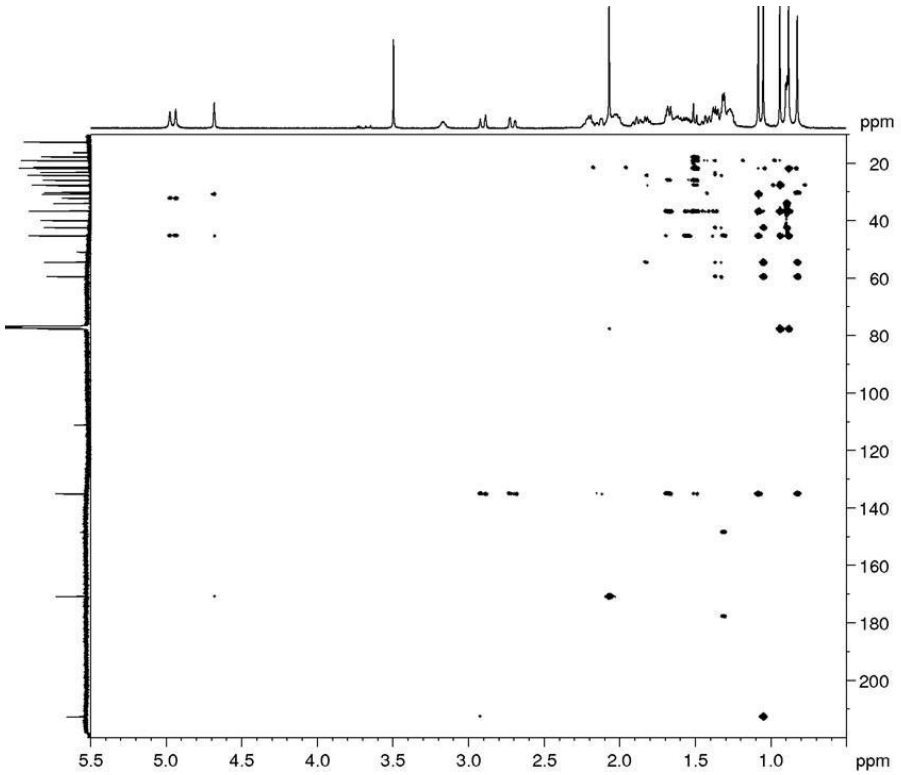

Figure A25. HMBC spectrum of **BGS-3** (600 MHz, $CDCl_3$, 295 K)

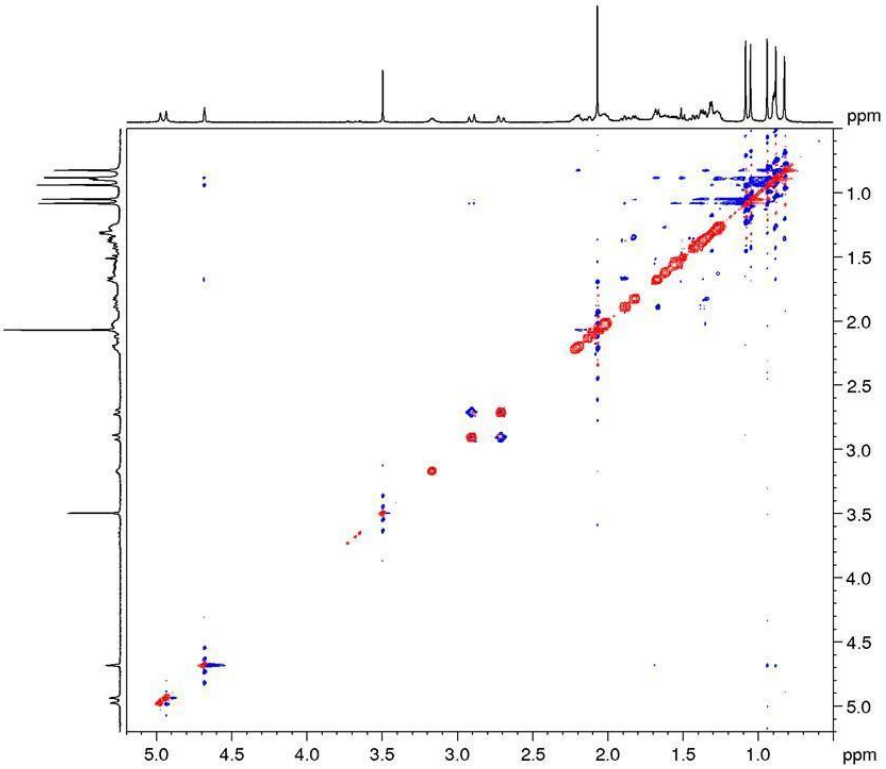

Figure A26. NOESY spectrum of **BGS-3** (600 MHz, $CDCl_3$, 295 K)

Spectra and spectral data on BGS-4

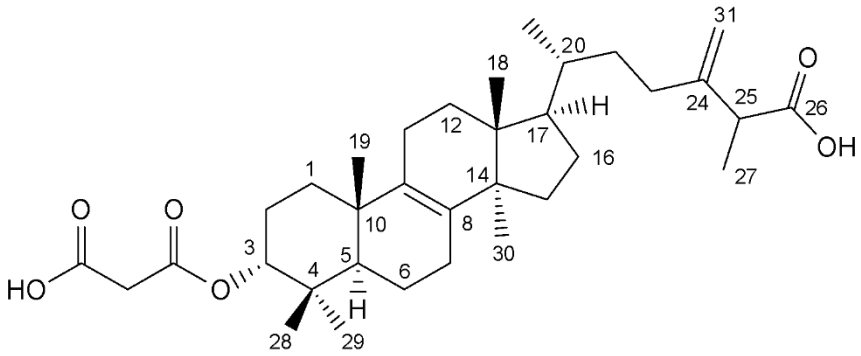

HRMS (-) *m/z* 555.3694 $[M - H]^-$ (555.3680 calcd. for $C_{34}H_{51}O_6$; *Δ* 2.6 ppm); HRMSMS (CID = 15%, 30%, 45%) *m/z* 511.3787

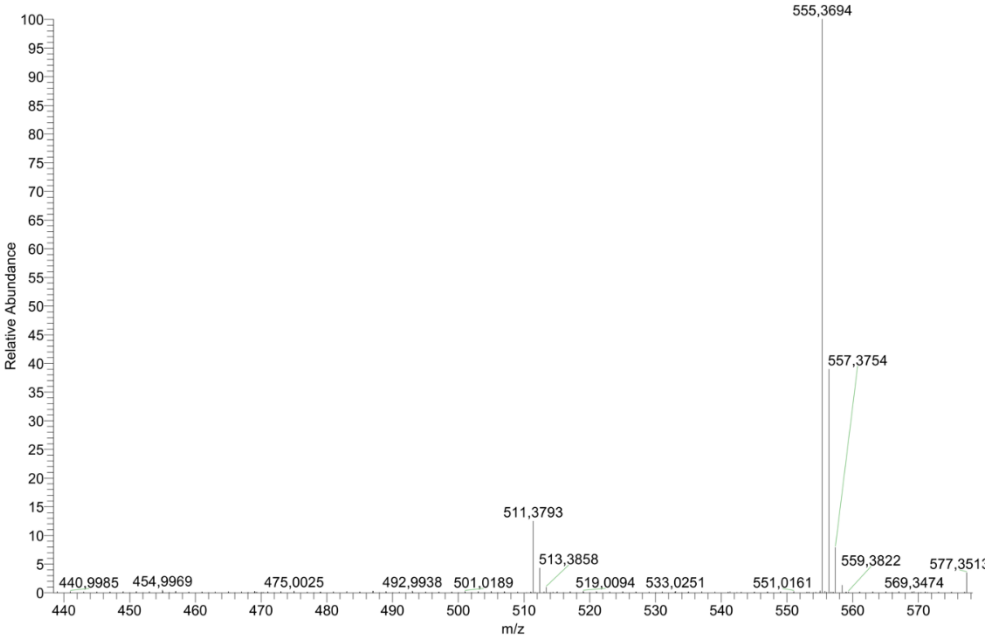

Figure A27. HRMS spectrum of **BGS-4**

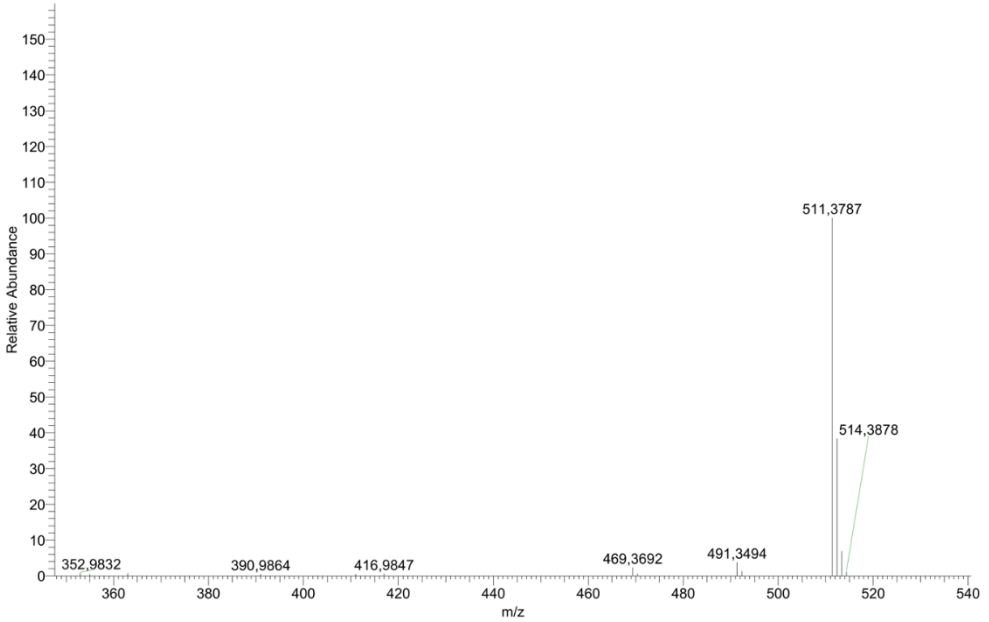

Figure A28. MS-MS spectrum of **BGS-4**

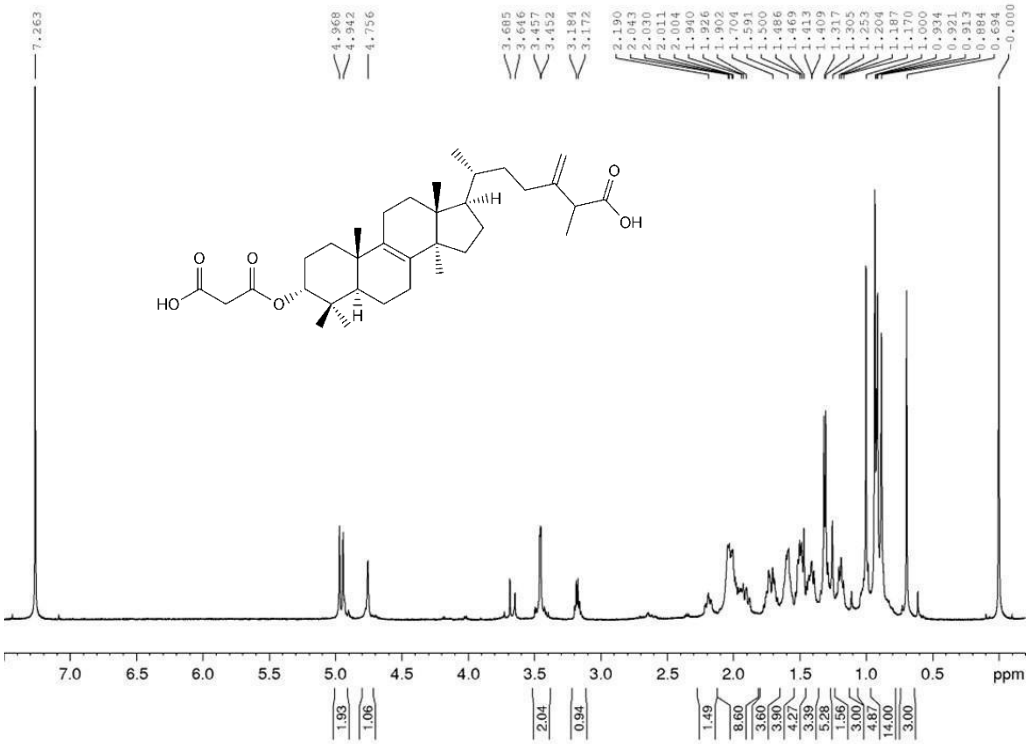

Figure A29. ^{1}H spectrum of **BGS-4** (600 MHz, $CDCl_3$, 295 K)

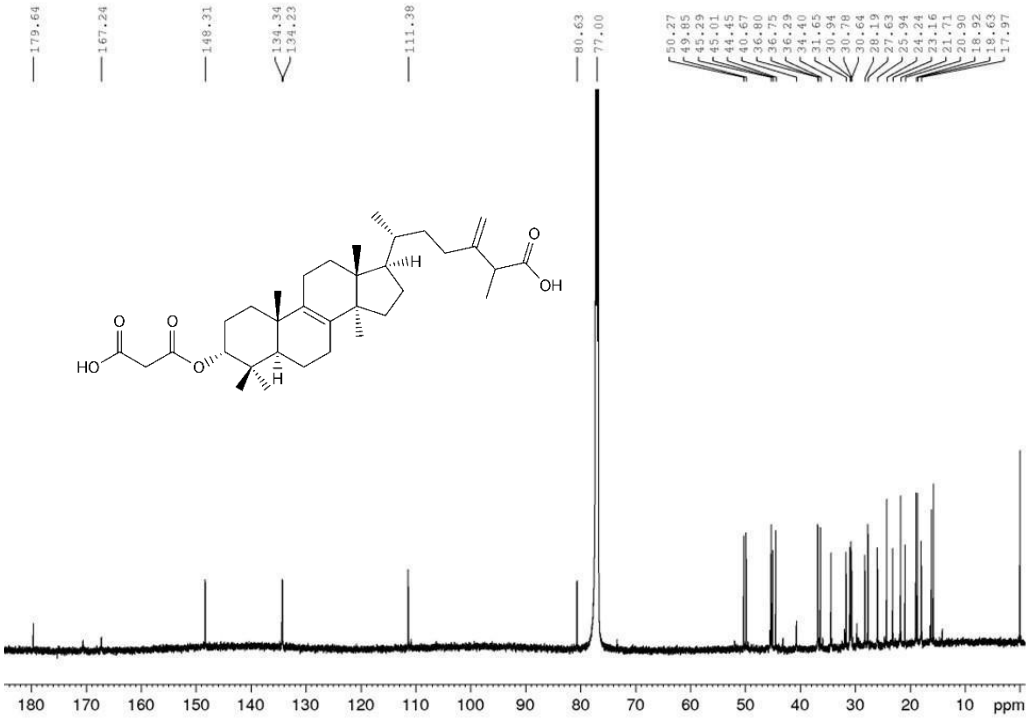

Figure A30. ^{13}C spectrum of **BGS-4** (150 MHz, $CDCl_3$, 295 K)

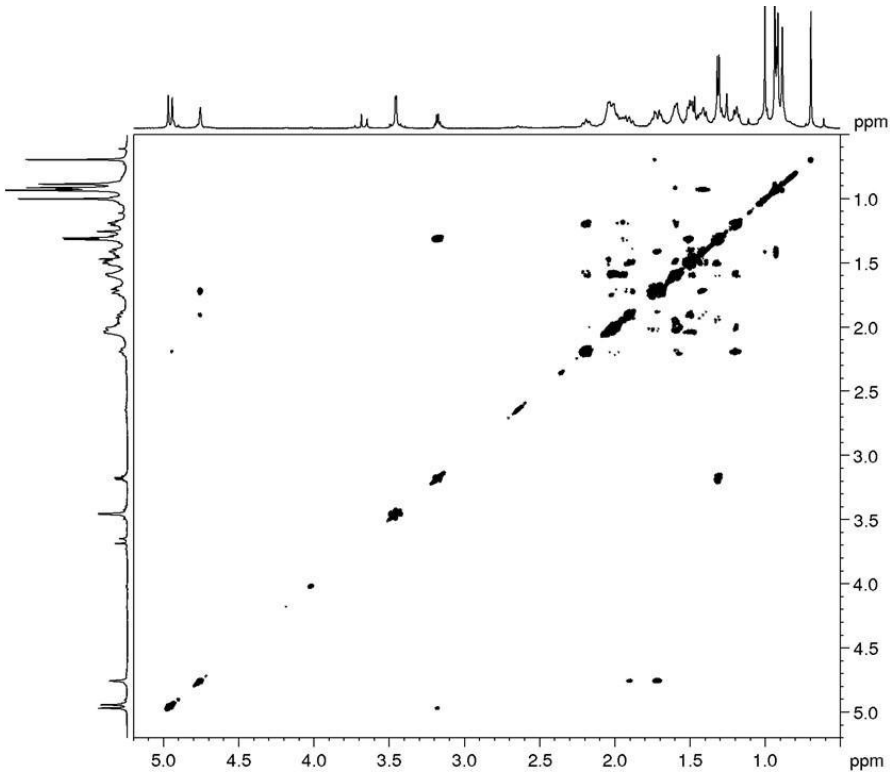

Figure A31. COSY spectrum of **BGS-4** (600 MHz, $CDCl_3$, 295 K)

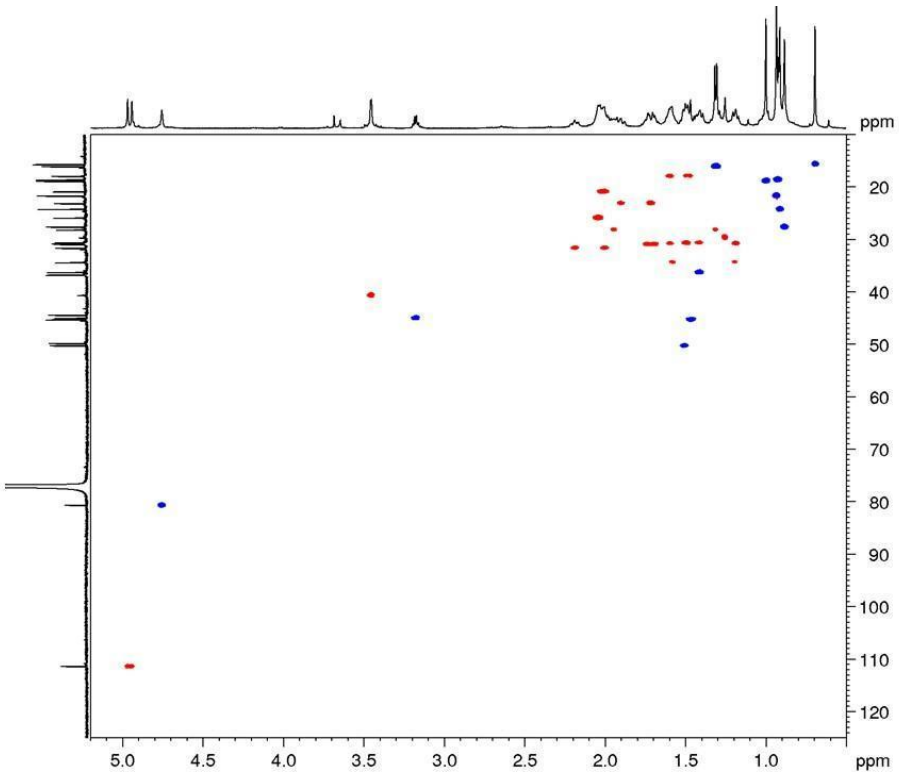

Figure A32. DEPT-edited HSQC spectrum of **BGS-4** (600 MHz, $CDCl_3$, 295 K)

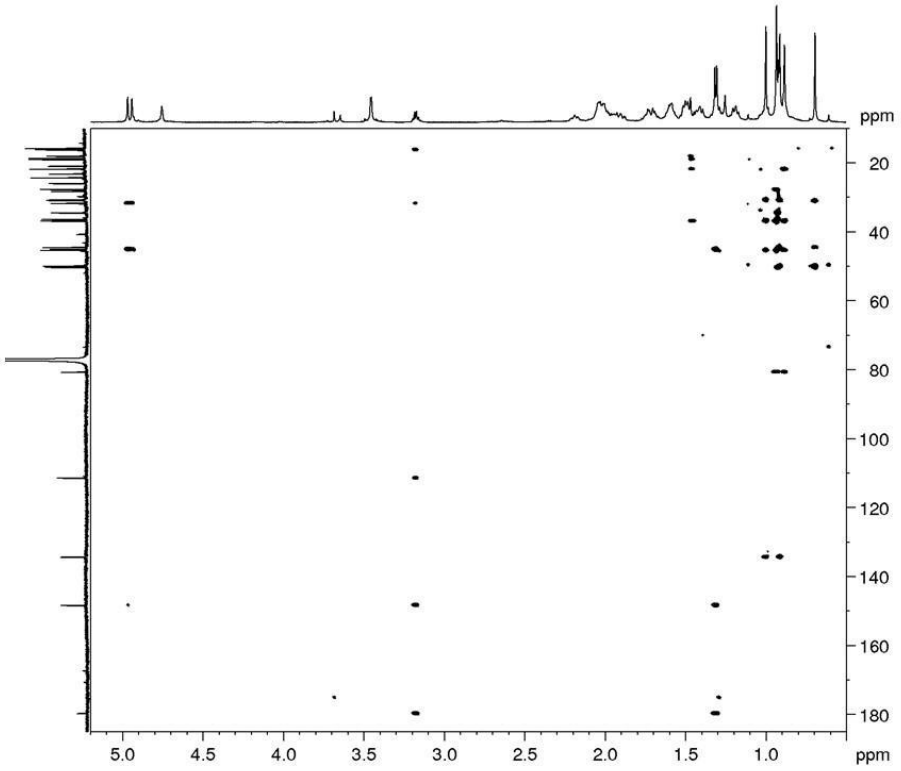

Figure A33. HMBC spectrum of **BGS-4** (600 MHz, $CDCl_3$, 295 K)

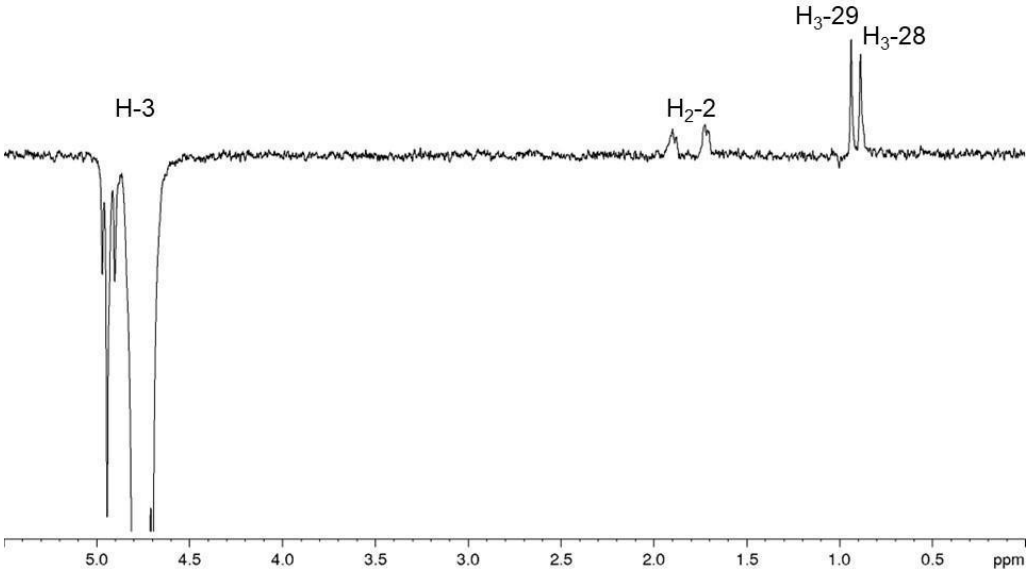

Figure A34. Selective gradient NOESY spectrum of **BGS-4** (600 MHz, $CDCl_3$, 295 K)

Spectra and spectral data on BGS-5

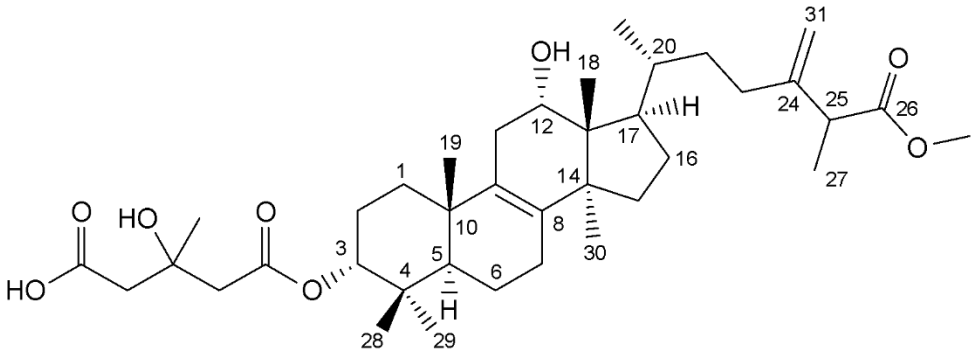

HRMS (+) *m/z* 645.4343 $[M+H]^+$ (645.4361 calcd. for $C_{38}H_{61}O_8$; Δ 2.8 ppm); HRMSMS (CID = 15%, 30%, 45%) 627.4243, 465.3715

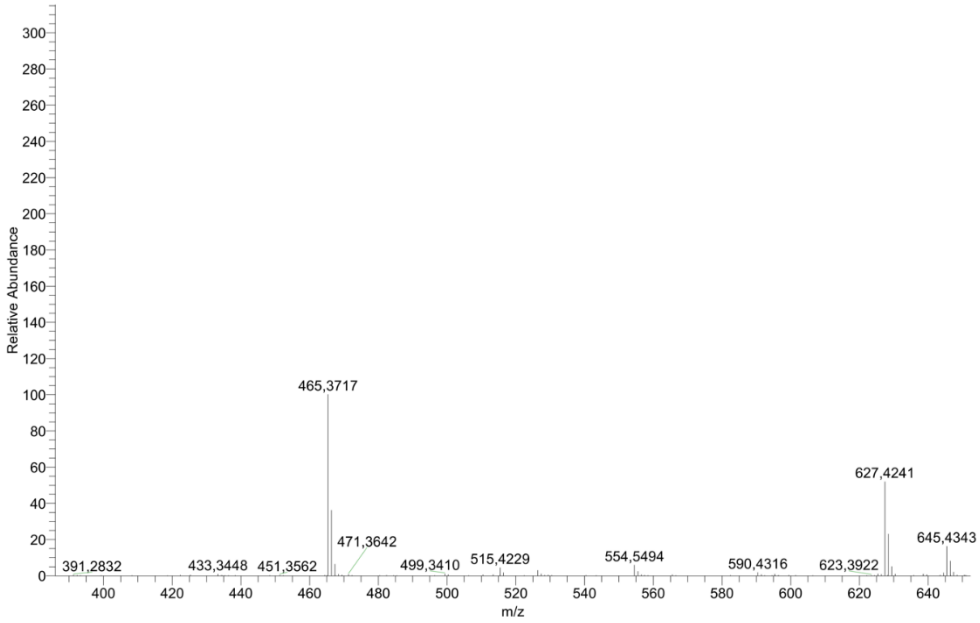

Figure A35. HRMS spectrum of **BGS-5**

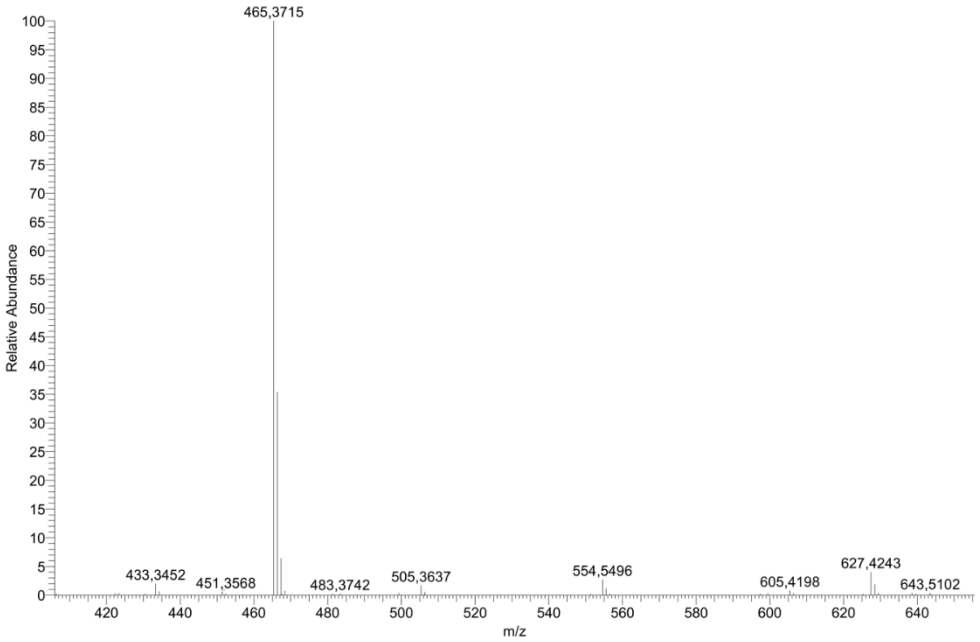

Figure A36. MS-MS spectrum of **BGS-5**

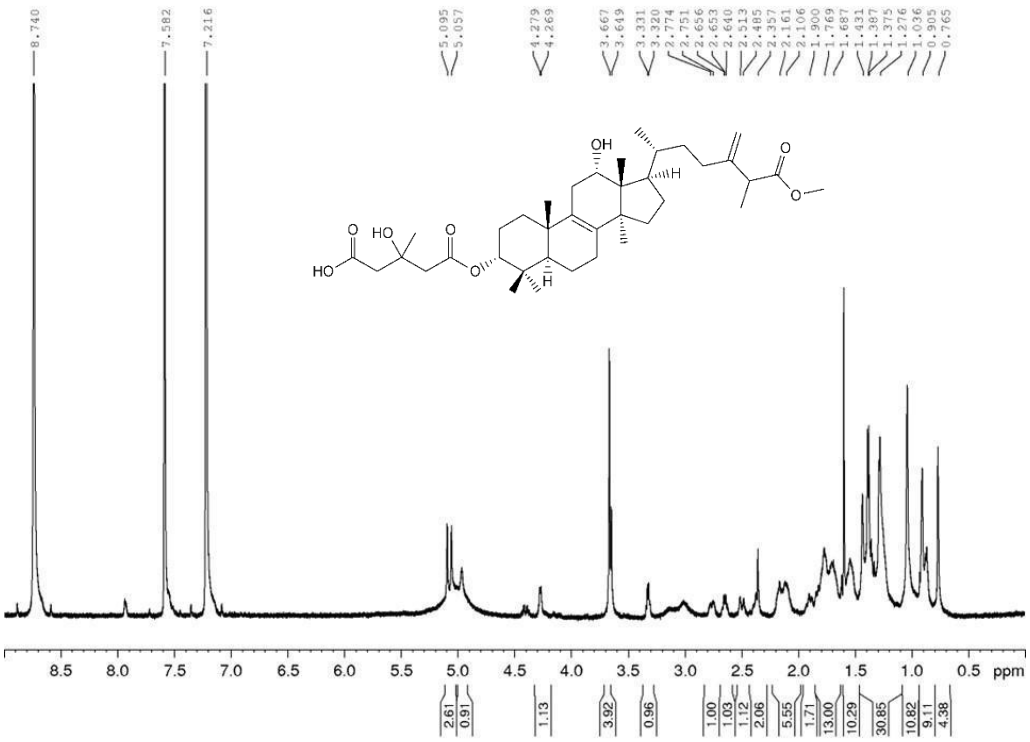

Figure A37. ^{1}H spectrum of **BGS-5** (600 MHz, pyridine-d_5, 295 K)

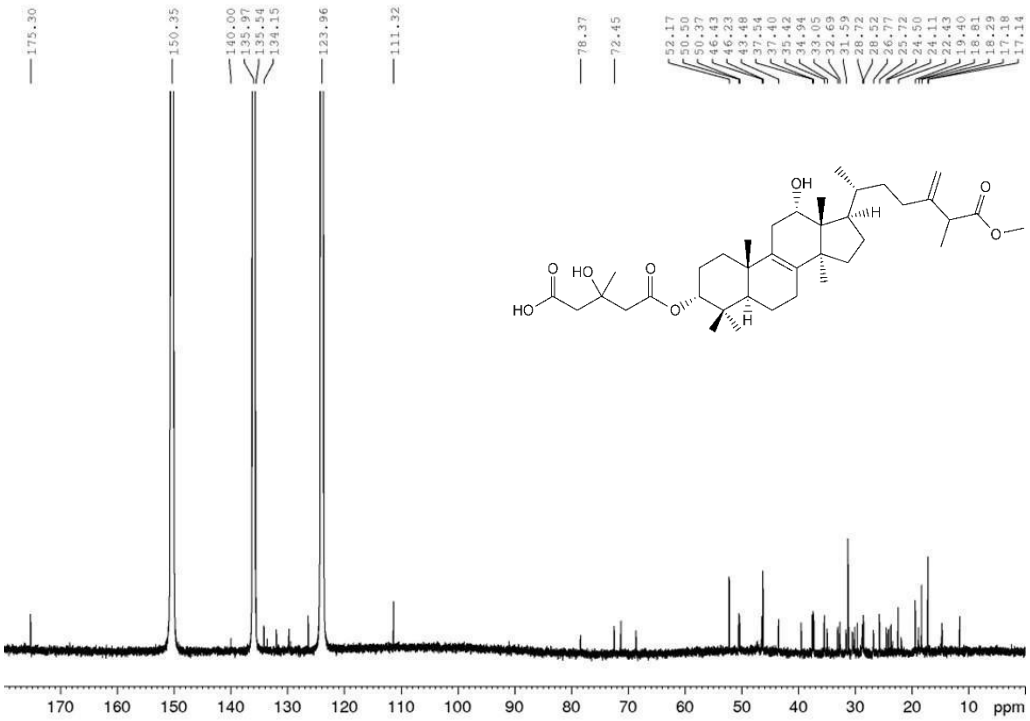

Figure A38. ^{13}C spectrum of **BGS-5** (150 MHz, pyridine-d_5, 295 K)

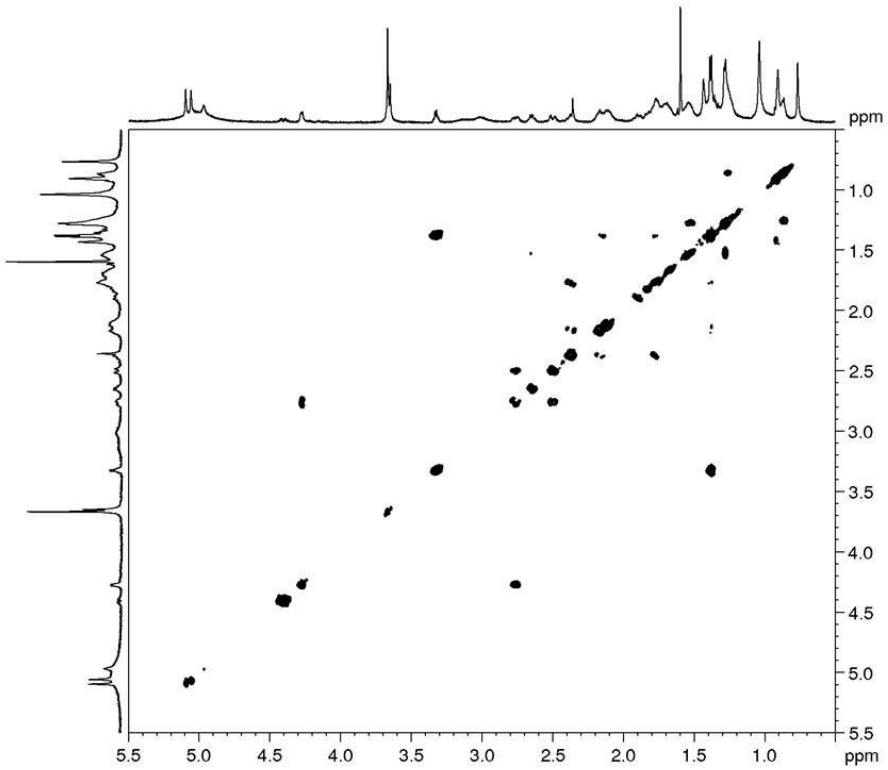

Figure A39. COSY spectrum of **BGS-5** (600 MHz, pyridine-d_5, 295 K)

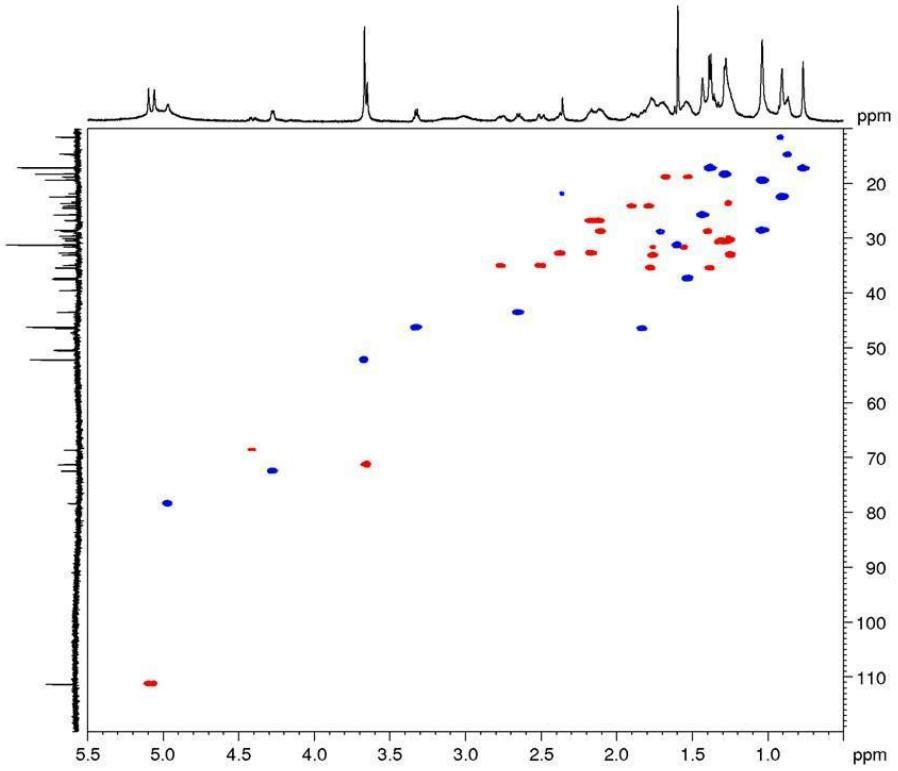

Figure A40. DEPT-edited HSQC spectrum of **BGS-5** (600 MHz, pyridine-d_5, 295 K)

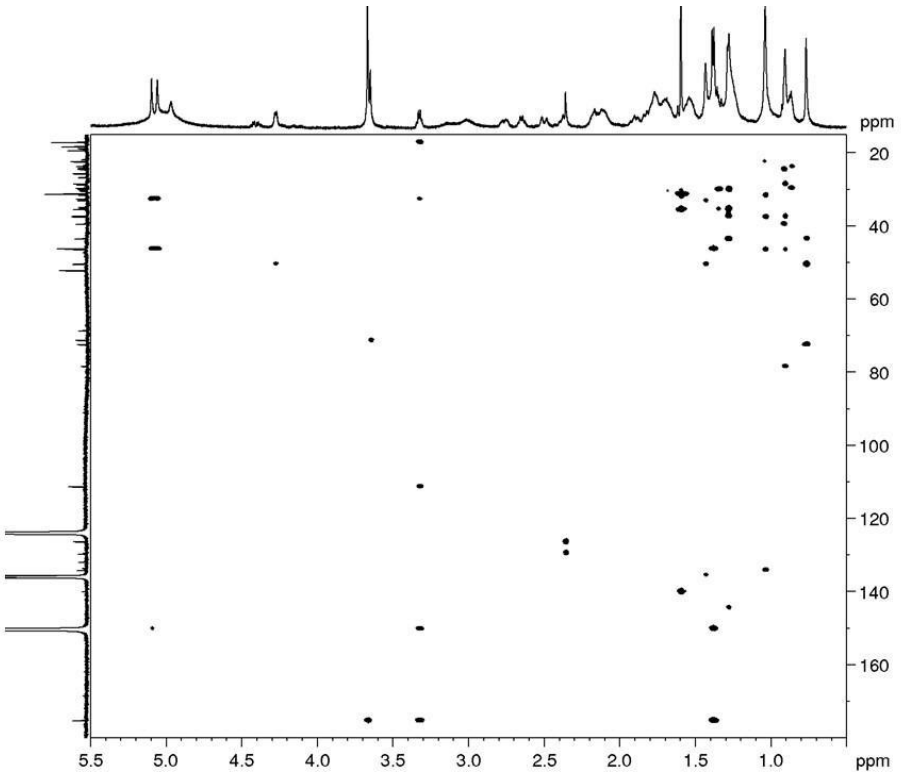

Figure A41. HMBC spectrum of **BGS-5** (600 MHz, pyridine-d_5, 295 K)

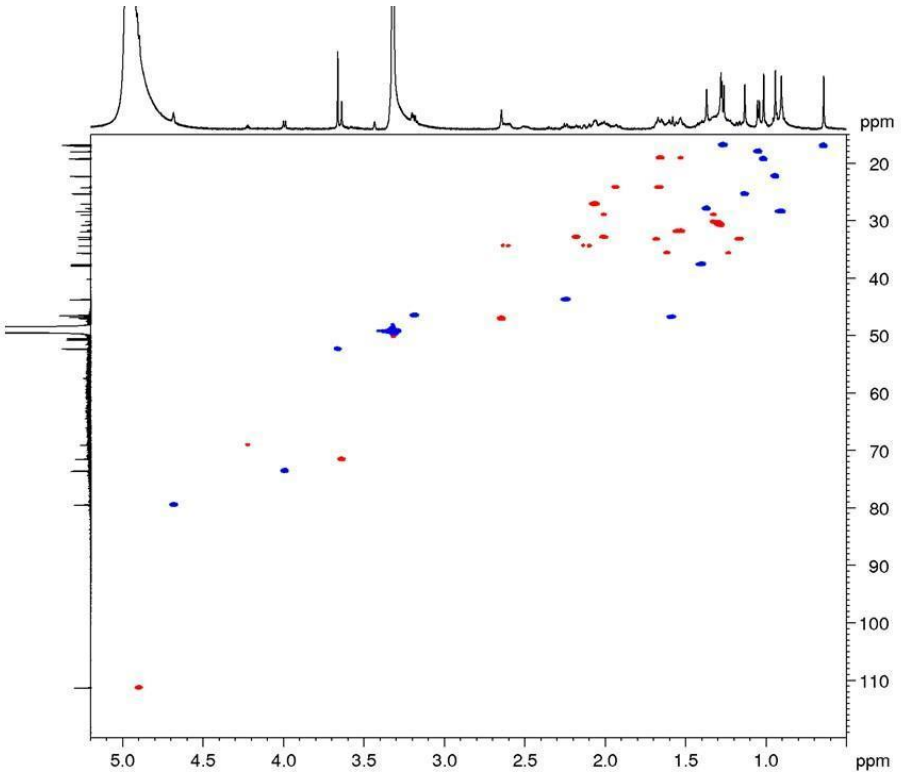

Figure A42. DEPT-edited HSQC spectrum of **BGS-5** (600 MHz, CD_3OD:pyridine-d_5 (19:1), 295 K)

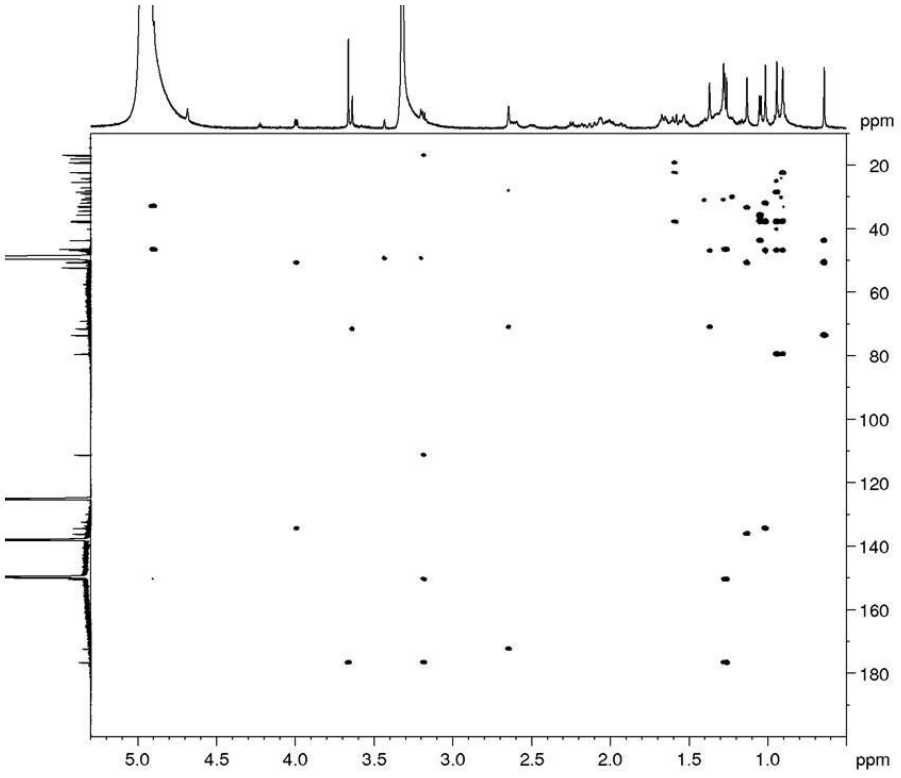

Figure A43. HMBC spectrum of **BGS-5** (600 MHz, CD_3OD: pyridine-d_5 (19:1), 295 K)

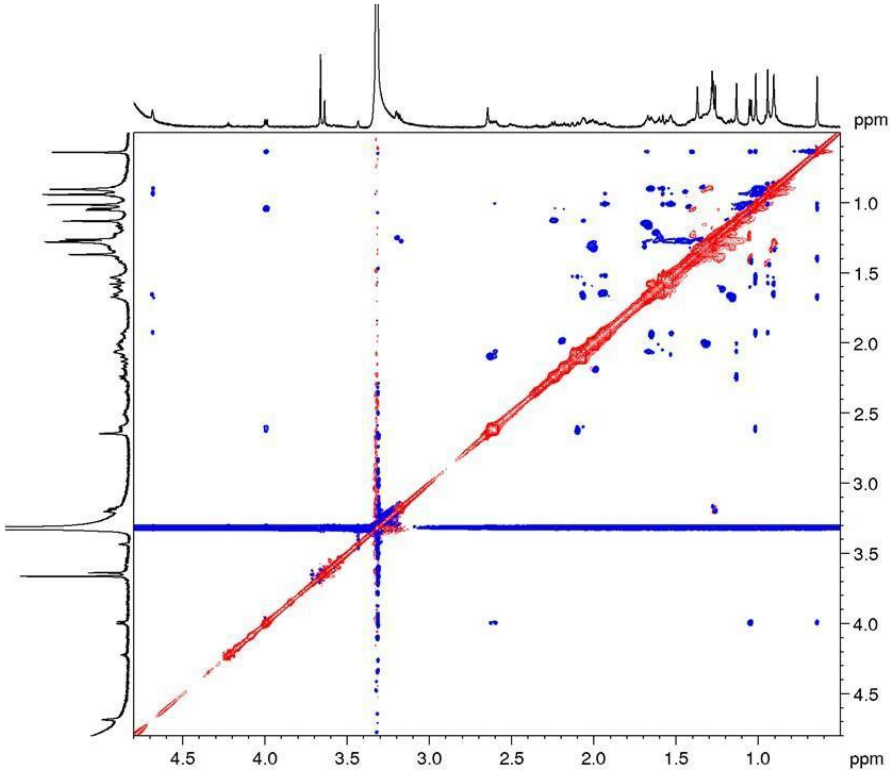

Figure A44. ROESY spectrum of **BGS-5** (600 MHz, CD_3OD:pyridine-d_5 (19:1), 295 K)

Spectra and spectral data on BGS-6

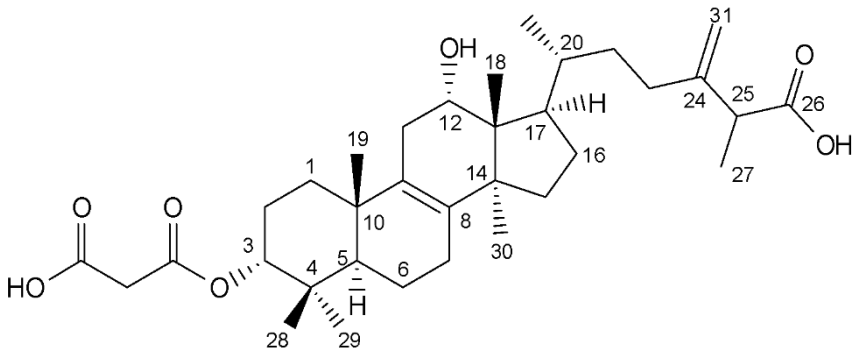

HRMS (-) *m/z* 571.3642 $[M-H]^-$(571.3629 calcd. for $C_{34}H_{51}O_7$; Δ 2.2 ppm;); HRMSMS (CID = 15%, 30%, 45%) 527.3740, 483.3840, 441.3737

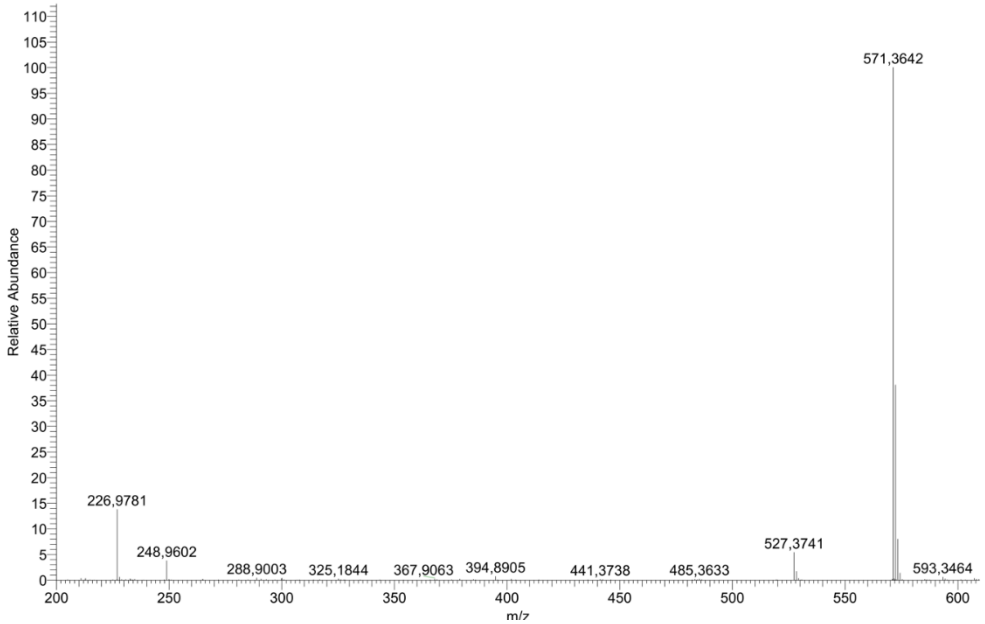

Figure A45. HRMS spectrum of **BGS-6**

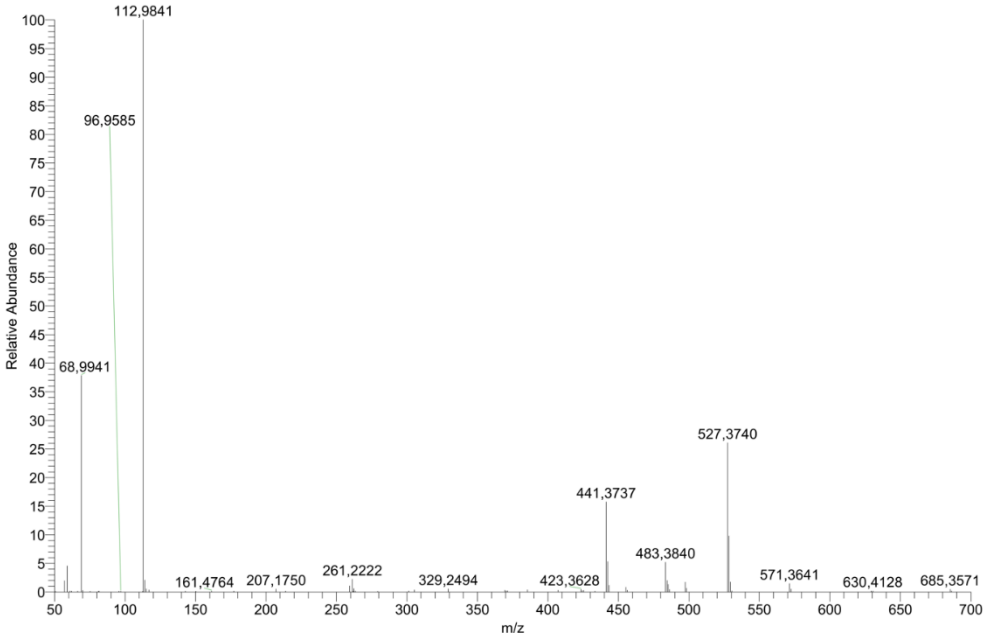

Figure A46. MS-MS spectrum of **BGS-6**

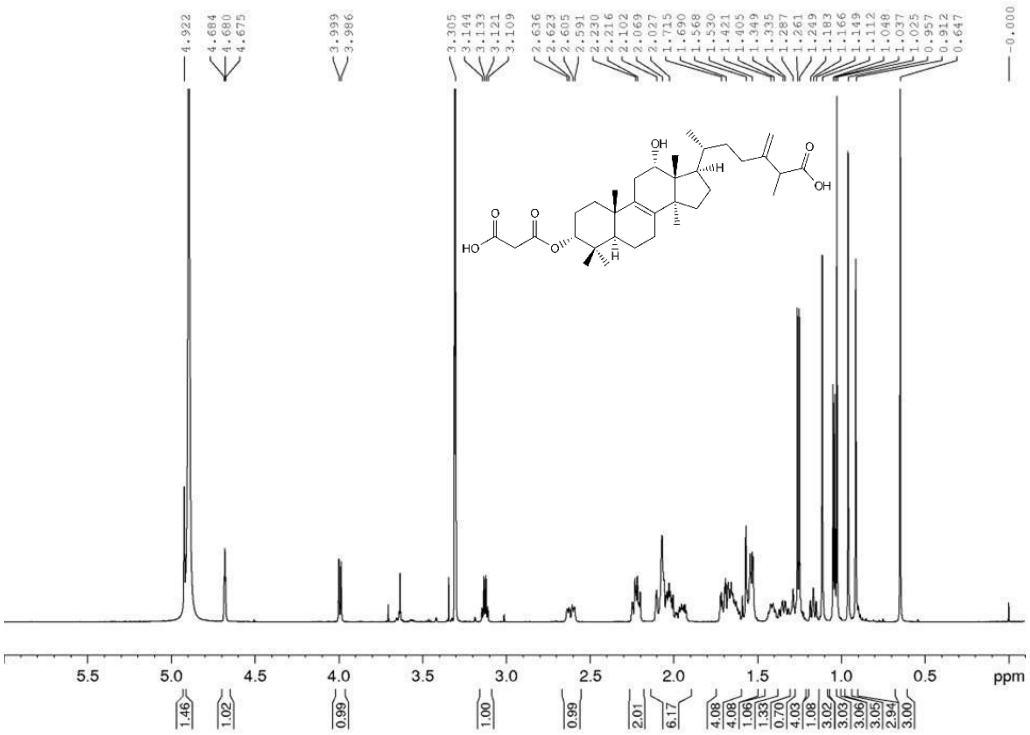

Figure A47. ^{1}H spectrum of **BGS-6** (150 MHz, CD_3OD, 295 K)

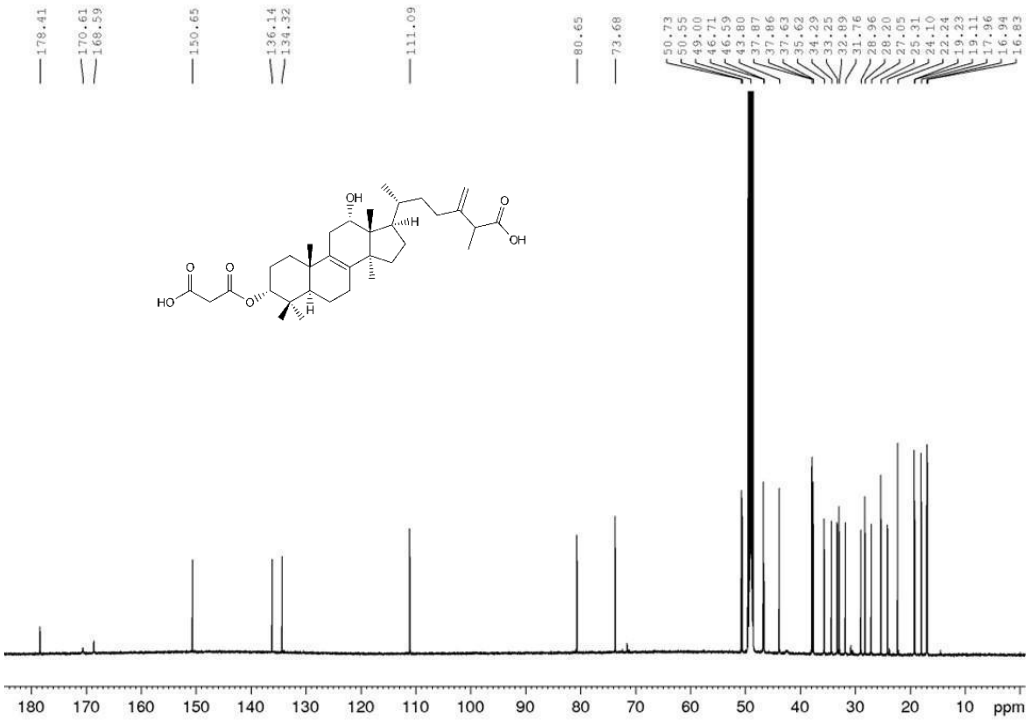

Figure A48. ^{13}C spectrum of **BGS-6** (600 MHz, CD_3OD, 295 K)

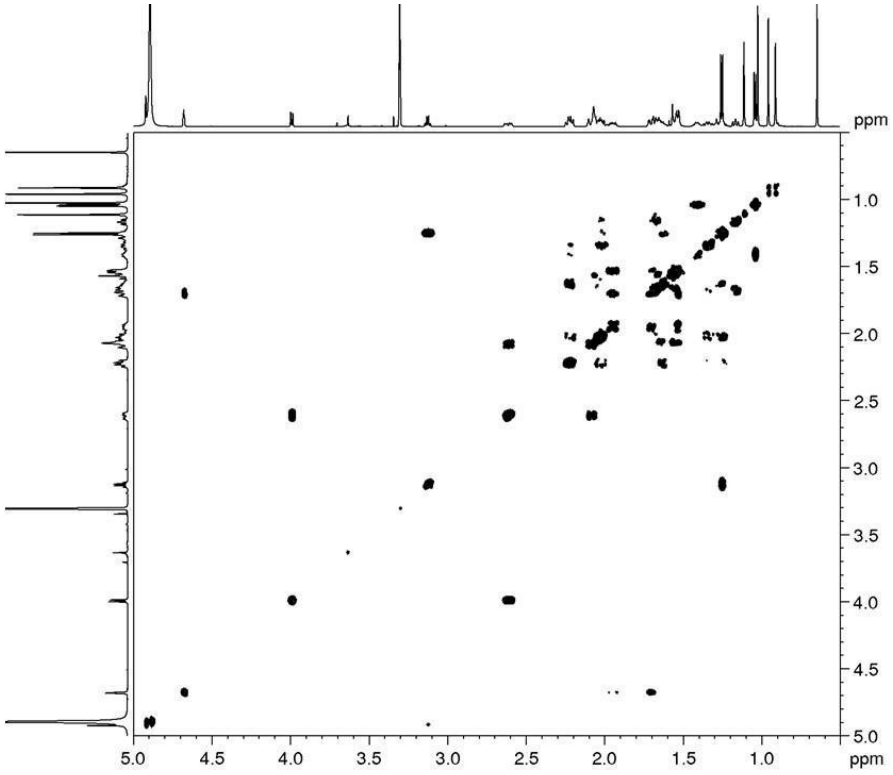

Figure A49. COSY spectrum of **BGS-6** (600 MHz, CD_3OD, 295 K)

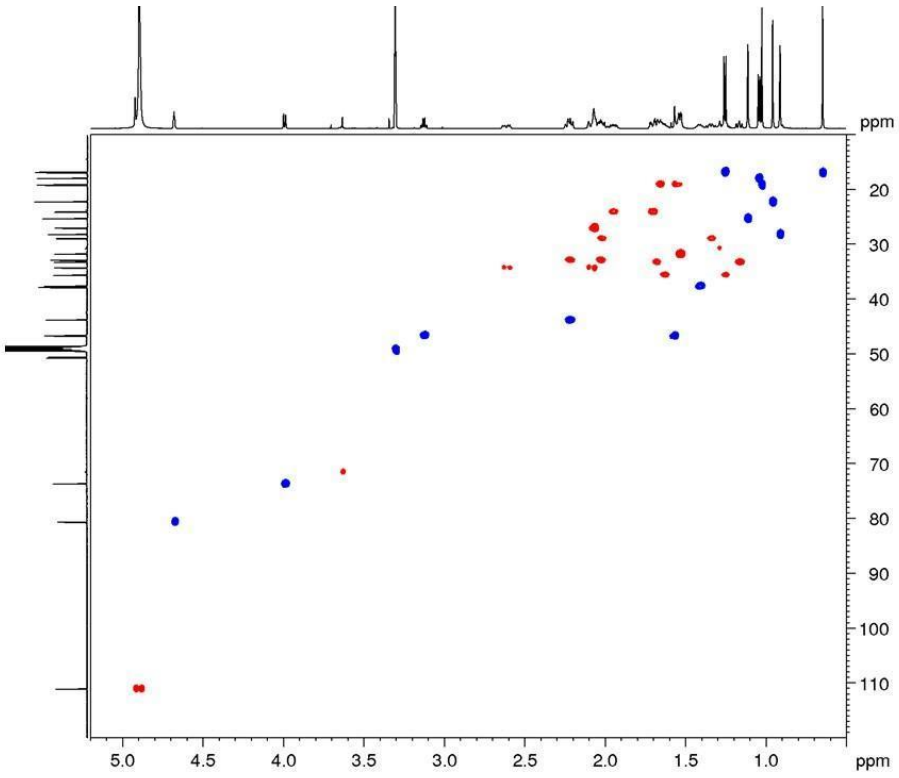

Figure A50. DEPT-edited HSQC spectrum of **BGS-6** (600 MHz CD_3OD, 295 K)

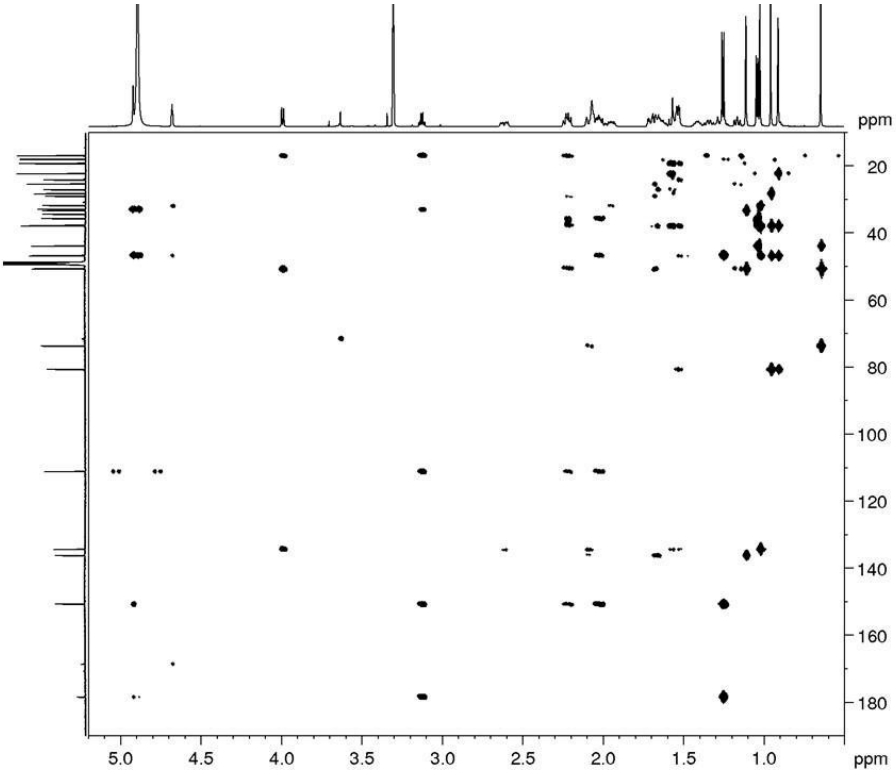

Figure A51. HMBC spectrum of **BGS-6** (600 MHz, CD_3OD, 295 K)

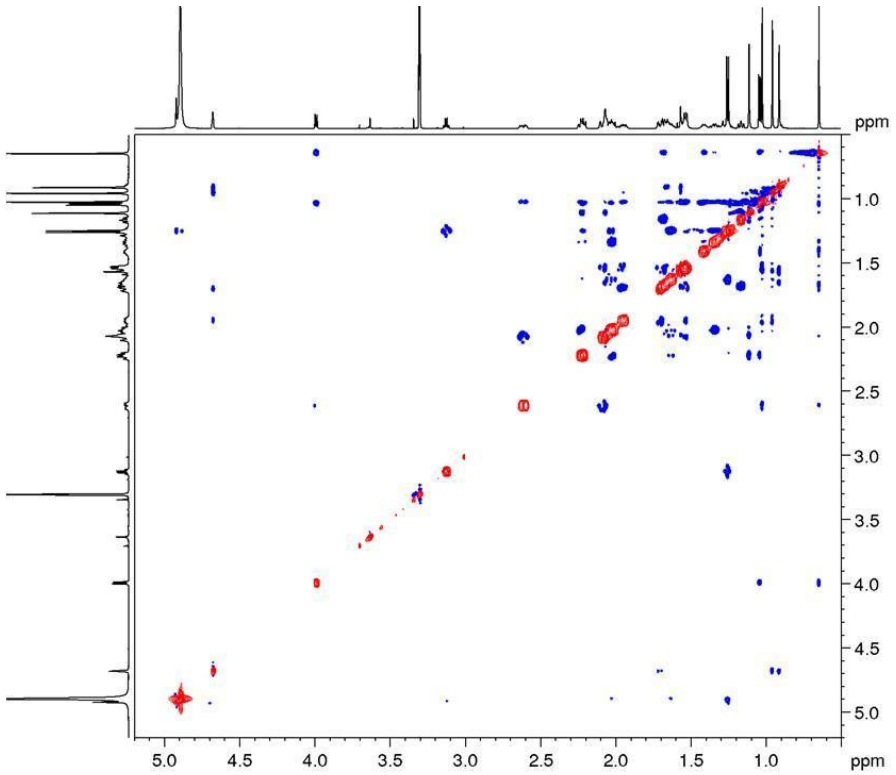

Figure A52. NOESY spectrum of **BGS-6** (600 MHz, CD_3OD, 295 K)

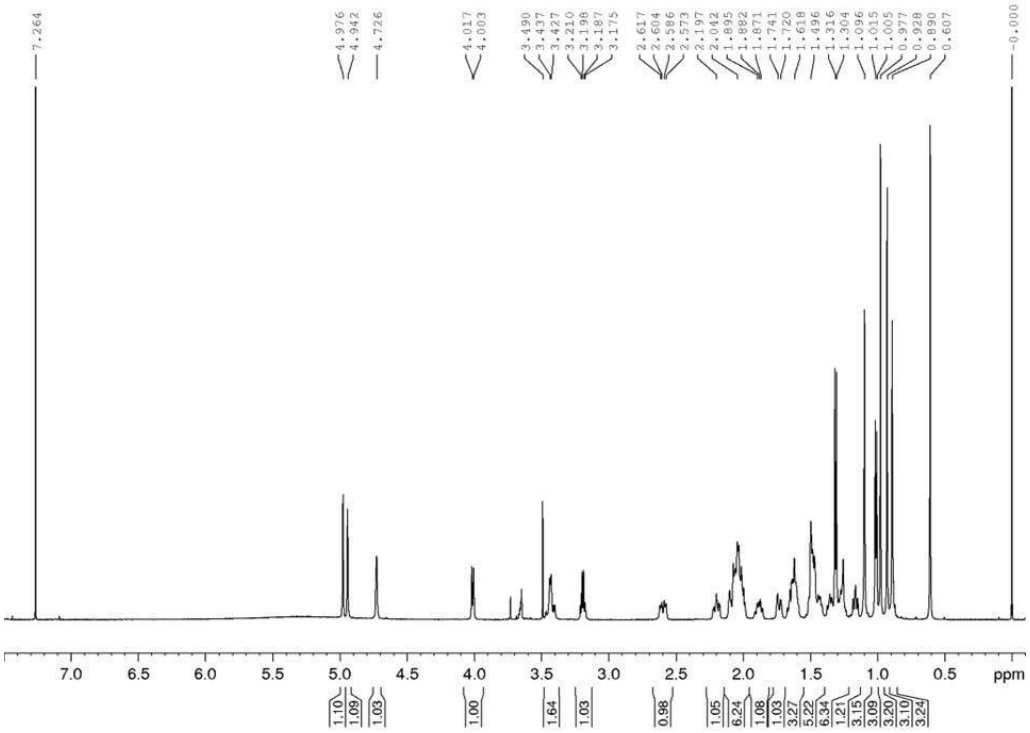

Figure A53. ^{1}H spectrum of **BGS-6** (600 MHz, $CDCl_3$, 295 K)

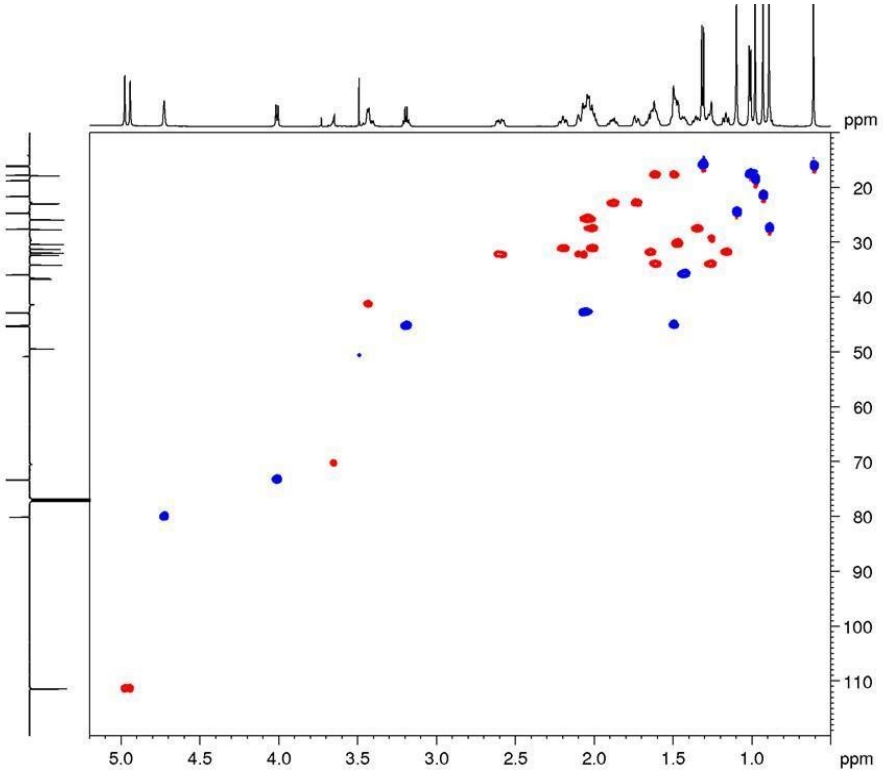

Figure A54. DEPT-edited HSQC spectrum of **BGS-6** (600 MHz, $CDCl_3$, 295 K)

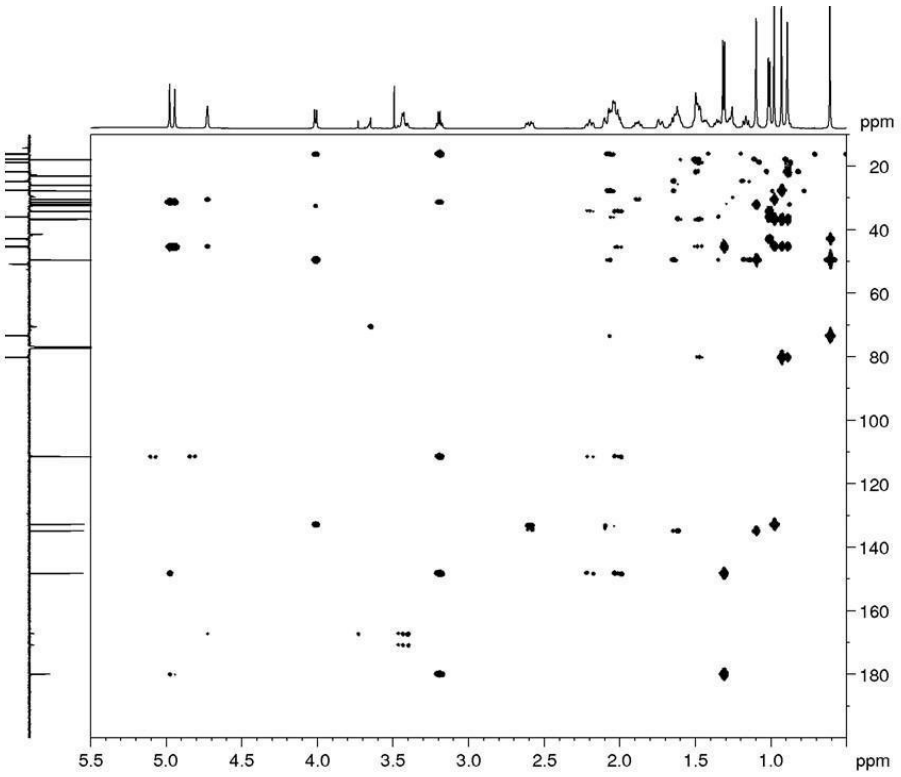

Figure A55. HMBC spectrum of **BGS-6** (600 MHz, $CDCl_3$, 295 K)

Spectra and spectral data on BGS-7

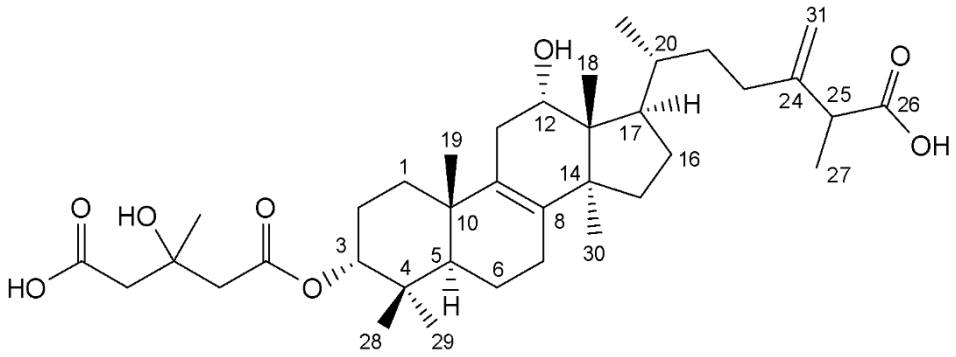

HRMS (-) *m/z* 629.4063 [M -H]$^-$(629.4048 calcd. for $C_{37}H_{57}O_8$ Δ 2.3 ppm;); HRMSMS (CID = 15%, 30%, 45%) 567.4055, 527.3735, 485.3621,441.3735

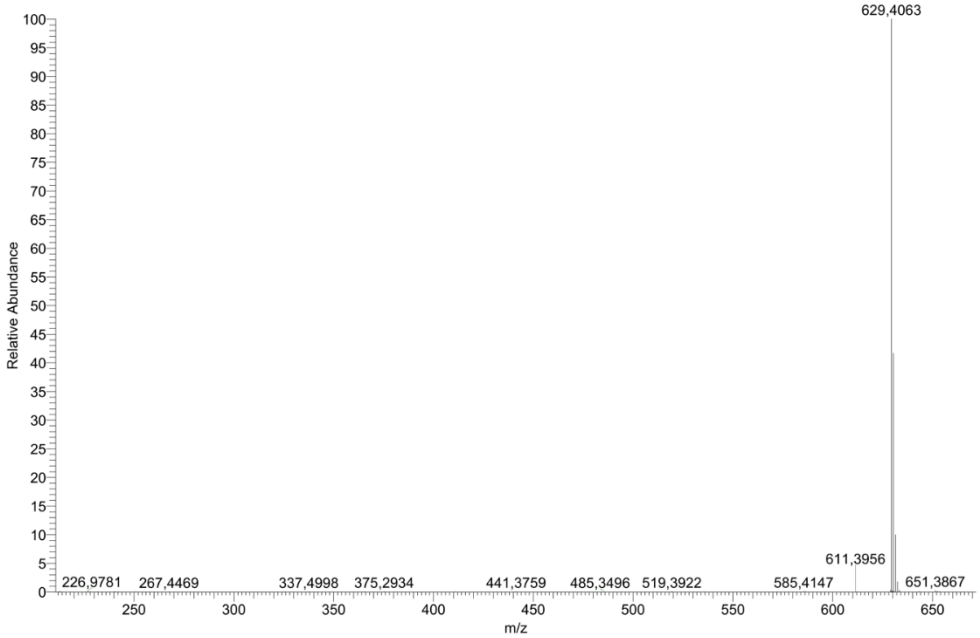

Figure A56. HRMS spectrum of **BGS-7**

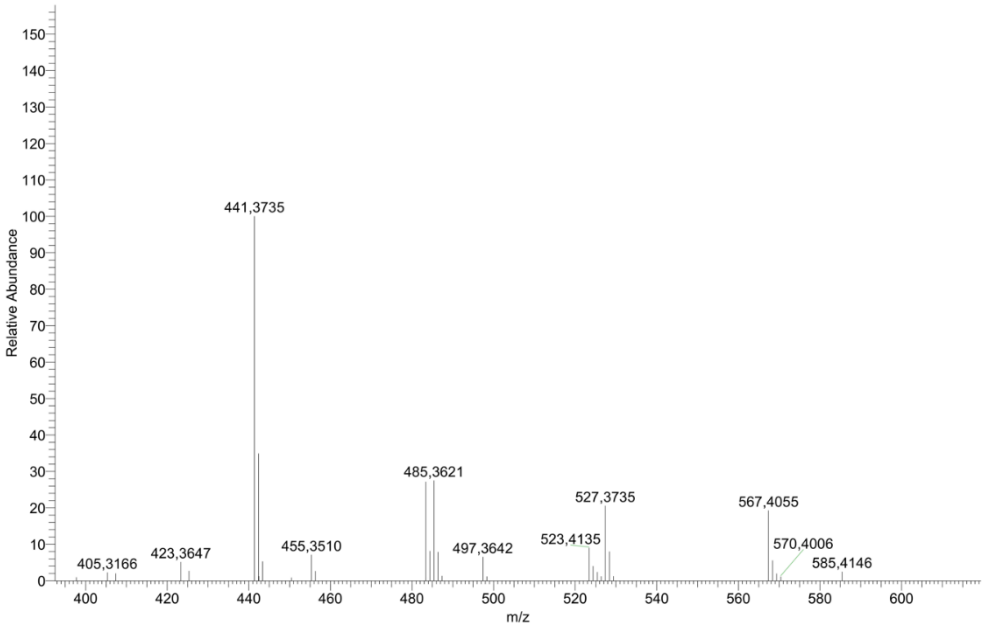

Figure A57. MS-MS spectrum of **BGS-7**

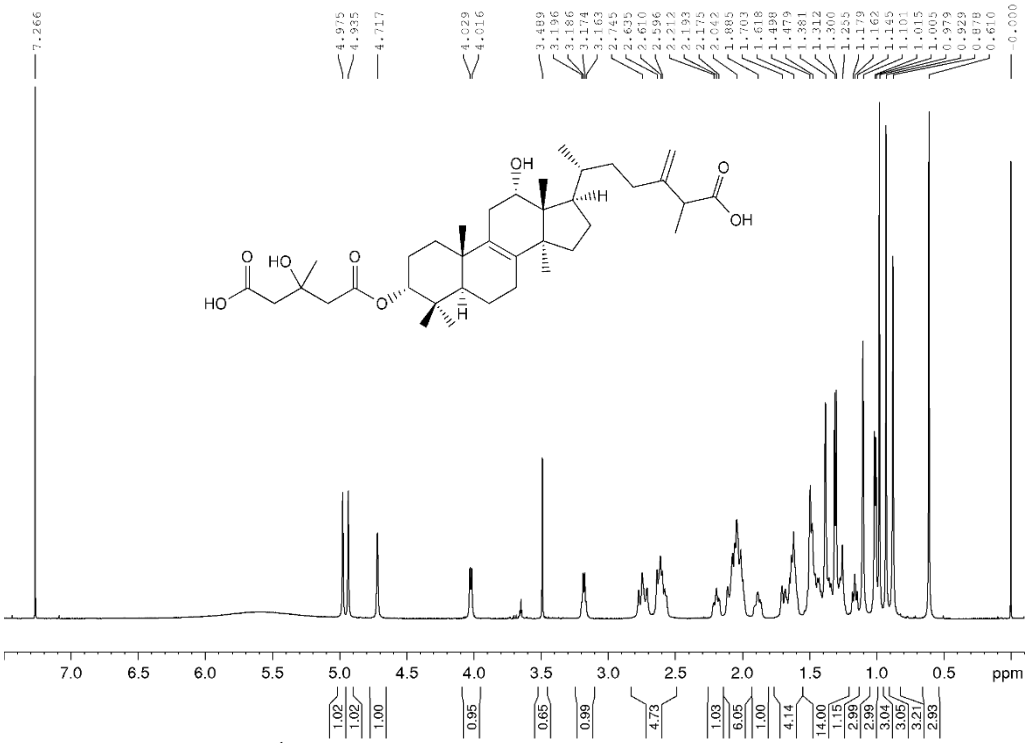

Figure A58. ^{1}H spectrum of **BGS-7** (600 MHz, $CDCl_3$, 295 K)

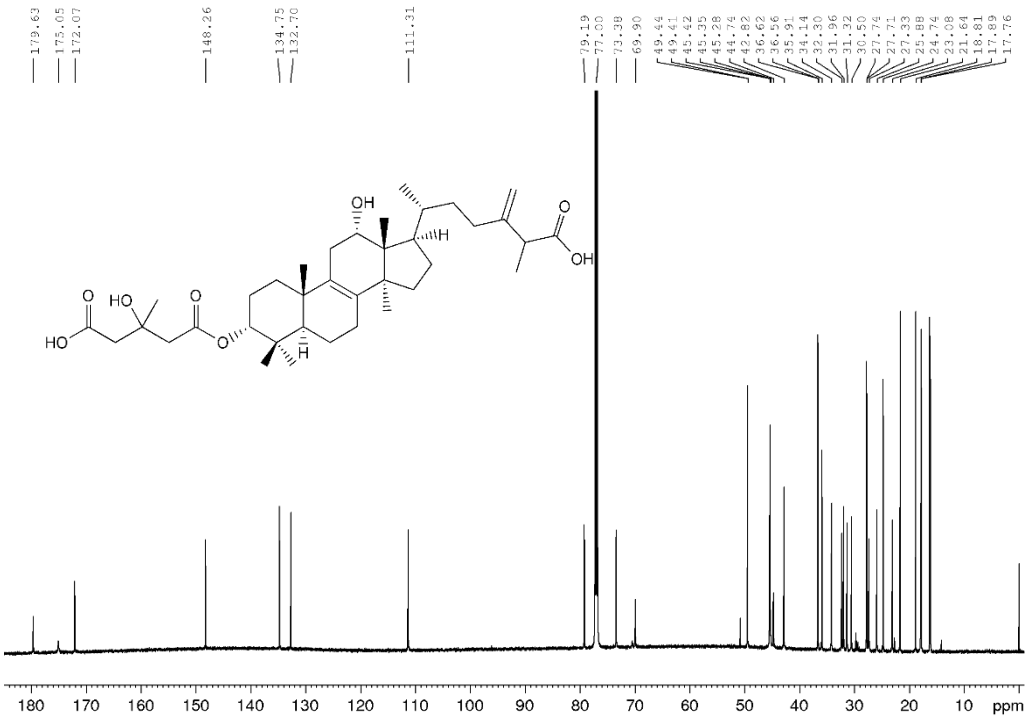

Figure A59. ^{13}C spectrum of **BGS-7** (150 MHz, $CDCl_3$, 295 K),

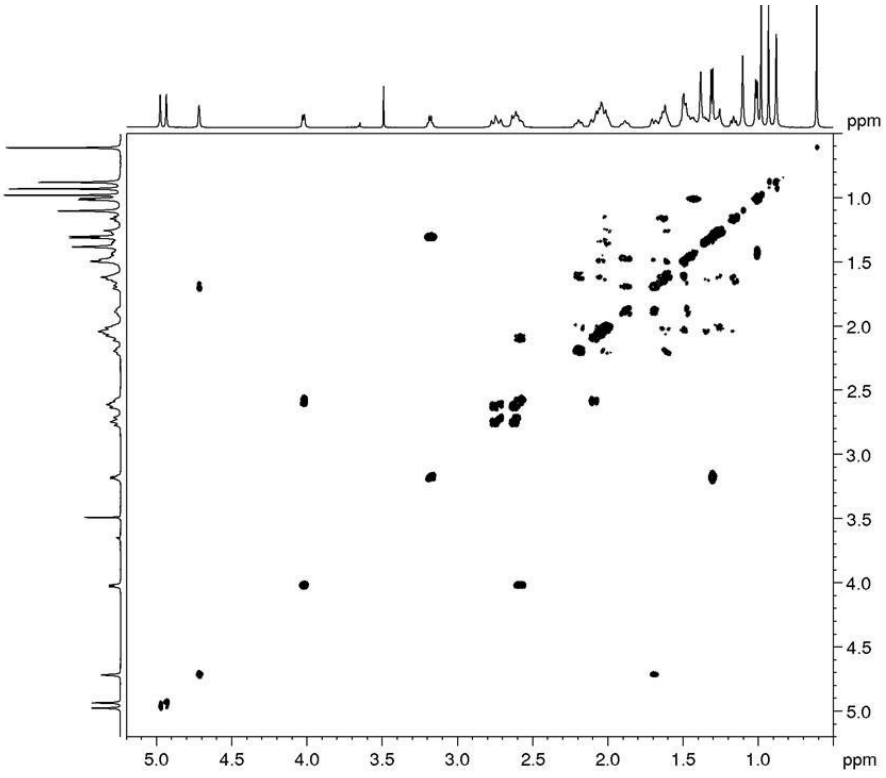

Figure A60. COSY spectrum of **BGS-7** (600 MHz, $CDCl_3$, 295 K)

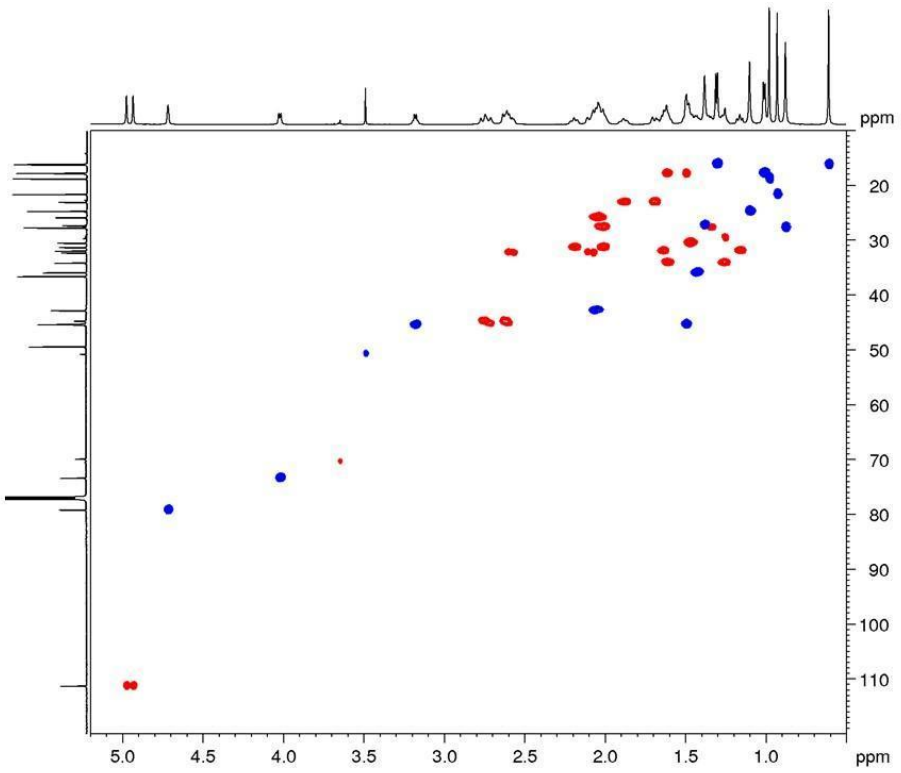

Figure A61. DEPT-edited HSQC spectrum of **BGS-7** (600 MHz, $CDCl_3$, 295 K)

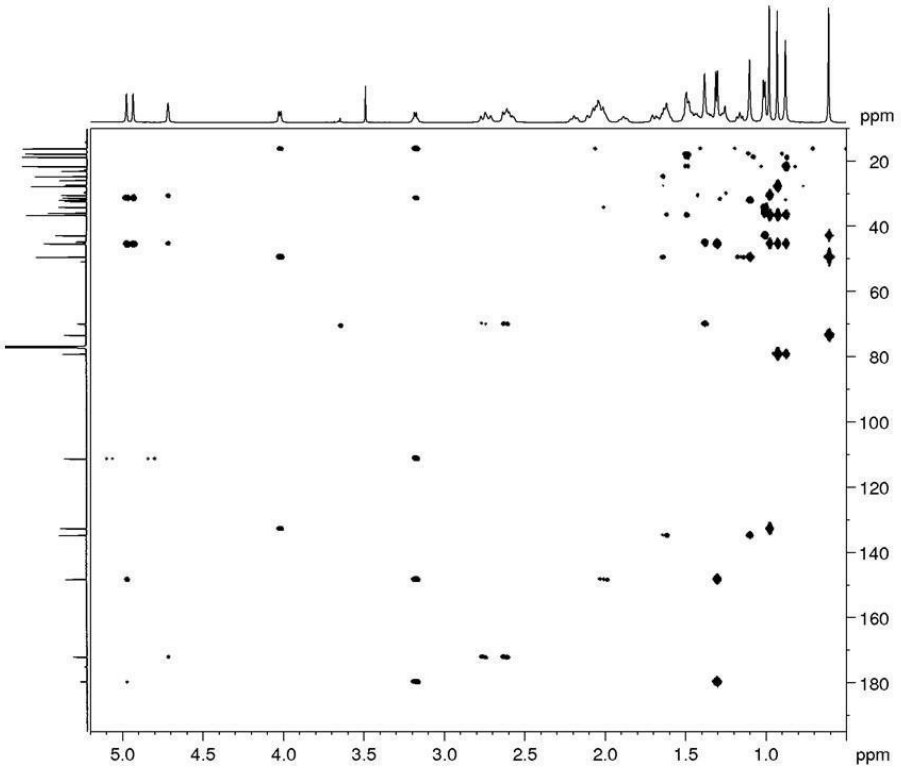

Figure A62. HMBC spectrum of **BGS-7** (600 MHz, $CDCl_3$, 295 K)

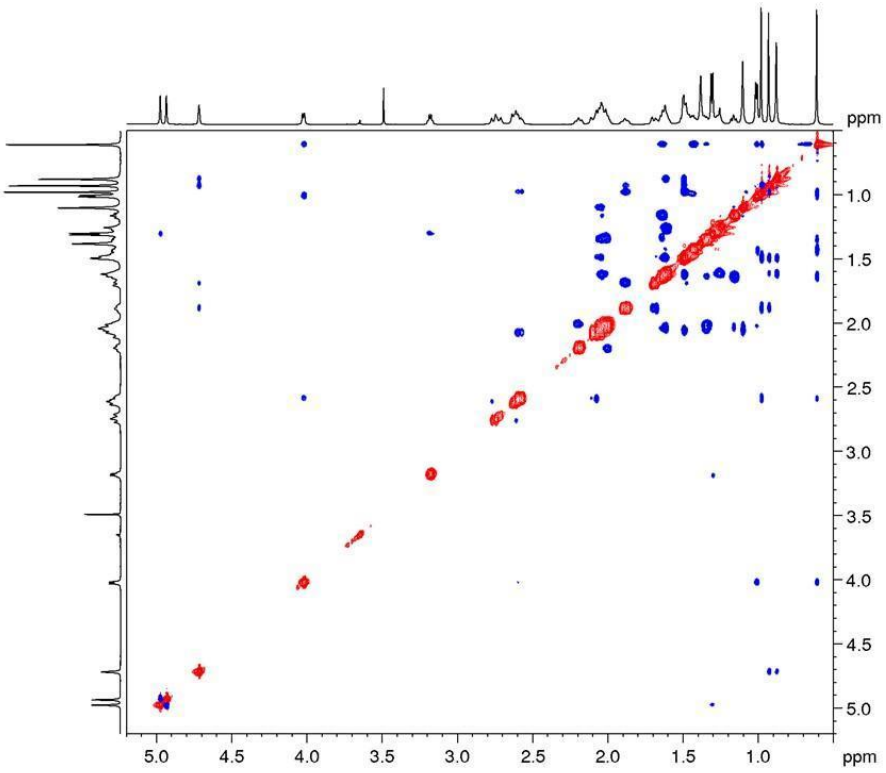

Figure A63. ROESY spectrum of **BGS-7** (600 MHz, $CDCl_3$, 295 K)

Spectra and spectral data on BGS-8

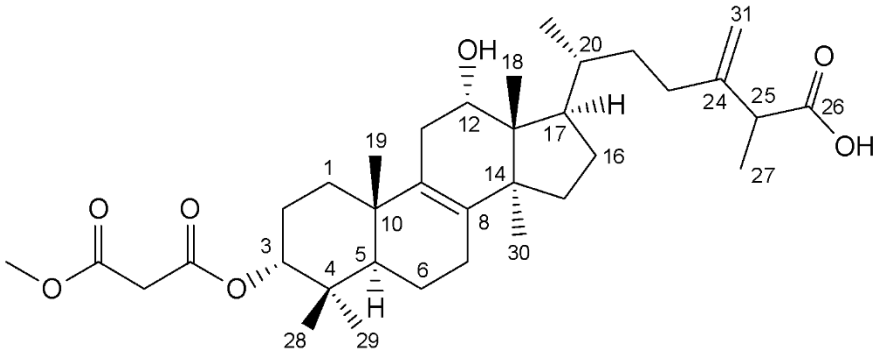

HRMS (-) *m/z* 585.3798 $[M-H]^-$(585.3786 calcd. for $C_{35}H_{53}O_7$; Δ 2.1 ppm); HRMSMS (CID = 15%, 30%, 45%) 541.3893, 509.3629, 441.3734

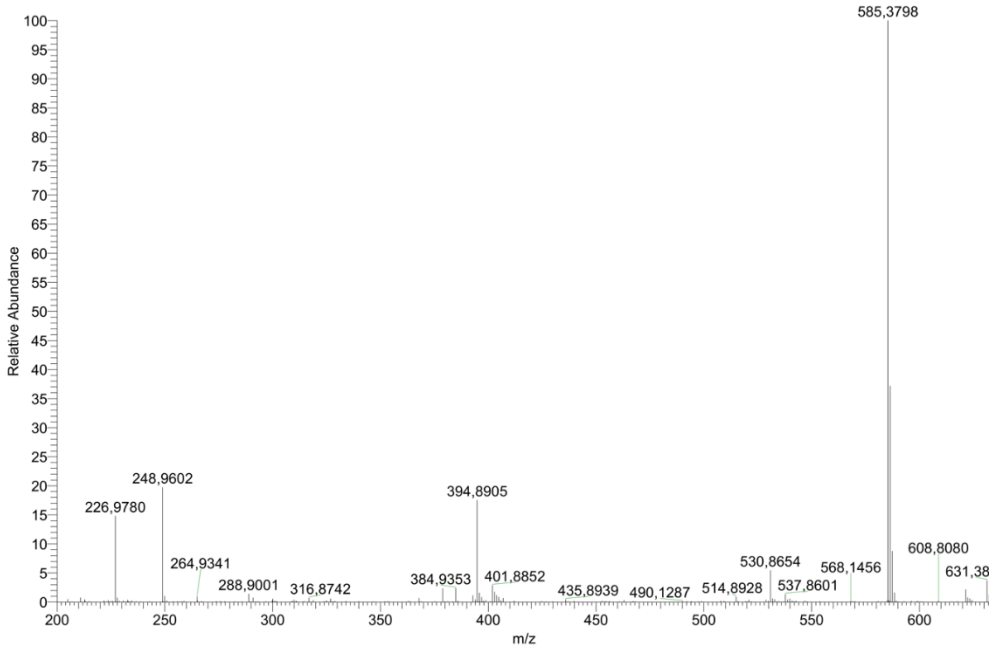

Figure A64. HRMS spectrum of **BGS-8**

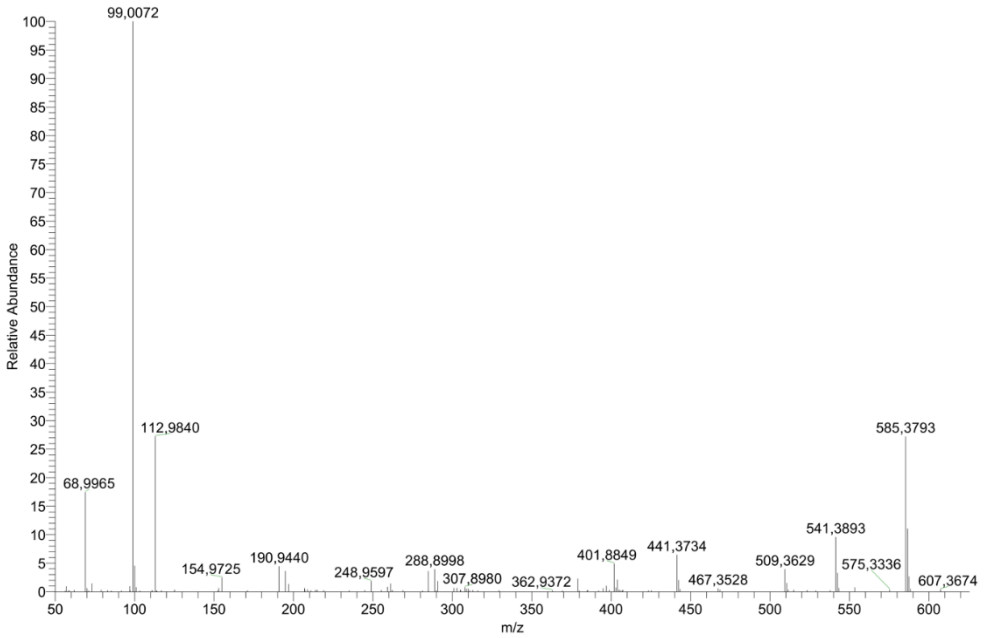

Figure A65. MS-MS spectrum of **BGS-8**

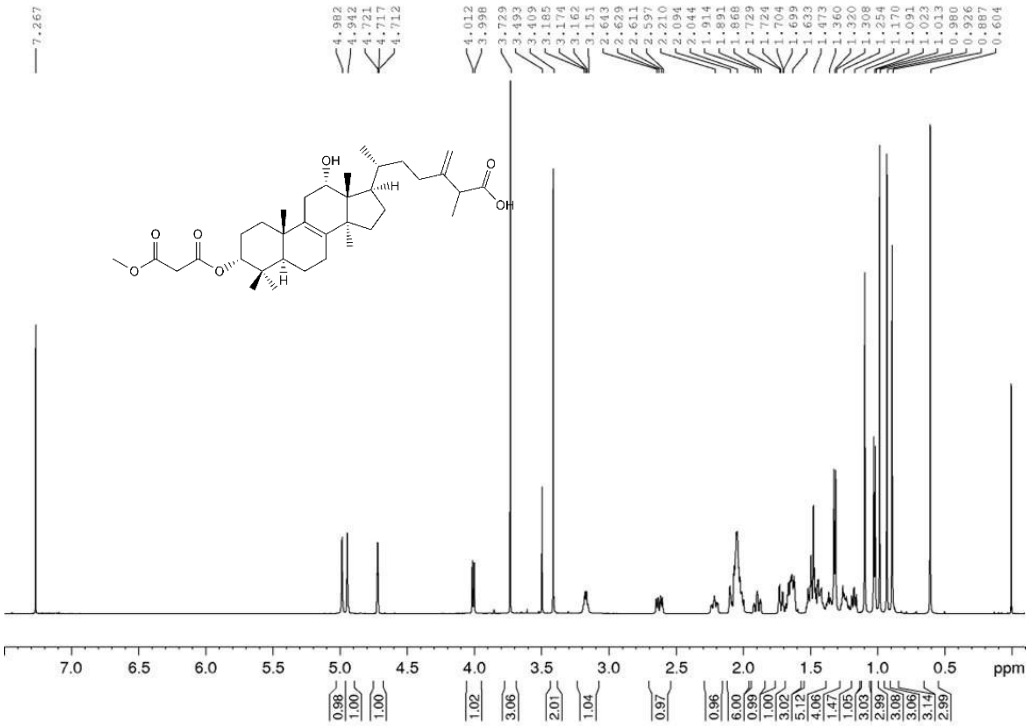

Figure A66. ^{1}H spectrum of **BGS-8** (600 MHz, $CDCl_3$, 295 K)

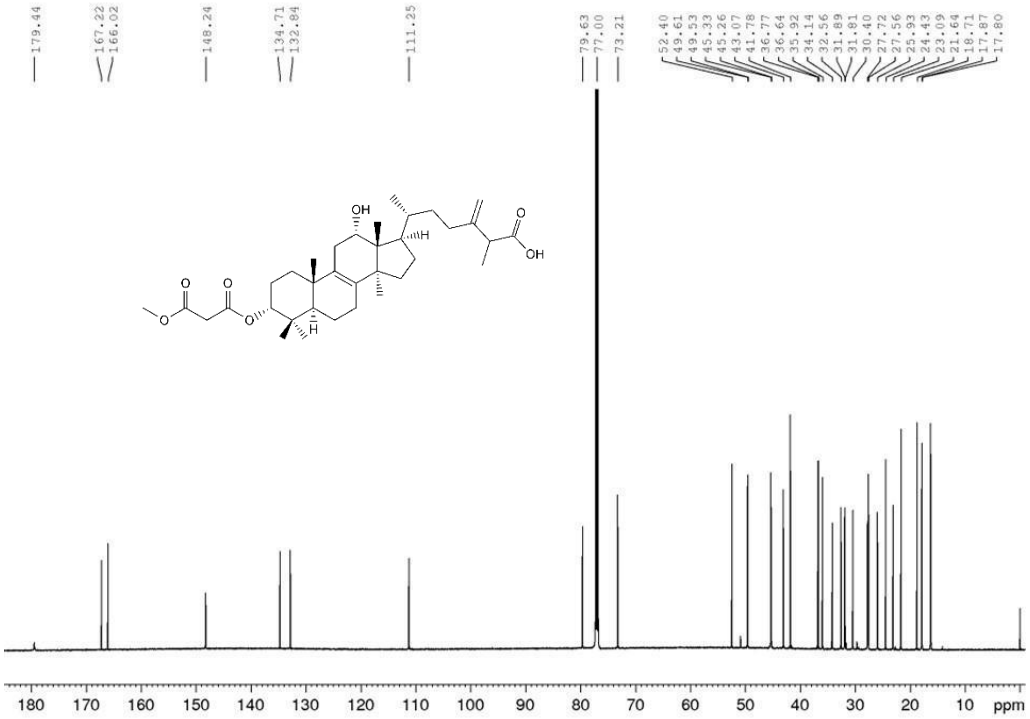

Figure A67. ^{13}C spectrum of **BGS-8** (150 MHz, $CDCl_3$, 295 K)

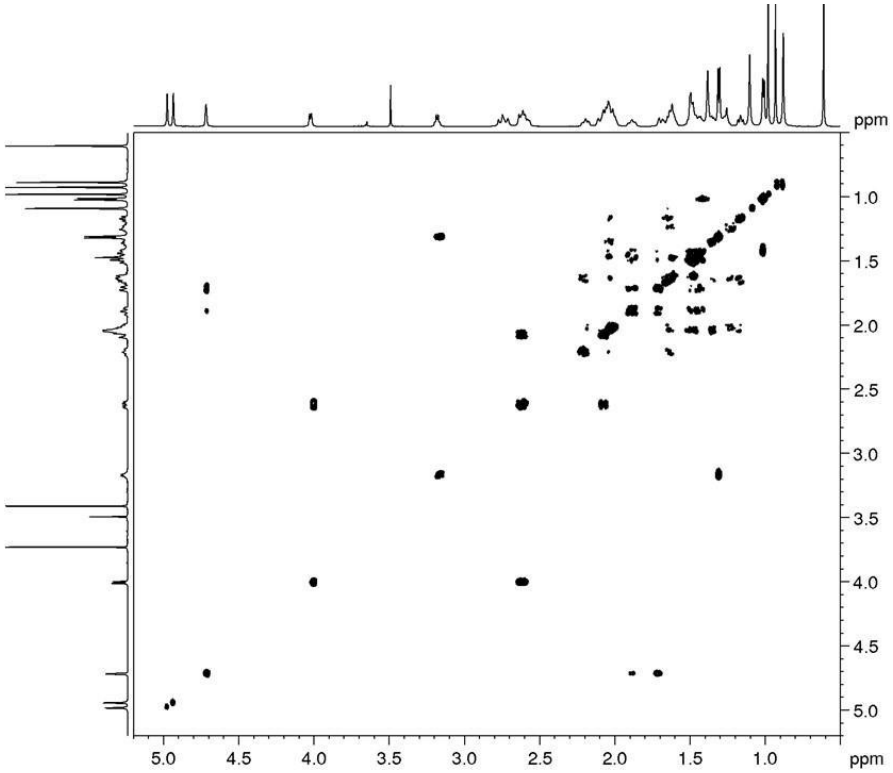

Figure A68. COSY spectrum of **BGS-8** (600 MHz, $CDCl_3$, 295 K)

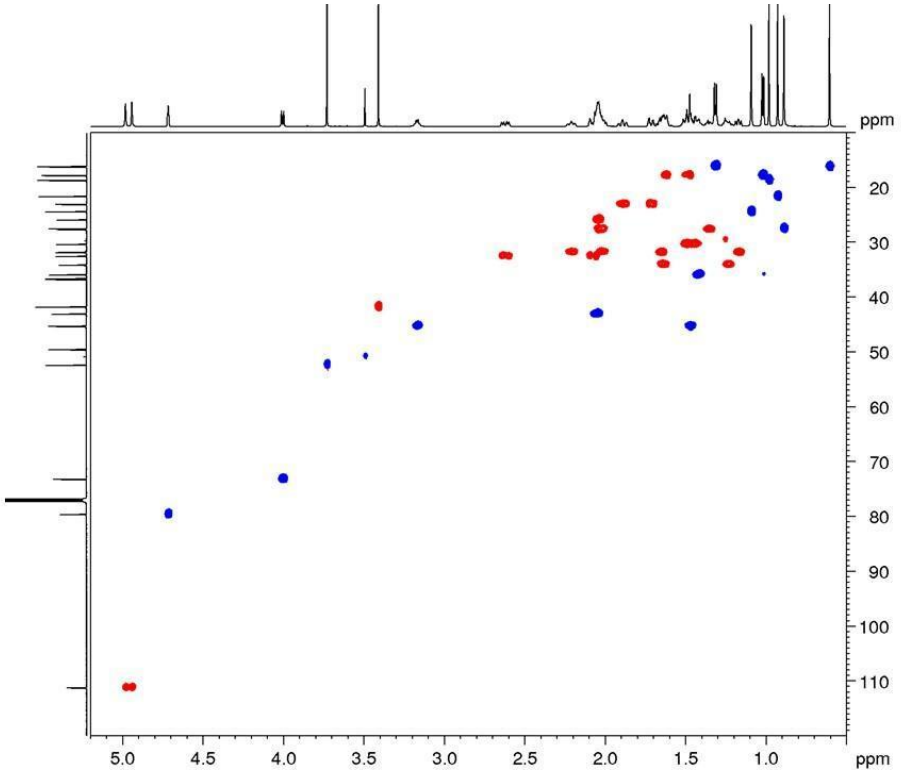

Figure A69. DEPT-edited HSQC spectrum of **BGS-8** (600 MHz, $CDCl_3$, 295 K)

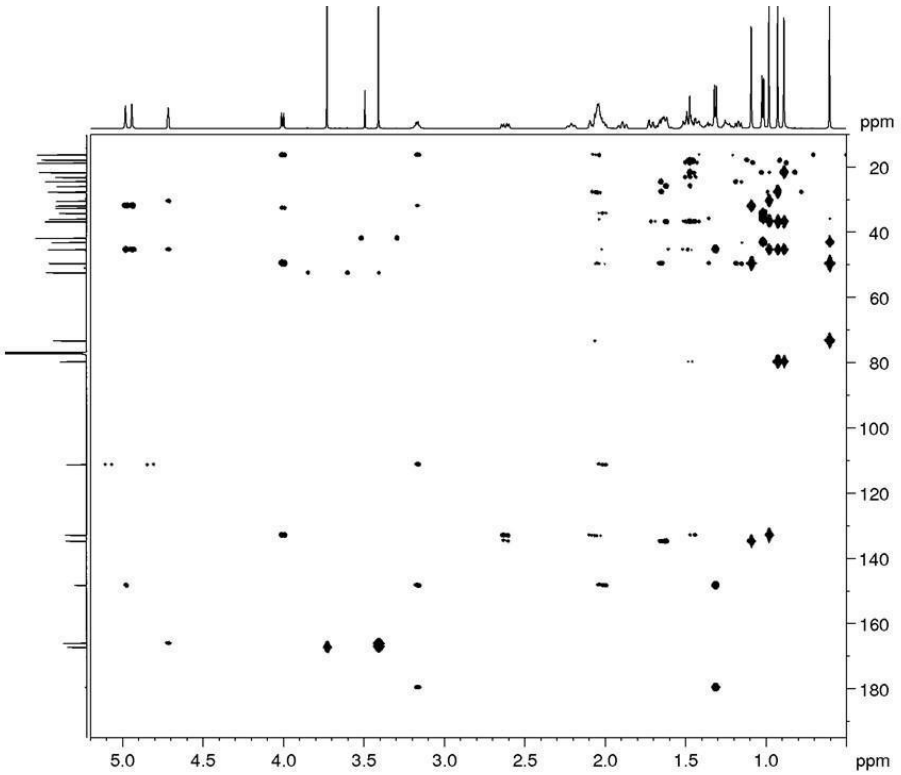

Figure A70. HMBC spectrum of **BGS-8** (600 MHz, $CDCl_3$, 295 K)

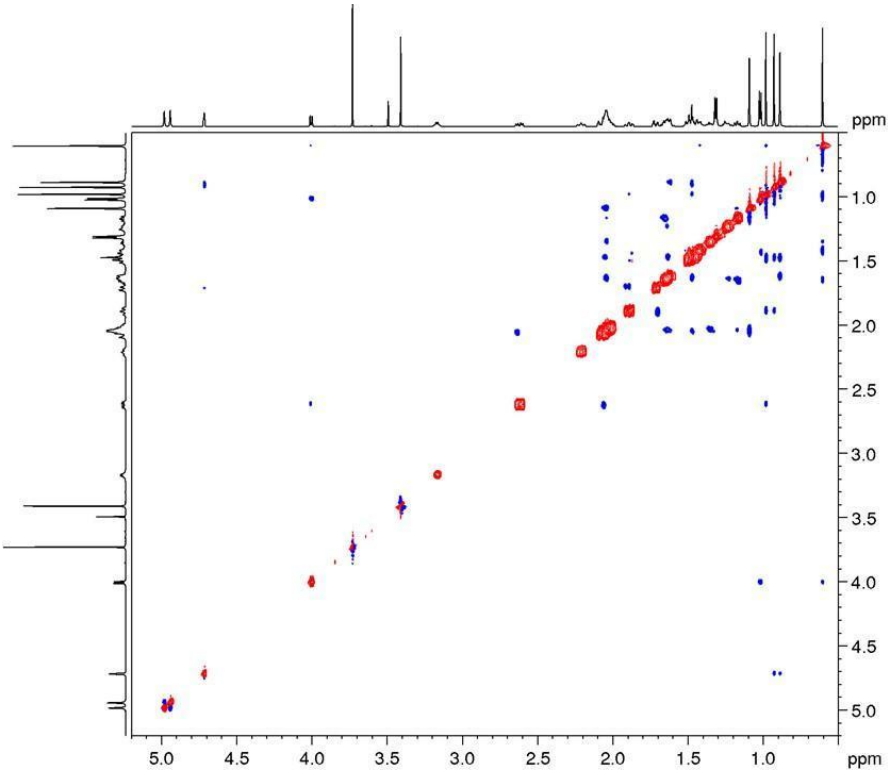

Figure A71. ROESY spectrum of **BGS-8** (600 MHz, $CDCl_3$, 295 K)

Spectra and spectral data on BGS-9

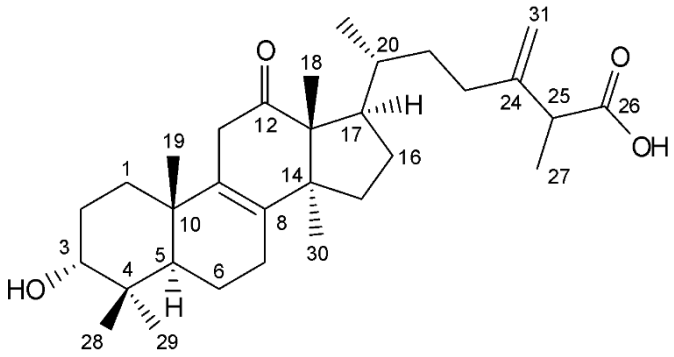

HRMS (+) *m/z* 485.3616 $[M+H]^+$ (485.3625 calcd. for $C_{31}H_{49}O_4$; Δ -1.9 ppm); HRMSMS (CID = 15%, 30%, 45%) 467.3510, 449.3404

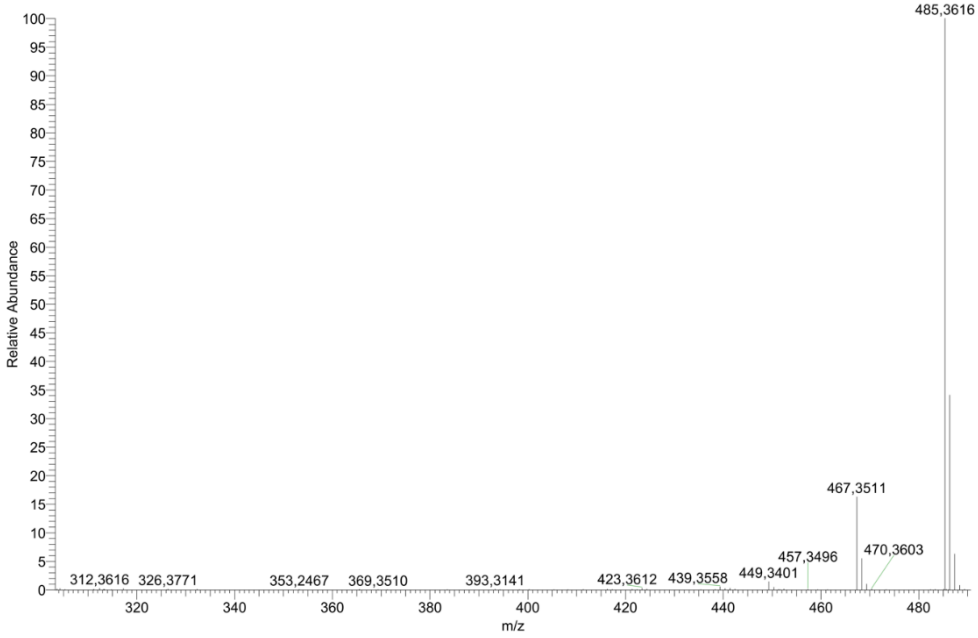

Figure A72. HRMS spectrum of **BGS-9**

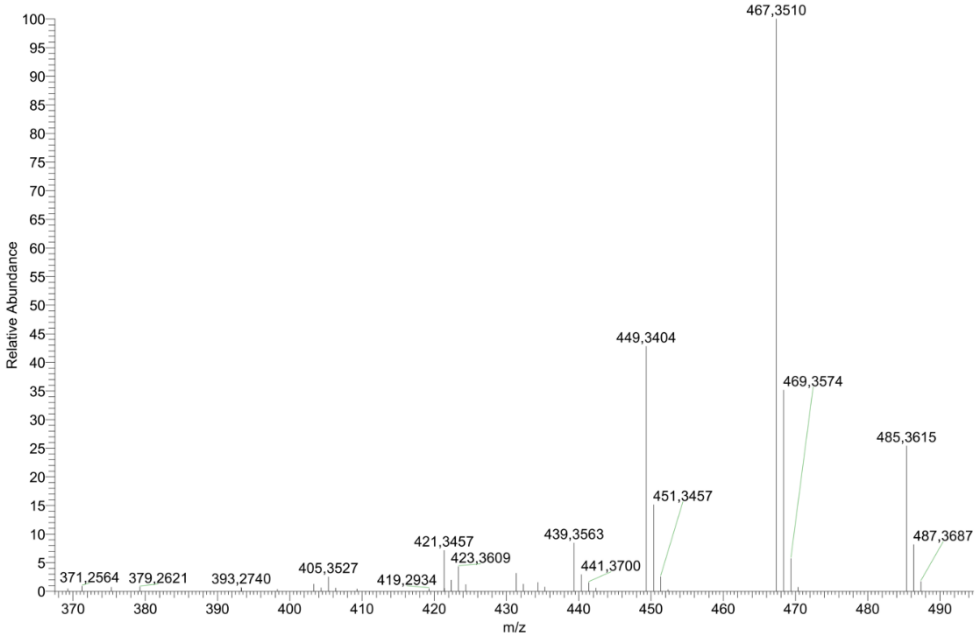

Figure A73. MS-MS spectrum of **BGS-9**

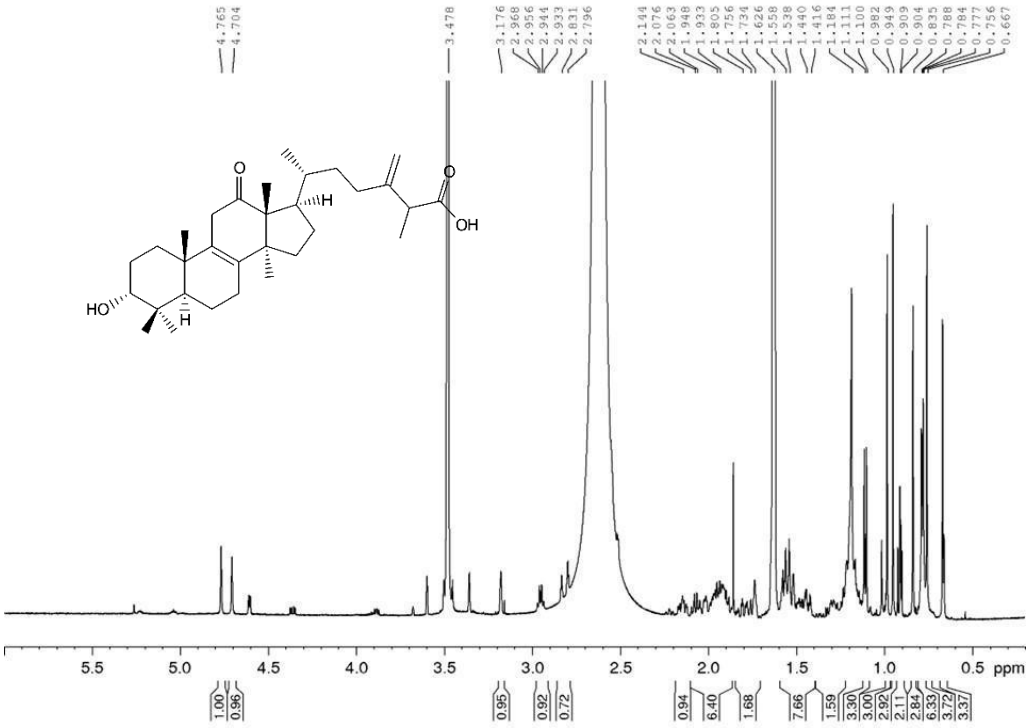

Figure A74. ^{1}H spectrum of **BGS-9** (600 MHz, $CDCl_3$, 295 K)

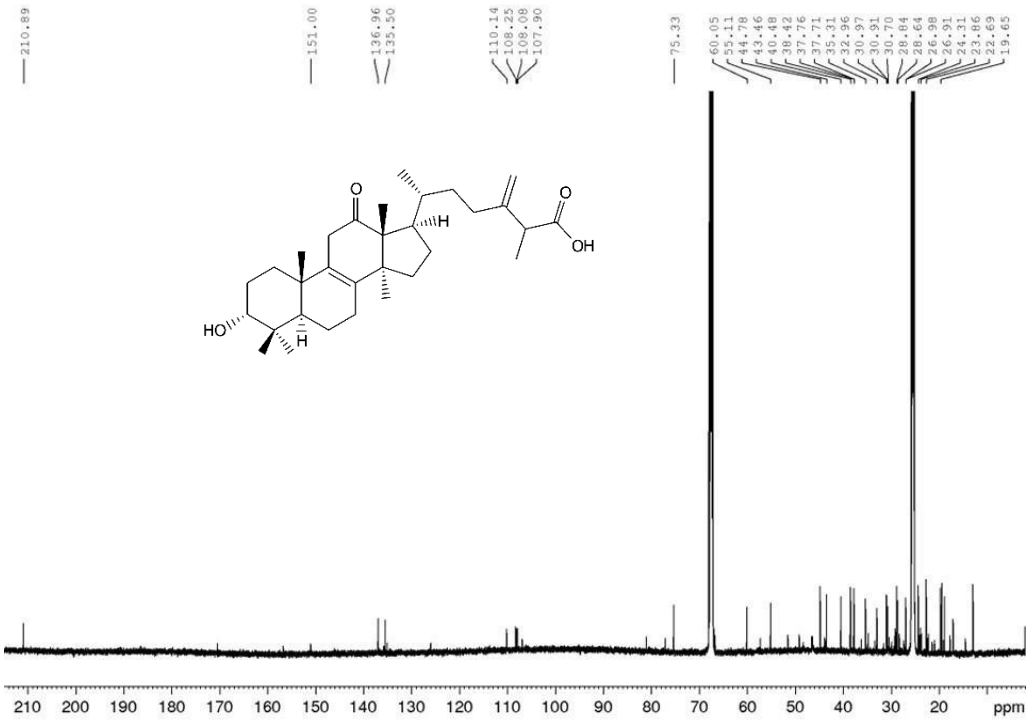

Figure A75. ^{13}C spectrum of **BGS-9** (150 MHz, $CDCl_3$, 295 K)

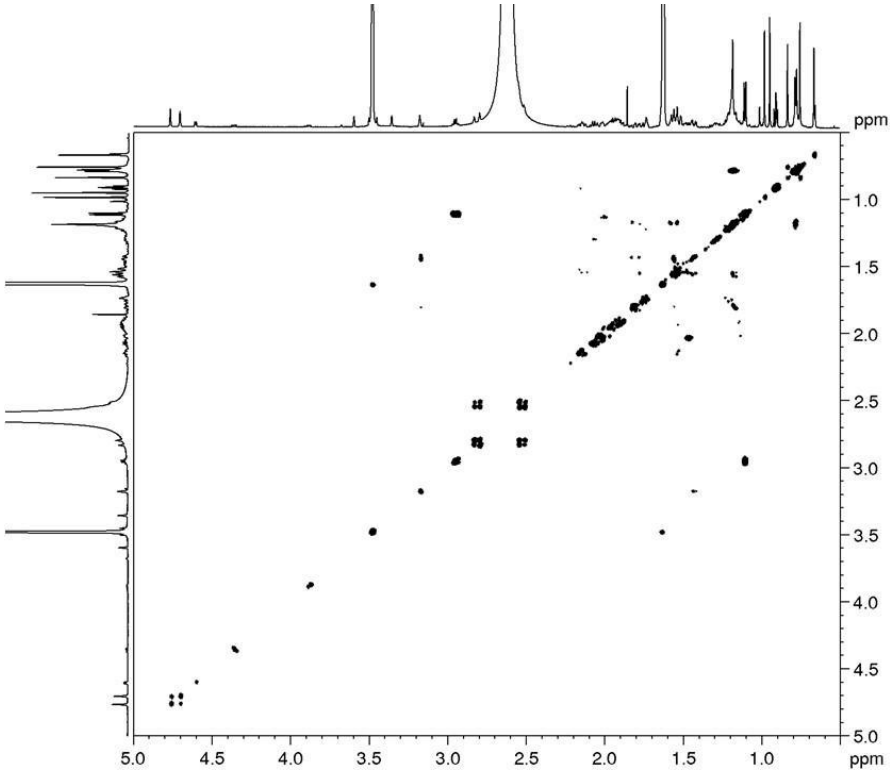

Figure A76. COSY spectrum of **BGS-9** (600 MHz, $CDCl_3$, 295 K)

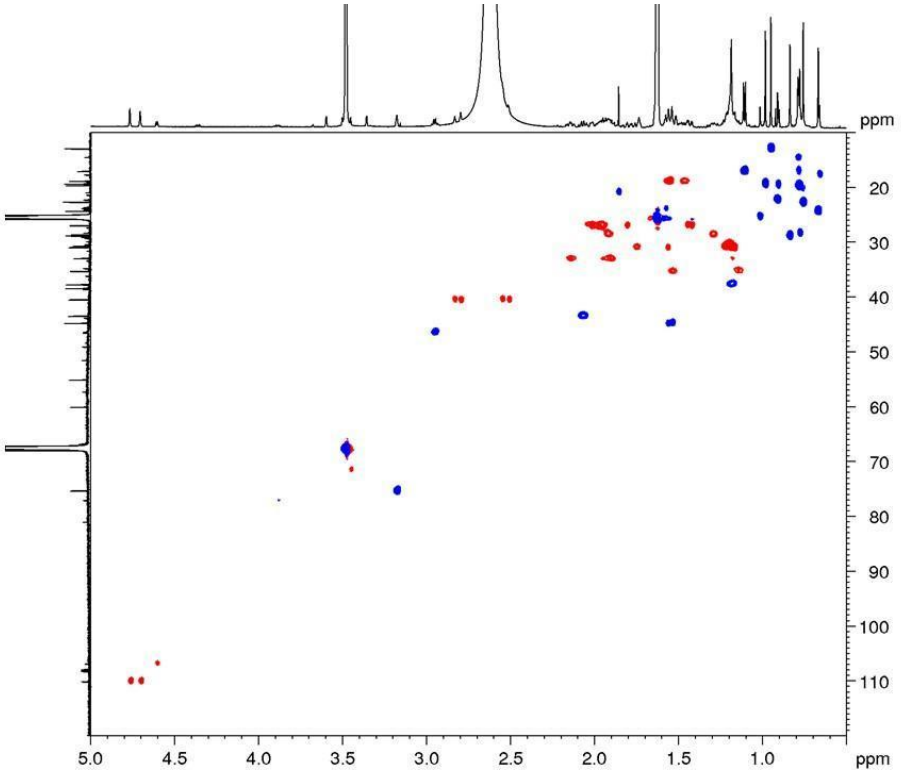

Figure A77. DEPT-edited HSQC spectrum of **BGS-9** (600 MHz, $CDCl_3$, 295 K)

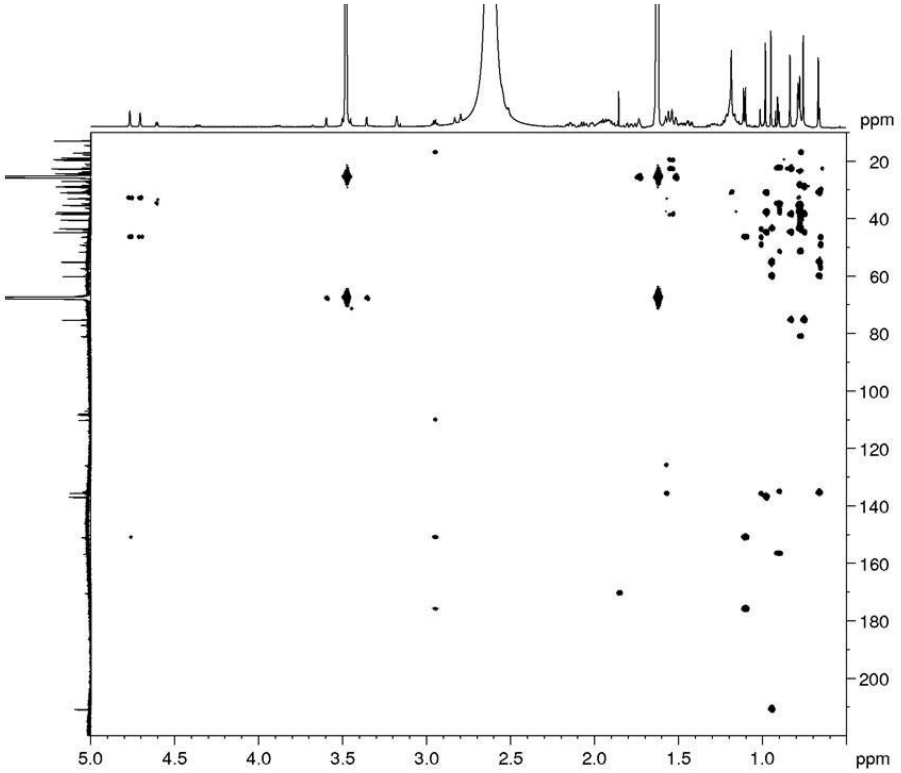

Figure A78. HMBC spectrum of **BGS-9** (600 MHz, $CDCl_3$, 295 K)

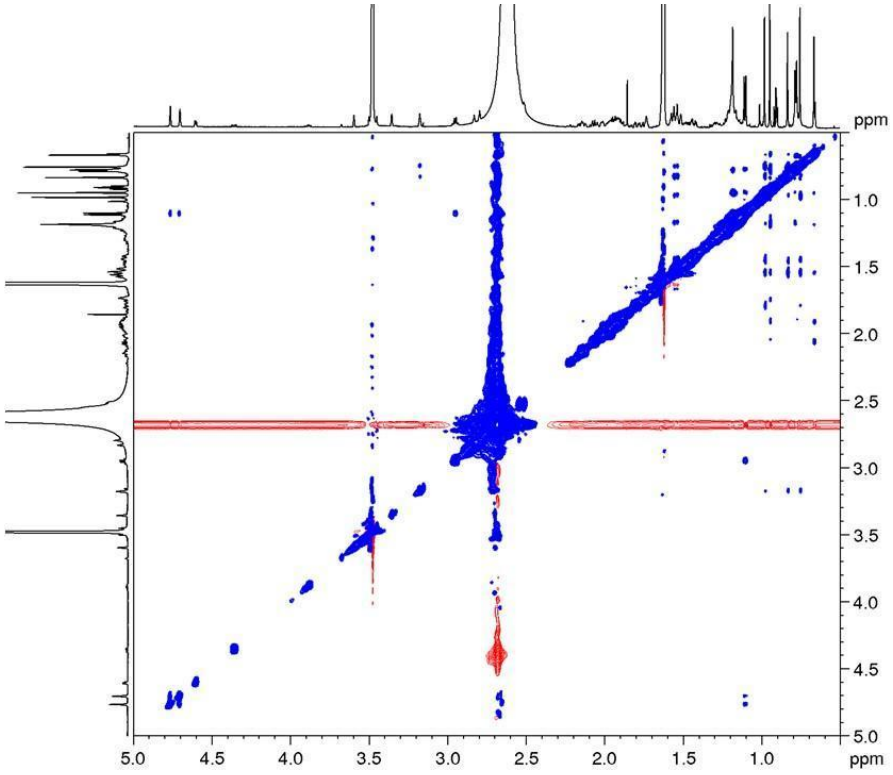

Figure A79. NOESY spectrum of **BGS-9** (600 MHz, $CDCl_3$, 295 K)

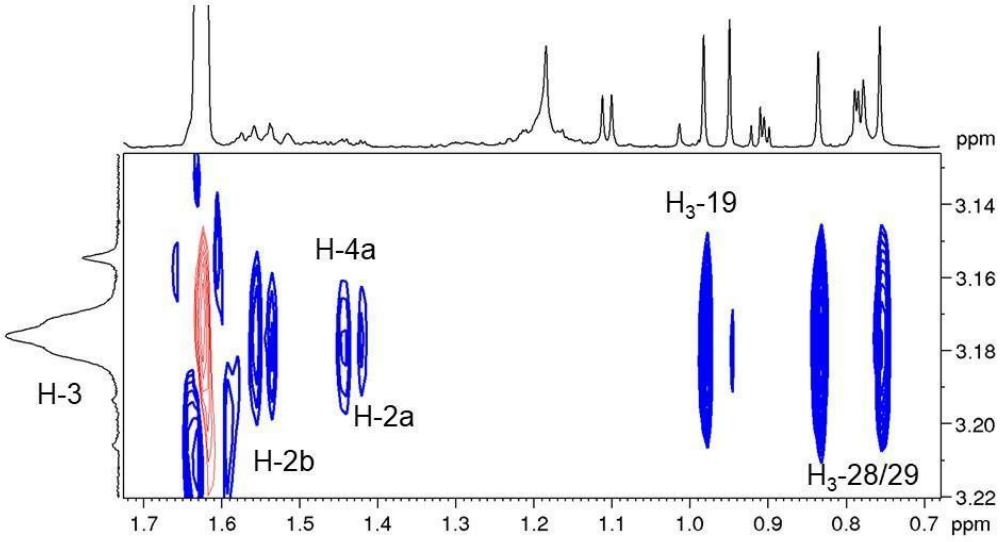

Figure A80. NOESY spectrum of **BGS-9** (600 MHz, $CDCl_3$, 295 K)

Spectra and spectral data on BGS-10

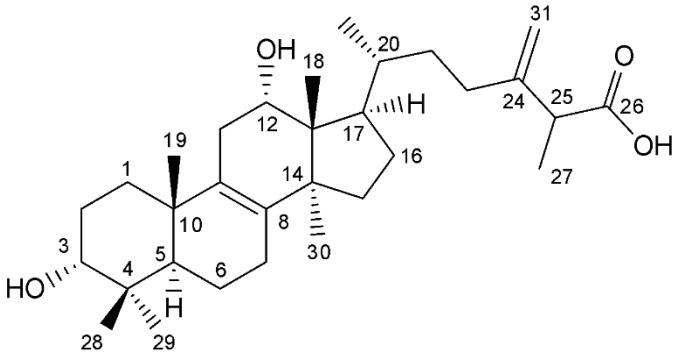

HRMS (-) *m/z* 485.3638 $[M-H]^-$(485.3625 calcd. for $C_{31}H_{49}O_4$; Δ 2.6 ppm); HRMSMS (CID = 15%, 30%, 45%) 455.3529, 441.3736, 423.3636

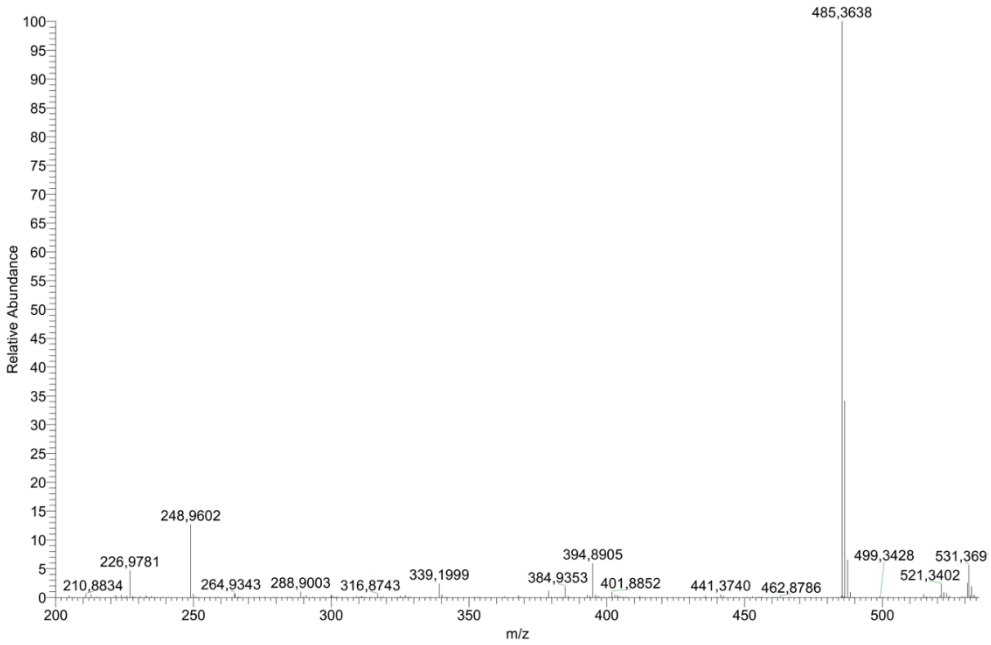

Figure A81. HRMS spectrum of **BGS-10**

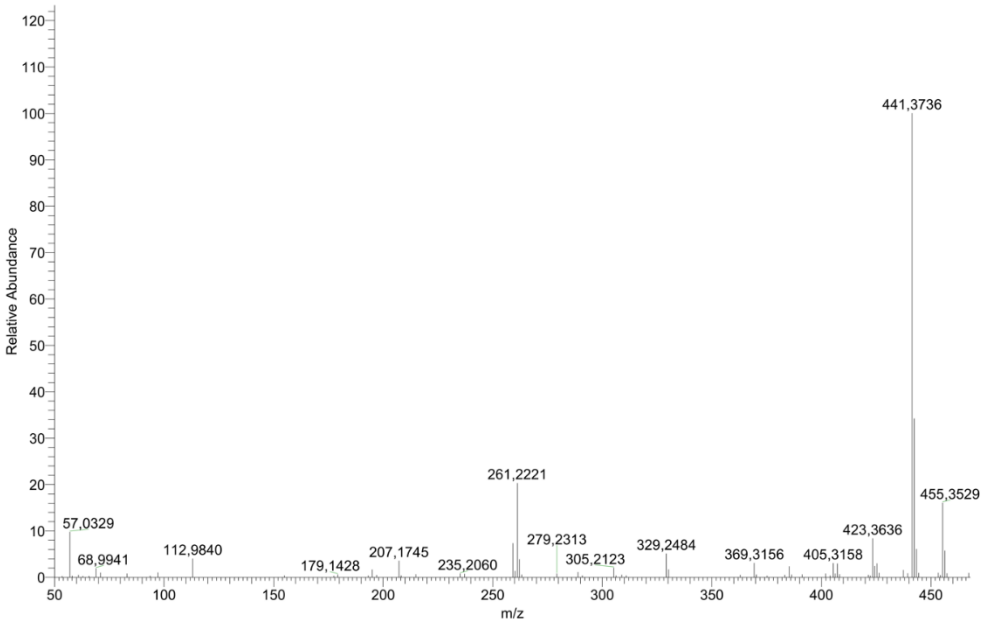

Figure A82. MS-MS spectrum of **BGS-10**

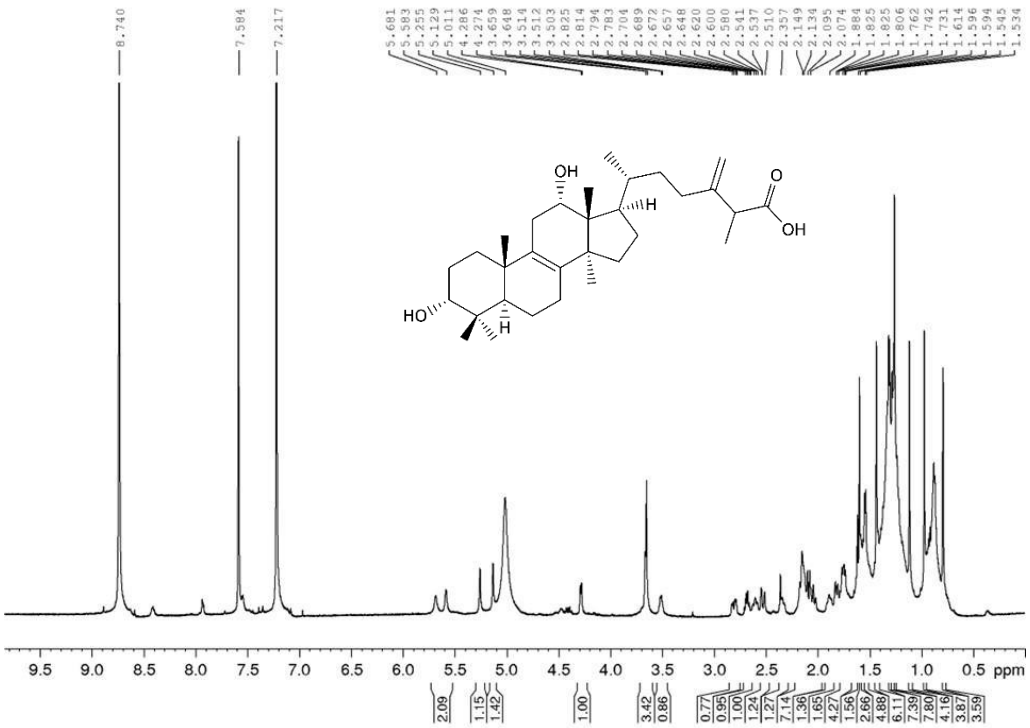

Figure A83. ^{1}H spectrum of **BGS-10** (600 MHz, pyridine-d_5, 295 K)

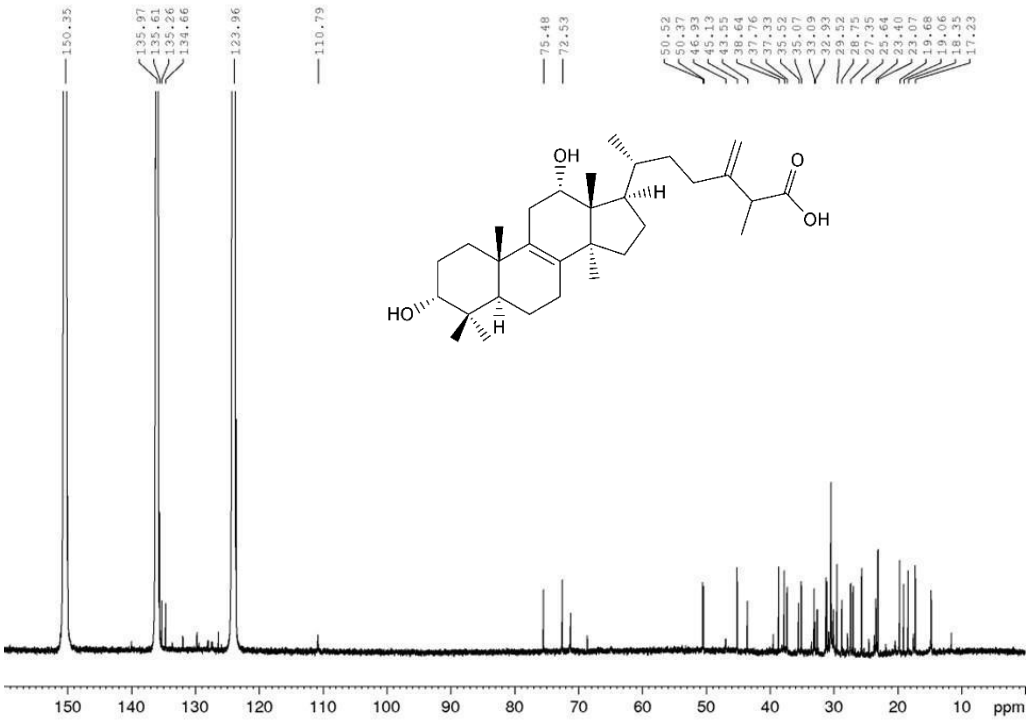

Figure A84. ^{13}C spectrum of **BGS-10** (150 MHz, pyridine-d_5, 295 K)

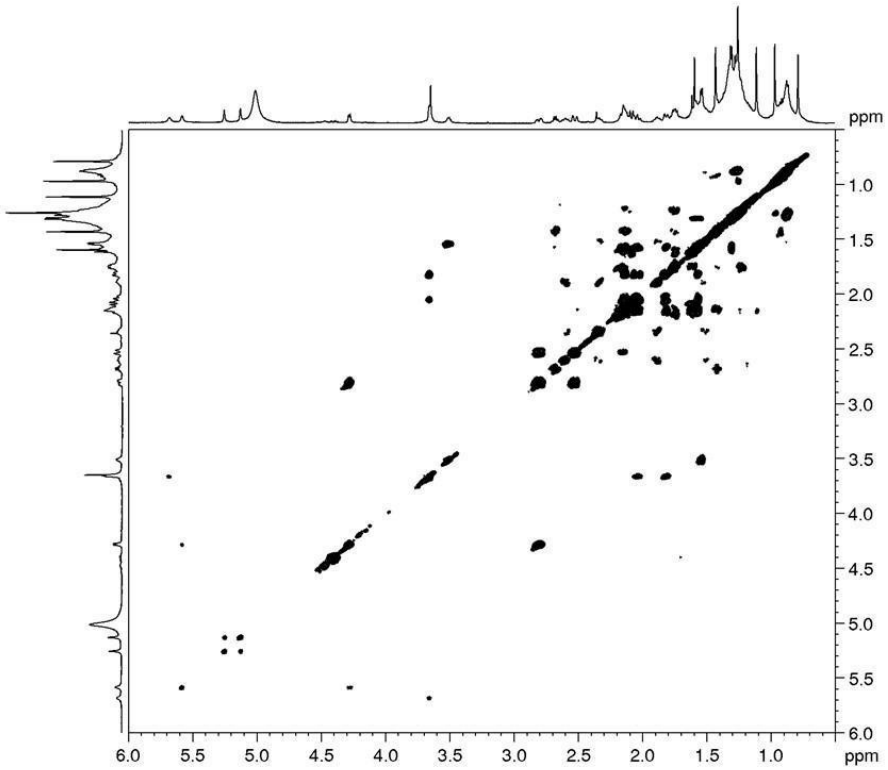

Figure A85. COSY spectrum of **BGS-10** (600 MHz, pyridine-d_5, 295 K)

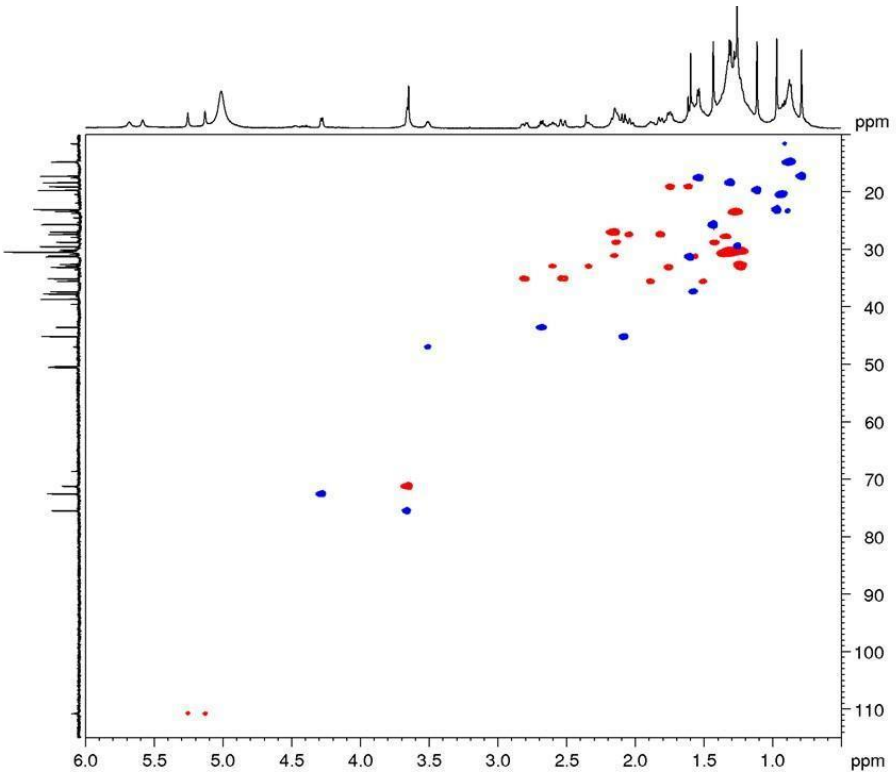

Figure A86. DEPT-edited HSQC spectrum of **BGS-10** (600 MHz, pyridine-d_5, 295 K)

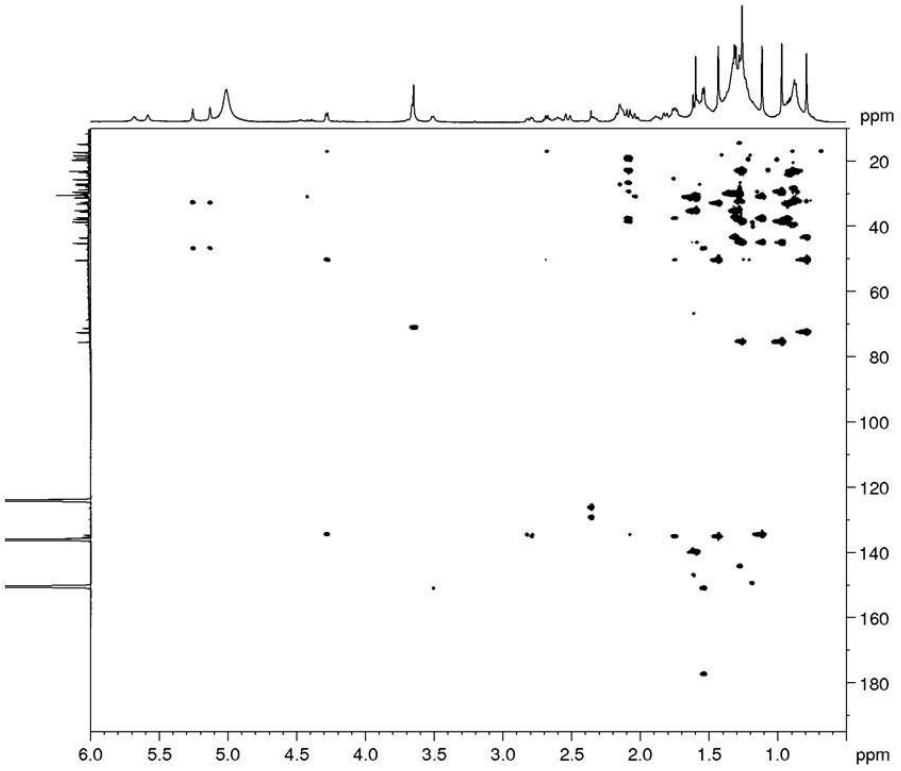

Figure A87. HMBC spectrum of **BGS-10** (600 MHz, pyridine-d_5, 295 K)

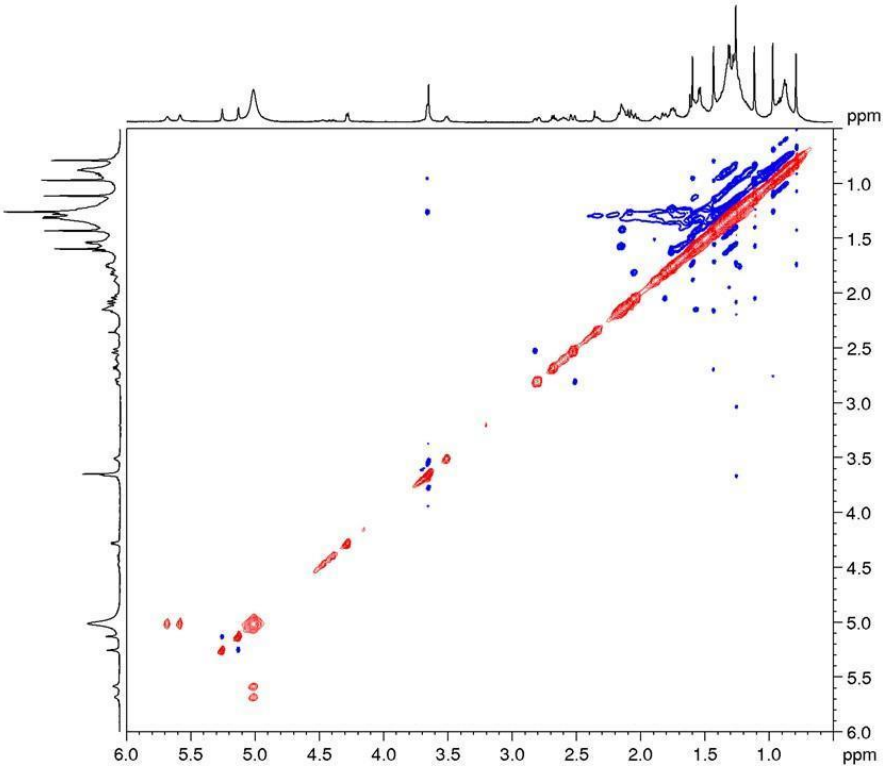

Figure A88. NOESY spectrum of **BGS-10** (600 MHz, pyridine-d_5, 295 K)

Spectra and spectral data on BGS-11

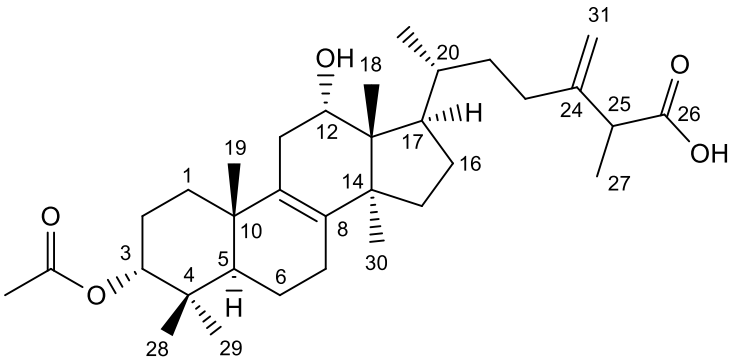

HRMS (-) *m/z* 527.3743 $[M-H]^-$(527.3731 calcd. for $C_{34}H_{51}O_5$ Δ 2.3 ppm); HRMSMS (CID = 15%, 30%, 45%) 497.3636, 483.3841, 441.3736

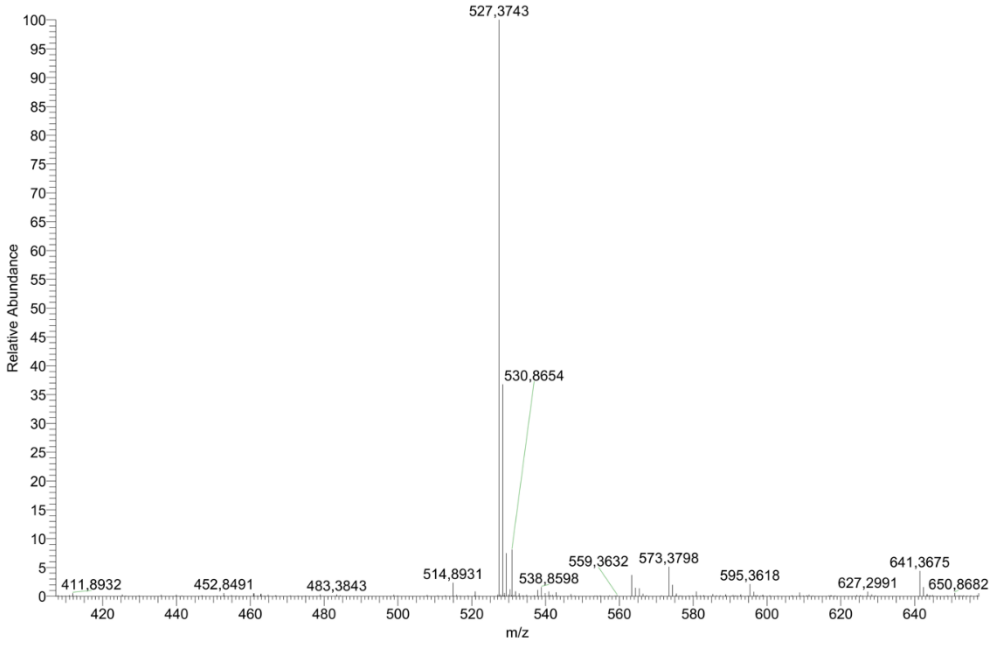

Figure A89. HRMS spectrum of **BGS-11**

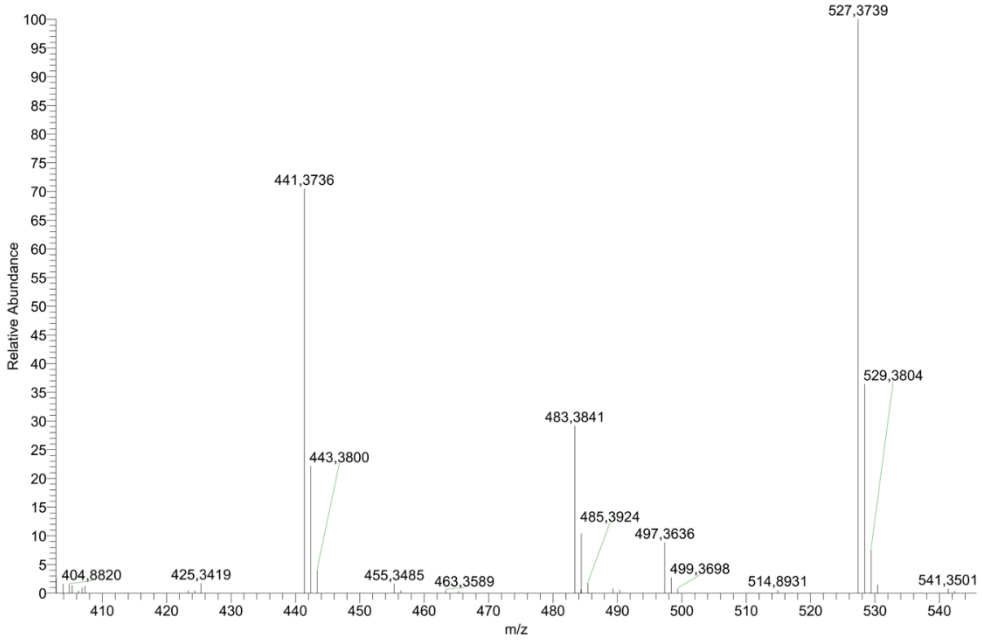

Figure A90. MS-MS spectrum of **BGS-11**

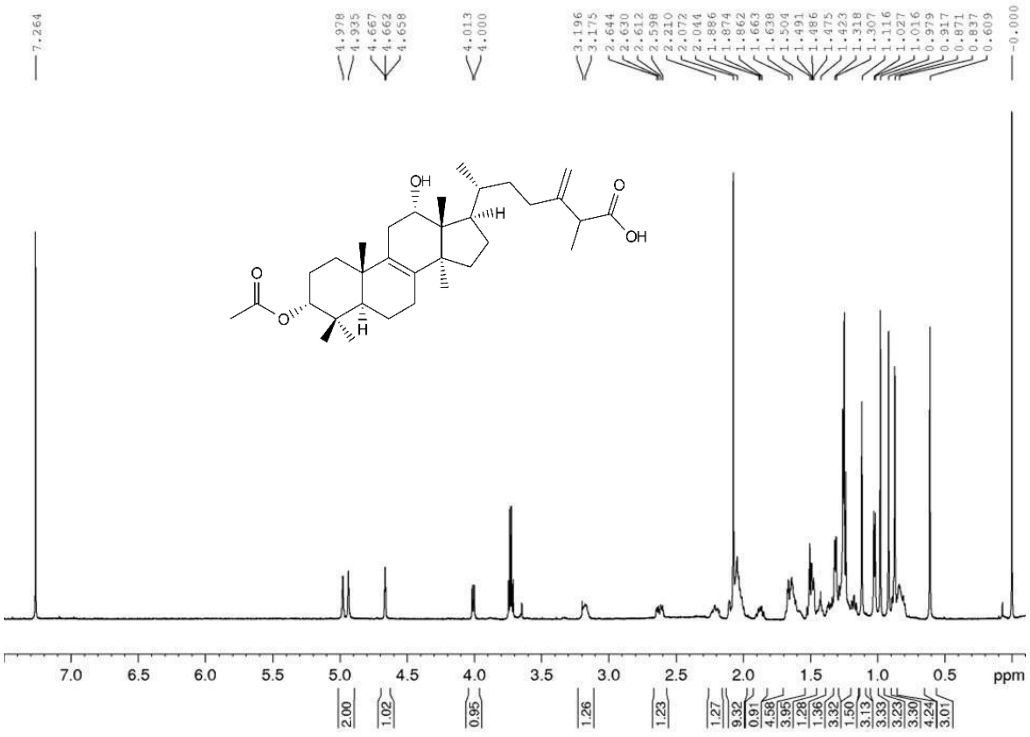

Figure A91. ^{1}H spectrum of **BGS-11** (600 MHz, $CDCl_3$, 295 K)

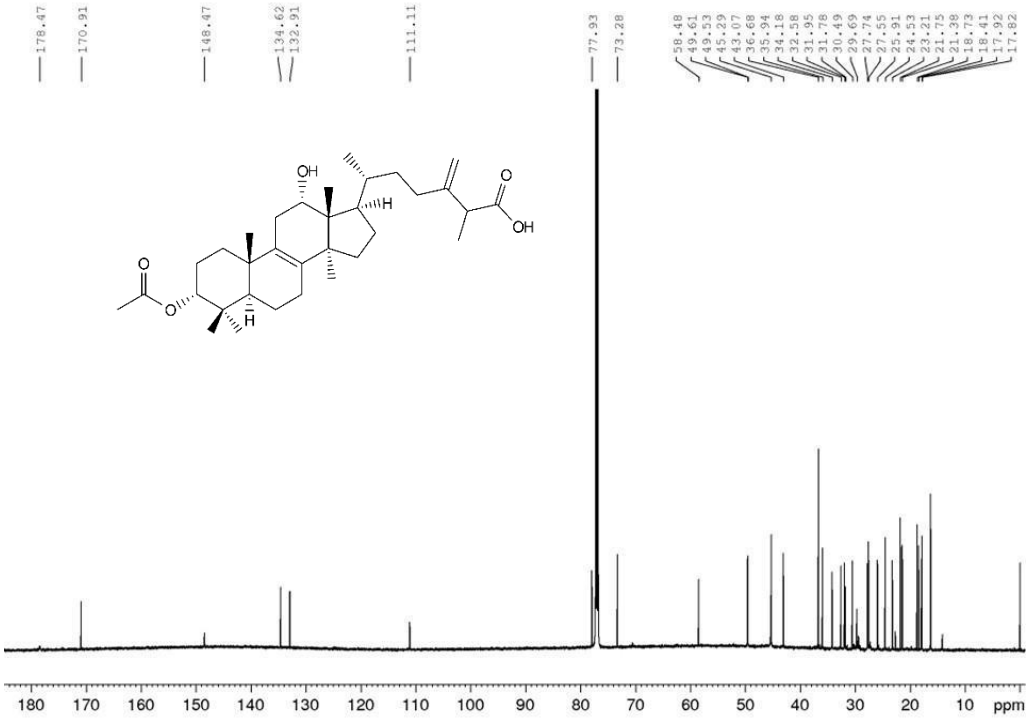

Figure A92. ^{13}C spectrum of **BGS-11** (150 MHz, $CDCl_3$, 295 K)

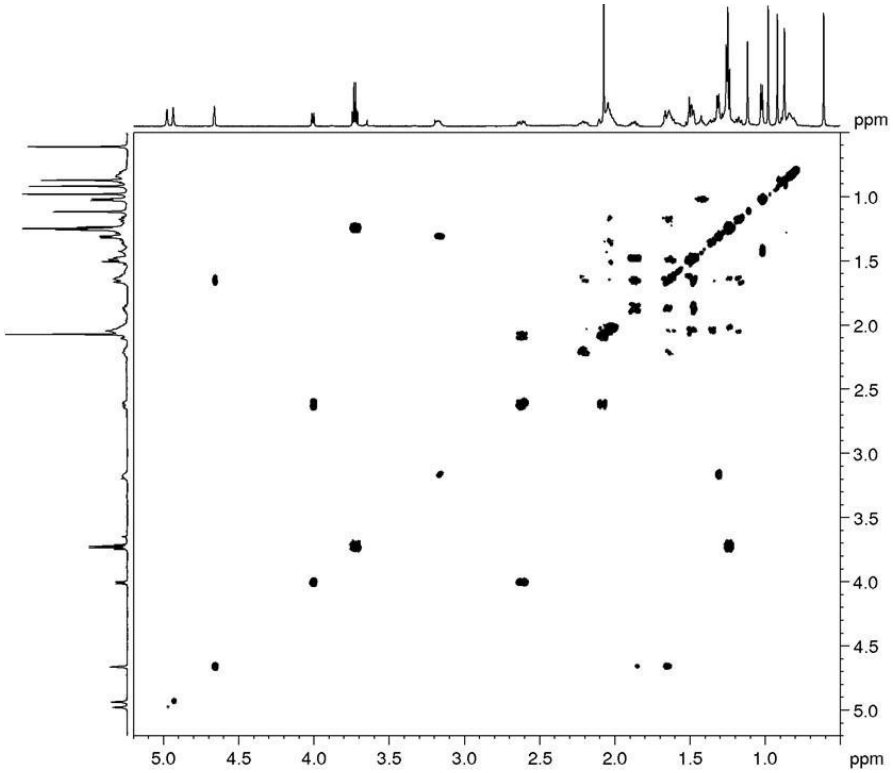

Figure A93. COSY spectrum of **BGS-11** (600 MHz, $CDCl_3$, 295 K)

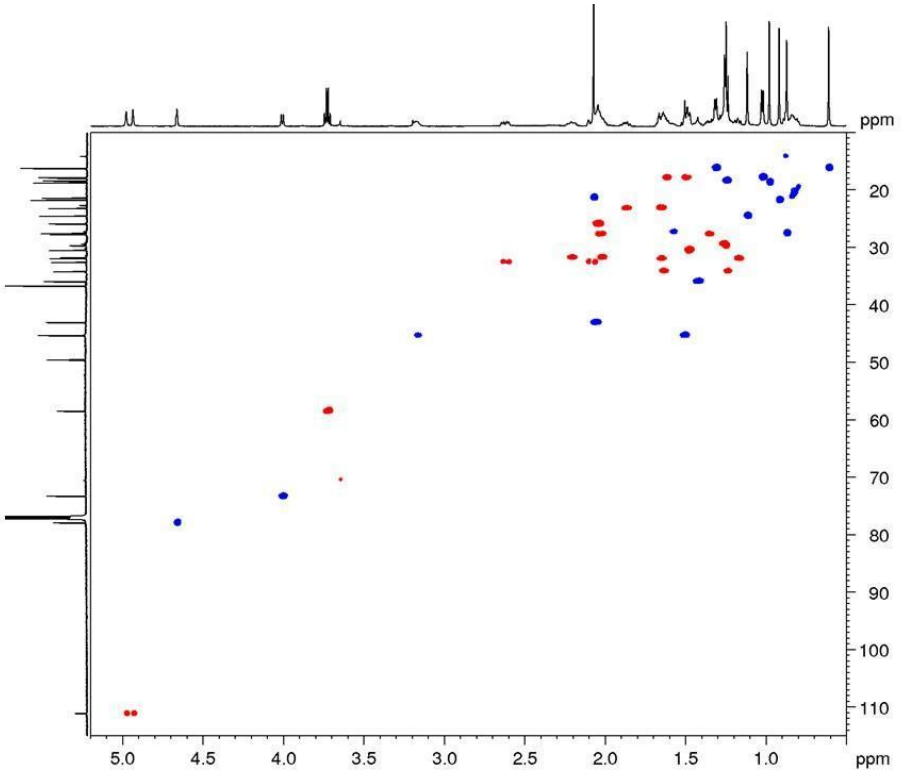

Figure A94. DEPT-edited HSQC spectrum of **BGS-11** (600 MHz, $CDCl_3$, 295 K)

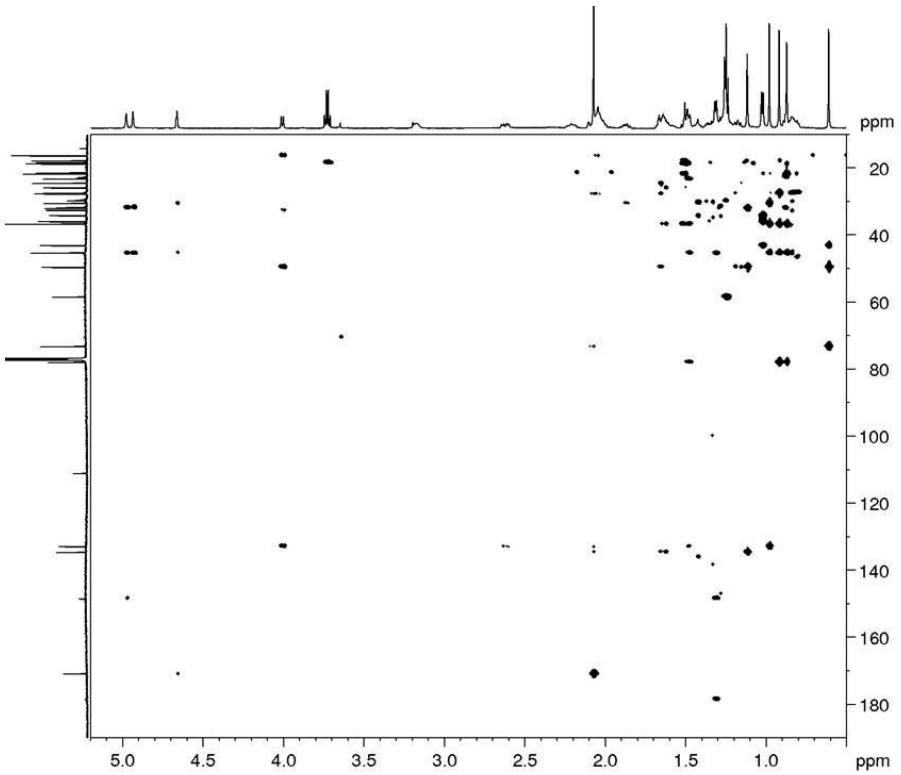

Figure A95. HMBC spectrum of **BGS-11** (600 MHz, $CDCl_3$, 295 K)

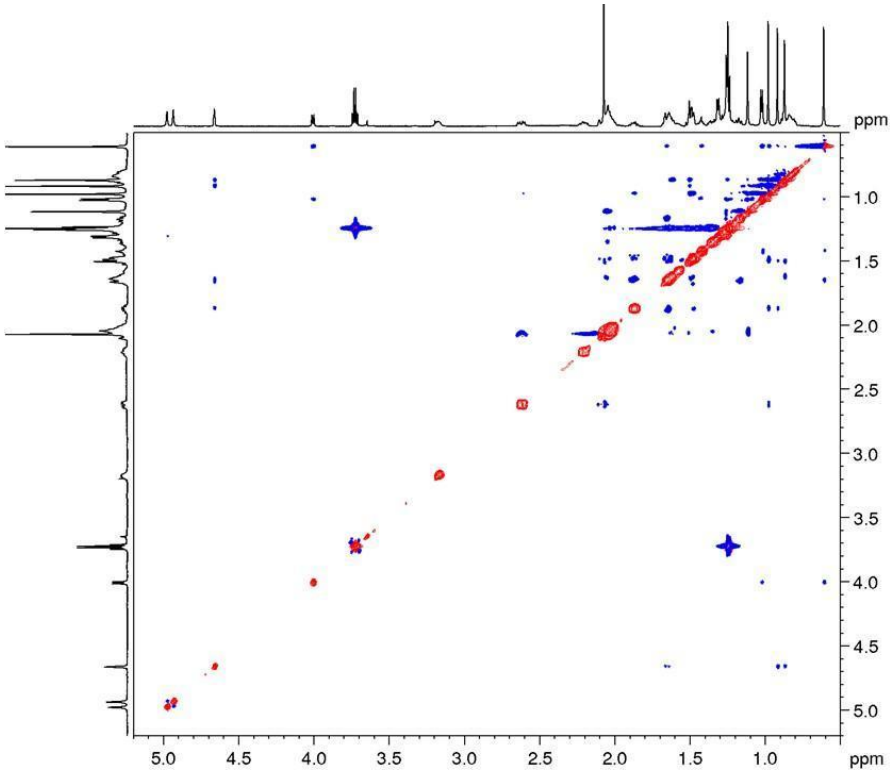

Figure A96. NOESY spectrum of **BGS-11** (600 MHz, $CDCl_3$, 295 K)

Spectra and spectral data on BGS-12

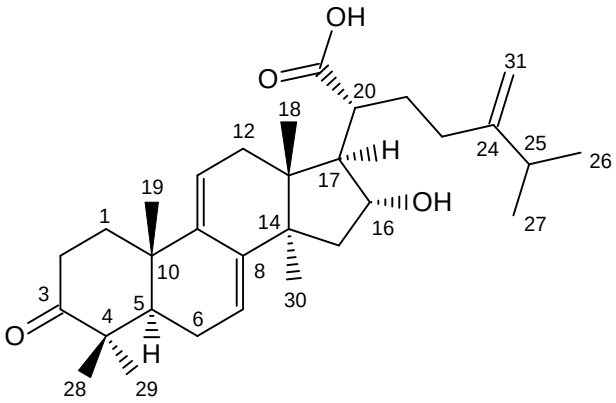

HRMS (+) *m/z* 483.3461 $[M+H]^+$ (483.3469 calcd. for $C_{31}H_{47}O_4$; Δ -1.6 ppm); HRMSMS (CID = 15%, 30%, 45%) 465.3354, 309.2205

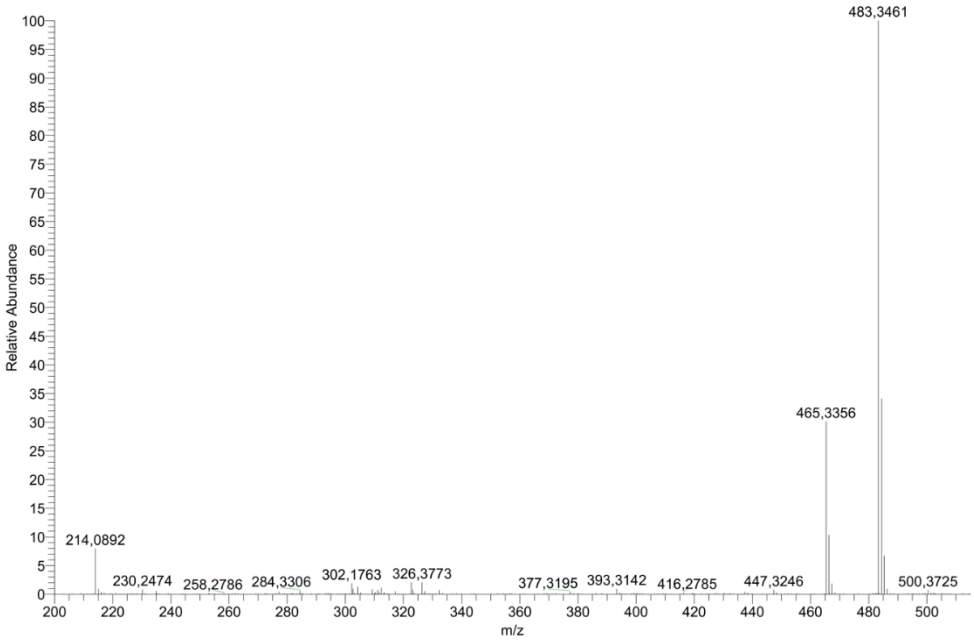

Figure A97. HRMS spectrum of **BGS-12**

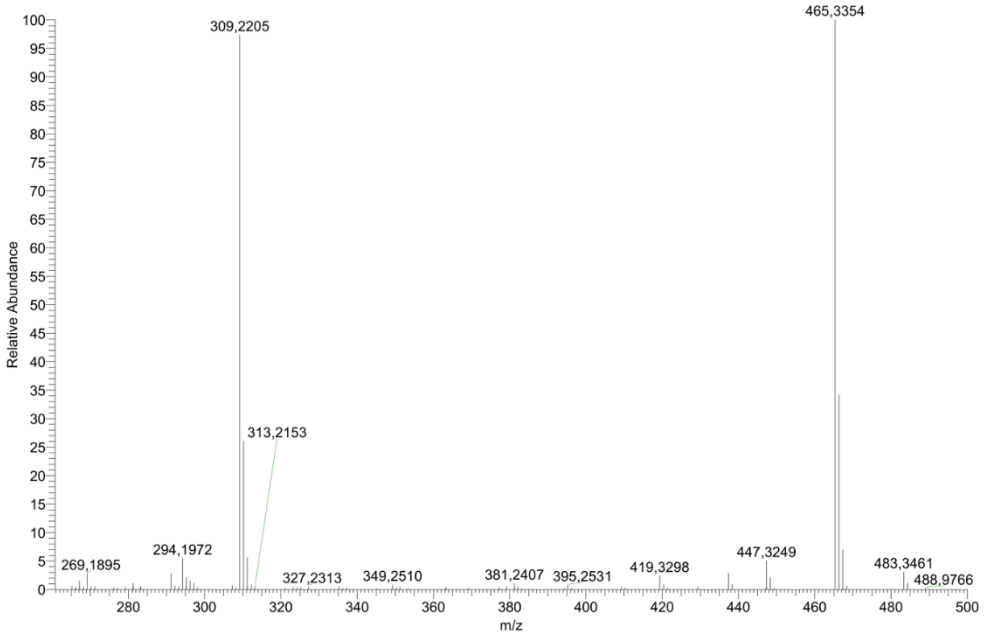

Figure A98. MS-MS spectrum of **BGS-12**

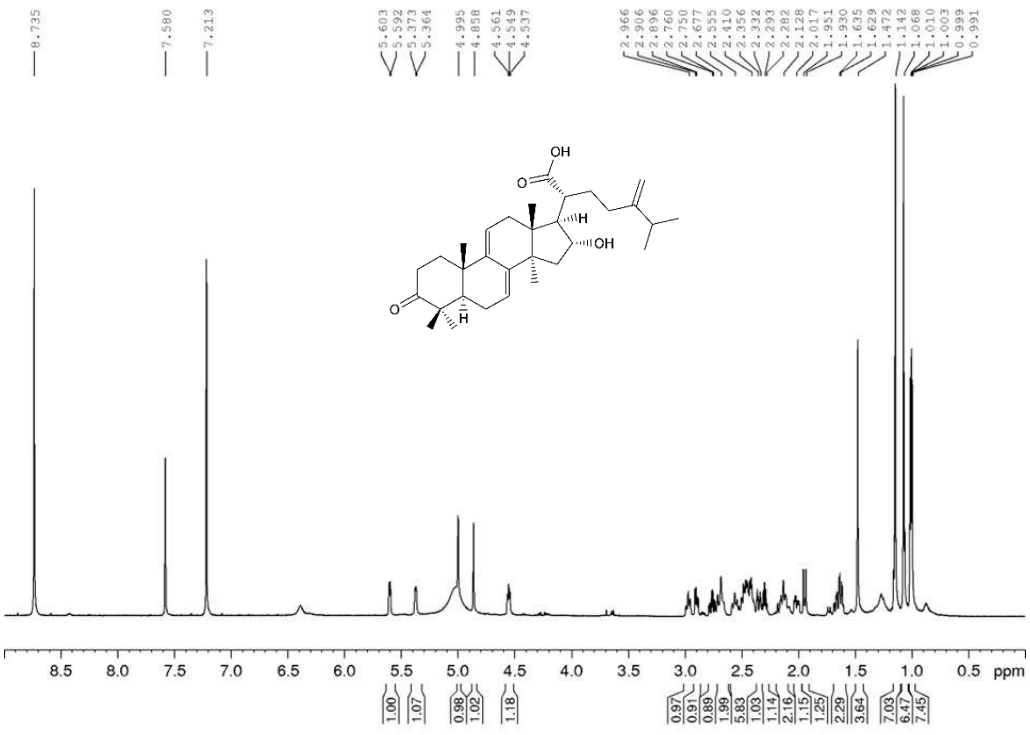

Figure A99. ^{1}H spectrum of **BGS-12** (600 MHz, pyridine-d_5, 295 K)

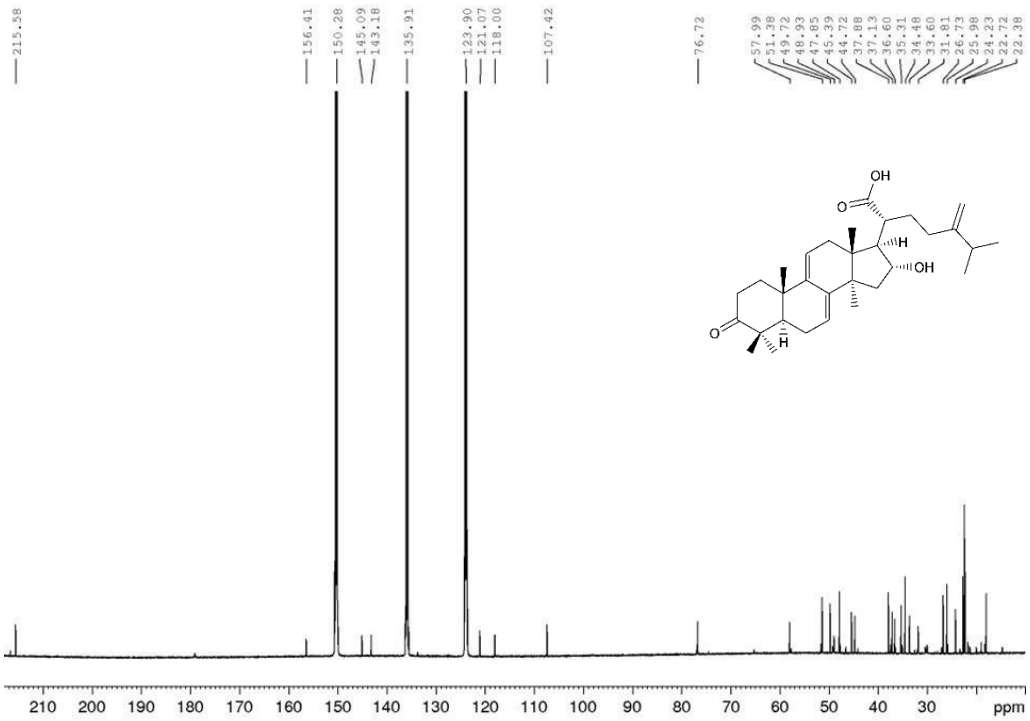

Figure A100. ^{13}C spectrum of **BGS-12** (150 MHz, pyridine-d_5, 295 K)

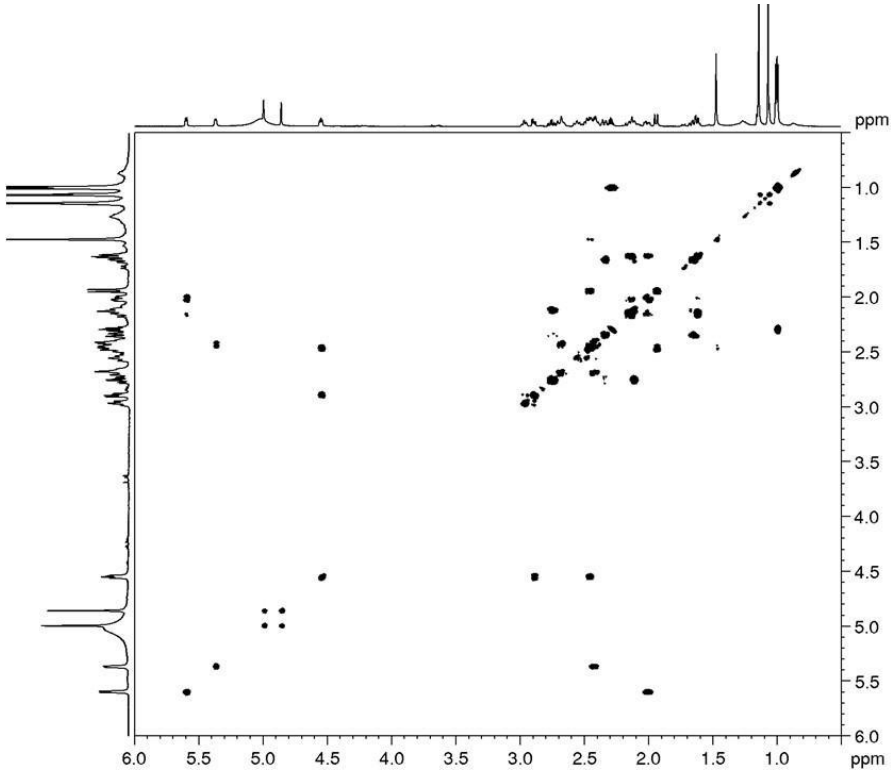

Figure A101. COSY spectrum of **BGS-12** (600 MHz, pyridine-d_5, 295 K)

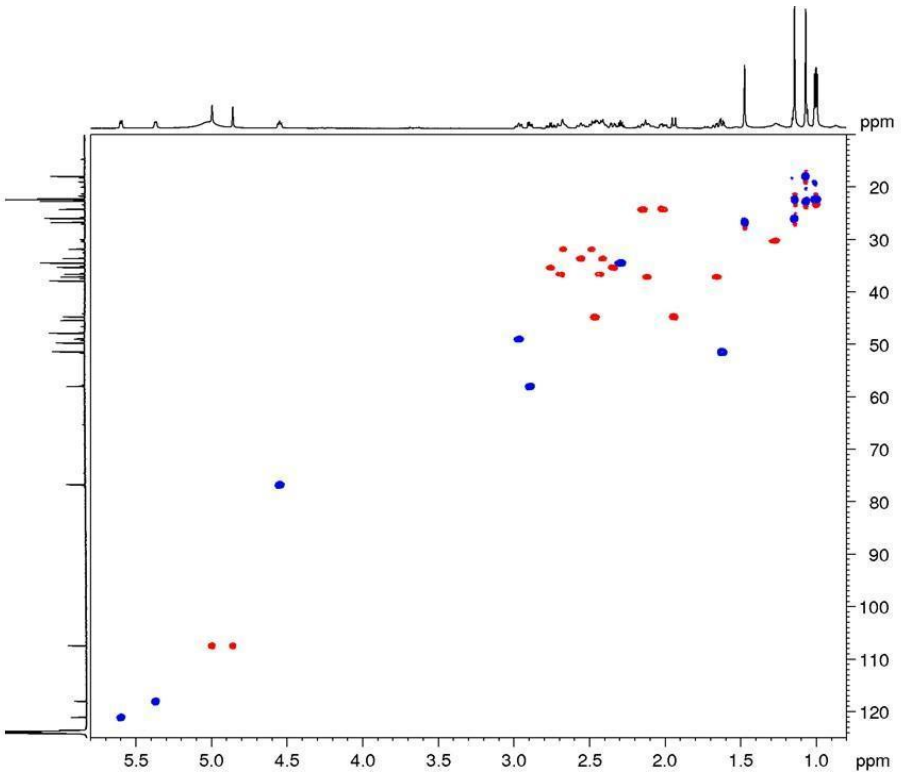

Figure A102. DEPT-edited HSQC spectrum of **BGS-12** (600 MHz, pyridine-d_5, 295 K)

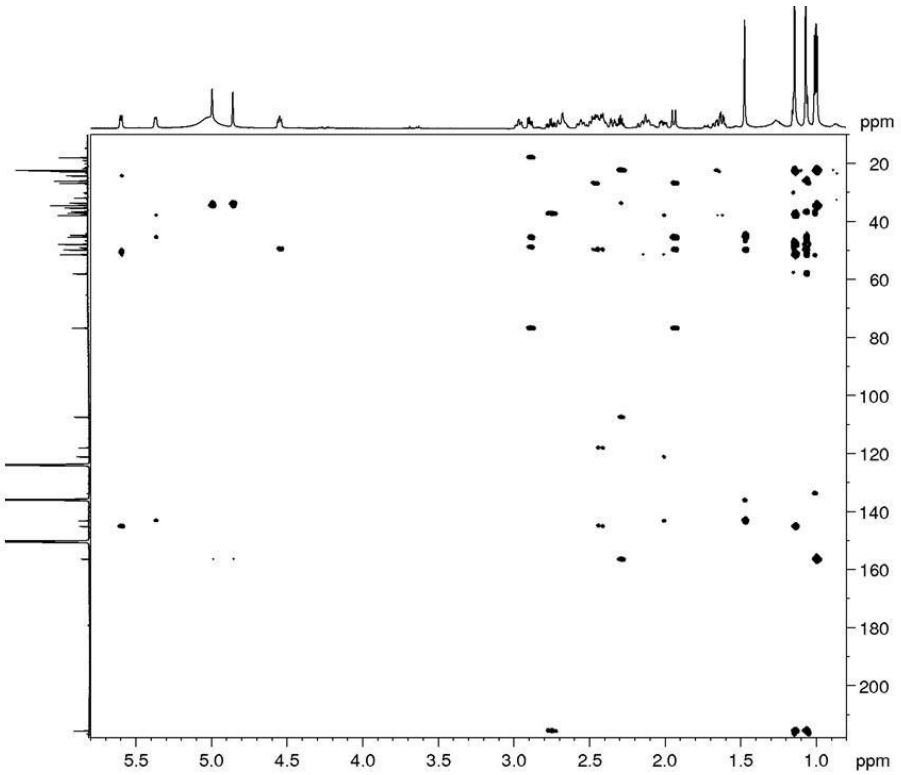

Figure A103. HMBC spectrum of **BGS-12** (600 MHz, pyridine-d_5, 295 K)

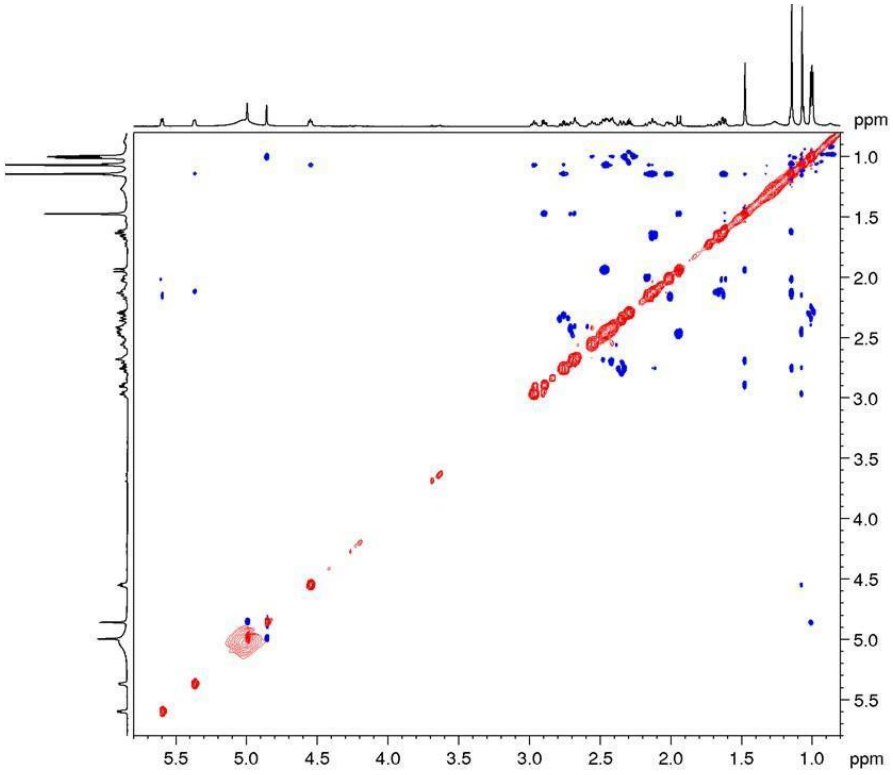

Figure A104. NOESY spectrum of **BGS-12** (600 MHz, pyridine-d_5, 295 K)

Table A1. NMR Spectroscopic Data (600 MHz, $CDCl_3$[a], pyridine-d_5[b], tetrahydrofuran-d_8[c], or methanol-d:pyridine-d_5 19:1[d], methanol-d[e]) for **BGS-6-9**

	1[c]			**2**[c]			**3**[a]			**4**[a]			**5**[b]		
position	δ_C type		δ_H (*J* in Hz)	δ_C type		δ_H (*J* in Hz)	δ_C type		δ_H (*J* in Hz)	δ_C type		δ_H (*J* in Hz)	δ_C type		δ_H (*J* in Hz)
1	35.7	CH_2	1.82, m 1.54, m	36.4	CH_2	1.51, m 1.09, m	30.7	CH_2	1.43, m 1.37, m	30.6	CH_2	1.49, m 1.41, m	31.6	CH_2	1.75, m 1.55, m
2	36.8	CH_2	2.31, dd, (10.0, 8.0) 2.28, dd, (8.0, 3.4)	28.8	CH_2	1.48, m	23.1	CH_2	1.87, m 1.67, m	23.2	CH_2	1.90, m 1.72, m	24.1	CH_2	1.90, m 1.78, m
3	216.0	C		78.3	CH	2.97, m	77.6	CH	4.68, br s	80.6	CH	4.76, br s	78.4	CH	4.97, br s
4	52.8	C		39.7	C		36.7	C		36.8	C		37.4	C	
5	44.3	CH	2.17, m	51.5	CH	0.96, m	45.2	CH	1.50, m	45.3	CH	1.47, m	46.4	CH	1.83, m
6	20.2	CH_2	1.49, m 1.44, m	19.1	CH_2	1.65, m 1.49, m	17.8	CH_2	1.67, m 1.56, m	18.0	CH_2	1.59, m 1.49, m	18.8	CH_2	1.62, m 1.52, m
7	27.2	CH_2	2.03, m 1.93, m	27.2	CH_2	2.06, m 1.95, m	25.8	CH_2	2.12, m 2.07, m	25.9	CH_2	2.04, m	26.8	CH_2	2.17, m 2.12, m
8	136.6	C		135.8	C		135.0	C		134.2	C		135.5	C	
9	134.0	C		136.6	C		135.1	C		134.3	C		134.2	C	
10	37.6	C		37.8	C		36.7	C		36.8	C		37.5	C	
11	21.4	CH_2	1.94, m	40.5	CH_2	2.82, m 2.49, m	39.9	CH_2	2.90, m 2.71, m	20.9	CH_2	2.01, m	34.9	CH_2	2.76, m 2.50, m
12	30.0	CH_2	1.71, m 1.39, m	210.5	C		212.7	C		30.9	CH_2	1.74, m 1.69, m	72.5	CH	4.27, d (7.6)
13	46.5	C		55.0	C		54.5	C		44.5	C		50.5	C	
14	49.4	C		60.0	C		59.4	C		49.9	C		50.4	C	
15	44.0	CH_2	2.03, m 1.15, m	30.9	CH_2	1.75, m 1.20, m	30.1	CH_2	1.82, m 1.35, m	30.8	CH_2	1.60, m 1.18, m	33.1	CH_2	1.76, m 1.25, m
16	77.1	CH	3.89, m	28.6	CH_2	1.91, m 1.29, m	27.8	CH_2	2.01, m 1.37, m	28.2	CH_2	1.94, m 1.31, m	28.7	CH_2	2.11, m 1.40, m
17	57.3	CH	1.96, m	43.5	CH	2.06, m	42.4	CH	2.19, m	50.3	CH	1.50, m	43.5	CH	2.65, m
18	17.8	CH_3	0.69, s	12.9	CH_3	0.94, s	12.6	CH_3	1.05, s	15.7	CH_3	0.69, s	17.2	CH_3	0.77, s
19	19.2	CH_3	0.95, s	19.5	CH_3	0.98, s	19.0	CH_3	1.08, s	18.9	CH_3	1.00, s	19.4	CH_3	1.03, s
20	48.3	CH	2.24, m	37.7	CH	1.18, m	36.6	CH	1.27, m	36.3	CH	1.41, m	37.3	CH	1.53, m

21	177.4	C		19.6	CH_3	0.78, d (6.4)	19.0	CH_3	0.89, d (5.8)	18.6	CH_3	0.93, m	18.3	CH_3	1.28, m
22	31.6	CH_2	1.92, m 1.64, m	35.3	CH_2	1.53, m 1.14, m	34.0	CH_2	1.62, m 1.27, m	34.2	CH_2	1.58, m 1.19, m	35.4	CH_2	1.77, m 1.38, m
23	33.4	CH_2	1.96, m 1.87, m	32.9	CH_2	2.14, m 1.09, m	32.1	CH_2	2.21 2.02	31.7	CH_2	2.19, m 2.00, m	32.7	CH_2	2.37, m 2.17, m
24	156.7	C		150.9	C		148.5	C		148.3	C		150.2	C	
25	34.8	CH	2.14, m	46.2	CH	2.96, m	45.1	CH	3.17, m	45.0	CH	3.18, q (7.0)	46.2	CH	3.32, q (7.1)
26	22.4	CH_3	0.91, d (6.9)	175.6	C		177.7	C		179.6	C		175.3	C	
27	22.2	CH_3	0.92, d (6.9)	17.0	CH_3	1.10, d (7.4)	16.3	CH_3	1.31, d (6.7)	16.1	CH_3	1.31, d (7.0)	17.1	CH_3	1.38, d (7.1)
28	68.3	CH_2	3.39, dd (10.2, 2.4) 3.16, dd (10.2, 2.4)	28.5	CH_3	0.88, s	27.5	CH_3	0.88, s	27.6	CH_3	0.88, s	28.5	CH_3	1.04, s
29	17.5	CH_3	0.78, s	16.1	CH_3	0.69, s	21.7	CH_3	0.94, s	21.7	CH_3	0.93, m	22.4	CH_3	0.91, s
30	25.3	CH_3	1.05, s	24.3	CH_3	0.65, s	24.1	CH_3	0.82, s	24.2	CH_3	0.91, s	25.7	CH_3	1.43, s
31	106.9	CH_2	4.61, br s	110.3	CH_2	4.77, br s 4.71, br s	111.1	CH_2	4.97, br s 4.94, br s	111.4	CH_2	4.97, br s 4.94, br s	111.3	CH_2	5.10, br s 5.06, br s
1’							170.8	C		167.2	C		172.4[d]	C	
2’										40.2	CH_2	3.64, m	47.0[d]	CH_2	2.64[d], m
3’										170.6	C		71.0[d]	C	
4’													47.0[d]	CH_2	2.64[d], m
5’													172.4[d]	C	
1’-CH_3							21.3	CH_3	2.07, s						
3’-CH_3													27.9[d]	CH_3	1.37[d], m
26-CH_3													52.3[d]	CH_3	3.67[d], m

Table A2. NMR Spectroscopic Data (600 MHz, $CDCl_3$[a], pyridine-d_5[b], tetrahydrofuran-d_8[c], or methanol-d:pyridine-d_5 19:1[d], methanol-d[e]) for **BGS-10-12**

	10[b]			**11**[a]			**12**[b]		
position	δ_C type		δ_H (J in Hz)	δ_C type		δ_H (J in Hz)	δ_C type		δ_H (J in Hz)
1	31.1	CH_2	2.14, m	30.5	CH_2	1.48, m	37.1	CH_2	2.12, m 1.66, m
2	27.4	CH_2	2.05, m 1.82, m	23.2	CH_2	1.87, m 1.65, m	35.3	CH_2	2.75, m 2.34, m
3	75.5	CH	3.66, br s	77.9	CH	4.66, br s	215.6	C	
4	38.6	C		36.7	C		47.9	C	
5	45.1	CH	2.08, m	45.3	CH	1.50, m	51.4	CH	1.62, m
6	19.1	CH_2	1.74, m 1.61, m	17.9	CH_2	1.62, m 1.50, m	24.2	CH_2	2.15, m 2.01, m
7	27.0	CH_2	2.15, m	25.9	CH_2	2.04, m	121.1	CH	5.60, d (6.4)
8	135.3	C		134.6	C		143.2	C	
9	134.7	C		132.9	C		145.1	C	
10	37.8	C		36.7	C		37.9	C	
11	35.1	CH_2	2.81, m 2.52, m	32.6	CH_2	2.62, m 2.09, m	118.0	CH	5.37, d (6.0)
12	72.5	CH	4.28, d (7.5)	73.2	CH	4.00, d (8.0)	36.6	C	2.69, m 2.43, m
13	50.5	C		49.5	C		45.4	C	
14	50.4	C		49.6	C		49.7	C	

15	33.1	CH_2	1.76, m	32.0	CH_2	1.65, m 1.17, m	44.7	CH_2	2.46, m 1.94, m	
16	28.8	CH_2	2.14, m 1.43, m	27.7	CH_2	2.02, m 1.35, m	76.7	CH	4.55, m	
17	43.6	CH	2.68, m	43.1	CH	2.06, m	58.0	CH	2.89, m	
18	17.2	CH_3	0.79, s	16.2	CH_3	0.61, s	18.0	CH_3	1.07, s	
19	19.7	CH_3	1.11, s	18.7	CH_3	0.98, s	22.4	CH_3	1.14, s	
20	37.3	CH	1.58, m	35.9	CH	1.42, m	48.9	CH	2.97, m	
21	18.4	CH	1.31, d (6.1)	17.8	CH_3	1.02, d (6.4)	179.1	C		
22	35.5	CH_2	1.89, m 1.51, m	34.2	CH_2	1.63, m 1.24, m	31.8	CH_2	2.67, m 2.49, m	
23	32.9	CH_2	2.60, m 2.34, m	31.8	CH_2	2.21, m 2.02, m	33.6	CH_2	2.56, m 2.41, m	
24	151.1	C		148.5	C		156.4	C		
25	46.9	CH	3.51, m	45.3	CH	3.18, m	34.5	CH	2.29, m	
26	177.4	C		178.5	C		22.2	CH_3	1.00, d (6.8)	
27	17.5	CH_3	1.54, d (6.7)	16.2	CH_3	1.31, d (6.9)	22.2	CH_3	1.00, d (6.8)	
28	29.5	CH_3	1.26, s	27.6	CH_3	0.87, s	26.0	CH_3	1.14, s	
29	23.1	CH_3	0.97, s	21.8	CH_3	0.92, s	22.7	CH_3	1.07, s	
30	25.6	CH_3	1.43, s	24.5	CH_3	1.12, s	26.7	CH_3	1.47, s	
31	110.8	CH_2	5.25, br s 5.13, br s	111.1	CH_2	4.98, br s 4.94, br s	107.4	CH_2	5.00, br s 4.86, br s	
1’				170.9	C					
1’-CH_3				21.4	CH_3	2.07, m				

Spectra and spectral data on **XB-1**

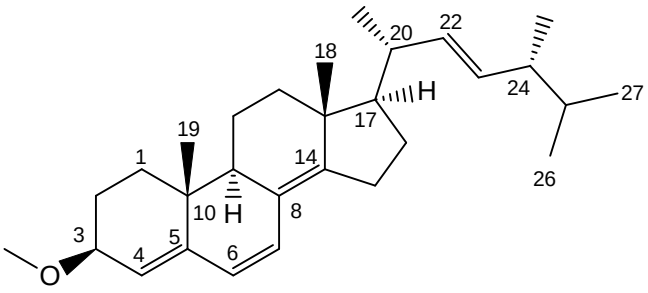

3β-methoxy-ergosta-6,8[14],22-trien (**XB-1**): amorphous solid; α_D^{25} -10.0 (*c* 0.09, $CHCl_3$, 25.5 °C); HRMS *m/z* 377,3192 $[M+H-CH_3OH]^+$ (Δ 2.2 ppm; $C_{28}H_{41}$); HRMSMS (CID = 15%, 30%, 45%; rel int %) *m/z* 293, 251

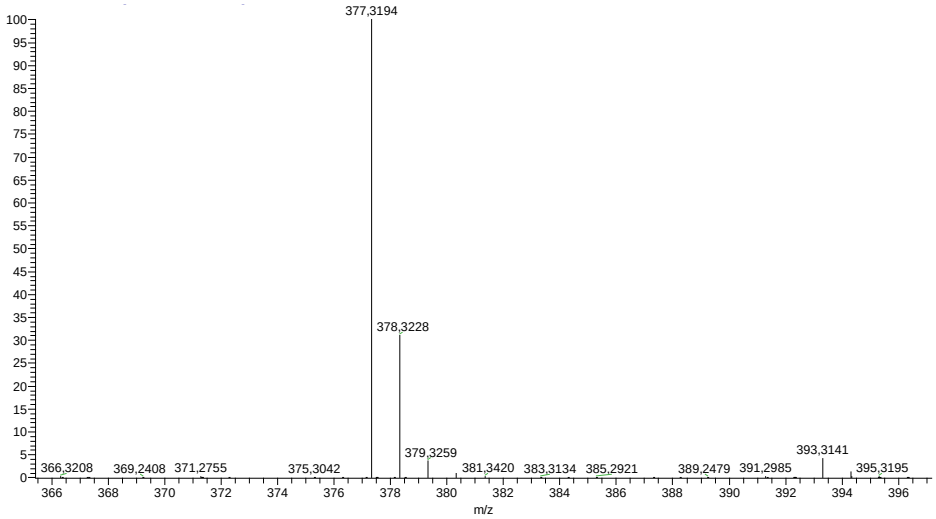

Figure A105. HRMS spectrum of **XB-1**

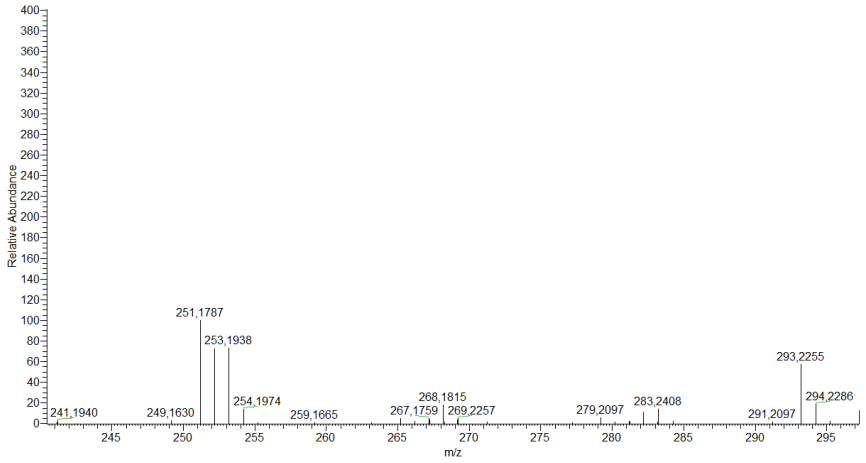

Figure A106. MS-MS spectrum of **XB-1**

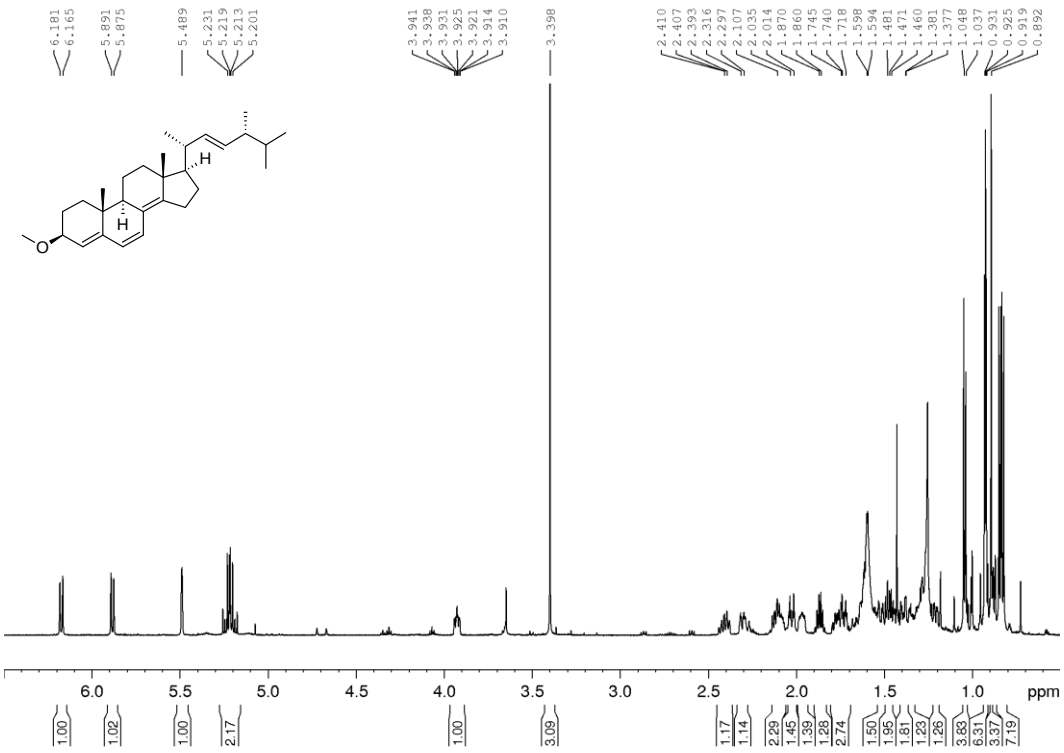

Figure A107. ^{1}H spectrum of **XB-1** (600 MHz, $CDCl_3$, 295 K)

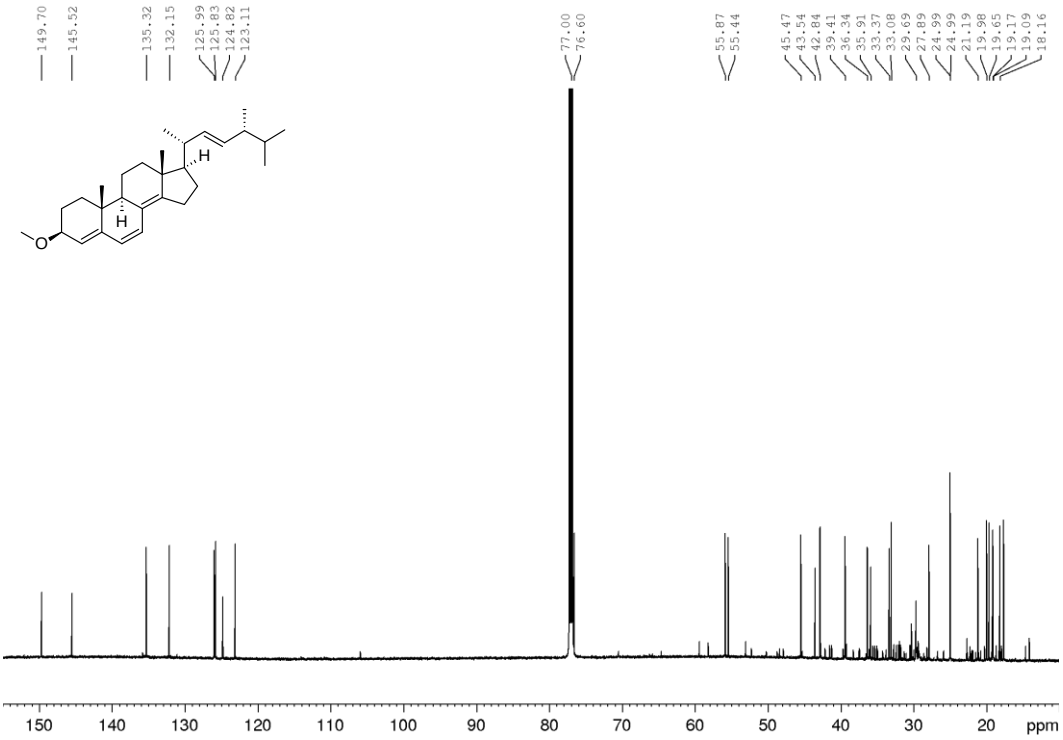

Figure A108. ^{13}C spectrum of **XB-1** (150 MHz, $CDCl_3$, 295 K)

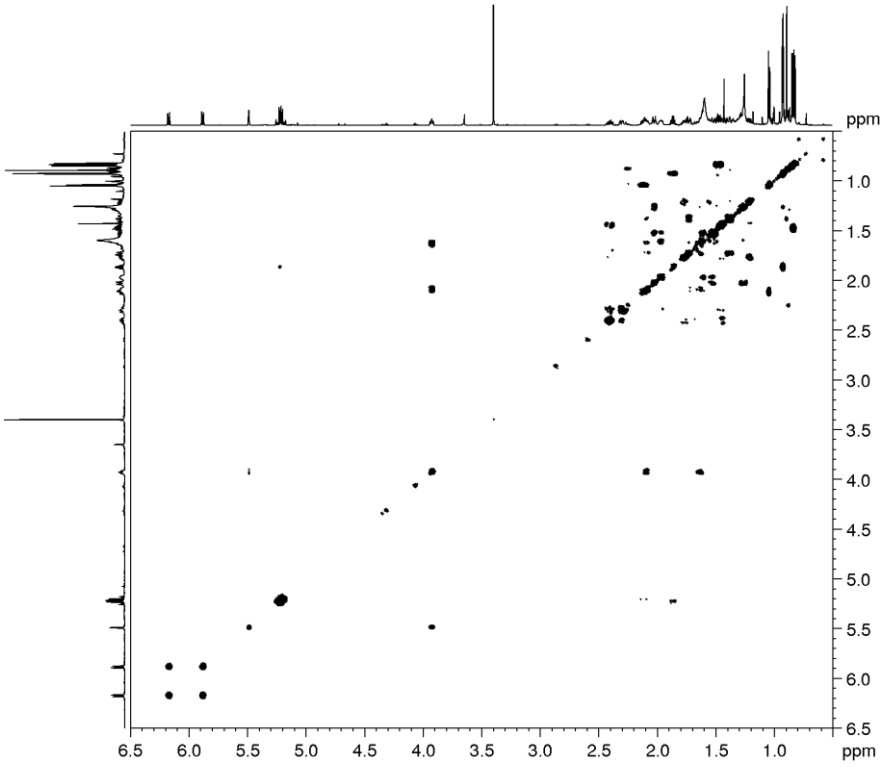

Figure A109. COSY spectrum of **XB-1** (600 MHz, $CDCl_3$, 295 K)

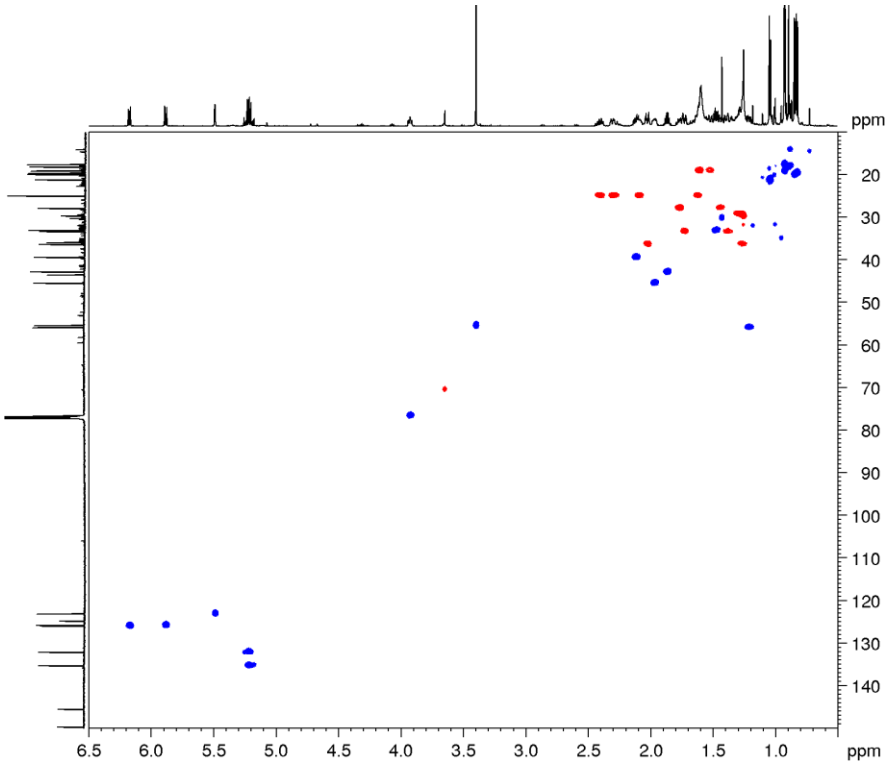

Figure A110. DEPT-edited HSQC spectrum of **XB-1** (600 MHz, $CDCl_3$, 295 K)

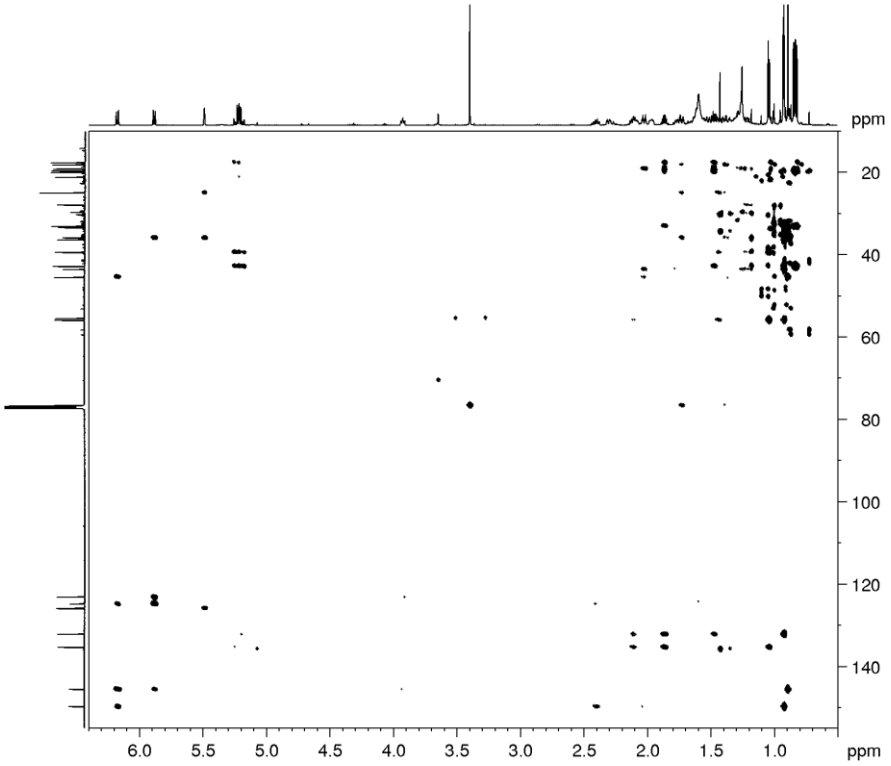

Figure A111. HMBC spectrum of **XB-1** (600 MHz, $CDCl_3$, 295 K)

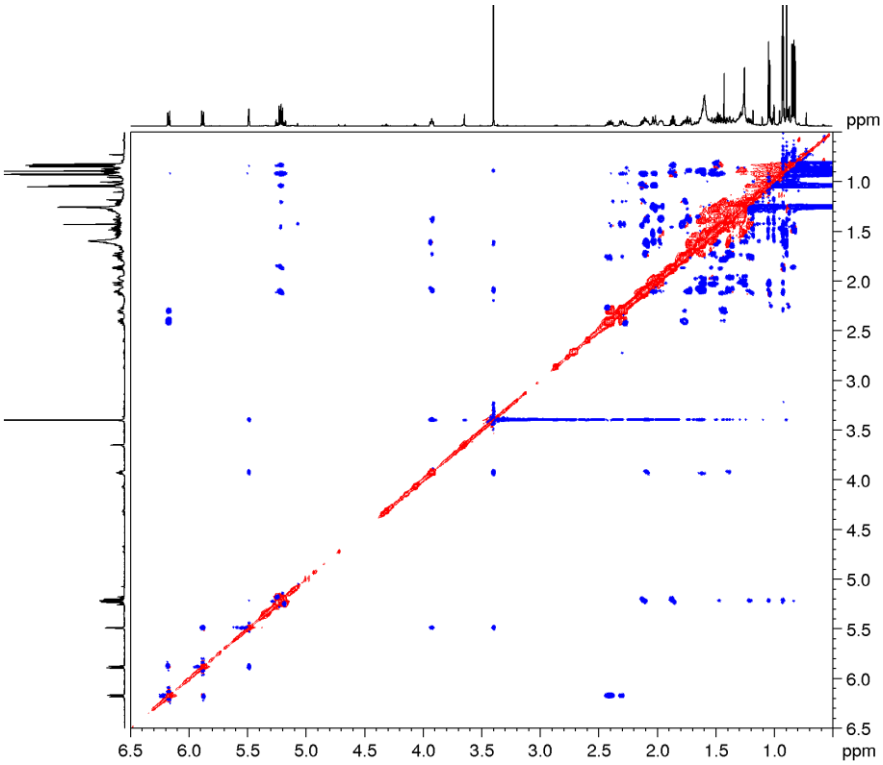

Figure A112. ROESY spectrum of **XB-1** (600 MHz, $CDCl_3$, 295 K)

Spectra and spectral data on **XB-2**

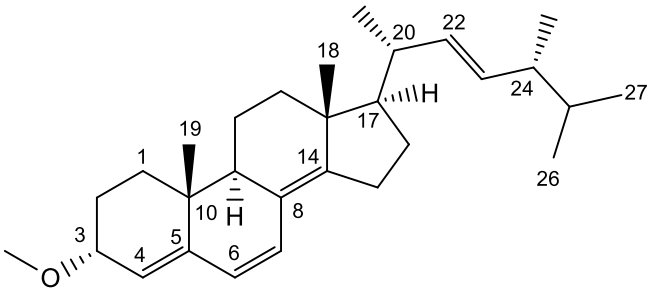

3α-methoxy-ergosta-6,8[14],22-trien (**XB-2**): amorphous solid;α_D^{25}+87.8 (*c* 0.42, $CHCl_3$, 25.4 °C); HRMS *m/z* 377,3194 $[M+H-CH_3OH]^+$ (Δ 2.2 ppm; $C_{28}H_{41}$); HRMSMS (CID = 15%, 30%, 45%; rel int %) *m/z* .293, 251

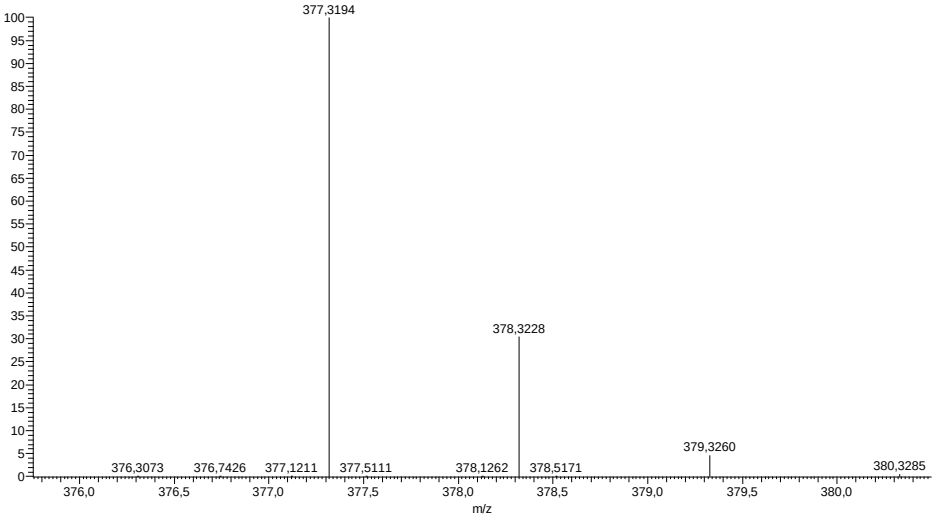

Figure A113. HRMS spectrum of **XB-2**

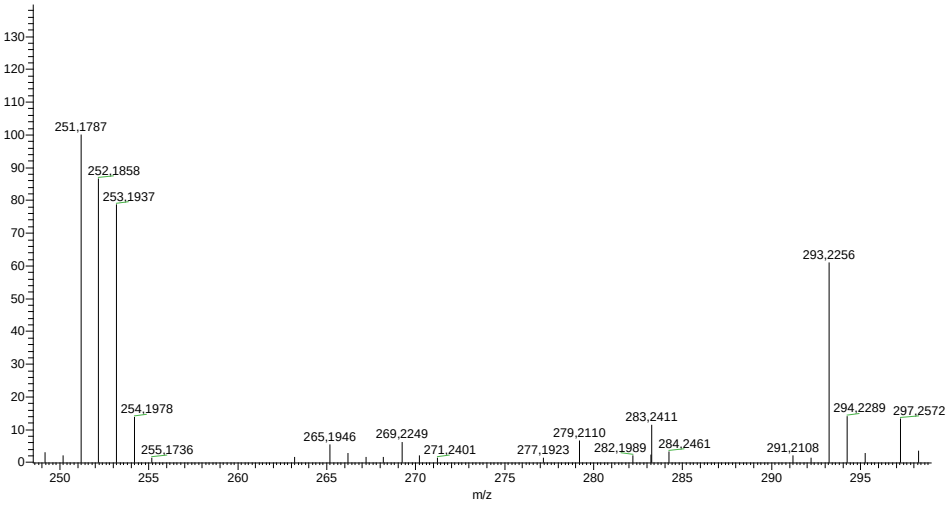

Figure A114. MS-MS spectrum of **XB-2**

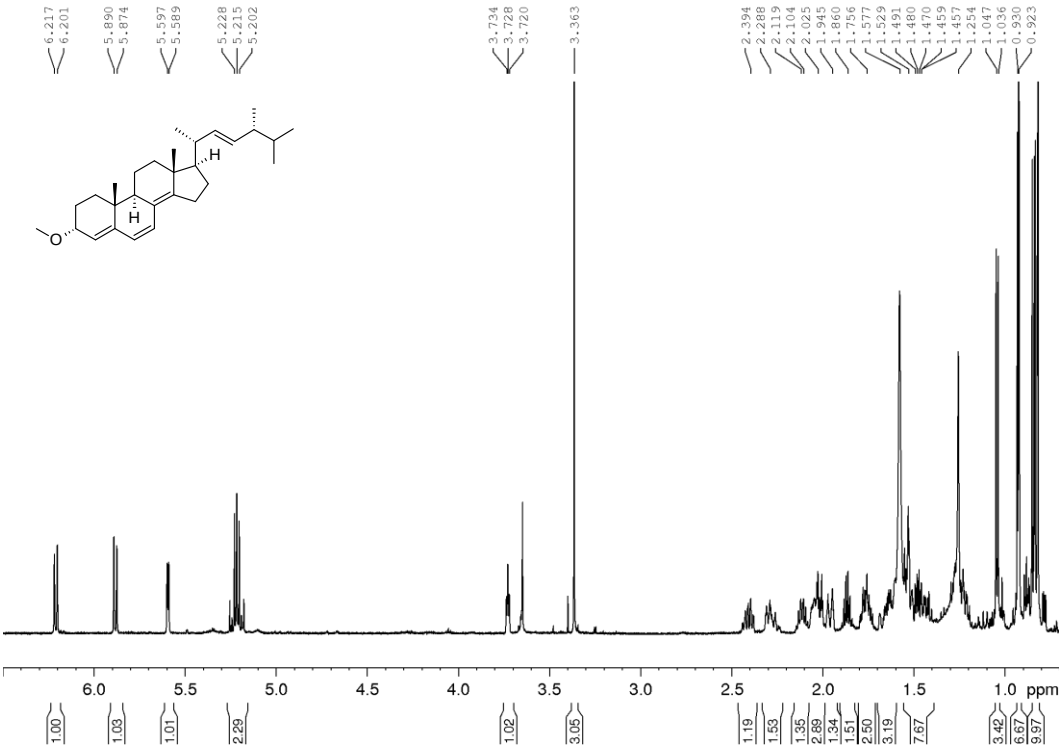

Figure A25. ^{1}H spectrum of **XB-2** (600 MHz, $CDCl_3$, 295 K)

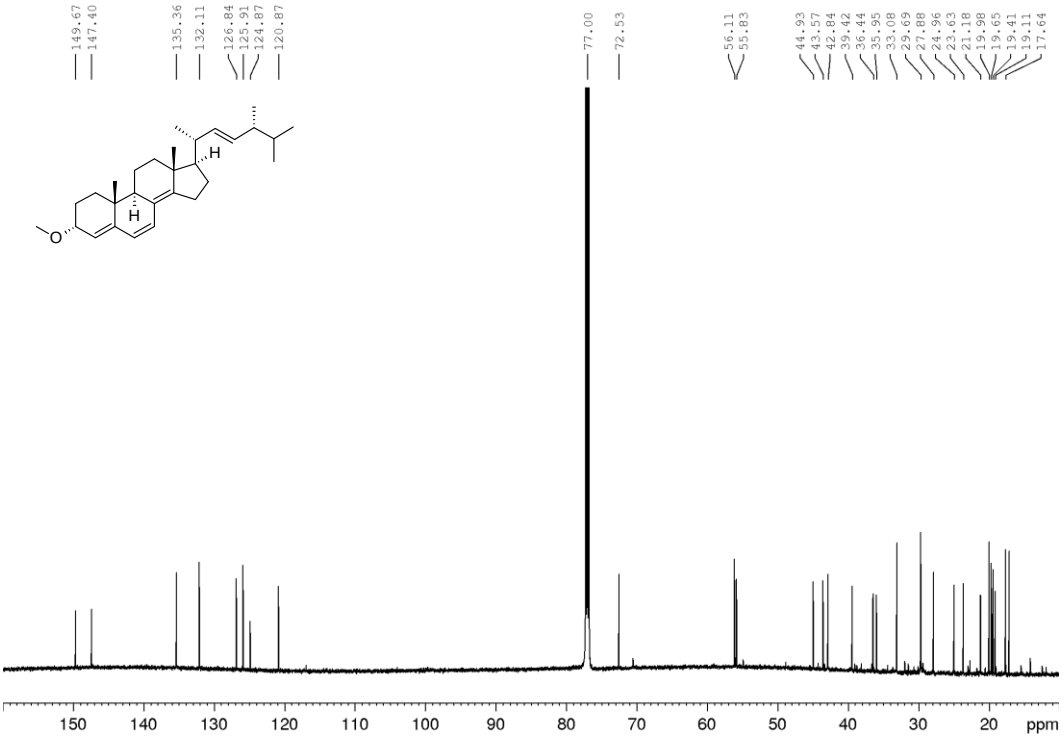

Figure A3. ^{13}C spectrum of **XB-2** (150 MHz, $CDCl_3$, 295 K)

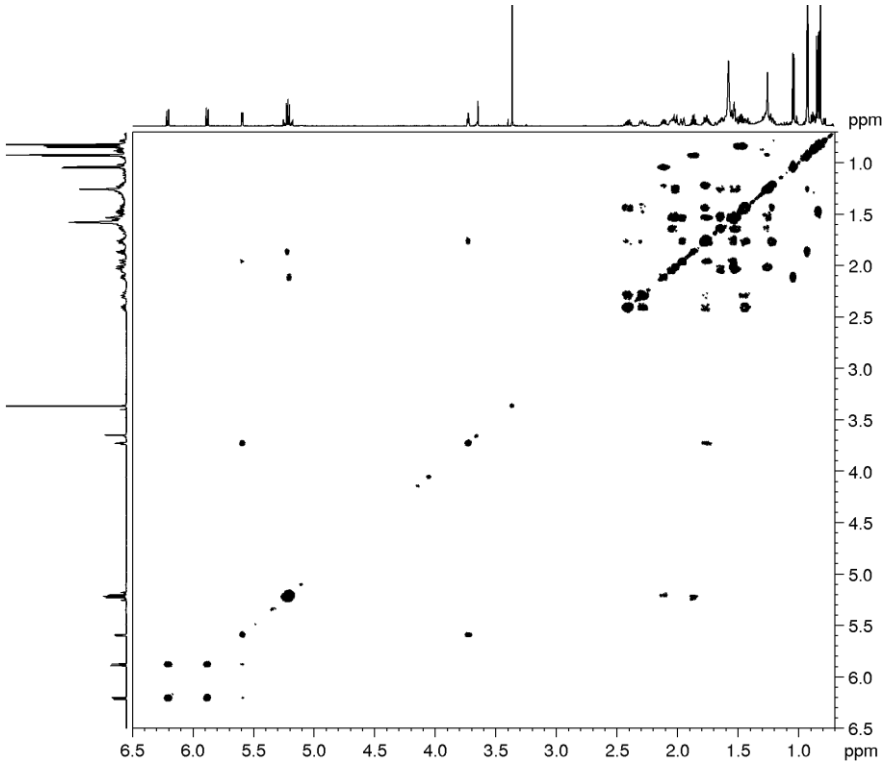

Figure A4. COSY spectrum of **XB-2** (600 MHz, $CDCl_3$, 295 K)

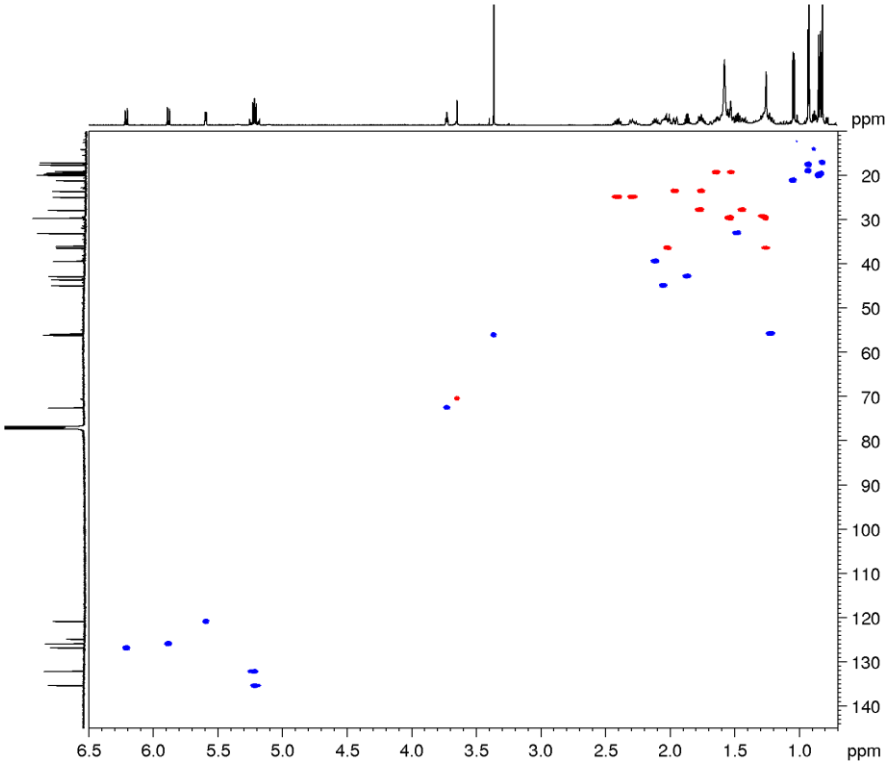

Figure A5. DEPT-edited HSQC spectrum of **XB-2** (600 MHz, $CDCl_3$, 295 K)

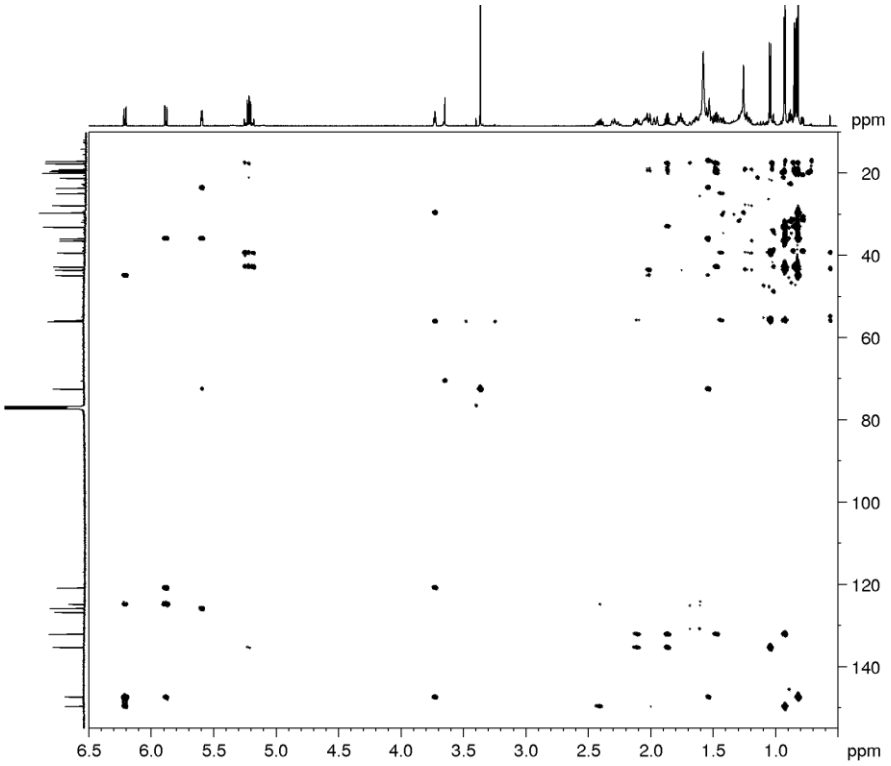

Figure A6. HMBC spectrum of **XB-2** (600 MHz, $CDCl_3$, 295 K)

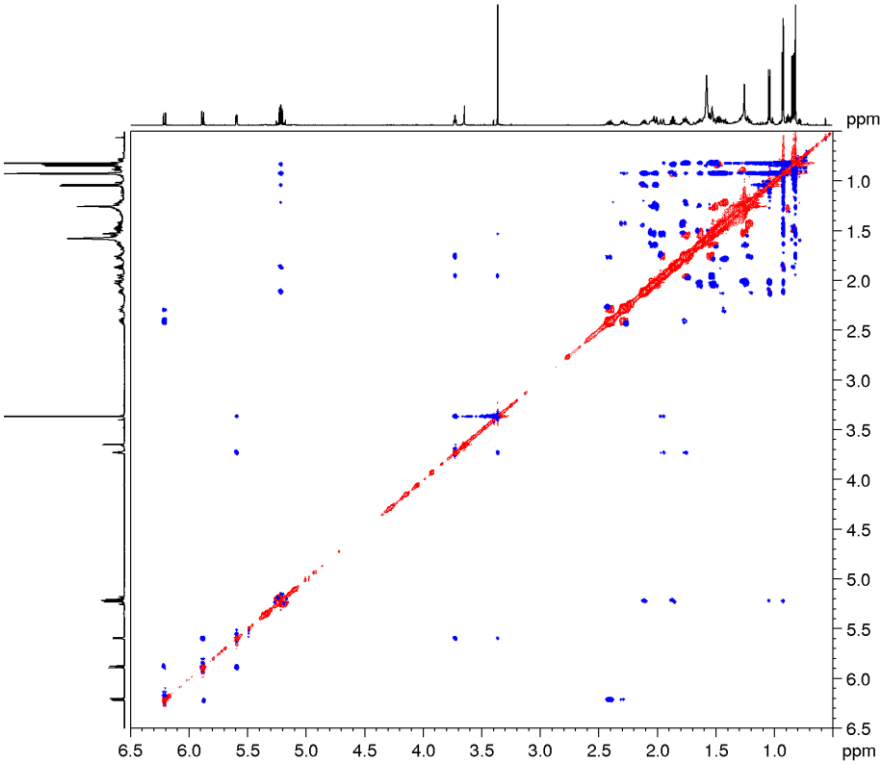

Figure A7. ROESY spectrum of **XB-2** (600 MHz, $CDCl_3$, 295 K)

Spectra and spectral data on **XB-3**

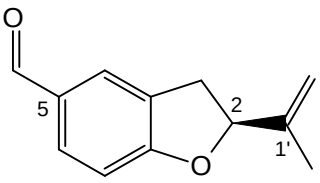

Fomannoxin (**XB-3**): amorphous solid; HRMS *m/z* 189.0906 $[M+H]^+$ (Δ 2.1 ppm; $C_{12}H_{13}O_2$); HRMSMS (CID = 15%, 30%, 45%; rel int %) *m/z* 161, 143, 133

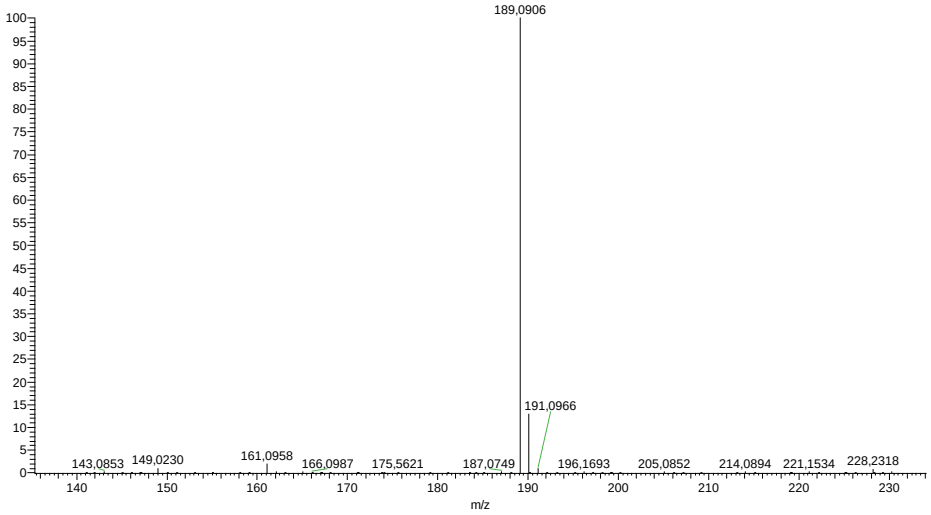

Figure A8. HRMS spectrum of **XB-3**

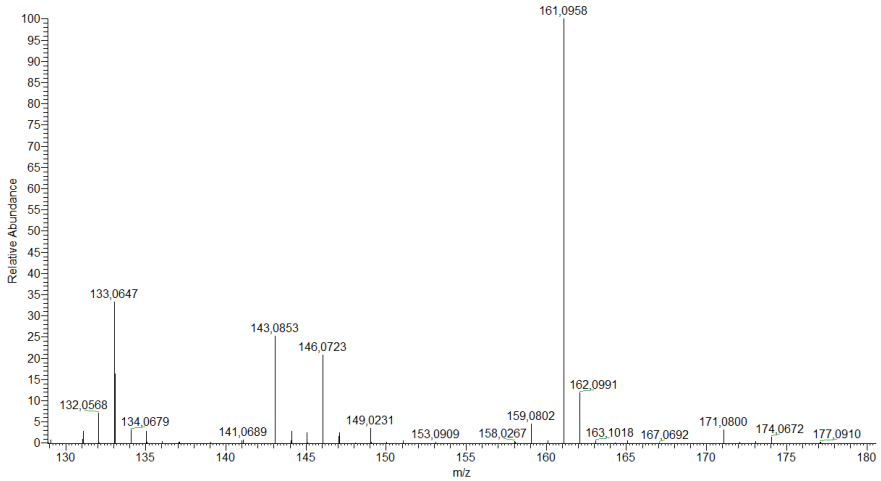

Figure A9. MS-MS spectrum of **XB-3**

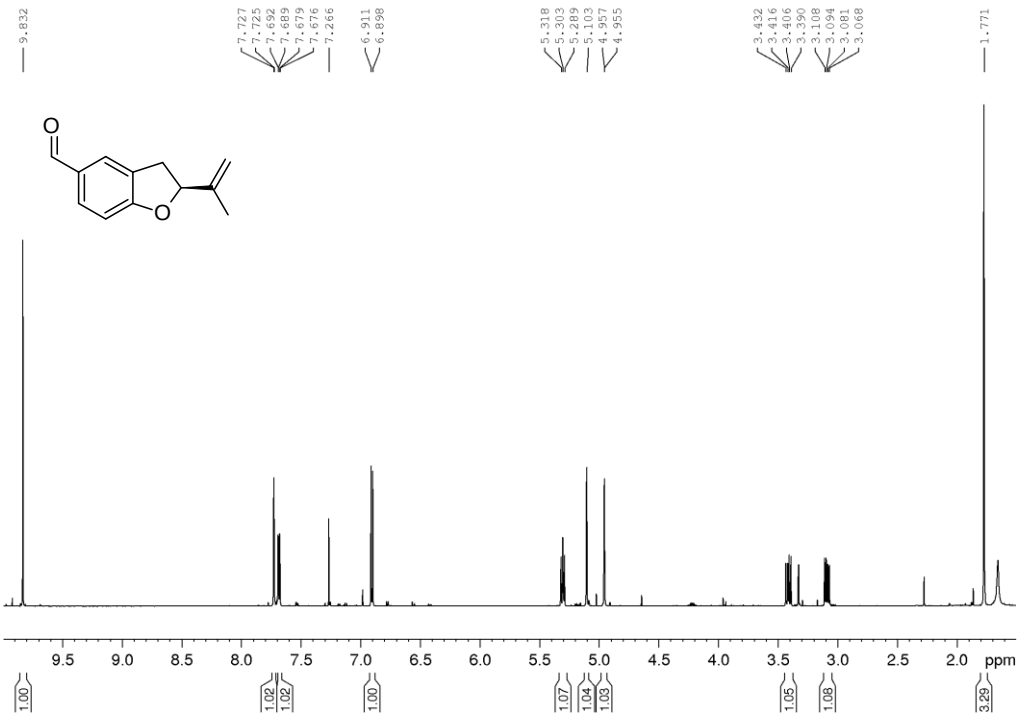

Figure A10. ^{1}H spectrum of **XB-3** (600 MHz, $CDCl_3$, 295 K)

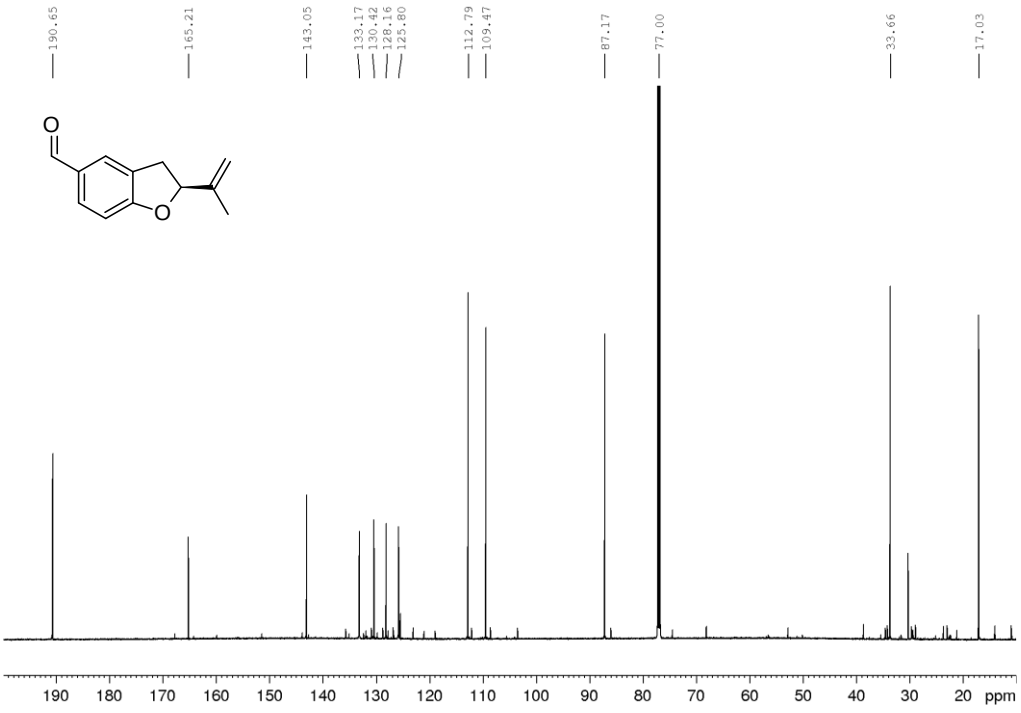

Figure A111. ^{13}C spectrum of **XB-3** (150 MHz, $CDCl_3$, 295 K)

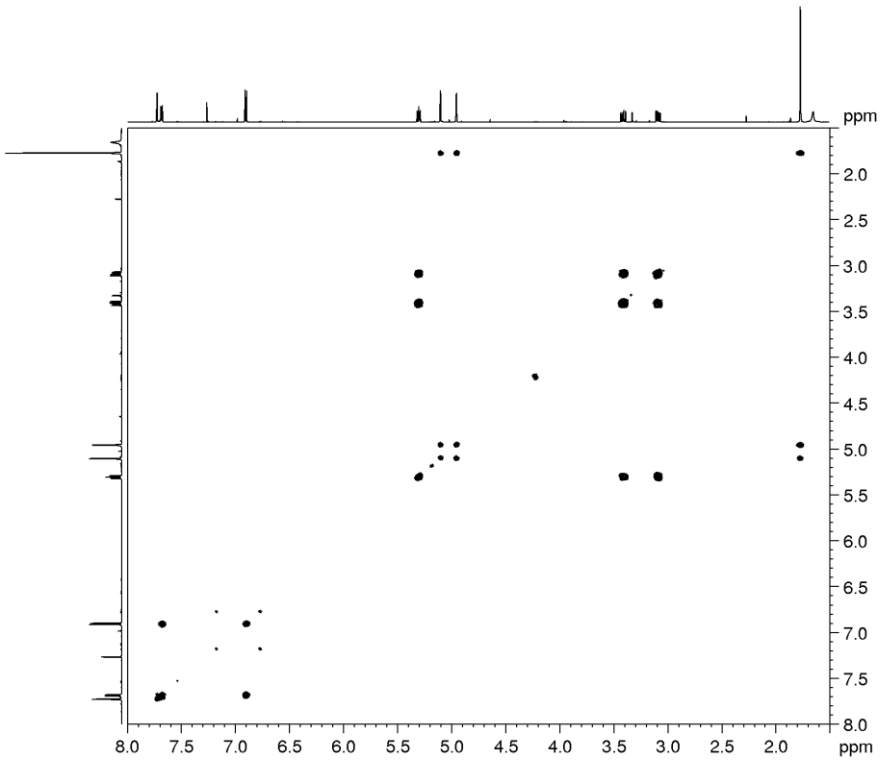

Figure A125. COSY spectrum of **XB-3** (600 MHz, $CDCl_3$, 295 K)

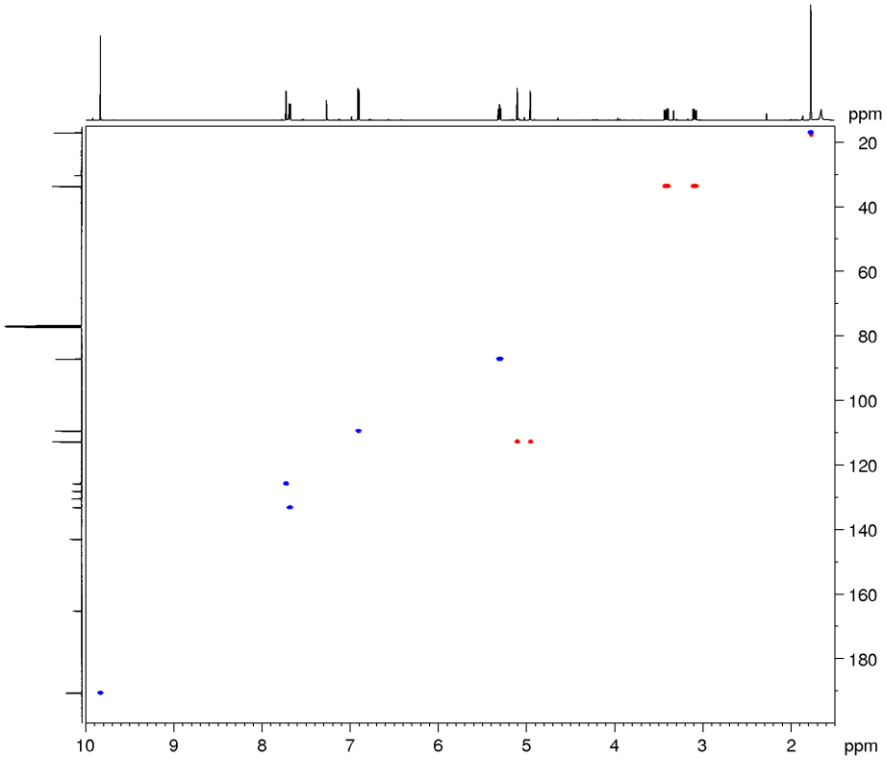

Figure A126. DEPT-edited HSQC spectrum of **XB-3** (600 MHz, $CDCl_3$, 295 K)

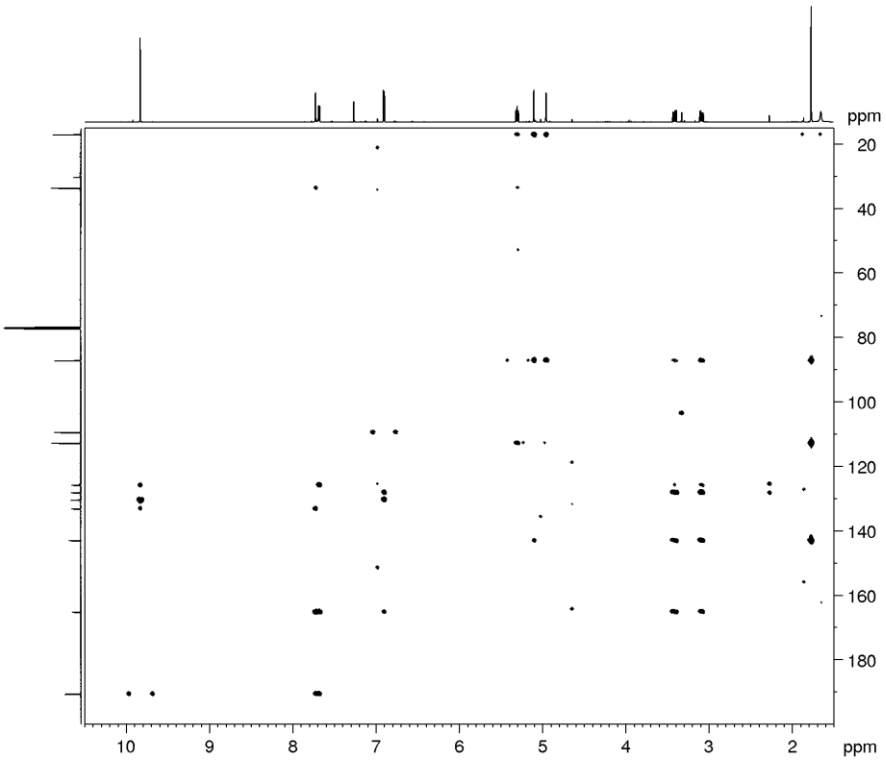

Figure A127. HMBC spectrum of **XB-3** (600 MHz, $CDCl_3$, 295 K

Spectra and spectral data on **XB-4**

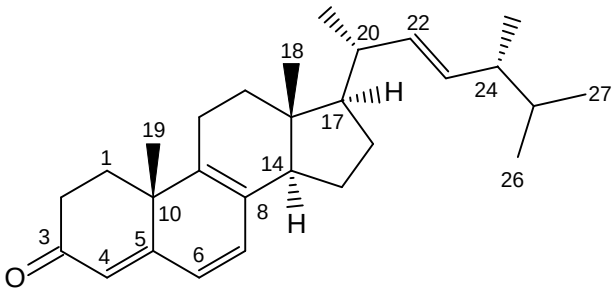

Ergosta-4,6,8[9]22-tetraene-3-one (**XB-4**): amorphous solid; HRMS *m/z* 393.3145 $[M+H]^+$ (Δ 1.6 ppm; $C_{28}H_{41}O$); HRMSMS (CID = 15%, 30%, 45%; rel int %) *m/z* 268

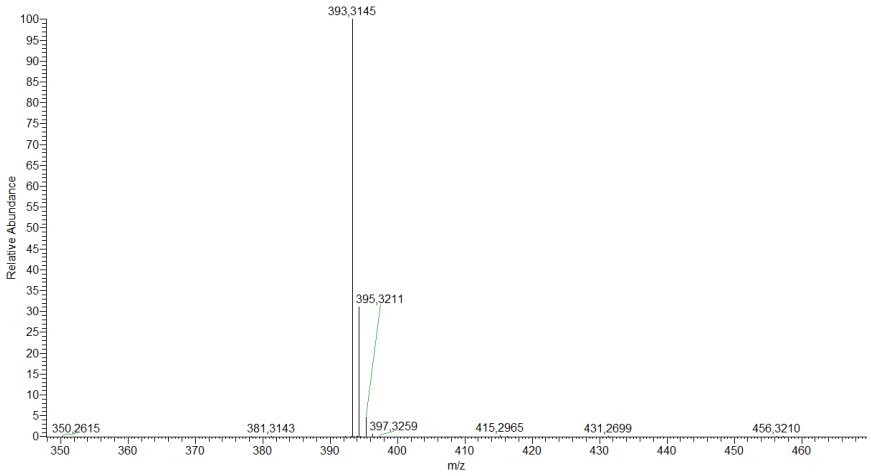

Figure A128. HRMS spectrum of **XB-4**

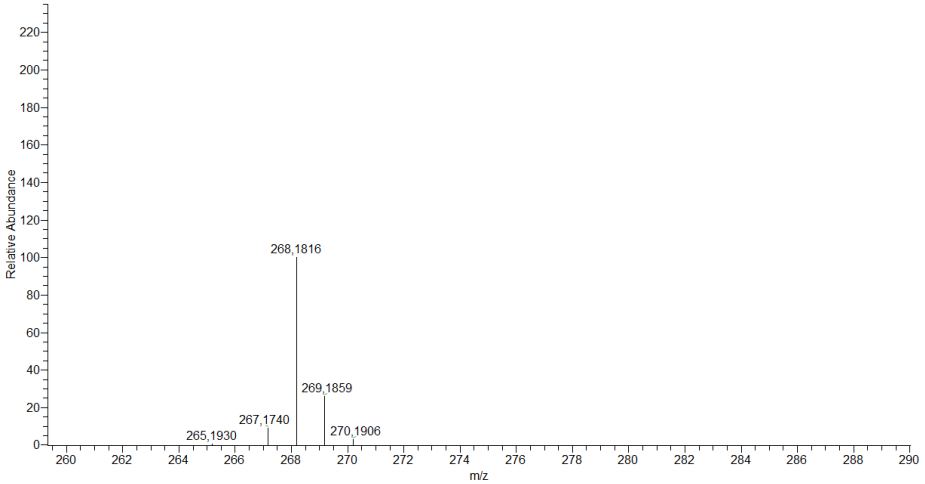

Figure A129. MS-MS spectrum of **XB-4**

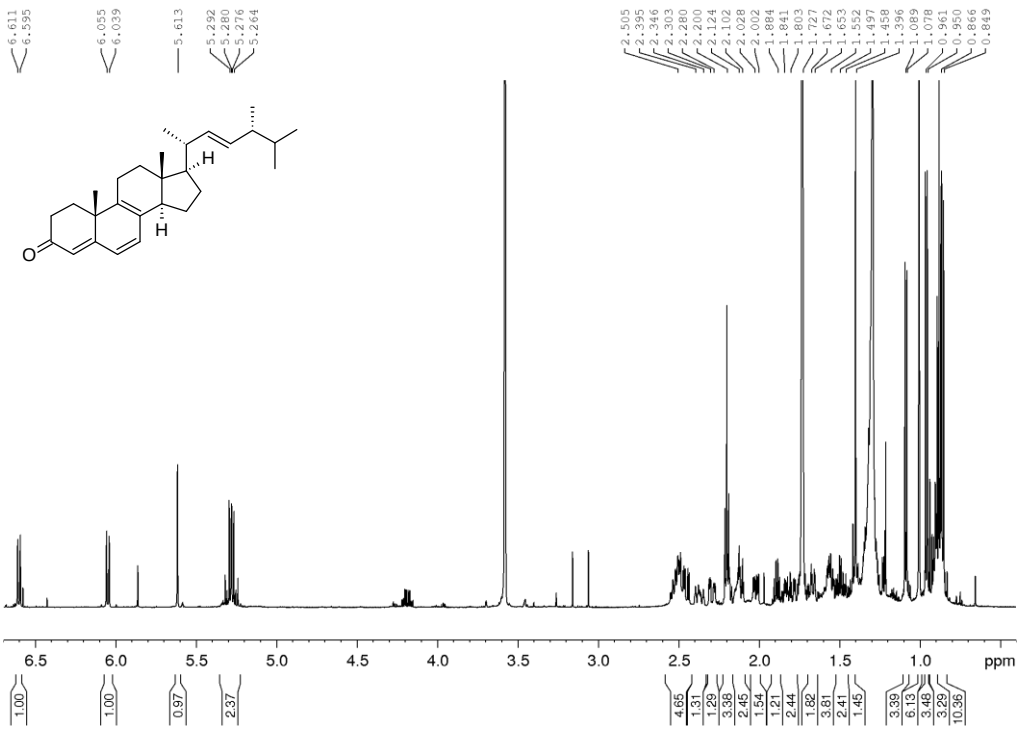

Figure A130. ^{1}H spectrum of **XB-4** (600 MHz, THF-d_8, 295 K)

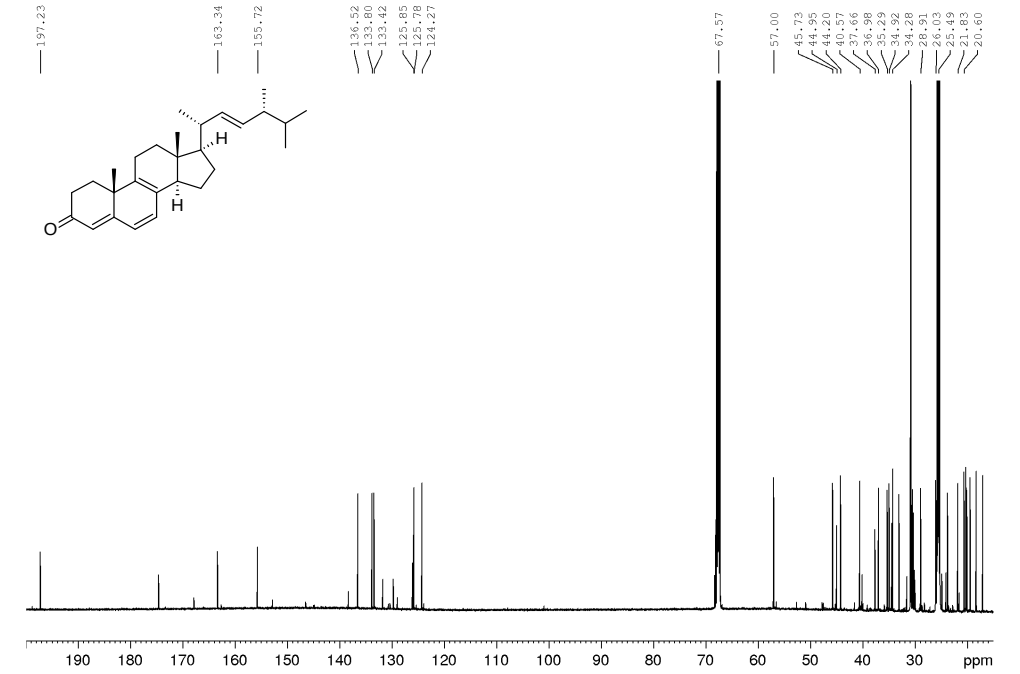

Figure A131. ^{13}C spectrum of **XB-4** (150 MHz, THF-d_8, 295 K)

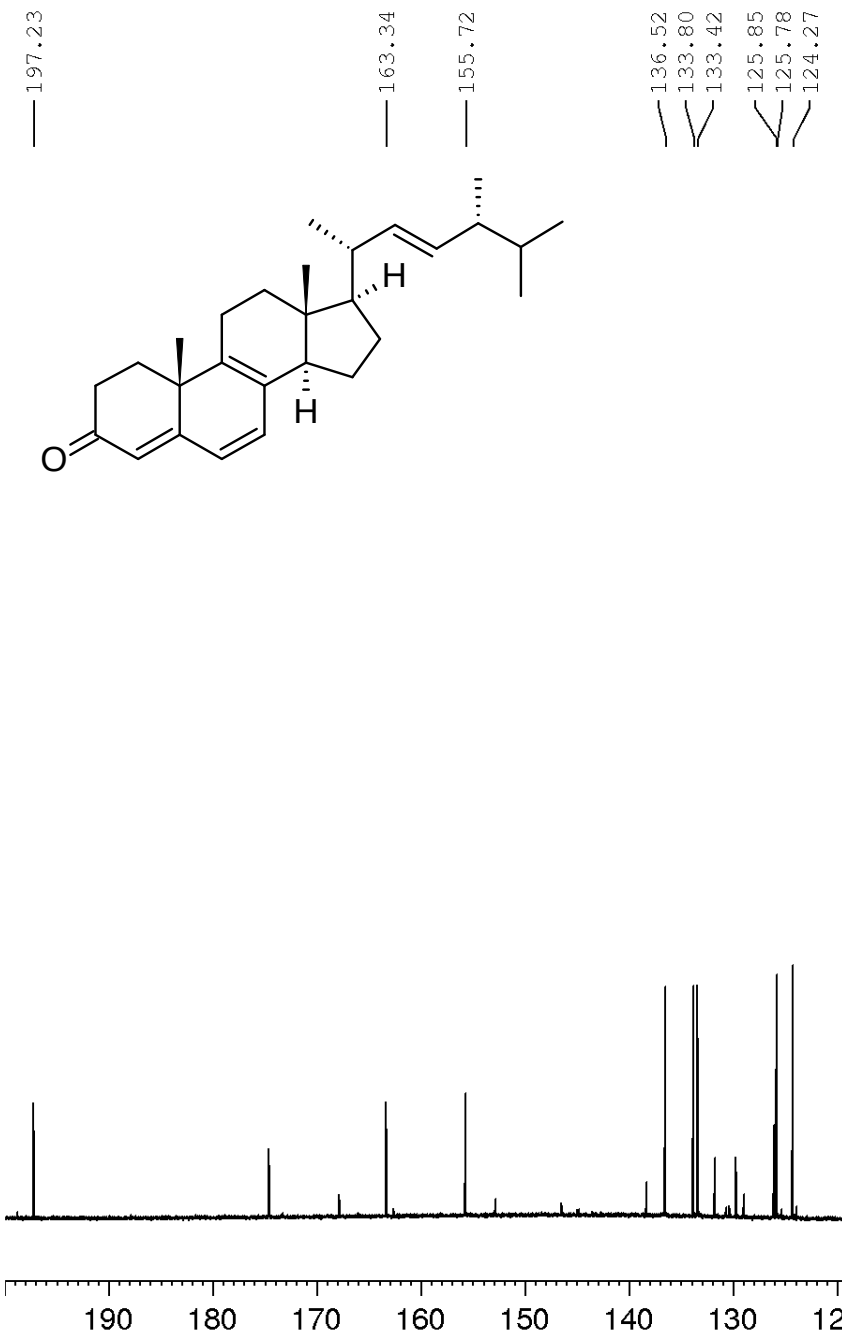
197.23
163.34
155.72
136.52
133.80
133.42
125.85
125.78
124.27
H
H
O
190
180
170
160
150
140
130
120
110
100
90
80
70

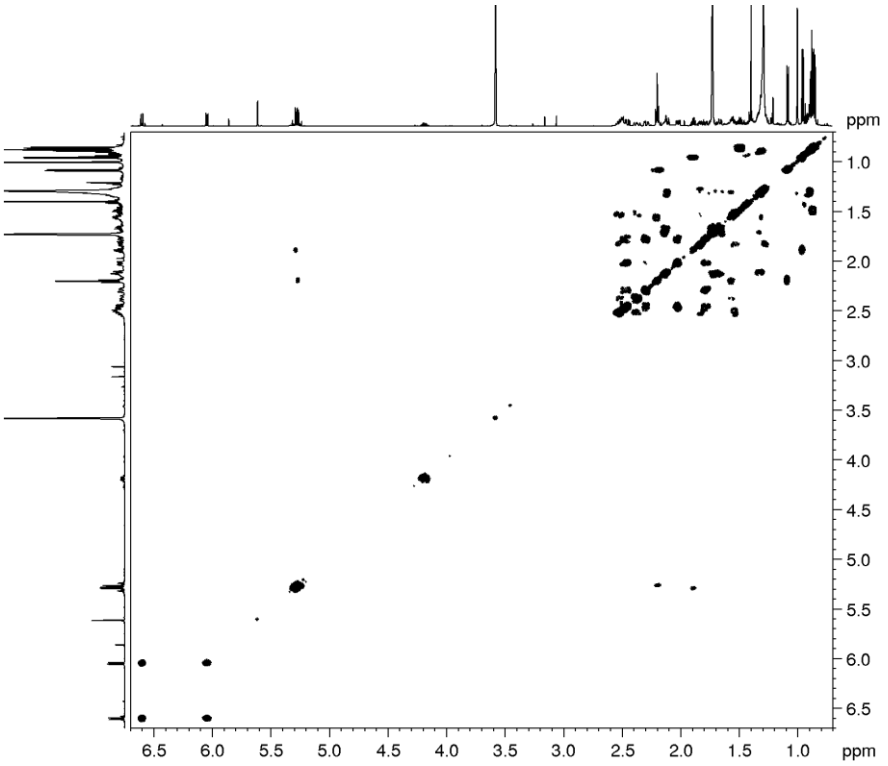

Figure A132. COSY spectrum of **XB-4** (600 MHz, THF-d_8, 295 K)

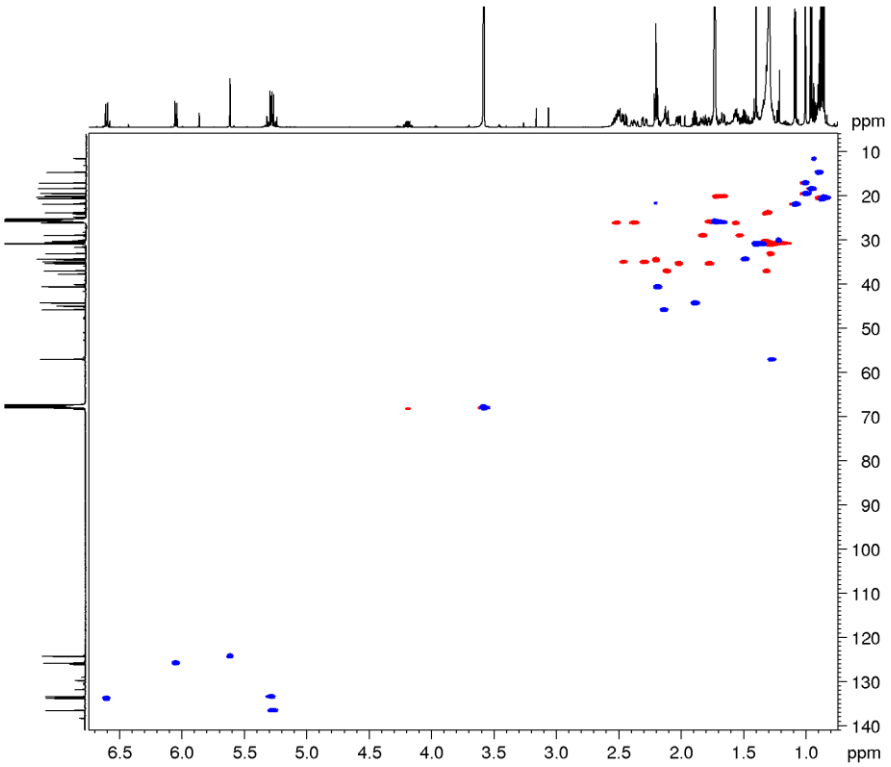

Figure A133. DEPT-edited HSQC spectrum of **XB-4** (600 MHz, THF-d_8, 295 K)

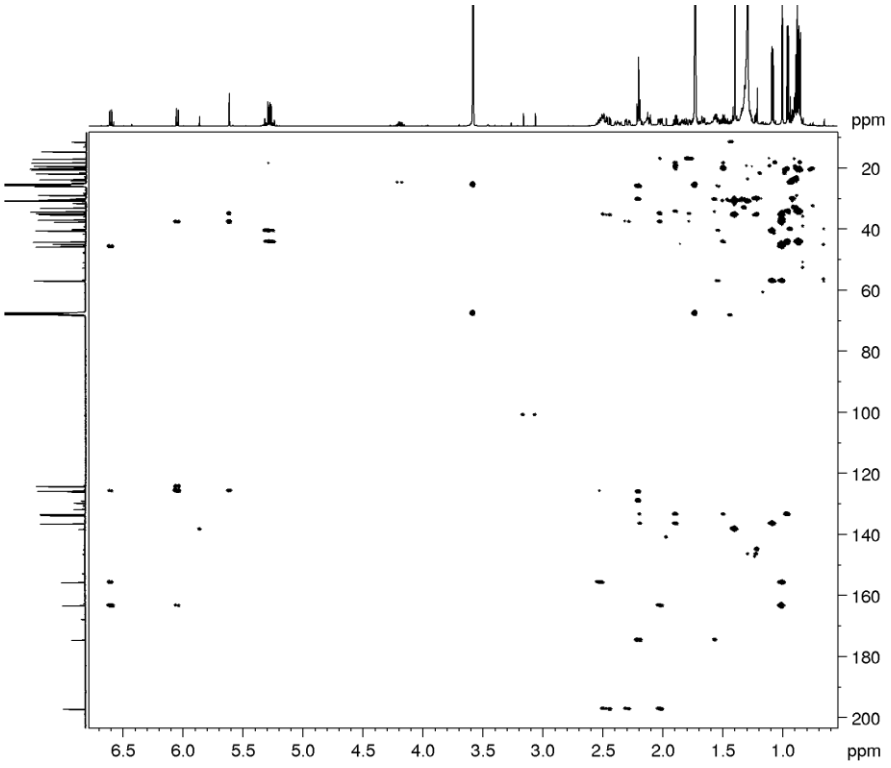

Figure A134. HMBC spectrum of **XB-4** (600 MHz, THF-d_8, 295 K)

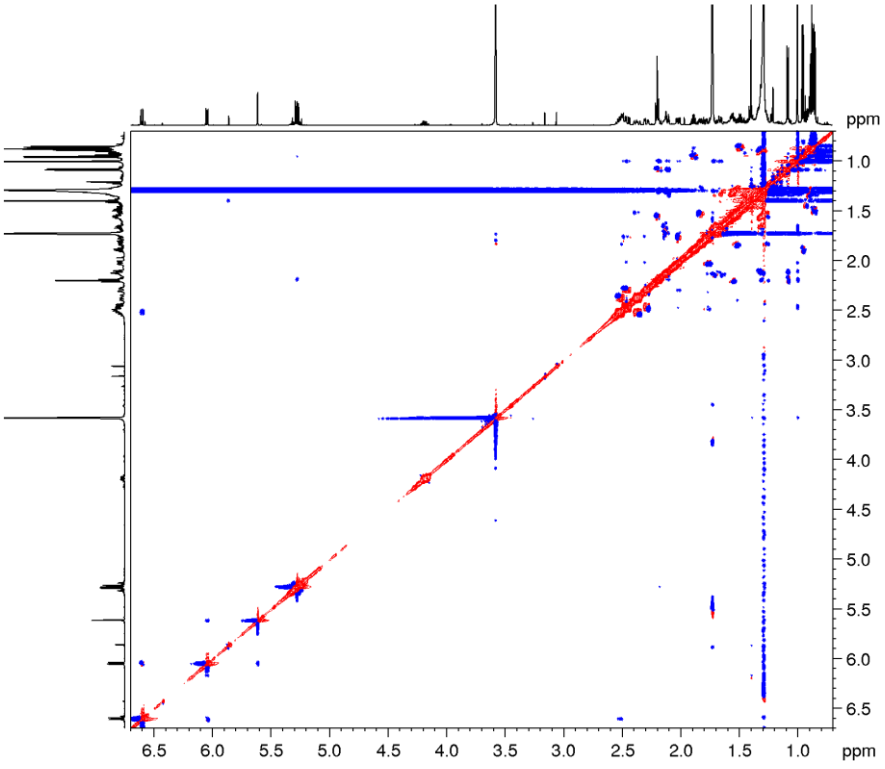

Figure A135. ROESY spectrum of **XB-4** (600 MHz, THF-d_8, 295 K)

Spectra and spectral data on **XB-5**

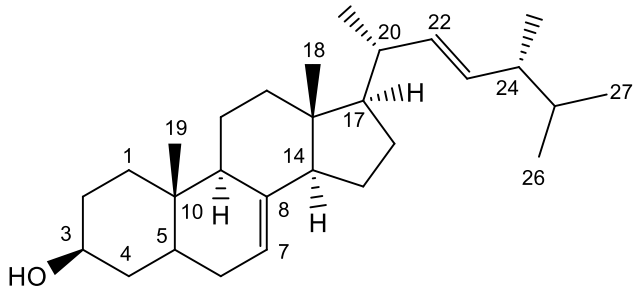

Ergosta-7,22-diene-3-ol (**XB-5**): amorphous solid; HRMS *m/z* no evaluable data.

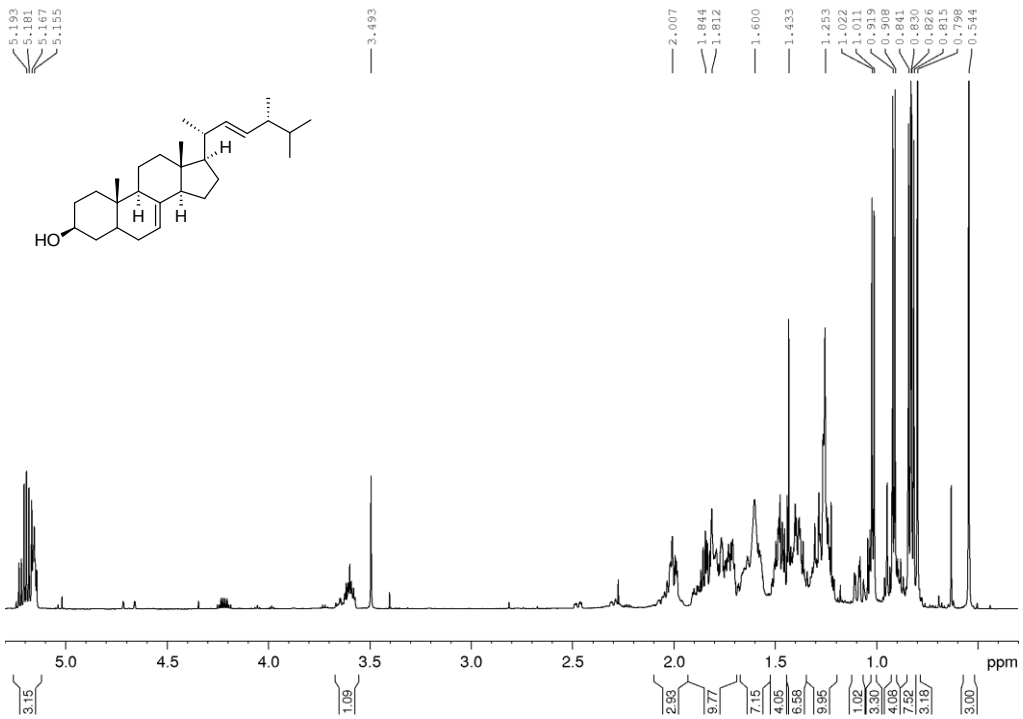

Figure A136. ^{1}H spectrum of **XB-5** (600 MHz, $CDCl_3$, 295 K)

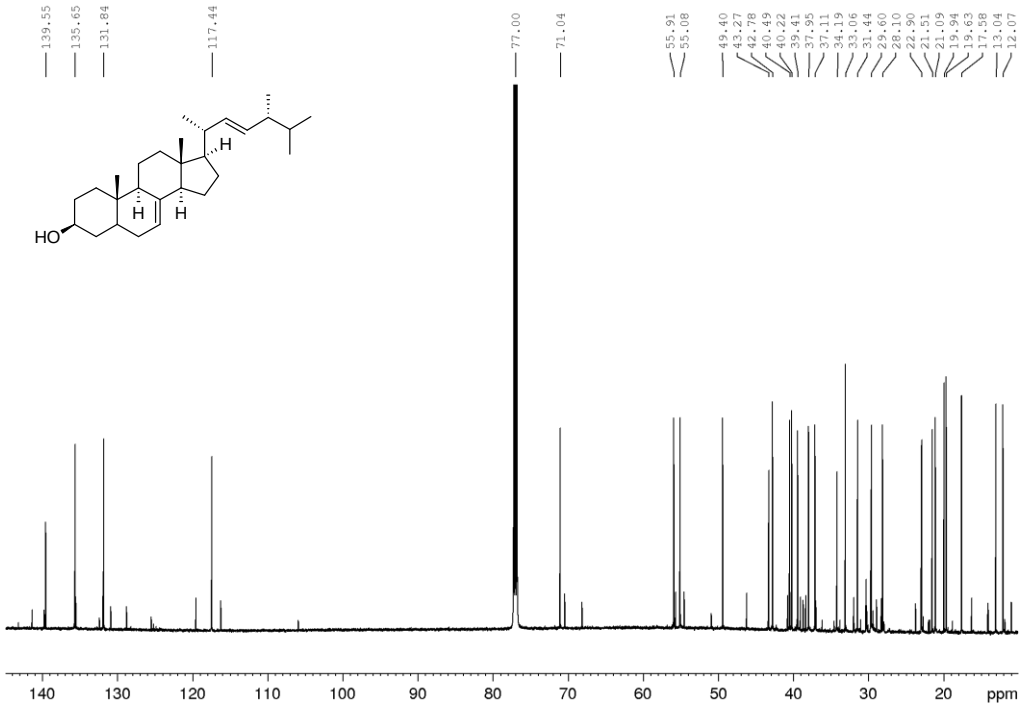

Figure A137. ^{13}C spectrum of **XB-5** (150 MHz, $CDCl_3$, 295 K)

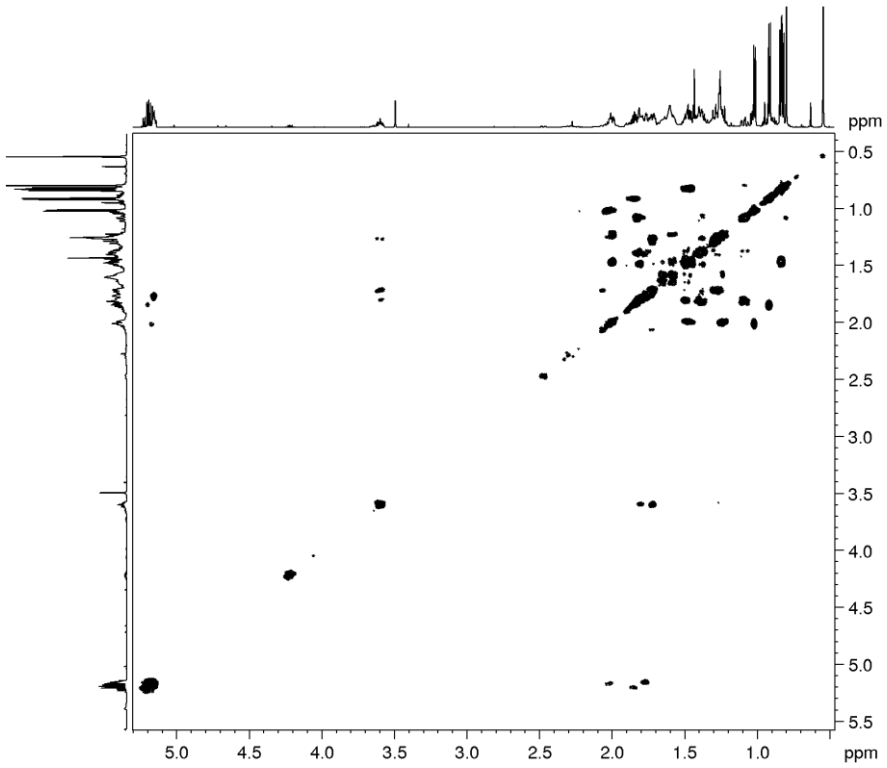

Figure A138. COSY spectrum of **XB-5** (600 MHz, $CDCl_3$, 295 K)

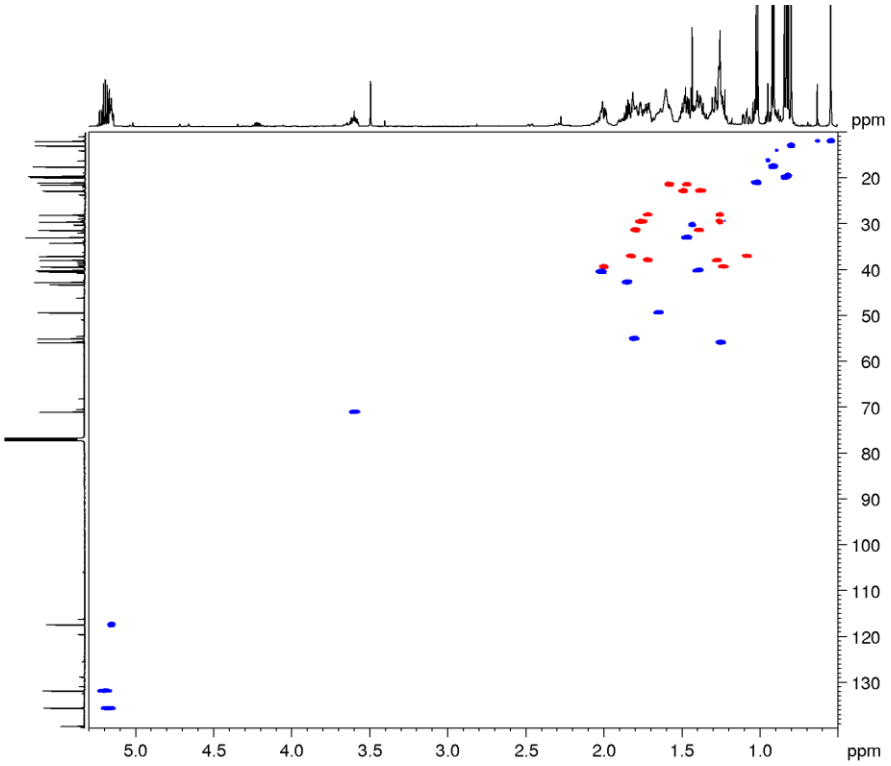

Figure A139. DEPT-edited HSQC spectrum of **XB-5** (600 MHz, $CDCl_3$, 295 K)

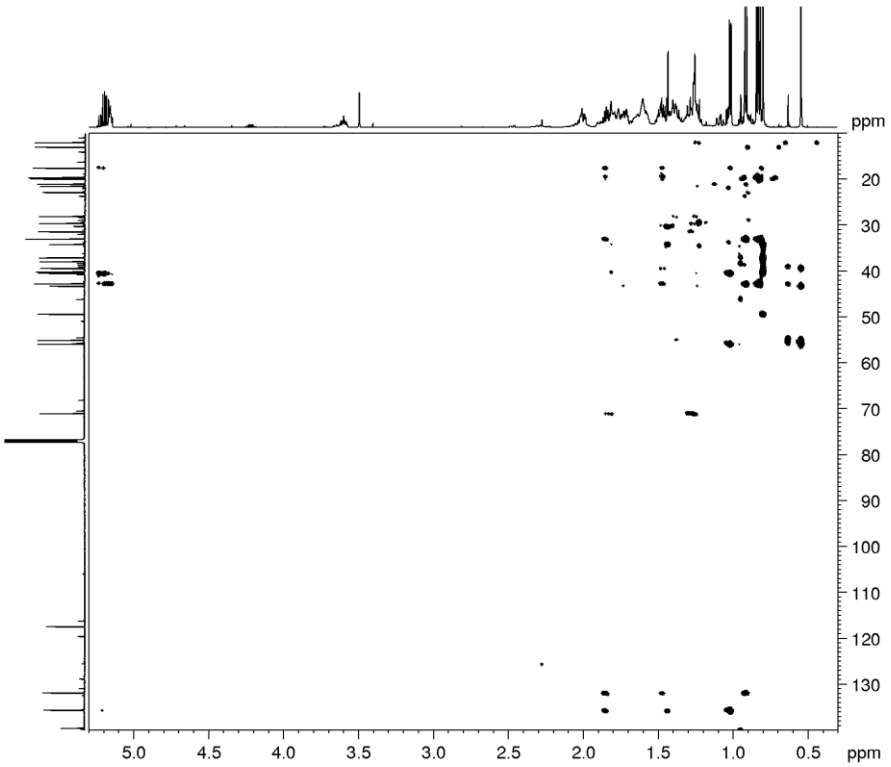

Figure A140. HMBC spectrum of **XB-5** (600 MHz, $CDCl_3$, 295 K)

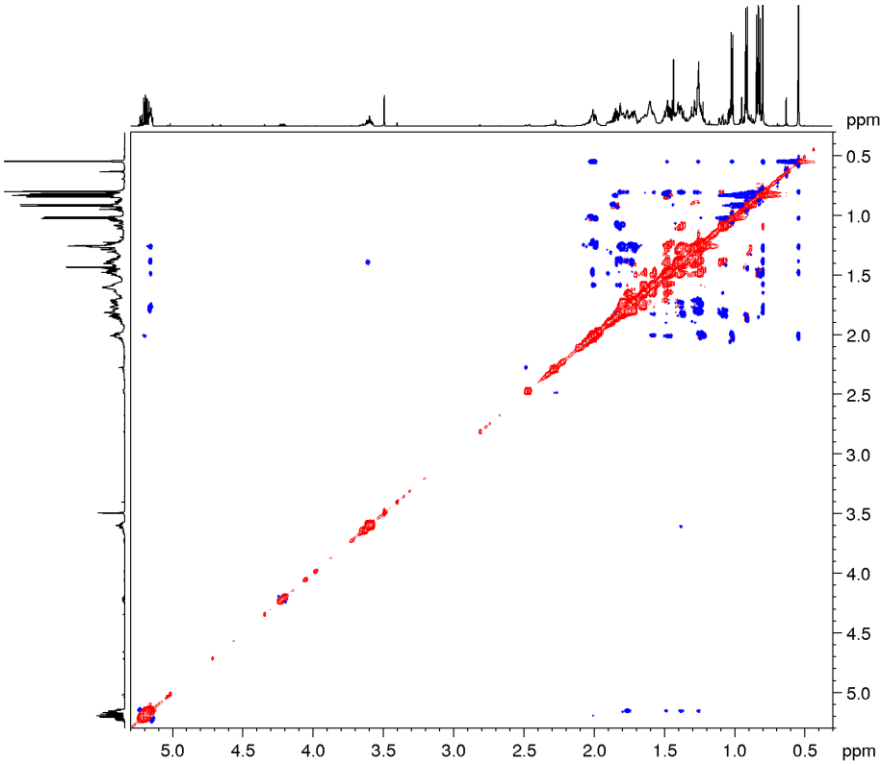

Figure A141. ROESY spectrum of **XB-5** (600 MHz, $CDCl_3$, 295 K)

Spectra and spectral data on **XB-6**

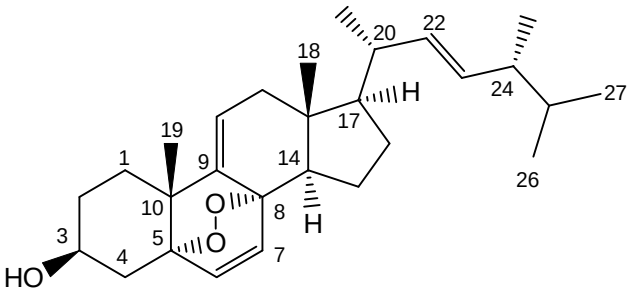

9,11-Dehydroergosterol peroxide **(XB-6)**: amorphous solid; HRMS *m/z* 427.3202 $[M+H]^+$ (Δ 1.1 ppm; $C_{28}H_{43}O_3$); HRMSMS (CID = 15%, 30%, 45%; rel int %) *m/z* 409), 391, 375

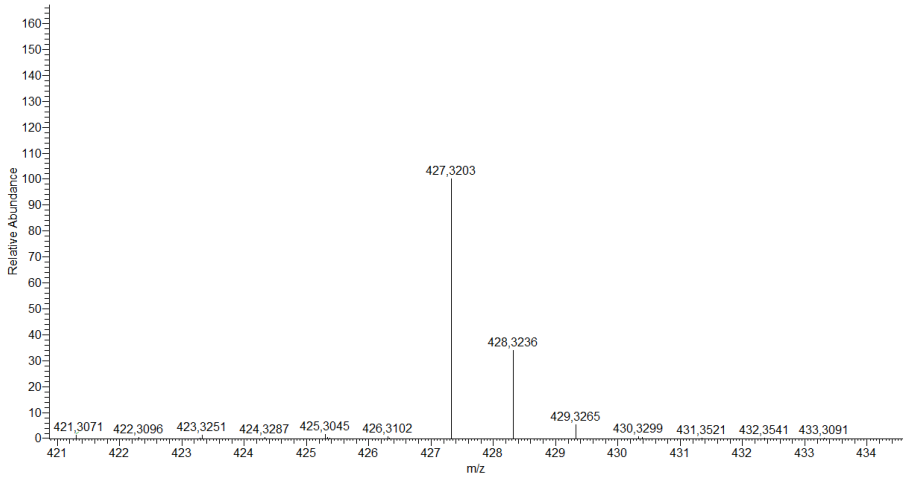

Figure A142. HRMS spectrum of **XB-6**

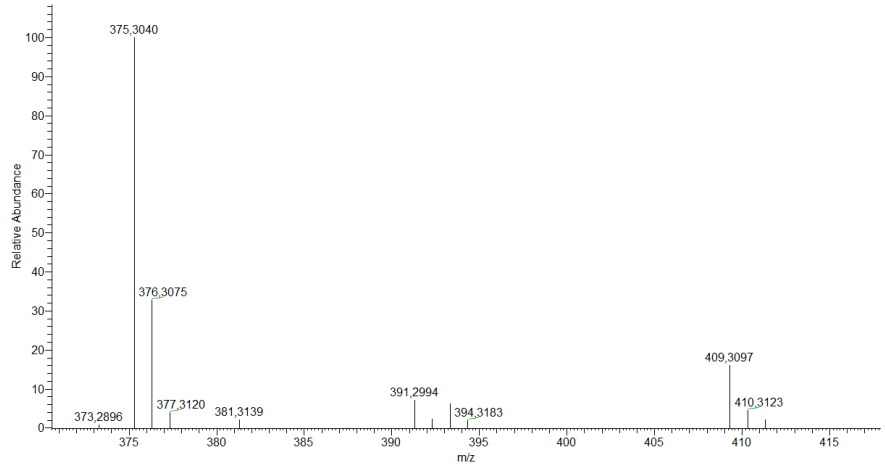

Figure A143. MS-MS spectrum of **XB-6**

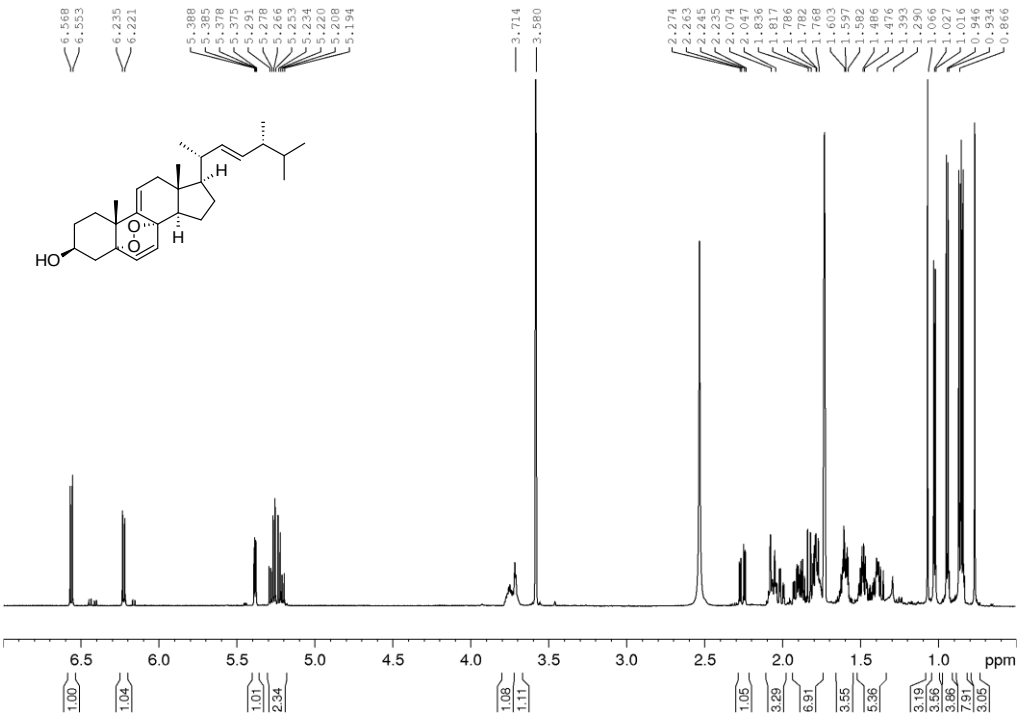

Figure A144. ^{1}H spectrum of **XB-6** (600 MHz, THF-d_8, 295 K)

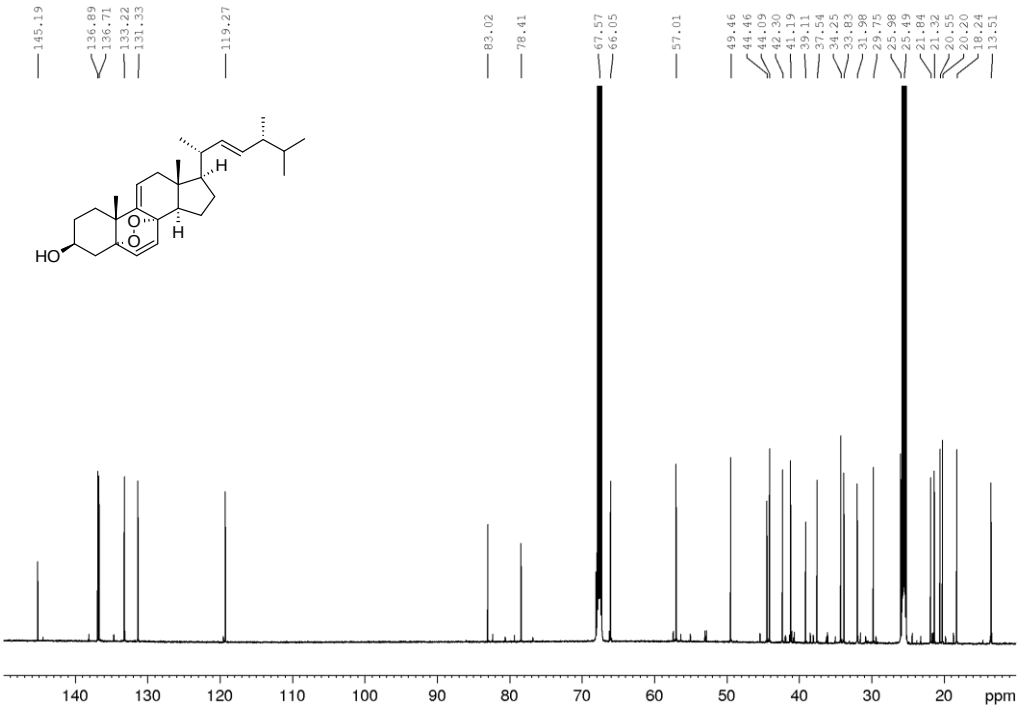

Figure A14512. ^{13}C spectrum of **XB-6** (150 MHz, THF-d_8, 295 K)

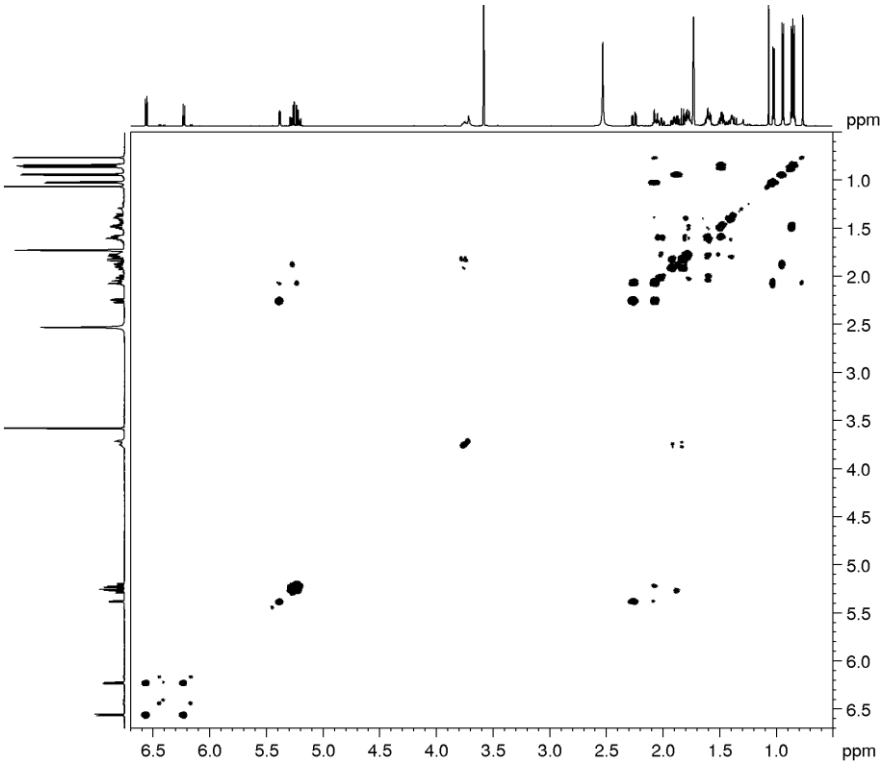

Figure A146. COSY spectrum of **XB-6** (600 MHz, THF-d_8, 295 K)

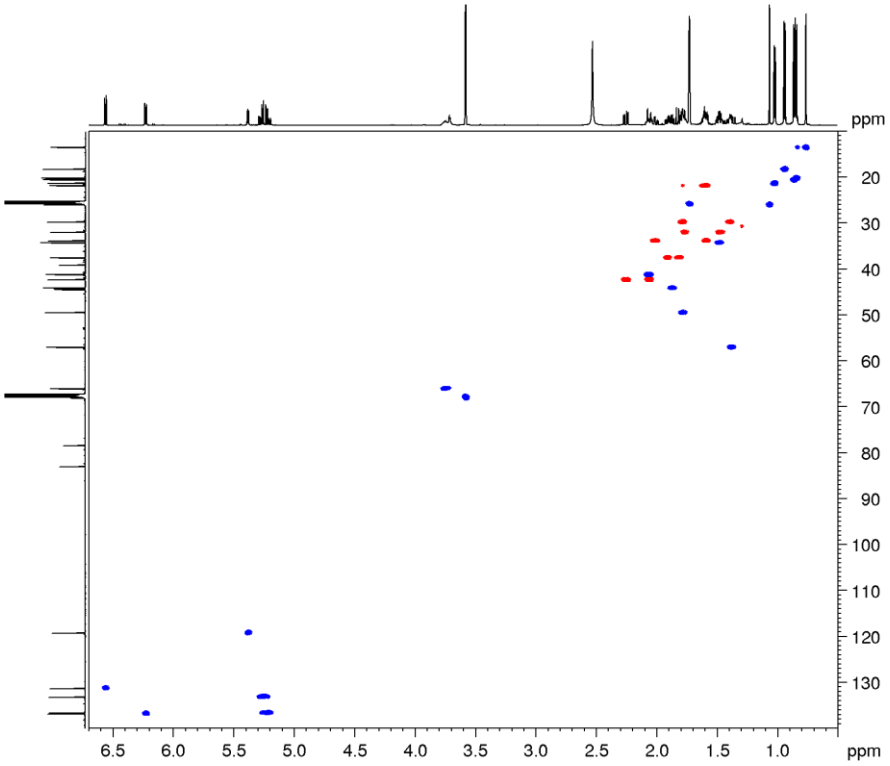

Figure A147. DEPT-edited HSQC spectrum of **XB-6** (600 MHz, THF-d_8, 295 K)

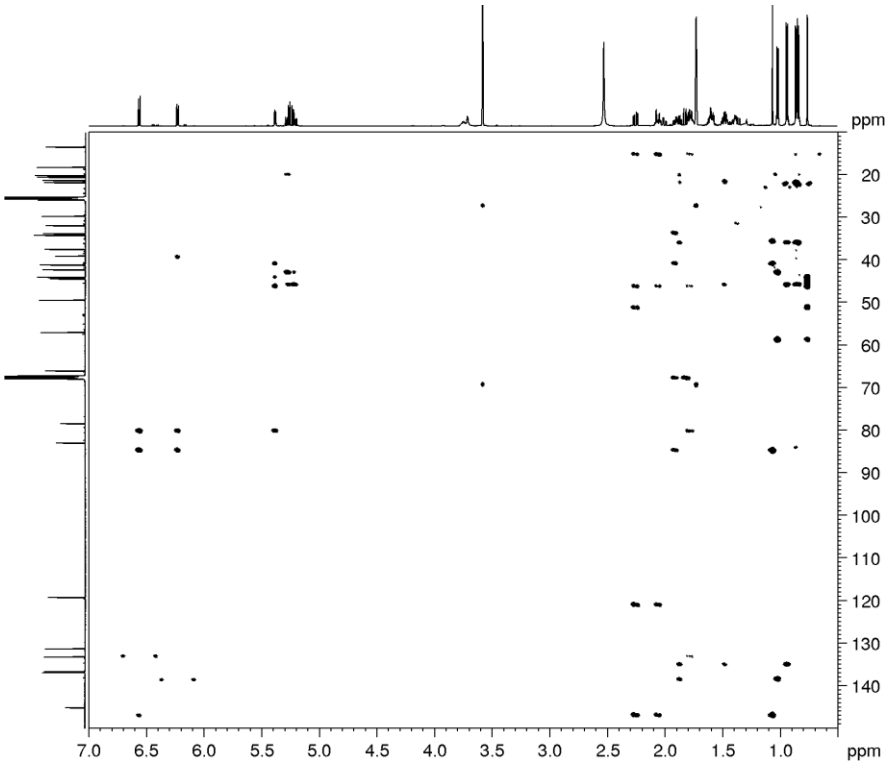

Figure A148. HMBC spectrum of **XB-6** (600 MHz, THF-d_8, 295 K)

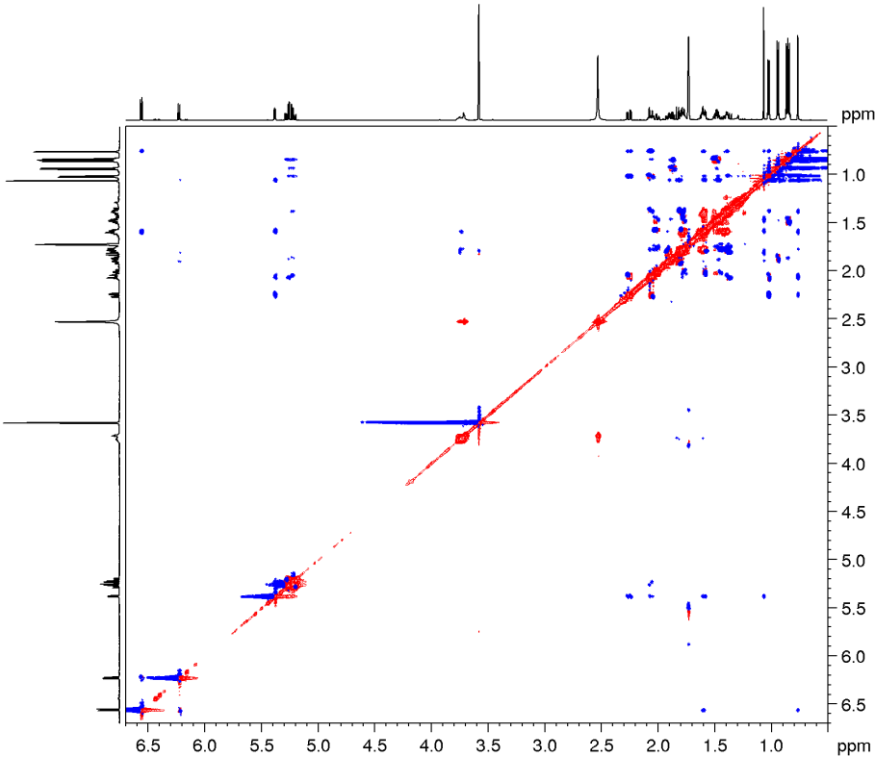

Figure A149. ROESY spectrum of **XB-6** (600 MHz, THF-d_8, 295 K)

Spectra and spectral data on **XB-7**

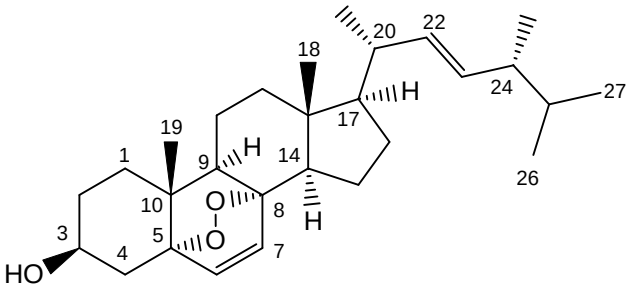

Ergosta-5,7,22-triene-3-ol (**XB-7**): amorphous solid; HRMS *m/z* 429.3359 $[M+H]^+$ (Δ 0.8 ppm; $C_{28}H_{45}O_3$); HRMSMS (CID = 15%, 30%, 45%; rel int %) *m/z* 411, 393, 377

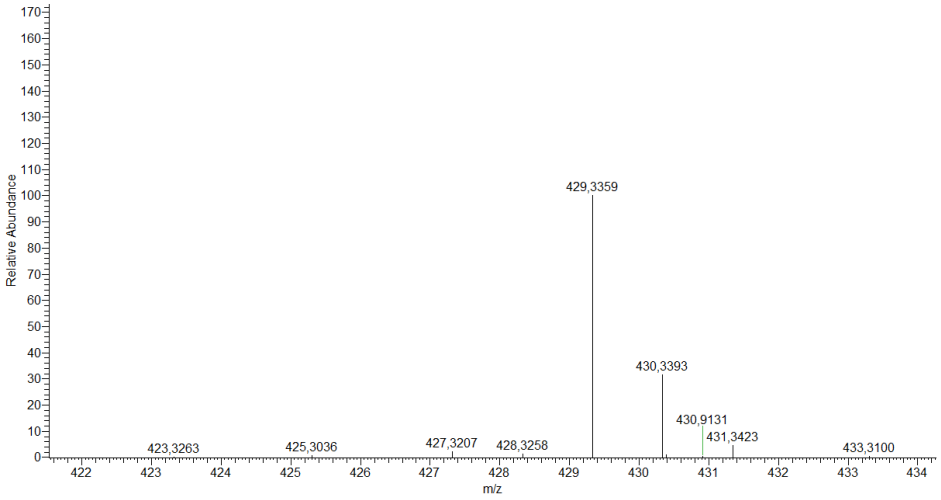

Figure A150. HRMS spectrum of **XB-7**

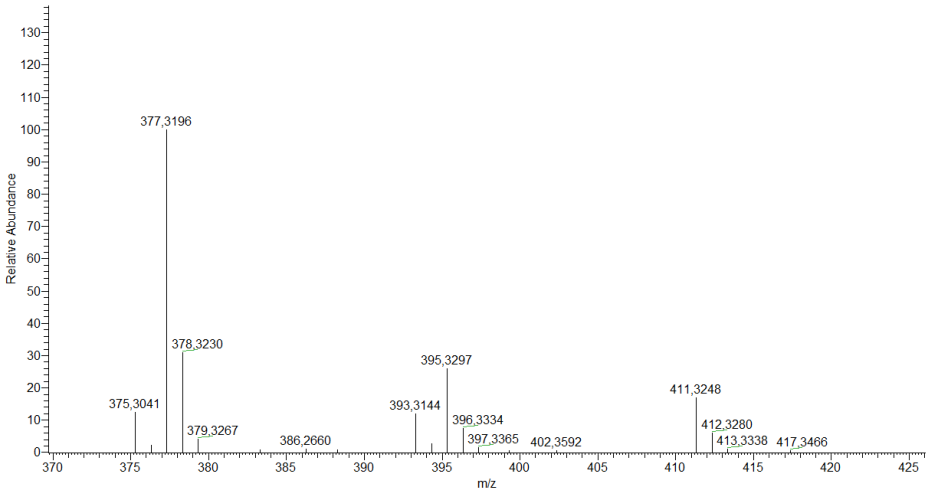

Figure A151. MS-MS spectrum of **XB-7**

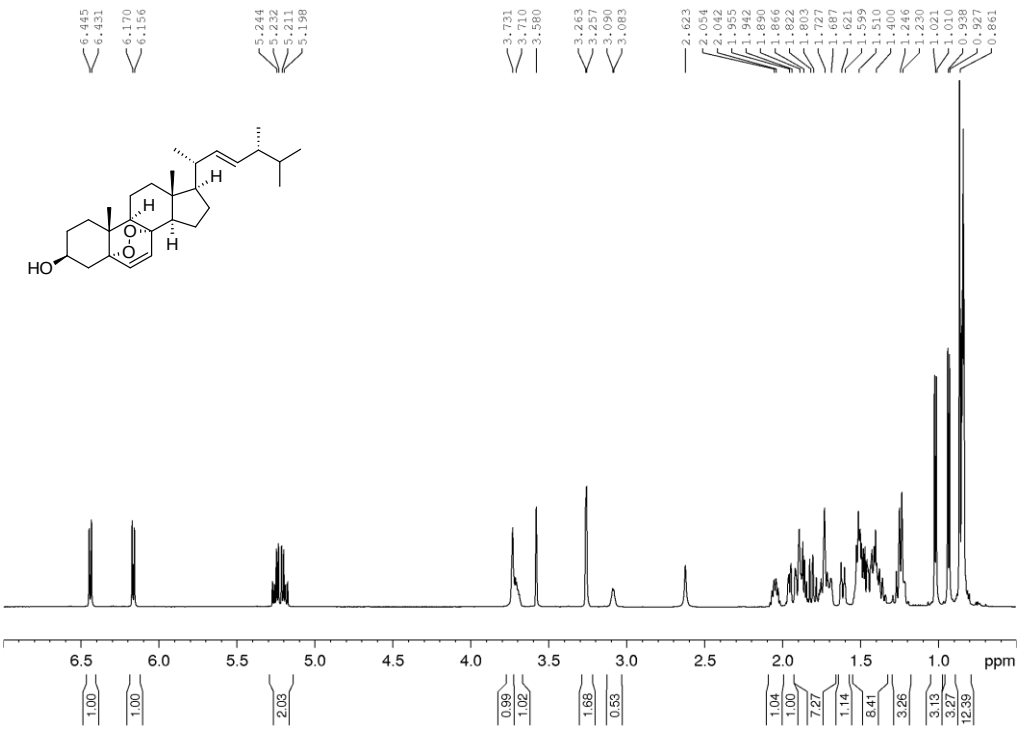

Figure A152. ^{1}H spectrum of **XB-7** (600 MHz, THF-d_8, 295 K)

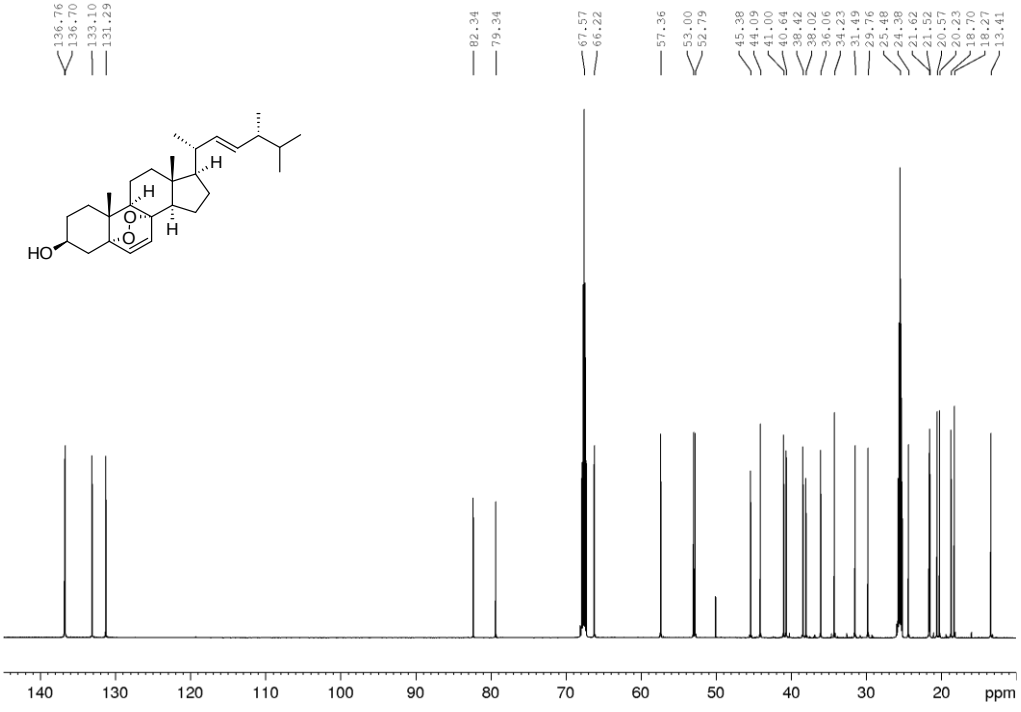

Figure A153. ^{13}C spectrum of **XB-7** (150 MHz, THF-d_8, 295 K)

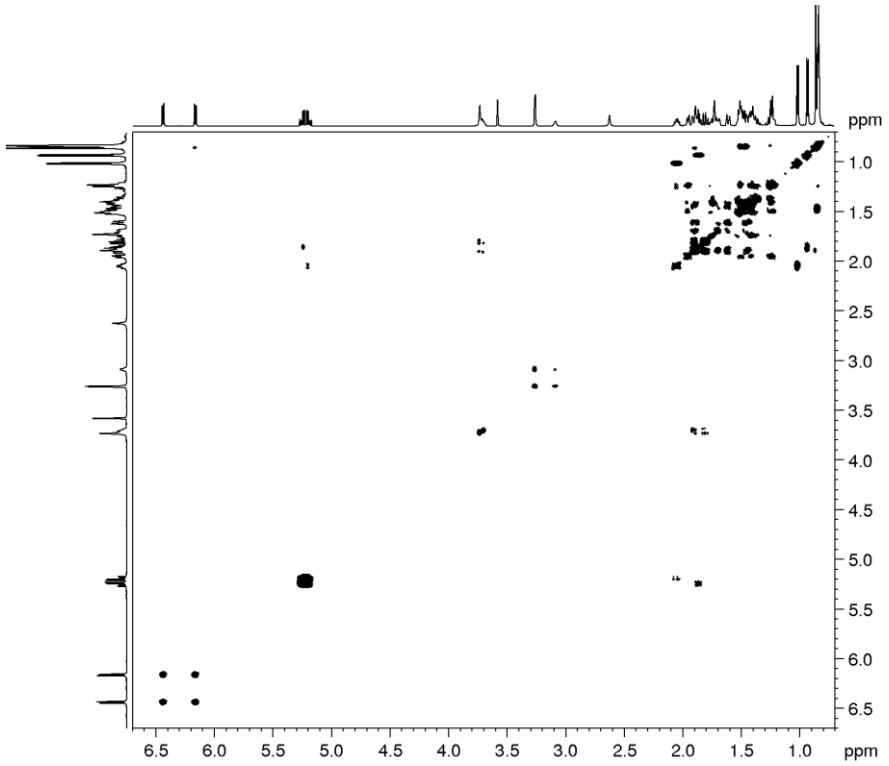

Figure A154. COSY spectrum of **XB-7** (600 MHz, THF-d_8, 295 K)

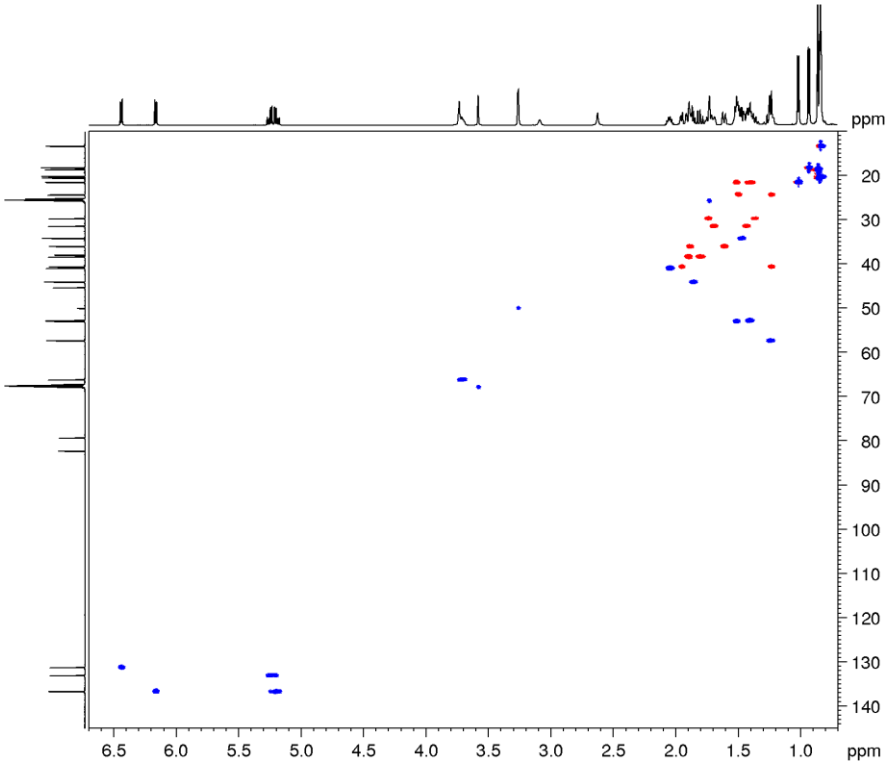

Figure A1135. DEPT-edited HSQC spectrum of **XB-7** (600 MHz, THF-d_8, 295 K)

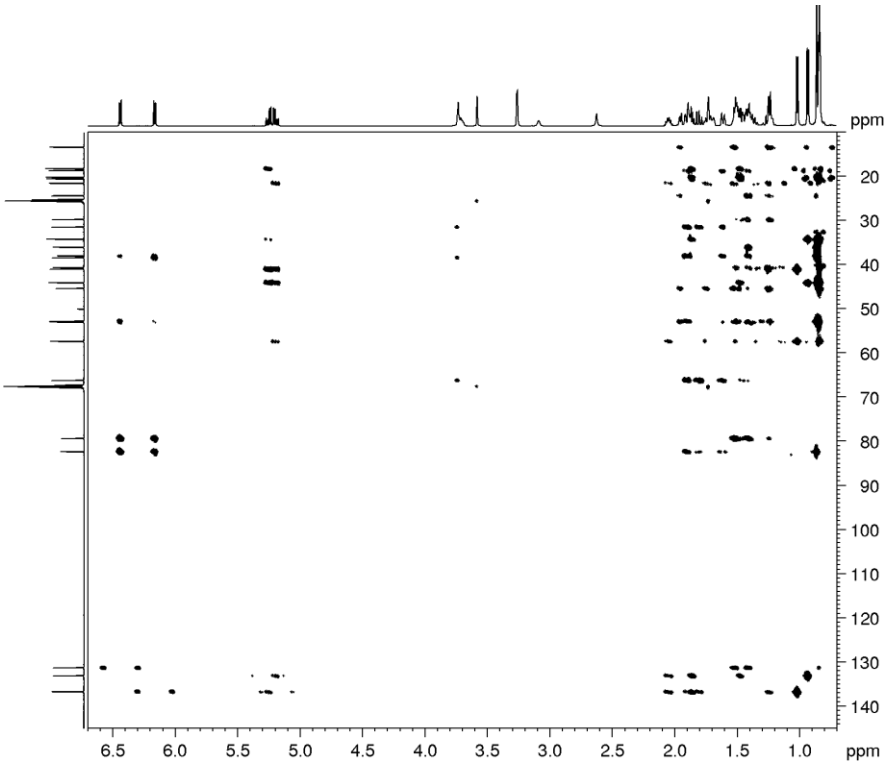

Figure A156. HMBC spectrum of **XB-7** (600 MHz, THF-d_8, 295 K)

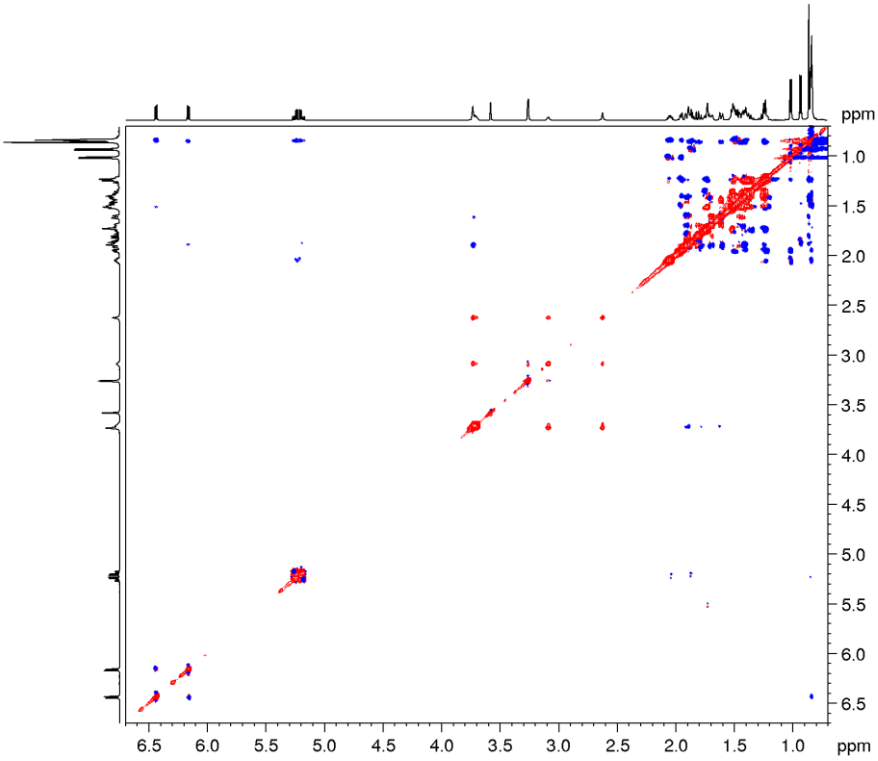

Figure A157. ROESY spectrum of **XB-7** (600 MHz, THF-d_8, 295 K)

Table A3. Complete ^{1}H and ^{13}C NMR resonance assignments for **XB-4-7**.

No.	4			6				7		5		
	δ ^{13}C	**δ ^{1}H**	**m, *J***	**δ ^{13}C**	**δ ^{1}H**	**m, *J***	**δ ^{13}C**	**δ ^{1}H**	**m, *J***	**δ ^{13}C**	**δ ^{1}H**	**m, *J***
1	35.3	2.02	m	37.1	1.82	m	33.8	2.01	m	36.1	1.88	m
		1.77	m		1.08	m		1.59	m		1.61	m
2	34.9	2.46	m	38.0	1.72	m	32.0	1.76	m	31.5	1.67	m
		2.29	m		1.28	m		1.47	m		1.43	m
3	197.2	-	-	71.0	3.60	m	66.1	3.75	m	66.2	3.71	m
4	124.3	5.61	s	31.4	1.80	m	37.5	1.90	m	38.4	1.89	m
					1.39	m		1.82	m		1.80	m
5	163.3	-	-	40.2	1.40	m	83.0	-	-	82.3	-	-
6	125.8	6.05	d, 9.5 Hz	29.6	1.76	m	136.9	6.23	d, 8.5 Hz	136.7	6.16	d, 8.5 Hz
7	133.8	6.60	d, 9.5 Hz	117.4	5.16	m	131.3	6.56	d, 8.5 Hz	131.3	6.44	d, 8.5 Hz
8	125.9	-	-	139.6	-	-	78.4	-	-	79.3	-	-
9	155.7	-	-	49.4	1.65	m	145.2	-	-	52.8	1.40	m
10	37.7	-	-	34.2	-	-	39.1	-	-	38.0	-	-
11	26.0	2.51	m	21.5	1.58	m	119.3	5.38	dd, 6.0. 1.9 Hz	24.4	1.49	m
		2.37	m		1.47	m					1.23	m
12	37.0	2.11	m	39.4	2.00	m	42.3	2.25	dd, 16.8. 6.0 Hz	40.6	1.94	m
		1.31	m		1.23	m		2.06	m		1.23	m
13	45.0	-	-	43.3	-	-	44.5	-	-	45.4	-	-

14	45.7	2.13	m	55.1	1.81	m	49.5	1.78	m	53.0	1.51	m
			m	22.9	1.49	m						
15	20.1	1.71	m		1.38	m	21.8	1.60	m	21.6	1.51	m
		1.66	m	28.1	1.72	m					1.40	m
16	28.9	1.82	m		1.25	m	29.8	1.79	m	29.8	1.73	m
		1.52	m	55.9	1.25	m		1.39	m		1.37	m
17	57.0	1.27	m	12.1	0.54	s	57.0	1.38	m	57.4	1.24	m
18	19.4	1.00	s	13.0	0.80	s	13.5	0.76	s	13.4	0.83	m
19	17.1	1.00	s	40.5	2.01	m	26.0	1.07	s	18.7	0.86	m
20	40.6	2.19	m	21.1	1.02	d, 6.8 Hz	41.2	2.07	m	41.0	2.04	m
21	21.8	1.08	d, 6.7 Hz	135.7	5.17	m	21.3	1.02	d, 6.7 Hz	21.5	1.02	d, 6.5 Hz
22	136.5	5.27	m	131.8	5.20	m	136.7	5.23	m	136.8	5.20	m
23	133.4	5.28	m	42.8	1.85	m	133.2	5.26	m	133.1	5.23	m
24	44.2	1.89	m	33.1	1.47	m	44.1	1.87	m	44.1	1.86	m
25	34.3	1.48	m	19.6	0.82	d, 6.8 Hz	34.3	1.48	m	34.2	1.47	m
26	20.2	0.85	d, 6.8 Hz	19.9	0.84	d, 6.8 Hz	20.2	0.84	d, 6.8 Hz	20.2	0.83	m
27	20.6	0.87	d, 6.8 Hz	17.6	0.91	d, 6.8 Hz	20.6	0.86	d, 6.8 Hz	20.6	0.85	m
28	18.3	0.96	d, 6.8 Hz				18.2	0.94	d, 6.8 Hz	18.3	0.93	m